UNIVERSITÉ DE MONTRÉAL

NON-INVASIVE NEAR-FIELD MEASUREMENT SETUP BASED ON MODULATED SCATTERER TECHNIQUE APPLIED TO MICROWAVE TOMOGRAPHY

HAMIDREZA MEMARZADEH-TEHRAN
DÉPARTEMENT DE GÉNIE ÉLECTRIQUE
ÉCOLE POLYTECHNIQUE DE MONTRÉAL

THÈSE PRÉSENTÉE EN VUE DE L'OBTENTION DU DIPLÔME DE
PHILOSOPHIÆ DOCTOR
(GÉNIE ÉLECTRIQUE)
JUILLET 2010

UNIVERSITÉ DE MONTRÉAL

ÉCOLE POLYTECHNIQUE DE MONTRÉAL

Cette thèse intitulée:

NON-INVASIVE NEAR-FIELD MEASUREMENT SETUP BASED ON MODULATED SCATTERER TECHNIQUE APPLIED TO MICROWAVE TOMOGRAPHY

présentée par: M. MEMARZADEH-TEHRAN Hamidreza, M.A.Sc
en vue de l'obtention du diplôme de: Philosophiæ Doctor
a été dûment acceptée par le jury constitué de:

M. AKYEL Cevdet, Ph.D., président.
M. LAURIN Jean-Jacques, Ph.D., membre et directeur de recherche.
M. KASHYAP Raman, Ph.D., membre et co-directeur de recherche.
M. BOUTAYEB Halim, Ph.D., membre.
M. BOLOMEY Jean-Charles, Ph.D., membre externe.

To my respected family.

Acknowledgements

First of all, I would like to thank Prof. Jean-Jacques Laurin, my supervisor, who let me join his group and opened for me a new horizon in my academic life. His patience, guidance, support, and also encouragement made the duration of my PhD program a wonderful and enjoyable experience. He also taught me how I can do a great job with principles by looking at them accurately and in detail.

I also would like to thank Prof. Raman Kashyap, my co-supervisor, whose support, mentoring and kindness were always there to help me move forward to solve problems in my PhD project. Moreover, I learnt from him to look at thing in a simple way which helped me overcome big obstacles over the past five years.

I would like to thank the members of the jury for considering my thesis.

I would like to thank our high-expertise technicians, Jules Gauthier, Steve Dube, Jean-Sébastien Decarie, and also Traian Antonescu, that without their help this project never becomes the end-all.

At the end, I also would like to specially thank Ginette Desparois, our secretary in Poly-Grames research center, whose help for me particularly in administrative paperwork was amazing.

Résumé

L'objectif principal de cette thèse est d'aborder la conception et le développement d'un montage d'imagerie en champ proche (CP) basé sur la technique de diffusion modulé (TDM). La TDM est une approche bien connue et utilisée pour des applications où des mesures précises et sans perturbations sont nécessaire. Parmi les applications possibles disponibles pour la fabrication d'une sonde TDM, que ce soit électrique, optique, mécanique, le diffuseur optique modulé DOM a été pris en considération afin de fournir des mesures quasi sans-perturbations en raison de l'invisibilité des fibres optiques face aux champs radiofréquence électromagnétiques. La sonde est composée d'une puce photodiode commerciale "off-the-shelf" (dispositif non-linéaire), d'une antenne dipôle courte agissant comme diffuseur et un réseau d'adaptation (circuit passif). Cet dernieér améliore les propriétés de diffusion et augmente également la sensibilité de la sonde DOM dans la bande de fréquence pour laquelle le réseau correspondant est optimisé. Les caractéristiques de rayonnement de la sonde, y compris sa réponse de polarisation croisée et sa sensibilité omnidirectionnelle, ont été théoriquement et expérimentalement étudiés. Enfin, la performance et la fiabilité de la sonde a été étudiée en comparant des mesures de distribution de champs proche avec une distribution de champs simulé. Une vitesse d'imagerie accrue a été obtenue utilisant un réseau de sondes DOM, ce qui réduit les mouvements mécaniques résultant ansi en une amélioration remarquable de la vitesse de mesure. Le couplage mutuel, le temps de commutation et l'effet d'obscurité, des effets qui peuvent affecter les performances du réseau ont été explorés. Ensuite, les résultats obtenus par le réseau ont été validé par une imagerie CP en mesurant la distribution des champs E d'une antenne sous test (AST) et la comparant à des résultats de simulation. Une calibration et un calcul de moyenne ont été appliqués à des données brutes pour compenser pour les incertitudes dans la fabrication et l'interaction entre réseau/AST et réseau/antenne de réception. La plage dynamique et la linéarité de la réponse de l'imagerie CP ont été améliorées en ajoutant un circuit suppresseur de porteuse en avant de l'antenne. Le suppresseur élimine la porteuse sur laquelle aucune information n'est transmise et laisse les bandes latérales intactes. Cela nous permet d'augmenter le gain d'amplification pour obtenir un meilleur rapport signal-bruit (RSB) et surtout

d'élargir la plage dynamique. La porteuse au port de réception est minimisée en combinant le signal reçu avec un signal hors phase de 180 dont l'amplitude et la phase sont ajustés de manière adaptative. Nous observons d'abord les performances du suppresseur, qui donne une réduction d'amplitude d'environ 60 dB de la porteuse, et étudions ensuite son impact sur les performances de l'imagerie CP. Des améliorations significatives des images CP ont été obtenues en termes de la portée dynamique et la linéarité.

Abstract

The main focus of this thesis is to address the design and development of a near-field (NF) imaging setup based on the modulated scatterer technique (MST). MST is a well-known approach used in applications where accurate and perturbation-free measurement results are necessary. Of the possible implementations available for making an MST probe, including electrical, optical and mechanical, the optically modulated scatterer OMS was considered in order to provide nearly perturbation-free measurement due to the invisibility of optical fiber to the radio-frequency electromagnetic fields. The OMS probe consists of a commercial, off-the-shelf (COTS) photodiode chip (nonlinear device), a short-dipole antenna acting as a scatterer and a matching network (passive circuit). The latter improves the scattering properties and also increases the sensitivity of the OMS probe within the frequency range in which the matching network is optimized. The radiation characteristics of the probe, including cross-polarization response and omnidirectional sensitivity, were both theoretically and experimentally investigated. Finally, the performance and reliability of the probe was studied by comparing measured near-field distributions on a known field distribution with simulations.

Increased imaging speed was obtained using an array of OMS probes, which reduces mechanical movements. Mutual-coupling, switching time and shadowing effect, which all may affect the performance of the array, were investigated. Then, the results obtained by the array were validated in a NF imager by measuring the E-field distribution of an antenna under test (AUT) and comparing it with a simulation. Calibration and data averaging were applied to raw data to compensate the probes for uncertainties in fabrication and interaction between array/AUT and array/receiving antenna.

Dynamic range and linearity of the developed NF imager was improved by adding a carrier canceller circuit to the front-end of the receiver. The canceller eliminates the carrier on which no information is transmitted and leaves the sidebands intact. This enables us to increase the amplification gain to achieve better signal-to-noise ratio (SNR) and more importantly to expand the imager's dynamic range. The carrier at the receiving port is minimized by combining the received signal with a 180-degree

out-of-phase canceller whose magnitude and phase are adjusted adaptively. We first examined the canceller performance, which leads to a reduction of about 60 dB in the magnitude of the carrier, and then studied its impact on the operation of the NF imager. Significant improvements of NF images were obtained in both dynamic range and linearity.

Condensé en Français

Les objectifs de cette thèse sont la conception et réalisation d'un système d'imagerie micro-onde avec une grande plage dynamique, qui peut fournir des mesures de champ diffusé suffisamment précises et de haute résolution pour être utile à la détection du cancer du sein. Le montage de tomographie micro-onde (TM) devrait fonctionner dans la bande des fréquences ISM (2.45 GHz) qui est dédiée à ce type d'application.

Motivation et objectifs

Au Canada, le cancer du sein est le deuxième type de cancer le plus répandu. En effet plusieurs femmes (rarement des hommes) sont affectées par cette maladie. Le cancer du sein est plus fréquent chez les femmes âgées de 20 ans et plus [25,26]. Il est fortement recommandé pour les femmes de faire des auto-examens pour détecter des anormalités. Il y a beaucoup des méthodes d'auto-examen disponibles. Par contre elles ne sont pas assez efficaces et ils peuvent causer une préoccupation permanente pour la patiente. Une telle situation peut affecter la vie quotidienne d'une femme même si finalement c'est un faux diagnostique. Donc, il est nécessaire d'utiliser un système de détection systématique pour la détection précoce du cancer du sein.

Un nombre croisant des techniques de détection sont utilisés en milieu clinique pour le diagnostique de cette maladie. La méthode la plus courante est la mammographie aux rayons X. Il existe une panoplie d'autres techniques comme l'imagerie par ultrason, l'imagerie par résonance magnétique (IRM), la tomographie par émission des positrons (PET) etc. Chacune de ces techniques présente des inconvénients comme le coût et les effets secondaires. Le besoin d'un système simple, précis et à faible coût constitue la principale motivation de cette thèse de doctorat. La méthode choisie pour cette recherche est la tomographie micro-onde (TM). Cette technique permet de reconstruire les propriétés électriques (permittivité et conductivité) d'un objet sous test (OST) à partir des mesures du champ diffusé par l'objet. Cette technique a besoin d'un système des mesures pour capturer les images du champ diffusé par l'OST et d'une série d'algorithmes pour la résolution du problème inverse afin de reconstruire les propriétés électriques de l'objet. Cette thèse consiste à étudier et à réaliser un système de mesures approprié. D'autres membres de notre groupe de recherche

s'occupent des autres aspects comme l'amélioration de l'illumination du sein, la conception d'un modèle réaliste du sein (fantôme) et la résolution du problème inverse, ainsi que réduction de la vitesse d'exécution des algorithmes pour cette tâche très lourde d'un point de vue calcul. Le système des mesures peut obtenir des images du champ diffusé à différents distances de l'OST. Dépendamment de cette distance, on peut faire les mesures dans le champ proche ou dans le champ lointain. Une meilleure résolution spatiale des images reconstruites et un meilleur rapport signal à bruit peuvent être obtenus si les mesures sont faites dans la zone de champ proche. La TM dans la zone de champ proche peut être la solution pour une technique de détection précoce du cancer du sein [92].

Où se trouve la région de champ proche?

Le champ rayonné par une source ou diffusé par un objet est souvent divisé en trois régions bien connues [1], la région des champs réactifs [2], la zone de champ proche (CP) ou région de Fresnel et la région de champ lointain (CL) ou région de Fraunhofer [1,3]. En plus, l'expression champ très proche est souvent définie [4] comme la zone située très proche de l'antenne (e.g. de l'ouverture de l'antenne) ou du diffuseur. Il n'existe pas de frontières clairement définies entre les trois régions, par contre, il y a quelques définitions communes pour ces frontières. Pour des antennes avec une taille comparable à la longueur d'onde, la frontière entre le CP et le CL est calculé comme étant égale à $2D^2/\lambda$, où D est la plus grande dimension de l'antenne et λ est la longueur d'onde. Le critère $r >> \lambda$ peut aussi être considéré comme la frontière approximative entre le CP et le CL, où r est la distance entre l'antenne et le point d'observation. Le critère $r >> \lambda/2\pi$ doit être utilisé pour les cas où les dimensions de l'antenne sont plus petits que la longueur d'onde. Le champ dans la région des champs réactifs varie rapidement, proportionnellement à r^{-2} ou r^{-3}, par contre le champ dans la région de Fresnel ou Fraunhofer varie proportionnellement à r^{-1}. À cause de la nature du champ électrique et magnétique dans la région réactive, une partie de l'énergie disponible est accumulé proche de l'antenne ou du diffuseur, et ne contribue pas à la radiation [1].

Importance des mesures en champ proche

L'information contenue dans le CP a été amplement utilisé dans plusieurs d'applications la caractérisation d'antennes et de circuits micro-onde ainsi que les tests d'émission de

produits électronique en compatibilité électromagnétique. Les chaque proches peuvent aussi être utilisés pour mesurer la profondeur de pénétration des ondes dans les matériaux et en faire la caractérisation radiofréquence (RF). L'imagerie micro-onde est une autre application des mesures en CP. Toutes ces applications ont fait des mesures en CP des champs électromagnétiques un sujet très intéressant pour la recherche.

Définition du problème : Comment obtenir une mesure précise du champ proche

Le rayonnement en champ proche d'un OST peut être obtenu par la résolution des équations de Maxwell si la structure de l'OST est simple [3]. Par contre, cette tache peut demander beaucoup de temps pour sa résolution. D'un autre coté, ces calculs pour des structures complexes, prendront beaucoup de temps et généralement ne sont pas basés sur des formules explicites. La solution par des méthodes numériques peut être un outil intéressant pour obtenir des distributions de CP à la place d'obtenir une solution analytique des équations de Maxwell, par contre un modéle très détaillé est requis si on a besoin des résultats très précis. Donc, un système de mesure en CP précis et très sensible peut être la solution aux problèmes mentionnés ci-haut. Par contre, les systèmes d'imagerie en CP ont besoin d'être bien conçus et fabriqués pour satisfaire les critères de précision et sensibilité. Les systèmes d'imagerie en CP ont principalement trois désavantages : précision et sensibilité limités, long temps d'acquisition des mesures et une plage dynamique réduite, laquelle dépend des instruments de mesures et des composants utilisés.

Par exemple, un système de mesures en champ proche très précis et avec une plage dynamique très grande est nécessaire pour l'imagerie micro-onde [19-23], où l'objectif est de détecter une inhomogénéité dans un milieu ambiant. Normalement, l'inhomogénéité (e.g. tumeur) a des caractéristiques RF (i.e. permittivité et conductivité) différentes de celles du milieu ambiant. Dans ce cas, le champ diffusé par la tumeur est très faible comparé au champ incident [24]. Pour mesurer ce type des champs diffusés pour une application d'imagerie, il est nécessaire d'avoir un système de mesure en CP qui accomplit toutes les caractéristiques requises.

Approche : Technique de diffusion modulée

Une distribution de champ proche peut être acquise en utilisant une technique directe ou indirecte. Pour la méthode directe une sonde de mesure est branchée à une ligne de transmission (e.g. câble coaxial) et balayée dans la région d'intérêt. La ligne de transmission transporte les signaux captés par la sonde aux instruments de mesure. Le plus grand désavantage de la technique directe est la perturbation des champs mesurés due à présence de la ligne de transmission métallique. En effet, la perturbation est produite puisque le champ électrique est court-circuité sur le métal faisant partie de la ligne de transmission. Aussi, des réflexions multiples entre l'OST et la ligne peuvent se produire ce qui vient perturber les champs mesurés. En plus, les lignes de transmission flexibles, comme le câble coaxial, ne peuvent pas produire des mesures précises et stables de l'amplitude et de la phase des champs. Ces phénomènes mènent à des résultats de mesures imprécis, particulièrement quand la région à balayer est grande. Par contre, les méthodes indirectes utilisent le phénomène de diffusion et ils n'ont pas besoin d'avoir une ligne de transmission attachée à la sonde de mesure (diffuseur). La sonde vient perturber le champ localement à sa position et elle produit une variation au récepteur. Ces variations sont interprétées comme les résultats des mesures (amplitude et phase) en utilisant un détecteur. Les méthodes indirectes utilisent un diffuseur raisonnablement petit, qui ne modifie pas significativement le champ à mesurer mais qui est suffisamment grand pour perturber le champ jusqu'au seuil de détection du système. Ainsi, un compromis doit être fait entre la précision et la sensibilité dans les résultats finaux. Ces pré-requis font en sorte que la conception de la sonde de mesure est plus compliqués que pour la méthode directe. D'un autre coté, la méthode indirecte conventionnelle (i.e. approche de diffusion passive) est limitée en plage dynamique et en sensibilité.

La technique de diffusion modulée (TDM) permet d'améliorer les résultats de la méthode indirecte passive. La TDM a été introduite et généralisée par Richmond [33] pour améliorer les inconvénients des méthodes directes et indirectes. Cette technique fait un marquage du champ à chaque point de l'espace en utilisant un diffuseur modulé [24, 29, 33]. Cette technique permet d'augmenter de manière significative la sensibilité et la plage dynamique du système de mesures. Du point de vue de la mise en œuvre de la sonde TDM, le marquage du champ (modulation) peut être obtenu de façon électrique [35-37], optique [38-41], et aussi de façon mécanique [42,43]. À l'exception de la modulation optique, les autres techniques de modulation présentent

certains des désavantages de la méthode de mesure directe. Pour un diffuseur modulé électriquement une paire de fils métalliques ou résistive torsadée transmet le signal de modulation à la sonde. La présence de ces fils peut aussi perturber la distribution de champ RF de l'OST, ce qui amène à des résultats imprécis. Par contre, avec un diffuseur modulé optiquement le signal de modulation est transféré à la sonde avec une fibre optique qui est invisible pour le champ électromagnétique RF [32,44]. Donc on peut assumer que l'influence de ce type de sonde est négligeable sur la distribution de champ à mesurer.

Dans cette thèse, la méthode de conception d'un système un d'imagerie en champ proche muni d'un réseau de sondes modulés optiquement et est présentée. En plus, la plage dynamique du système d'imagerie est améliorée en utilisant une technique d'annulation de la porteuse au niveau du récepteur.

Diffusion optique modulé (DOM)

Une sonde DOM est modulée par un signal optique fourni par une fibre optique couplée à une photodiode. L'état de cette dernière change de 'ouvert' à 'ferme' a une fréquence d'environ cent KHz ce qui provoque une modulation du champ RF diffusé par la sonde.

Dans les prochaines sections on explique, la conception et la mise en œuvre d'une sonde DOM. Ainsi, des critères pour la sélection de l'antenne et du modulateur, la conception et la mise en œuvre d'un réseau d'adaptation et la fabrication de la sonde DOM seront présentées.

Type d'antenne

Normalement, le diffuseur doit avoir une interaction minime avec la source des champs à mesurer. La plage dynamique du système de mesures dépend du niveau minimal et maximal que la sonde est capable de diffuser, ainsi que du seuil de détection et du niveau de saturation du récepteur. Pour accomplir une grande plage dynamique, on a besoin d'un diffuseur suffisamment grand dans le but d'introduire des perturbations dans la mesure. En général, pour une sonde électriquement petite, plus la dimension est petite, moins les perturbations sont importantes. Un compromis entre la plage dynamique et la sensibilité de la sonde est nécessaire.

En pratique, il y a un nombre limité d'antennes qui peuvent fonctionner comme des sondes TDM. L'utilisation des dipôles, boucles, cornet et antennes micro ruban

est détaillée dans la littérature. Le concept d'antenne à diffusion minimal (ADM) nous permet d'avoir un critère pour la sélection du diffuseur. Conceptuellement, une ADM est invisible aux champs électromagnétiques quand elle est en circuit-ouvert ou connectée à une charge réactive approprié. Les antennes cornet et micro ruban, ne sont pas des ADM à cause, respectivement, de la structure volumineuse de l'un et du grand plan de masse de l'autre. Ceux-ci causent de la diffusion structurale considérable, peu importe la charge aux bornes de l'antenne. Le dipôle court et la petite boucle sont des antennes qui peuvent approcher le comportement ADM désiré. Un dipôle peut être un meilleur choix à cause de sa structure plus simple comparé à une boucle. En plus, une sonde boucle peut mesurer une combinaison de champs électriques et magnétiques si elle n'est pas bien conçue.

Choix du modulateur

Idéalement, l'impédance d'entrée du modulateur doit varier du court-circuit au circuit-ouvert, ce qui n'est pas possible en pratique. La sonde proposée ici utilise une photodiode produite par la compagnie Albis (PDCS30T). Ce composant a été sélectionné à cause de sa grande variation d'impédance à la fréquence de 2.45 GHz en fonction du niveau de puissance lumineuse appliquée. L'impédance d'entrée de la photodiode a été mesurée dans une station de mesure sous pointe avec un analyseur de réseau Agilent 8510 pour les états 'OFF' (i.e. pas de lumière appliquée) et 'ON' (i.e. avec une puissance lumineuse de +6dBm) dans la plage fréquentielle entre 2 et 3 GHz. L'impédance de la photodiode peut être approximativement modélisée comme un circuit RC série, avec R_{OFF}=38.8Ω et C_{OFF}=0.31pF, et R_{ON}=15.8Ω et C_{ON}=13.66pF, respectivement [72].

Réseau d'adaptation

À cause de la longueur de l'antenne du dipôle ($L \approx \lambda/12$) choisie dans la conception de l'antenne, celle-ci la présente une impédance d'entrée capacitive. Comme conséquence, le niveau de champ diffusé par la sonde sera faible, même si on utilise un modulateur idéal ($Z_{ON} = 0$ et $Z_{OFF} \to \infty$). Une telle sonde souffrira d'une sensitivité réduite, ce qu'implique une plage dynamique limitée. La sensibilité de la sonde peut être augmentée en ajoutant un circuit inductif à la structure.

En pratique, un tel circuit de syntonisation a été mis en œuvre en ajoutant une inductance à la sonde de telle façon qu'une résonance est provoquée dans un des deux

états. La valeur d'inductance est choisie de façon que le quotient entre les courants pour les états 'ON' et 'OFF' est maximisé. L'impact de l'ajout d'un tel circuit à la structure de la sonde est montré dans la figure 3.11, où elle est comparée avec une sonde sans inductance. Une inductance sous forme spirale plane est utilisée et un 'wire-bond' est utilisé pour connecter la photodiode et le bloc central. Il est aussi connecté aux terminaux de la sonde. La symétrie de la sonde DOM avant l'ajout de l'inductance spirale est conservée avec la séparation de l'inductance en deux et la connexion de celui-ci aux bras du dipôle.

Circuits micro-onde et optique du système d'imagerie champ proche

Cette section décrit la mise en œuvre des circuits électroniques, micro-onde et optique qui sont nécessaires pour la transmission, réception et analyse des champs diffusés par une sonde DOM. La partie micro-onde est composée d'une source RF, d'un circuit actif équivalent à un démodulateur I-Q conventionnel et d'un circuit d'annulation de la porteuse. Le partie bande de base analogique et numérique comprend un amplificateur verrouillé en phase (LIA en anglais), SR830, manufacturé par Stanford Research Systems, qui est capable de fournir des mesures de signaux vectoriels (amplitude et phase), un circuit source de courant pour exciter une diode laser, et un contrôleur qui génère le signal verrouillé en phase qui est requis pour le LIA et qui contrôle un commutateur RF. Ce contrôleur envoie aussi des commandes à la diode laser pour moduler la sonde DOM. Le système complet est contrôlé par un programme d'ordinateur écrit en LabView.

Circuit d'annulation automatique de la porteuse

Dans un système de mesure TDM les signaux reçus (modulé) sont composés d'une fréquence porteuse et deux bandes latérales. Dans le signal modulé, l'amplitude de la porteuse est généralement beaucoup plus élevé ($\sim$50dB) que celle des bandes latérales. La réception d'une porteuse de haute puissance peut générer des comportements non-linéaires comme la saturation et la compression du récepteur. Ces signaux de haute puissance peuvent aussi générer des débalancements d'amplitude et phase des signaux I et Q dans un modulateur I-Q, ce qui a un effet adverse sur les mesures du champ [2].

Le circuit d'annulation permet d'éliminer la porteuse de façon continue au récepteur en laissant les bandes latérales du signal modulé intactes. Cette circuit permet non seulement de corriger les erreurs de mesure mais aussi permet d'augmenter le signal transmis, ce qui produit une augmentation de la plage dynamique dans la quelle le système travaille dans sa zone linéaire. Aussi, l'effet de garder le niveau de la porteuse plus bas qu'une certaine limite permet d'amplifier les signaux I et Q sans produire la compression et la saturation dans le circuit mélangeur. On évite ainsi de travailler proche du plancher de bruit du LIA. Tout ceci a pour effet d'augmenter la plage dynamique du système. La figure 5.20 montre un signal modulé avant et après son passage dans le circuit d'annulation.

Résultats de validation de la sonde DOM

Pour vérifier les performances de la sonde DOM, elle a été utilisée pour mesurer la distribution du champ électrique d'une ligne de transmision micro-ruban de 50Ω en mode monostatique, où le signal mesuré est proportionnel au carré du champ électrique ($v \approx E^2$). La ligne de transmission est fabriquée sur un substrat Rogers (RO3035) avec une permittivité relative de 3.8 et une épaisseur de 60 mil (voir figure 3.30). Le champ électrique qui varie rapidement proche de la ligne est adéquat pour prouver la résolution et plage dynamique du système. Dans cette mesure, la sonde est balayée perpendiculairement à l'axe de la ligne micro-ruban à une hauteur de 3mm au dessus de celle-ci, et elle mesure la distribution de champ électrique selon l'axe des x (figure 3.31). La ligne de transmission est connectée à une charge adaptée.

Pour valider les résultats de mesure, ces dernies sent comparés à ceux obtenus par simulation numérique ave le logiciel HFSS. Les résultats de simulation ont besoin d'être traités pour tenir en compte l'effet des dimensions de la sonde. Dans un intervalle de 15mm, la différence moyenne entre la simulation (avec la correction pour la sonde) et le champ mesuré est de 6.4% en amplitude et de 3.2° en phase. Il faut souligner que la correction de la sonde n'affecte pas la phase du signal mesuré.

Amélioration de la vitesse des mesures : Réseaux des sondes DOM

Un important désavantage d'un système d'imagerie TDM est le temps requis pour la prise de mesure. Évidement, le balayage mécanique de la sonde sur la région d'intérêt est considéré comme le paramètre le plus important à cet égard.

En plus, le déplacement mécanique signifie que les supports et le système de positionnement peuvent perturber les champs considérablement. Pour résoudre ce problème, un réseau des sondes TDM au lieu d'une sonde isolée est proposé comme alternative. La configuration proposée est composée d'un réseau de sept sondes DOM placés sur une ligne perpendiculaire à l'axe de des sondes. Le réseau est balayé mécaniquement selon une direction, aux même temps que les sondes sont commutés électroniquement (aussi mécaniquement si la résolution spatiale requis est plus grande que l'espace entre les sondes) dans la direction orthogonal pour un balayage 2D. Donc, cette configuration réduit le mouvement mécanique à une seule direction. Le nombre de mouvements nécessaires est réduit par un facteur égal au nombre de sondes.

Il peut être démontré que non seulement le balayage mécanique du système de positionnement mais aussi le temps de commutation entre les sondes peut ralentir le temps total de prise de mesures de façon importante. Donc, pour réduire le temps total de prise des mesures, il est nécessaire de tenir compte des deux facteurs en même temps. C'est-à-dire que la vitesse de commutation entre les sondes doit-être plus grande qu'un certain seuil pour profiter du nombre réduit de mouvements mécaniques.

Réseau des diodes laser : Conception spécifique du commutateur optique

En pratique, un commutateur optique est nécessaire pour envoyer un signal modulé à la sonde désirée et pour commuter la lumière entre les différentes sondes. Pour accomplir cette tâche, un réseau de diode laser contrôlé électroniquement a été conçu, chacune des diodes est connecté à une des sondes. En activant une diode laser, la sonde DOM est modulé (commuté ON/OFF). Un contrôleur numérique a été conçu pour fournir les signaux adéquats à chaque sonde. Ce contrôleur produit un signal de référence utilisé par le LIA. La stabilité de ce signal de référence est assurée en utilisant un cristal dont la fréquence de résonance est 8MHz, ce qui évite d'avoir du bruit de phase dans les données mesurées. Ce circuit numérique est également contrôlé par un programme écrit en Labview. Ce commutateur électronique augmente non seulement la vitesse de mesure mais il élimine aussi la diaphonie entre les différentes sorties, qui avait était observée avec un commutateur opto-mécanique utilisé en [75]. Une amélioration par un facteur 14 est observée dans le temps de prise de mesures comparées au système présenté en [75], où un commutateur opto-mécanique commercial avait été utilisé.

Mise en œuvre d'un système d'imagerie micro-onde appliqué à la détection précoce du cancer du sein

En général, les systèmes utilisés en tomographie micro-onde, et pour la détection du cancer du sein en particulier, sont composés d'un système des mesures et d'un algorithme pour la résolution du problème inverse associé avec les données mesurés. Dans les prochaines sections, les différentes parties du système traitées dans cette thèse sont discutées.

Fantôme

Avant d'utiliser un appareil d'imagerie, il est nécessaire de valider le bon fonctionnement du système de mesures et de l'algorithme d'inversion utilisé. Pour cela, il est possible d'utiliser un modéle artificiel d'un sein précis et réaliste (fantôme). Ce fantôme doit être suffisamment robuste pour inclure une grande variabilité de types de sein, un organe très hétérogène, en termes de taille et des matériaux constitutifs. En [94], une vaste recherche a été effectuée pour déterminer les propriétés électriques d'un sein qui est un mélange hétérogène de gras, muscle et tissue glandulaire. En utilisant cette information et en choisissant des matériaux similaires en termes de permittivité et conductivité [95], un collègue, M. Alvaro Diaz-Bolado a conçu et mis en œuvre un fantôme pour cette application. Ce fantôme a été conçu pour présenter approximativement les mêmes propriétés électriques qu'un sein. Le fantôme proposé simule un sein compressé entre deux plaques de plexiglas ce qui forme une guide diélectrique capable de guider différents modes dans la structure. Le fantôme est illuminé avec un réseau des deux antennes qui sont excitées en phase (mode pair) et avec un déphasage de 180° (mode impair) (voir figure 6.3). Dans le mode pair (i.e. TM_1) le champ électrique a une distribution sinusoïdale entre les plaques avec un champ électrique plus intense au milieu de la structure. Donc, cette mode doit être plus efficace pour détecter des tumeurs localisées dans le milieu du fantôme. Comme montré dans la figure 6.3, dans le mode impair (TM_0) les antennes sont excitées en anti-phase et elles vont concentrer le champ incident dans la zone proche des plaques.

Solution pour le problème inverse

Cette partie n'est un des objectifs de cette thèse et elle ne sera pas discutée en profondeur. Les problèmes inverses [86,21] et ses solutions étaient le sujet central de la thèse de mon collègue Dr. Paul-André Barrière [96].

Résultats de détection

Pour vérifier la capacité des mesures du système des mesures en champ proche et le fantôme développé, le système a été utilisée pour mesurer le champ diffusé par un objet inséré dans le fantôme sur une région d'intérêt. Le fantôme étais rempli de glycérine avec une permittivité complexe de 7.17 +j23.41 à la fréquence de 2.45 GHz. Dans cette expérience, la distribution de champ électrique est mesurée deux fois sur le fantôme, premièrement avec la présence d'un diffuseur (cylindre rempli d'air avec un diamètre d'un pouce) et deuxièmement en absence du diffuseur. Les résultats obtenus pour chacune des cas sont soustraits pour obtenir le champ diffusé. Pour les deux modes excités, le pic du champ diffusé se trouve exactement à la position du diffuseur. Les résultats des mesures sont aussi comparés avec une simulation utilisant le logiciel CST Microwave Studio et un bon accord entre les deux résultats est obtenu. Ces résultats montrent la capacité du système de mesurer le champ diffusé avec une plage dynamique plus grande que 30 dB.

Conclusions

Cette thèse a porté sur la conception et la mise en œuvre d'un système de mesures en champ proche qui utilise la technique de diffusion modulé (TDM). Le système est composé de plusieurs sondes à diffusion optique modulé (DOM) qui sont très précises et hautement sensibles. Chaque sonde est optimisée pour la fréquence de 2.45 GHz (bande ISM). L'invisibilité de fibres optiques utilisées pour les sondes DOM aux signaux micro-onde a été étudiée et vérifiée. Cette sonde permet la mesure des champs presque sans perturbation du champ. Le comportement de la sonde est vérifié en utilisant la sonde pour mesurer la distribution des champs proches des différents objets sous test. La mise en œuvre d'un réseau des sondes DOM, permet d'augmenter la vitesse des mesures par un facteur 14 comparé à des systèmes disponibles sur le marché qui utilisent des commutateurs opto-mécanique. Pour augmenter la précision des résultats de mesures avec le réseau, les données brutes sont corrigées pour permettre de compenser certaines déviations de la réponse des sondes. Le système d'imagerie et le fantôme construit ont été testés et validés.

Contents

List of Tables

List of Figures

List of Appendices

List of Acronyms and Abbreviations

NF	Near-Field
FF	Far-Field
MST	Modulated Scatterer Technique
OMS	Optically Modulated Scatterer
LIA	Lock-In Amplifier
CPW	Co-Planar Waveguide
MS-TL	Microstrip Transmission Line
MST Probe	Modulated Scatterer Technique Probe
OMS Probe	Optically Modulated Scatterer Probe
DUT	Device Under Test
AUT	Antenna Under Test
BUT	Body Under Test
E	Electric Field
H	Magnetic Field
E-field	Electric Field
H-field	Magnetic Field
EM	Electromagnetic
EMC	Electromagnetic Compatibility
MRI	Magnetic Resonant Imaging
PET	Positron Emission Tomography
MT	Microwave Tomography
MI	Microwave Imaging
ISM	Industrial Scientific Medical
EO	Electro-Optic
E_{inc}	Incident Electric Field
H_{inc}	Incident Magnetic Field
E_s and $E_{scattered}$	Scattered Electric Field
H_s and $H_{scattered}$	Scattered Magnetic Field

SNR	Signal-to-Noise ratio
1D	One Dimensional
2D	Two Dimensional
3D	Three Dimensional
Z_L	Load impedance
m	Modulation Depth
CR	Modulation index
E_{min}	Sensitivity
HFSS	High Frequency Structure Simulator
CST	Computer Simulation Technology
λ	Wavelength
Ω	Resistance unit
ω	Angular velocity of waves
ϵ_r	Permittivity or dielectric constant
$tan\sigma$	Dielectric losses

Chapter 1

Introduction

1.1 What is near-field (NF) and where is the near-field region?

The scattered field is sometimes divided into three well-known regions [1], namely reactive near-field [2], near-field(NF) or Fresnel region and far-field (FF) or Fraunhoffer zones [1, 3]. In addition, the term "very-near-field" region is sometimes defined [4] as very close to the antenna (e.g., antenna aperture). There are no clear or abrupt boundaries between the three zones, however there are some commonly used definitions for those boundaries. For antennas with a size comparable to the wavelength, the NF and FF boundary is calculated as $2D^2/\lambda$, where D is the maximum dimension of the antenna. Criterion $r >> \lambda$ can also be considered to approximately determine the NF and FF boundary, where r is the distance between the antenna and observation point. Criterion $r >> \lambda/2\pi$ should be used for the cases where the antenna dimensions are smaller than the wavelength. The field in the reactive near field region varies rapidly, proportionally to r^{-2} or r^{-3}, whereas in the Fresnel and Fraunhoffer regions it varies with r^{-1}. Due to the nature of electric and magnetic fields in the reactive region, a portion of available energy is stored close to the antenna, and does not contribute to radiation [1].

1.1.1 Definition of NF region

In the reactive near-field region of an antenna, (see Figure 1.1), the equality of $|E|/|H| = \sqrt{\mu/\epsilon}$ is not respected, as opposed to the far-field region. As an example to show how the ratio of E and H varies at different distances from the radiator, we considered an infinitesimal dipole antenna whose E and H fields are given by Equation 1.1. Figure 1.2 shows real and imaginary part of E_θ/H_ϕ at different observation points. It is clear that the impedance does not take a value near 120π close to the

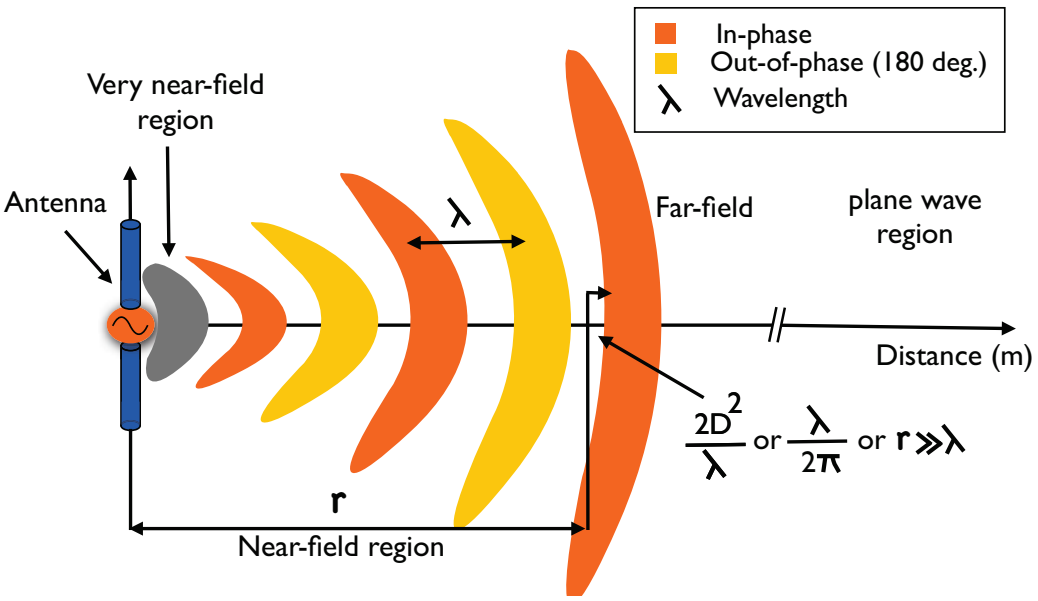

Figure 1.1 Near-field region of a dipole antenna.

dipole, but it does so away. As it can be seen in Figure 1.2 the calculated ration close to the antenna takes complex values as opposed to the far-field region.

$$
\begin{aligned}
E = \frac{I\Delta z}{4\pi} j\omega\mu \left[1 + \frac{1}{j\beta r} - \frac{1}{(\beta r)^2}\right] \frac{e^{-j\beta r}}{r} sin\theta\ \hat{\theta} + \\
\frac{I\Delta z}{2\pi}\eta \left[\frac{1}{r} - j\frac{1}{\beta r^2}\right] \frac{e^{-j\beta r}}{r} cos\theta\ \hat{r} \\
H = \frac{I\Delta z}{4\pi} j\beta \left[1 + \frac{1}{j\beta r}\right] \frac{e^{-j\beta r}}{r} sin\theta\ \hat{\phi}
\end{aligned}
\tag{1.1}
$$

1.2 Importance of the NF distribution

Information on the near fields has been widely used in many applications such as in antennas [5], microwave circuits [6] and devices emission tests [7, 8]. It can also be used to measure the wave penetration into materials and their radio-frequency (RF) characterization [9, 10]. Microwave imaging [11] is another impressive use of NF measurement. Measuring the coupling between components of microwave circuits

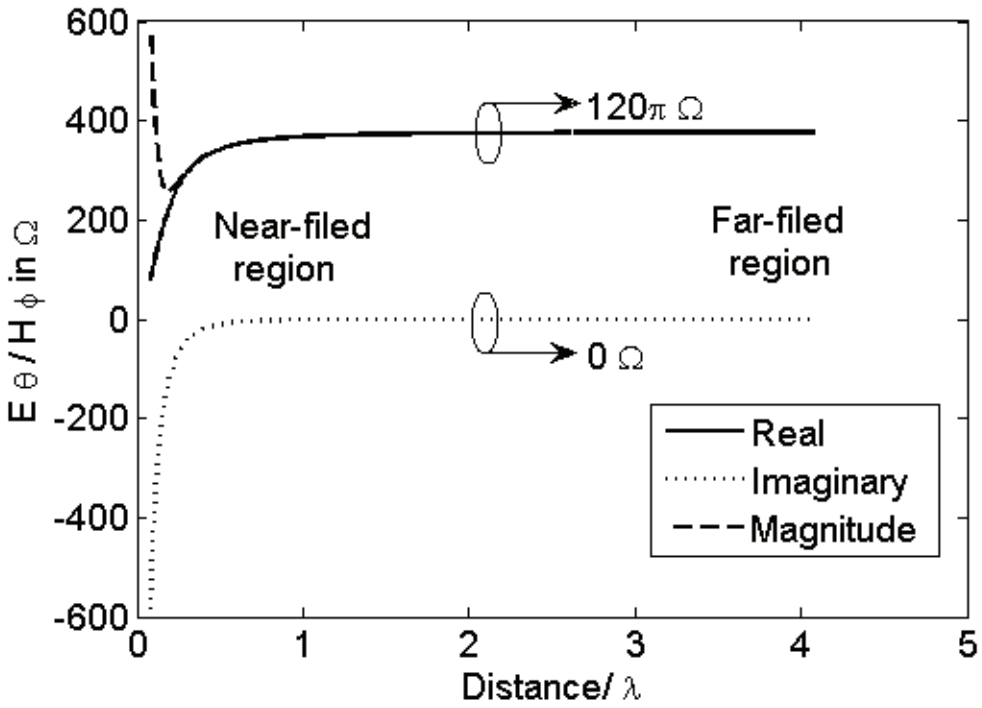

Figure 1.2 Calculation of η at different distances from a dipole antenna.

[12], calculating FF radiation pattern of large antennas [6, 13, 14], and electromagnetic compatibility EMC [12, 15, 16] and EMI [17, 18] are the other uses of NF measurement. These have made NF measurements a very interesting topic for many researchers.

1.3 Problem definition: obtaining an accurate NF fields measurement

The near-field radiation pattern of any DUT or AUT can be obtained by solving Maxwell's equations if the AUT or DUT structure is simple [3]. However, this may be a very time-consuming process. In contrast, such calculations for complex structures, may require a long time and generally will not be based on a closed and explicit formulations.

Computer simulation software based on numerical methods can be a helpful tool

for obtaining NF field distributions instead of seeking an analytical solution for Maxwell's equations, although it requires very detailed models if accurate results are needed.

Thus, having an accurate and sensitive NF measurement system can remedy the previously mentioned issues. However, NF imagers need to be well-designed and implemented to meet the required accuracy and sensitivity criteria. Conventional NF imagers always suffer from three important issues: limited accuracy and sensitivity, long measurement duration and reduced dynamic ranges, all of which depend on the measuring instruments and components used.

For instance, a highly accurate and sensitive as well as large dynamic range NF imager is necessary in microwave imaging (microwave tomography) [19, 20, 21, 22, 23], where the goal is to detect a small region within a background medium. Normally, the inhomogeneity (e.g., tumour) has different RF characteristics (i.e., permittivity and conductivity) compared to the background region. In this case, the scattered fields by the tumour is very weak in contrast to the incident wave [24] . To measure these types of scattered fields for diagnostic purposes, it is necessary to have an NF measurement system that fulfills the above-mentioned requirements.

1.4 Objectives and ultimate application

The objective of this thesis is to design and fabricate a computerized NF imaging setup for non-invasive, accurate and rapid field distribution measurement applied to microwave tomography, especially for breast cancer detection. Achieving high dynamic range measurements is another objective of this thesis.

In Canada, breast cancer is the second most prevalent type of cancer, just after lung cancer. Women and even men in rare cases are affected. Breast cancer is mostly observed in women over 20 years old [25, 26]. Early detection plays a key role in providing a cure, limit damage to the patient or to save the patient's life[25]. Women are strongly recommended to self-examine their breasts monthly to see if there are any abnormalities. There are many self-examining methods available. They do not always detect breast changes accurately and may cause permanent worry. Such a feeling may affect a woman's daily life even if she remains healthy. Therefore, the necessity of a systematic scheme is obviously needed for early breast cancer detection.

An increasing number of breast cancer detection methods are used to make highly

accurate scanning of breasts for diagnostic purposes. Mammography, is which consists in X-ray imaging of the breasts provides views at different angles. Ultrasound, also called sonography, is an imaging technique in which high-frequency sound waves are bounced off tissue and internal organs. For magnetic resonance imaging (MRI), a DC magnet and an RF source linked to a computer, create detailed pictures without the use of ionizing radiation. A positron emission tomography (PET) scan creates computerized images of chemical changes that take place in tissues. The patient is given an injection of a substance that consists of a combination of a sugar and a small amount of radioactive material. Electric impedance scanning is based on the fact that different breast tissues show different impedances to electrical signals and biopsy techniques use a sample of the breast for examination under microscope. These are some of widely used methods of breast cancer detection.

Unfortunately, each method of detection has its disadvantages, such as expensive service and setup, side effects, limited availability, and so on. Thus, the strong requirement for a simple, highly accurate, and inexpensive method of detection for breast tumours is the main motivation behind this research and thesis. It is also worth noting that microwave tomography is not simply an imaging technique. Such a technique requires also intensive data processing after image capture. This thesis addresses only the first task; other team members are currently working on other aspects such as improving the illumination technique of the breast, designing a realistic breast model (i.e., phantom), solving the inverse scattering problem and also increasing the data processing speed.

In order to remedy the issues mentioned above, this thesis will strive to achieve the following objectives: design and realization of a microwave near-field imaging system with large dynamic range, that provides accurate and high resolution scans useful for breast cancer detection. The microwave tomography (MT) setup will be working at S-band frequency, Industrial Scientific Medical(ISM) frequencies, which is dedicated to science and industry. The most important criteria in the selection of the test frequency is the need for high contrast between malignant and healthy breast tissue and also low RF signals dissipation.

1.5 Approach

The distribution of near fields can be acquired using one of the two well-known techniques, namely *direct* [27, 28] or *indirect* [24, 29, 30, 31]. In the *direct* method a measuring probe is pigtailed with a transmission line (e.g., coaxial cable), and scans over the region on interest. The transmission line carries the signals picked-up by the probe to the measurement instruments. The major drawback associated with the *direct* technique is the perturbation applied to the fields to be measured by the presence of the metallic transmission line. In fact, the perturbation comes from the fact that electric fields are short-circuited on the metallic constituents of the transmission line [24]. Multiple reflections may also occur between the DUT and the line [24, 29] resulting in perturbed fields measurement. Moreover, the flexible transmission lines such as a coaxial cable, which is widely used in microwave systems, do not always give accurate magnitude and phase stable measurements [24, 32]. This phenomenon in turn leads to inaccurate measurement results, particularly where the measuring probe has to scan a large area. In contrast, *indirect* methods [33, 34] are based on scattering phenomenon and requires no transmission line attached to the measuring probe (scatterer). The probe locally perturbs the fields at its position and yields a variation at the receiver output port, which could be the AUT itself (i.e., monostatic mode) or an auxiliary antenna held remotely (i.e., bistatic mode). These variations correspond to the probe positions and are interpreted as the field measurement results (magnitude and phase) by means of a detector. The *indirect* method employs a scatterer which is reasonably small, which does not perturb the fields but which is sufficiently large so that it is able to perturb the field minimum up to the system's measurement threshold. Thus, a trade-off has to be made between accuracy and sensitivity in the final results. Such assumptions make the probe design more complicated compared to its counterpart, the *diret* method. Beside that, the conventional *indirect* method suffers from limited dynamic range and sensitivity [29].

To overcome the drawbacks mentioned above, a technique known as the modulated scatterer technique (MST) was proposed and developed. For the first time, MST was addressed and generalized by Richmond [33] to remedy the drawbacks of both the *direct* and *indirect* methods, simultaneously.

Principally, it is based on marking the field at each spatial set point using an MST scatterer, which is called the MST probe [24, 29, 33]. This technique brings some out-

standing advantages in the context of NF imaging such as eliminating the need to attach a transmission line to the measuring probe and improving the sensitivity and dynamic range of the measurement. From the point of view of implementation of the MST probe, tagging the field (modulation) can be done either electrically [35, 36, 37] or optically [38, 39, 40, 41], and sometimes, mechanically [42, 43]. Unlike optical modulation, the other modulation techniques somehow show the same disadvantages as the *direct* method. In an electrically modulated scatterer (EMS) a pair of twisted metallic or resistive wires carry modulation signals to the probe. The presence of these wires may perturb the field distribution of DUT, resulting in inaccurate measurements, whereas in an optically modulated scatterer (OMS) the modulating signal is transferred throughout an optical fiber that is invisible to the electromagnetic radio-frequency signal [32, 44]. Thus, it can be assumed that it will barely influence the DUT's field distribution to be measured.

Beside all the outstanding features of an MST-based NF imager, a time-consuming measurement process still remains a disadvantage [45, 46]. Obviously, an MST probe's mechanical translation over the region of interest is considered as the most effective parameter in this regard. Moreover, mechanical means such as actuators, support, and positioning system may perturb the AUT's NF fields considerably. To tackle this problem, an array of MST probes replacing an isolated one was proposed [46]. An MST array eliminates or at least restricts mechanical movements. This replacement will yield remarkable improvements in measurement duration when NF measurement is performed by an imager [47].

In this thesis, considering the outstanding advantages of the MST such as low-perturbation, phase stable, low cost and simple microwave circuitry, a NF imager equipped with an array of optically modulated scatterer (OMS) probes that is able to overcome the drawbacks associated with the conventional *direct* and *indirect* methods is addressed and a detailed implementation procedure is discussed. Moreover, the dynamic range of the NF imager is improved by proposing a technique called carrier cancellation, which consists in eliminating the carrier in the modulated signals that are received by the receiver.

1.6 Thesis Structure

In the following, the contents of this thesis are highlighted and briefly explained. These contents are covered within three successive chapters in the order explained below.

- **Single OMS Probe:** Design and implementation of a non-invasive and perturbation-free measurement setup based on a modulated scatterer technique (MST) that is equipped with an optically modulated (OMS) probe.

- **OMS Probe Array:** Achieve increased measurement speed using a linear array of OMS probes.

- **Carrier Cancellation:** Improve the dynamic range and linearity of the developed NF imager by a carrier cancellation, a circuit eliminating carrier at the receiving stage. It increases the potential of higher amplification levels leading to a higher dynamic range and consequently improved linearity of the imager.

1.7 Publications

- Journal Papers:

  1. Memarzadeh-Tehran, H. , Laurin, J.-J., and Kashyap, R. (2010). Optically Modulated Probe for Precision Near-Field Measurements. IEEE Transactions on Instrumentation and Measurement, To appear.
  2. Memarzadeh-Tehran, H., Laurin, J.-J., and Kashyap, R. (2010). A Rapid Near-Field Measurement System Equipped with Array of Light Modulated Probes. IEEE Transactions on Instrumentation and Measurement, To be submitted in 2010.
  3. Memarzadeh-Tehran, H., Diaz-Bolado, A., Laurin, J.-J., J.-F., and and Kashyap, R. (2010). Bandwidth Improvement in a Resonant Optical MST-Probe Applicable in Near-Field Imaging . Antennas and Wireless Propagation Letters. To be submitted in 2010.

- Conference Papers:

1. Memarzadeh-Tehran, H., Laurin, J.-J., and Kashyap, R., Goussard Y.(2007). Dielectric Resonator Antennas for Application in Microwave Tomography. ANTEM 2006.
2. Memarzadeh-Tehran, H., Laflamme-Mayer, N., Laurin, J.-J., and Kashyap, R. (2007). A near-field measurement setup using an array of optically modulated scatterers. In Signals, Systems and Electronics, 2007. ISSSE 2007. International Symposium on, pages 481-484.
3. Memarzadeh-Tehran, H., Lamarche, M., Laurin, J.-J., and Kashyap, R. (2009). A technique to improve the dynamic range and linearity of a near-field imager based on the modulated scatterer approach. In Antennas and Propagation, 2009. APS/URSI 2009. International Symposium on, pages 481-484.
4. Memarzadeh-Tehran, H. M., Laurin, J.-J., and Kashyap, R. (2009). A low-perturbation near-field imager equipped with optical mst probes. In Antennas and Propagation, 2009. EuCAP 2009. 3rd European Conference on, pages 3649-3653.
5. Tehran, H. M., Laurin, J.-J., and Kashyap, R. (2010). Microwave Imaging System Incorporating an Array of Optically Modulated Probes for Rapid and Low-Perturbation Near-Field Measurements. AMTA2010. Accepted.

1.8 Organization of the thesis

This thesis is organized into four main chapters.

1. Chapter 2:
   - Literature review
2. Chapter 3:
   - OMS probe design and implementation
   - OMS probe characterization
   - The NF imager microwave circuitry
   - Validation of the OMS probe results

- Discussion and conclusions

3. Chapter 4:

   - OMS probes array design and implementation
   - Laser-diode array and controlled driver development
   - Mutual coupling and shadowing effect study

4. Chapter 5:

   - Carrier cancellation circuit design and implementation
   - NF canceller test and result validation of the NF imager

5. Chapter 6:

   - Microwave Tomography Setup
   - Validation of the measurement results (i.e., detection) obtained using the developed NF imager

Chapter 2

Literature Review

2.1 Near-field measurement techniques

Direct and *indirect* measurement techniques were introduced in Chapter 1. In the following, we will discuss the advantages and disadvantages of the probes used in both techniques. Finally, Opto-electronic NF probes will be briefly described.

2.2 *Direct* technique probes

2.2.1 Probe loaded with a RF detector

This type of probe is one of the simplest to implement; it consists of an antenna loaded with an RF detector and is depicted in Figure 2.1 [28]. The picked-up signal is converted to a DC voltage (e.g., $\propto |E^2|$ in E-field measurement) and then is transferred by a pair of wires, metallic, or resistive [28], to the measurement instruments. The antenna can be a dipole, a horn or a loop antenna. As RF signals are rectified by a detector in this probe, only a magnitude measurement is possible and it does not give any information on the phase of signals (Although phase could be recovered with magnitude-only measurement if holographic techniques are used).

In practice, using straight (i.e., untwisted) wires to transfer the signal picked up by the probe to the measurement instruments, is susceptible to coupling between those wires and the fields to be measured [48]. Such coupling can be reduced by using a pair of twisted wires as illustrated in Figure 2.1. However, twisted wires are only capable of reducing inductive crosstalk (i.e., magnetic field coupling) and not capacitive crosstalk (i.e., electric field coupling). So, one can conclude that this type of probe is not essentially crosstalk free. However,"twisted wires can reduce capacitive crosstalk only if the terminations at both ends are balanced," as mentioned in [48].

In [28], it is proposed that resistive wires should be used instead of metallic ones

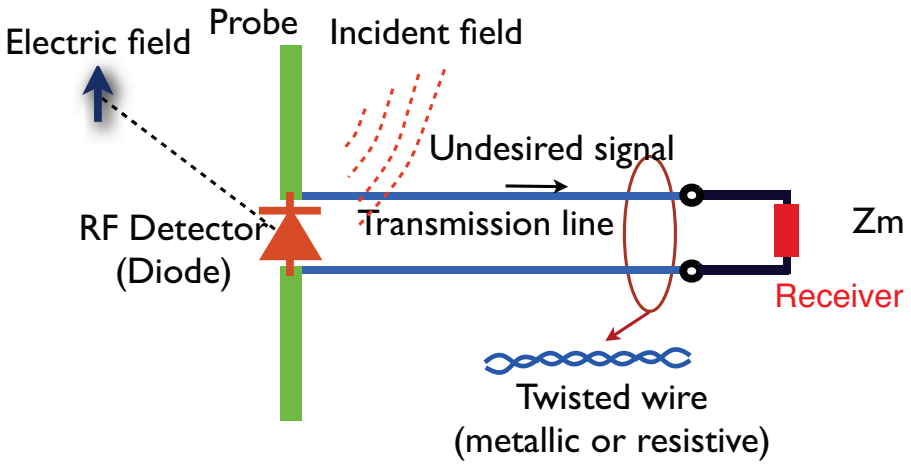

Figure 2.1 NF probe with an RF detector.

to minimize the interaction between the fields and transmission line. However, using resistive wires reduce the strength of the signals available for the measurement system, leading to a limited dynamic range. Noise susceptibility is another issue when such probes are used.

2.2.2 Conventional NF probe

This is the most popular type of NF probe in the *direct* measurement technique [49]. It consists of a small antenna such as a dipole, loop and horn antenna that is pigtailed by a transmission line (e.g., coaxial cable). The schematic of such a probe (dipole) is followed by a balun and is demonstrated in Figure 2.2. Similar to the probe introduced in Section 2.2.1, the presence of its metallic transmission line can perturb the field to be measured. However, the effect of the transmission line can be reduced by properly orienting the probe and putting absorber around it [29].

2.2.3 Electro-optic (EO) probe

In probes of this kind, a small antenna is loaded with a piece of electro-optic (EO) crystal. The crystal's optical behaviour changes when exposed to electromagnetic fields and an optical fiber is also coupled to the crystal providing illumination. The

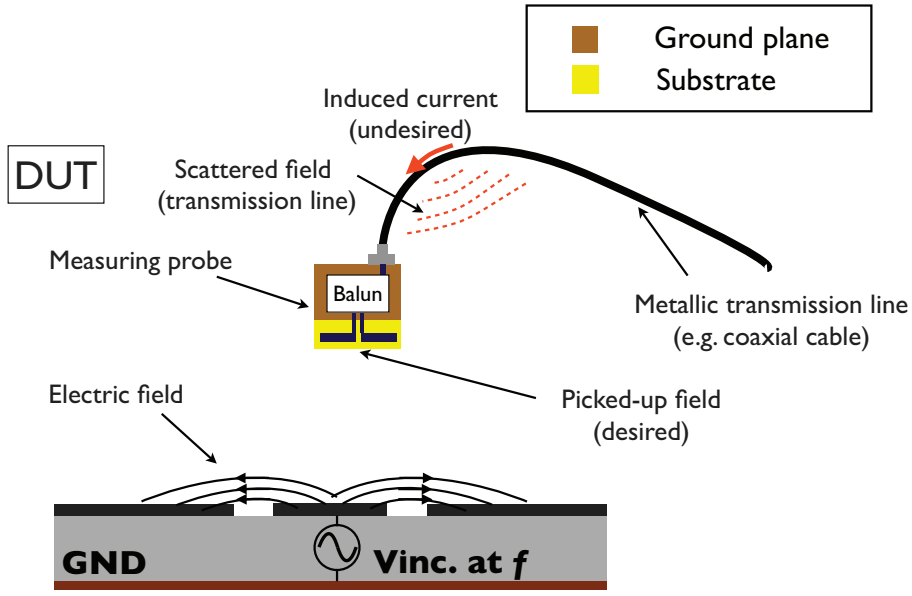

Figure 2.2 Schematic depicts a conventional NF probe scanning a co-planar waveguide (CPW).

crystal is continuously illuminated at an appropriate wavelength. When the probe is moved over the region of interest, the optical characteristics of the crystal (i.e., refractive index) changes due to a variation of electromagnetic fields accordingly. As a consequence, the polarization of the reflected light is changed by the probe crystal [51]. Such variation causes the phase of the reflected laser beam to change, which is then measured by an optical detector and interpreted as an indicator for the measured fields. Figure 2.3 shows a schematic of the probe (i.e., Mach-Zehnder interferometer), which is loaded with $LiNbO_3$ crystals and the setup needed to establish a NF measurement [52]. Even if this technique is perturbation-free and there is no metallic transmission lines attached to the measuring probe for S_{21} measurement, S_{21} is defined as the coupling between the DUT's fields and EO probe, it has a complicated setup that is not cost effective. Moreover, due to the associated losses with the optical probe, the excitation signal fed to the DUT has to be very high [52, 50]. Otherwise, the field to be measured, may fade in spurious signals and background noise. Being a complicated setup, the need for a high-power level to test a DUT and long warm-up time for optical parts (e.g., laser and detector), make it rather difficult to

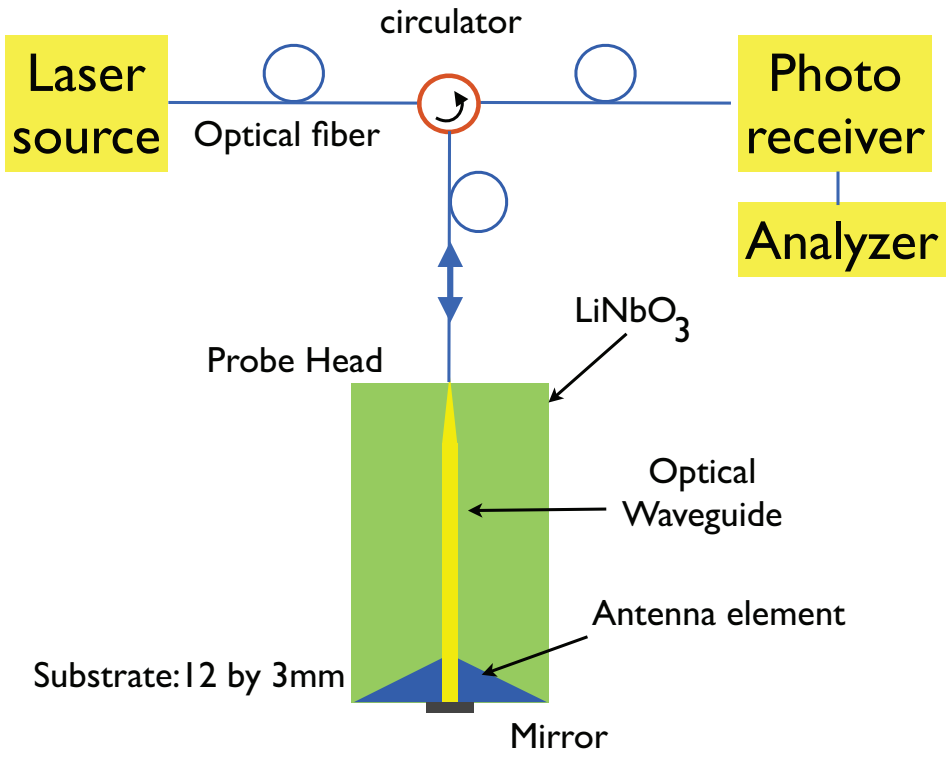

Figure 2.3 An example of an EO NF probe [50].

take measurement using EO probes. However, it has a remarkably high measurement resolution.

2.3 *Indirect* techniques probes

In Section 2.2, it was shown that the *direct* method except EO NF probes, can not essentially be considered as a perturbation-free method for measuring a field distribution profile [24]. Therefore, in order to overcome the associated drawbacks with the *direct* method, NF measurement using the *indirect* was introduced.

In the following, *indirect* NF measurement techniques and the associated probes will be discussed in detail. The *indirect* method includes two different techniques: perturbation technique and the modulated scatterer technique (MST). Advantages and disadvantages of each technique will be discussed as well.

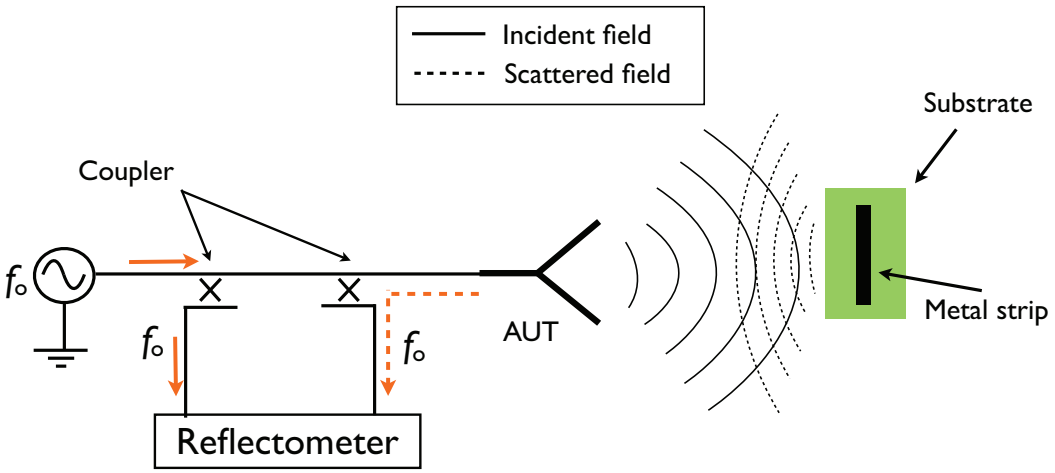

Figure 2.4 Schematic of the scattering technique, monostatic implementation. Drawing is not to scale.

2.3.1 Perturbation technique: passive scattering probe

The *indirect* method is based on the scattering phenomenon in which the measuring probe is not connected to a transmission line [53, 54]. Instead, the small scatterer (i.e., probe), which is designed to have an optimum width, length and material, is moved over the region where the field distribution is required. The principle of this technique is shown in Figure 2.4. The probe perturbs the fields locally and causes a variation at the receiving front-end, which could be AUT itself (monostatic mode) or an auxiliary antenna (bistatic mode). Then, the variations corresponding to the probe positions are interpreted as the field measurement results. In this technique, the scatterer has to be reasonably small so that it does not perturb the near field, and at the same time it should be able to perturb the fields at least up to the measurement system's threshold. Thus, a trade-off has to be made between the accuracy and sensitivity of the results. Such an assumption will introduce some complications in probe design and will limit its dynamic range.

In order to improve the sensitivity and dynamic range of the scattering technique, it is recommended to use a resonant scatterer that is able to re-radiate stronger fields than a nonresonant probe [54]. In addition, the AUT has to be well-matched to the excitation port so that the reflected signals is mainly coming from the scattering

probe. Additionally, it is necessary to increase the isolation between the excitation port of AUT and the receiver input port in order to decrease the leakage from the excitation to the receiver port. In [29], it is recommended to improve this isolation to as high as 90 dB. To do this, one can use a microwave tuner before the AUT to improve the matching. However, tuners can limit the measurement frequency bandwidth.

2.3.2 Perturbation technique: modulated probe

To overcome the drawbacks of the perturbation technique, Richmond first proposed a method known as the modulated scatterer technique[33]. It is perturbation-free, rapid and low-cost as well as accurate and sensitive. These advantages make the modulated technique a feasible alternative in many NF imaging applications. In the following sections, the principles of the MST probe and its design and implementation are extensively discussed and explained.

2.4 MST principle

The principle of the MST is based on marking the field at each point using an MST scatterer, which is also known as an MST probe. This technique is an indirect one. Therefore, there is no need to connect a transmission line to the measuring probe. As mentioned before, this is improving the sensitivity, accuracy, and dynamic range compared to the direct NF measurement techniques. In this technique, the AUT does not need to be well-matched to the excitation port as mentioned in Section 2.3.2 and isolation between the incident and reflected signals is not as crucial.

In practice, a small antenna such as a dipole with βl <0.1, where β and l are propagation constant and physical length of the antenna respectively, is loaded with a nonlinear device such as a diode or photosensitive device. The response of the so obtained loaded scatter is modulated with an external modulation signal (low frequency) applied to the probe [29]. Consequently, the probe modulates and scatters the field at its location and toward the receiving antenna. From the implementation point of view, an MST-based NF imager can be implemented in the monostatic or bistatic mode. In monostatic, the AUT itself picks up the modulated scattered fields and sends the signals to the receiving equipment. In this case, the setup is simple and there is no need to have an auxiliary antenna to pick up the scattered fields. However,

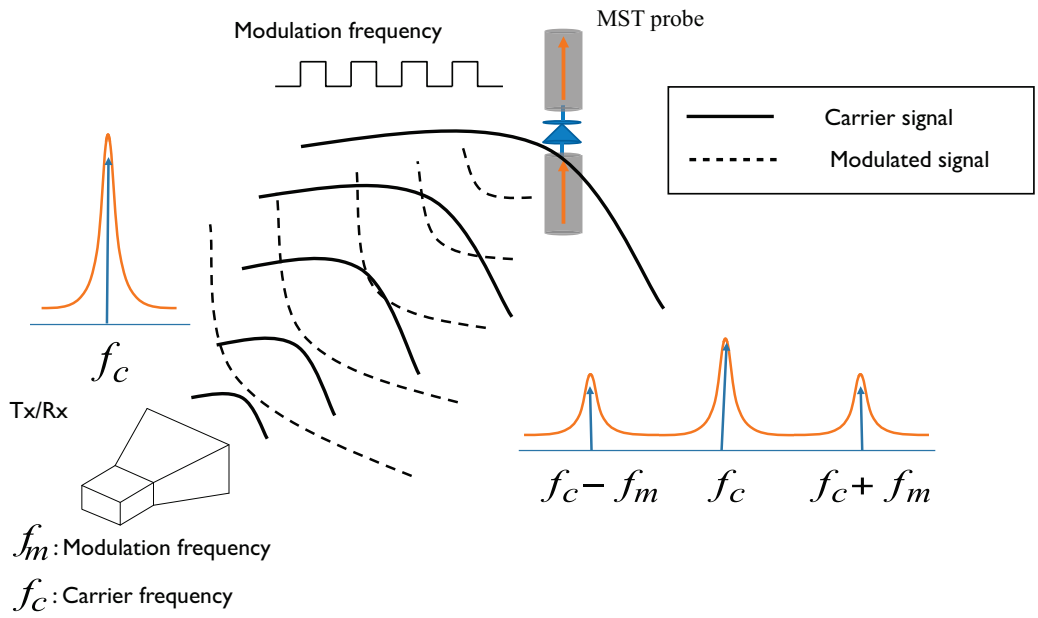

Figure 2.5 Schematic of an MST-based NF imager in monostatic mode.

the monostatic mode suffers from sign ambiguity when data is post-processed (square root) to obtain the electric field distribution [44]. As opposed to the monostatic mode, the bistatic mode needs an auxiliary antenna, which is held away to collect the scattered fields. Multiple reflections phenomena between the auxiliary antenna/probe and AUT are inevitable and should be compensated for if the NF imager is configured in the bistatic mode [55].

2.4.1 Monostatic

In the monostatic setup, the measured voltage is proportional to the square root of the electric field at each point, namely $E \propto \sqrt{I^2 + Q^2}$), where for convenience, I and Q can be measured with a lock-in amplifier (LIA). Figure 2.5 demonstrates a monostatic setup in which an MST probe measures the E-field distribution of a horn antenna.

Mathematically, a square root of a complex number has two answers. Thus, in order to obtain the field distribution of an AUT, it is necessary to remove sign

ambiguity from the equation $E \propto \pm\sqrt{v}$, where v is the measured voltage ($I+jQ$). If one simply uses the square root value obtained by a data processing software (e.g. Matlab) directly without paying attention to field continuity, sharp non-physical will be observed in the field distributions. This is illustrated in Figure 2.6, where the returned phase values are always in the first and fourth quadrant of the complex plane.Therefore, the phase measurement of the data varies ±90 degrees instead of ±180.

To overcome this problem and choose the correct sign, the sign of an arbitrary data point (maximum gain) within the data set is considered as a reference and to which the rest the data points and square root sign are compared, accordingly [44]. The corrected results after the removal of the sign ambiguity is demonstrated in Figure 2.6 (solid line), varying between ±180 degree.

Practically in a monostatic setup, the excitation signal is fed to the AUT via a coupler or circulator, which enables the measurement system to receive the backscattered signals. As addressed in [56], one of the leading criteria in selecting a suitable coupler or circulator is the level of isolation which can be achieved between the excitation port of the AUT and the receiving stage input port [29].

2.4.2 Bistatic

Unlike the monostatic setup, the bistatic setup needs an auxiliary antenna to collect the signals scattered by the MST probe. In this case, the measured fields are directly proportional to the signals to be measured, that is $E \propto v$, and obviously there is no sign ambiguity. However, in a bistatic setup the interaction between the auxiliary antenna and the AUT, and also with the measuring probe, can perturb the fields and lead to inaccurate results [24].

From a practical point of view, when a measurement is performed the distance between the probe and the auxiliary antenna has to be kept constant. Otherwise, the measured results do not represent the field distribution of the AUT, unless the radiation pattern of the auxiliary antenna is compensated and extracted from raw data. Figure 2.7 shows an example of an MST-based NF imager working in the bistatic mode.

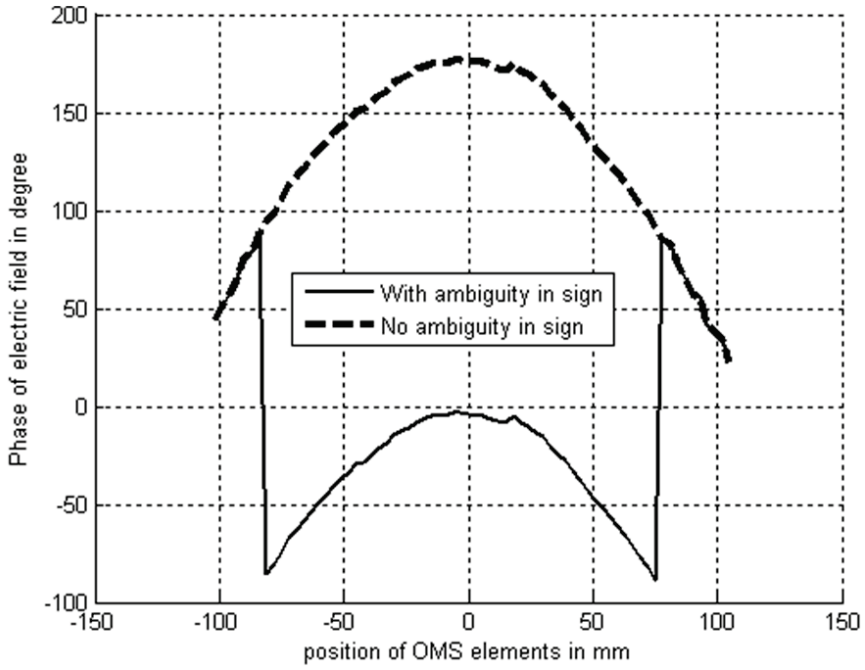

Figure 2.6 The result showing the effect of sign ambiguity in a monostatic setup.

2.5 MST probe implementations

2.5.1 Electrical

In electrically modulated probes similar to any basic MST probes, the probe consists of a small antenna and a nonlinear device that acts as a scatterer and a modulator, respectively [36, 57]. The modulator can receive the modulation signal via a pair of twisted metallic or resistive wires [37]. The scatterer can be selected between dipoles, loop and horn antennas, and also patch antennas. Figures 2.8 demonstrates two MST probes. However, horns and patch antennas are rarely used in practice due to their bulky structure and large ground planes. Short-dipole and small-loop antennas are the best alternatives for making MST probes. However, small loop antennas have disadvantage due to the fact that they can pick-up the electric field as well as a magnetic field. Basically the recorded signal (v) results from a superposition of two field components, with generally not well known weighting. This effect will be discussed in Section 3.4. Figure 2.9 shows a photograph of the electrically modulated probes developed in this project, which are modulated via pairs of low scattering

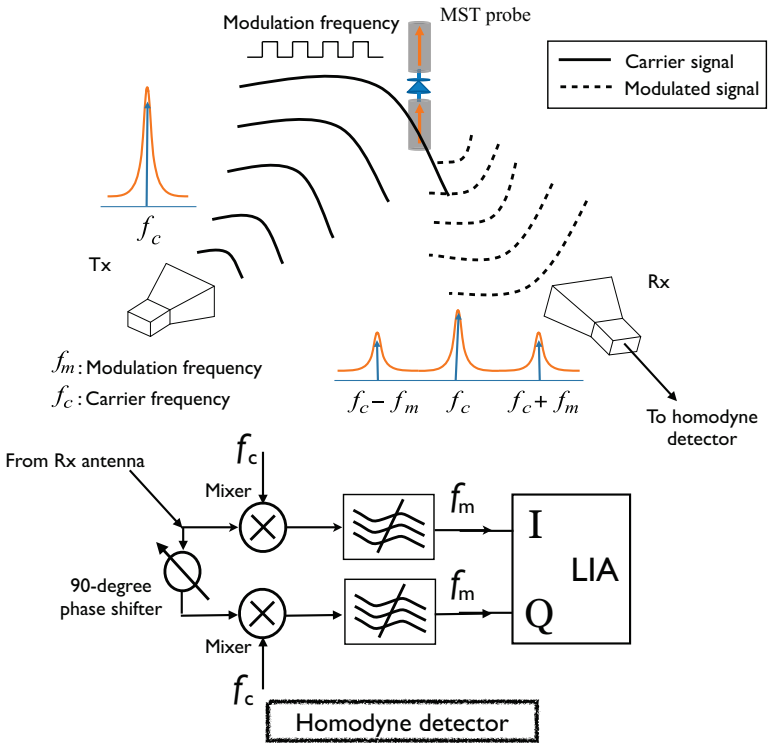

Figure 2.7 Schematic of an MST-based NF imager in bistatic mode.

resistive wires ($394\Omega/cm$).

The probe shown in Figure 2.9 was set to measure a normal component of the E-field above a transmission line, as demonstrated in Figure 2.10. One can notice that when the probe scans toward negative x values, the probe crosses the transmission line. Due to interaction between the line and the resistive wires the measurement results are perturbed significantly ($>$ 5dB), as shown in Figure 2.11. Whilst the probe measures on the other side of the line (positive x) because the wires are away, such perturbation is not seen. Therefore, it can be concluded that using this type of a probe does not always provide very accurate results. Moreover, the probe incorporates a built-in loop antenna as indicated in Figure 2.10, that acts as a parasitic probe and disturbs the outcome results.

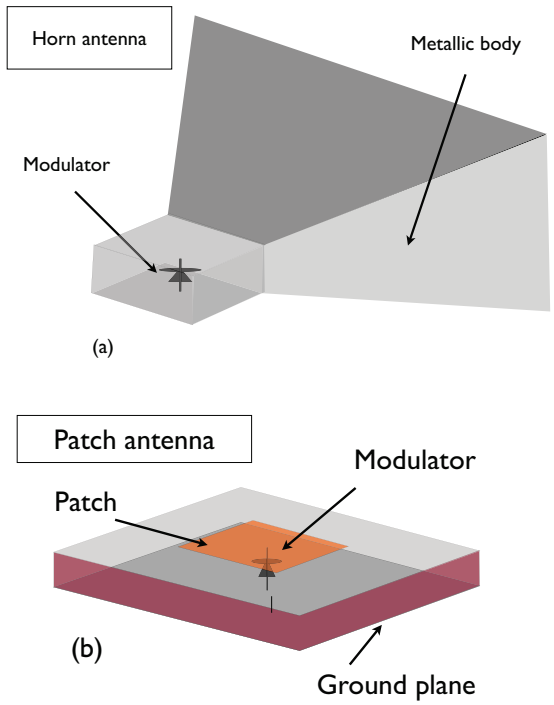

Figure 2.8 Schematic of a horn and a patch antenna based MST probe.

2.5.2 Optical

The optically modulator scatterer (OMS) probe structure is similar to its electrical counterparts and only differs in the type of modulator used. In OMS probes, a photosensitive device such as a photodiode and a phototransistor can act as a modulator [32]. Using such modulators implies using direct illumination techniques or optical fibers to carry modulating light. Optical fibers as opposed to other transmission lines are transparent to RF electromagnetic fields (see Figure 2.12). Thus, it can be assumed that measurements using an OMS probe are nearly perturbation-free. It is worth mentioning that in an early OMS probe prototype [58], the photo-activated device (i.e., photoconductive) was modulated remotely by a chopped light beam. In the early 90's, Hygate reported for the first time a fiber-based OMS probe consisting of a short-dipole integrated with a phototransistor [44]. The principle and benefits of the OMS probe were also demonstrated. However, the fiber and photodiode combination were custom-designed for the application. It was thus not available commercially

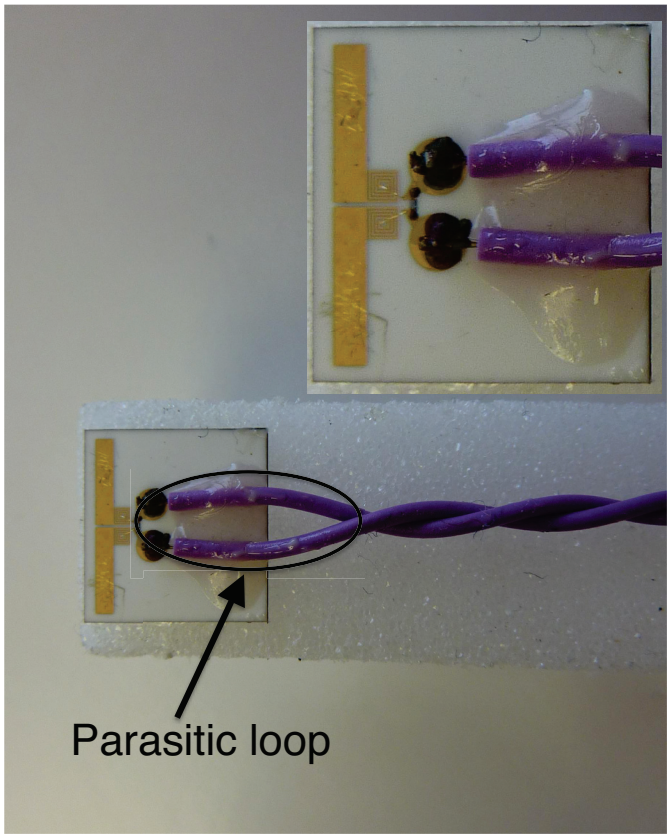

Figure 2.9 Photograph of an EMS probe operating at 2.45 GHz modulated via pair of resistive wires (394 Ω/cm).

and was expensive to make [32]. The growth of the optics industry and increasingly available low-cost optical components have had led to an increasing number of probes. In recent years, Liang [59], Nye [60] and Sowa [61] made contributions in the development of probes for application in antenna measurement, calibration of electromagnetic interference test facilities and far-field calculation of large antennas.

2.5.3 Mechanical

The mechanical method of modulation can be obtained by spinning or vibrating the probe monotonically right at the position where the field distribution is required [42, 43, 37]. Such perturbation modulates the fields at the probe position and no matter whether or not it is loaded with a nonlinear device. Simultaneous mechanical

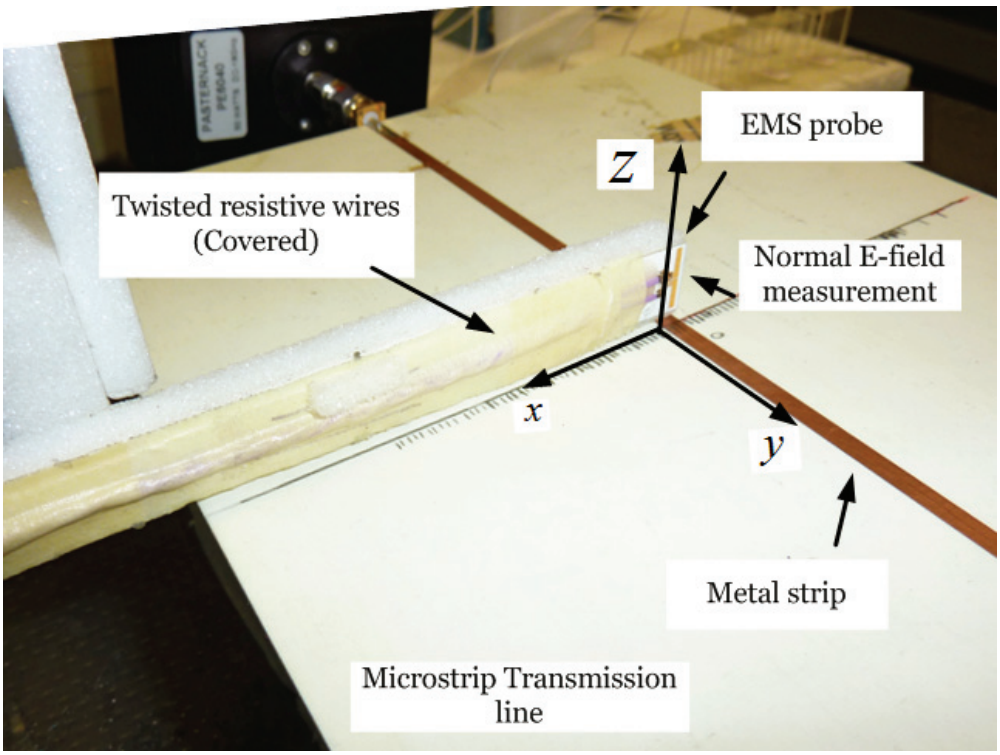

Figure 2.10 The photograph shows the MST probe measuring normal component of E-field at a distance of 5mm above a microstrip line.

and electrical modulation can also be used. Figure 2.13 shows two different types of mechanical MST probe: one modulates fields by spinning around its axis and the other by rotating along a line perpendicular to the strip surface. The use of MEMS[1] switch in fabricating an MST probe has also been reported [62].

2.6 MST probes array: a remedy for long measurement duration in NF imagers

In addition to accuracy, sensitivity and dynamic range, measurement speed is a very crucial parameter in NF imagers, particularly in biomedical applications [63, 24].

[1]Micro-Electro-Mechanical Systems (MEMS)

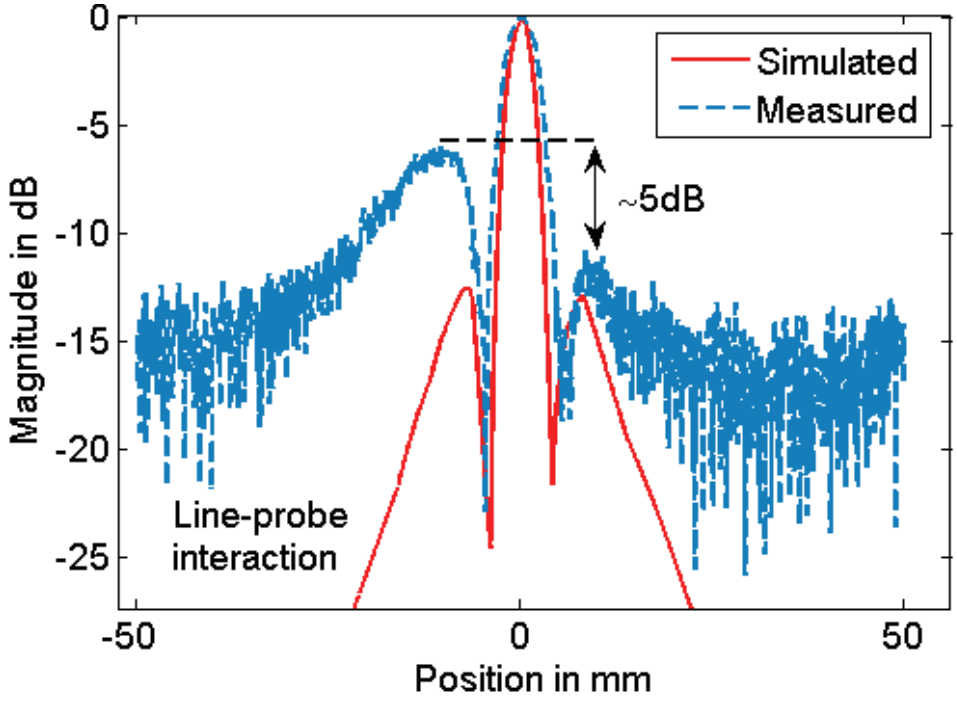

Figure 2.11 The measurement results of normal component of E-field at h=5mm.

Conventional NF imagers generally implement mechanical translation of the measuring probe over the region of interest, which implies a slowing-down of the process [47]. Also, support, holders and actuators can perturb fields by producing parasitic scattering. Thus, instead of using a single MST probe, introducing an array of them is recommended to minimize mechanical movements. Table 2.1 summarizes an investigation by Bolomey [46] that shows the benefits of using different kinds of MST arrays (e.g., 1-D [64] or 2-D [55]) to improve measurement speed.

2.6.1 Array configuration

In theory, MST arrays can be developed by arranging a number probes into one dimensional (e.g., linear) and two dimensional (e.g., planar) setups. Arrays of linear and 2D probes are among the most popular configurations utilized. A linear array developed with E-plane extent is shown in Figure 2.14. Examples of a circular and a 2D arrays are also demonstrated in Figure 2.15.

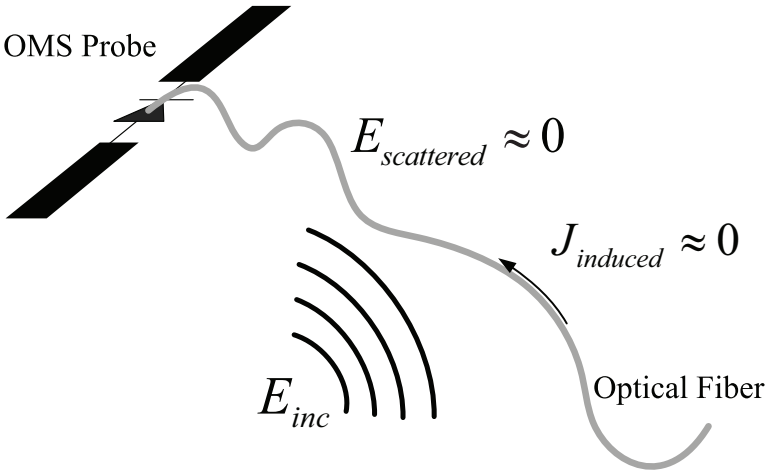

Figure 2.12 Schematic of an OMS probe.

Table 2.1 Estimation of Measurement time using different NF imager setups [24]

Antenna size (D/λ)	**Single Probe**	**1D MST Array**	**2D MST Array**
1120	698 h	2 h	1.2 h
280	44 h	20 min	10 min
70	3 h	2 min	40 sec
25	25 min	40 sec	5 sec

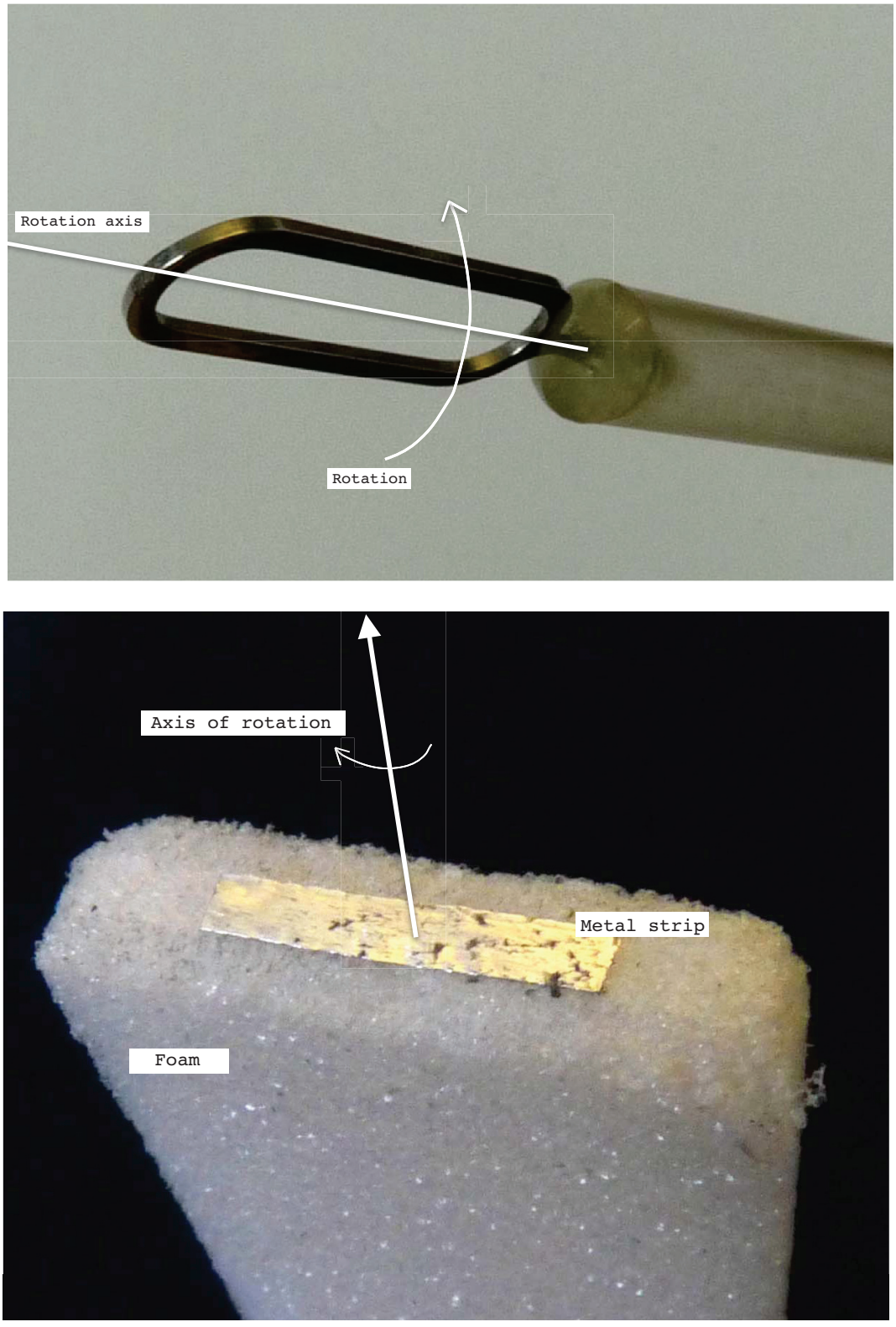

Figure 2.13 Photograph of an mechanical probe.

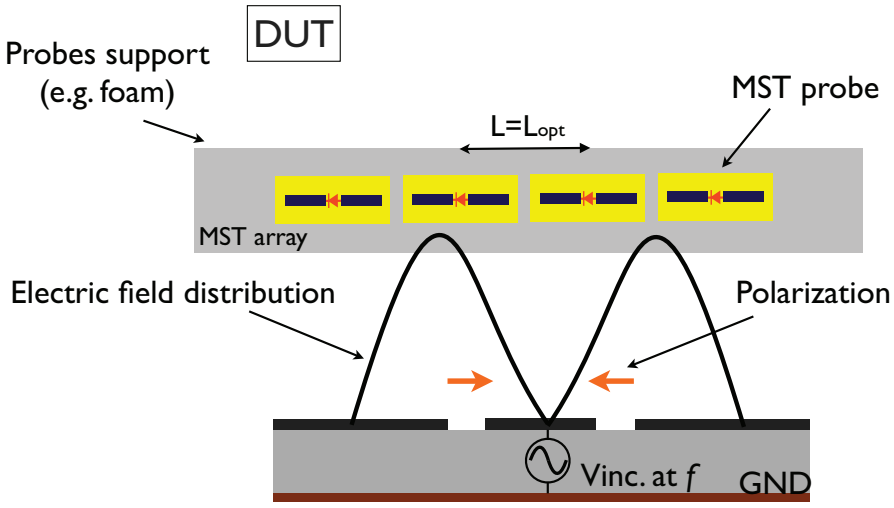

Figure 2.14 Schematic of a linear MST probe.

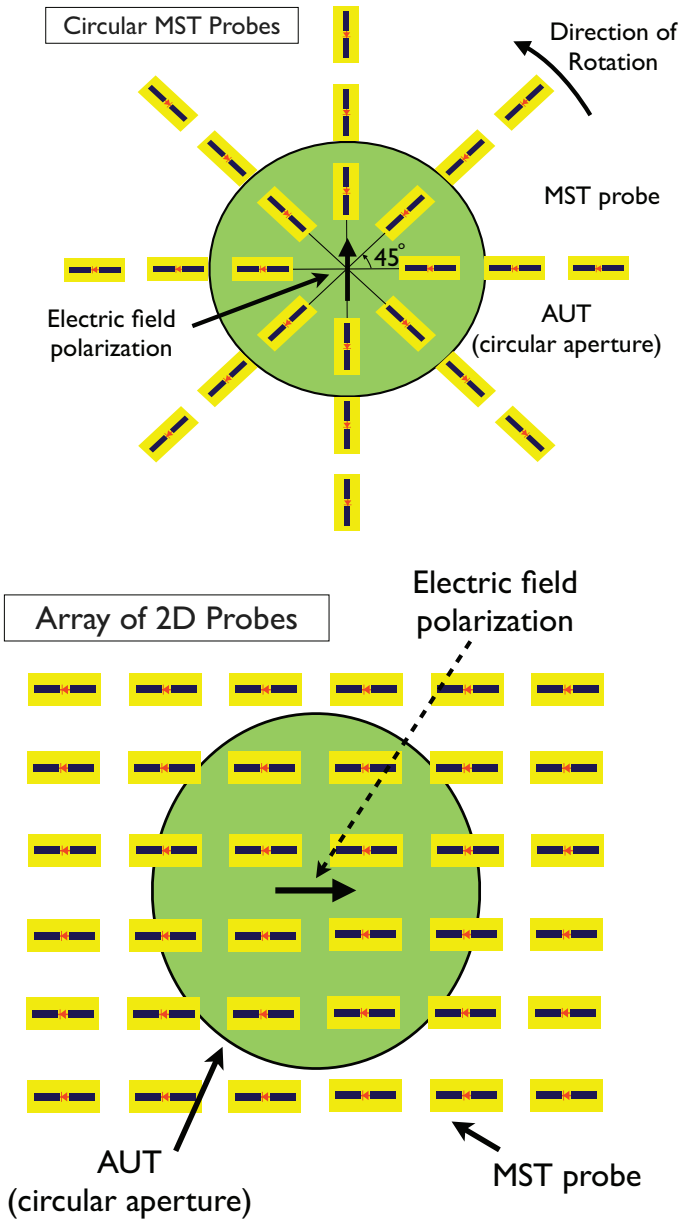

Figure 2.15 Schematic of a circular and a 2D array [24].

2.7 Criteria on selecting optimum working frequency [65]

In [65], the authors extensively investigated the performance of biological tissue imaging at different frequencies. Below, the discussion has been shown from [65]:

> "The operating frequency in imaging system intended for biological applications is a compromise between spatial resolution and tolerable attenuation. Spatial resolution of electromagnetic images is limited by diffraction to the order of a half wavelength of the radiation in the object explored; thus the resolution improves when the frequency is increased. It is worth mentioning that a half wavelength limit is true when the scattered fields are measured away from the body under test (BUT) (i.e., its far-field region). While, one can obtain much better resolution within in the near-field region (i.e., sub-wavelength imaging) of the BUT at the same frequency.
>
> The wavelength in biological tissues is substantially shorter than values in air because of the high water content. Water has a relative dielectric constant of the order of 70 to 80 at microwave frequencies and room temperatures. The wavelength is reduced in this medium by a factor of almost 9 in relation to air values. Therefore a theoretical resolution of several millimetres can be achieved with operating frequencies of a few gigahertz. On the other hand, biological bodies exhibit strong attenuation at microwave frequencies because of the high content of water and conducting solutes [66]. The attenuation increases rapidly with frequency, which limits effectively the working frequency depending on the size of the body, the illumination power, and the receiver sensitivity. For safety reasons, the illumination power density must be kept below the microwave radiation standards for continuous exposure. Receiver sensitivity is linked to the integration time of each measurement and consequently is proportional to the acquisition time. Imaging usually requires the measurement of thousands of scattered field complex data, which means that in order to have acquisition times of the order of seconds the integration time must be around 1 ms. From these considerations the useful frequency range

for microwave imaging is found to be from below 1 GHz for larger bodies such as the thorax or pelvis to several GHz for smaller ones such as limbs. In our case a frequency of 2.45 GHz has been chosen, which is assigned to industrial-scientific-medical applications."

Chapter 3

Optically Modulated Scatterer (OMS) Probe: Accurate and Sensitive Near-Field Probe

In this chapter, we address the design and implementation of an accurate, sensitive and low-profile OMS probe. The small size of the probe structure (one-twelfth of a wavelength) leads to a non-invasive measurement [56], contrary to many reported probes of half or quarter of a wavelength [67]. The probe that is proposed and that has its development discussed in this chapter, is made with commercial off-the-shelf optical components and a printed circuit fabricated using a standard PCB process. It is therefore low-cost and easily reproducible. To compensate for the reduced sensitivity due to the short probe length, a built-in matching network is added. This network is optimized for operation at 2.45 GHz, which is used in industrial, scientific and medical (IMS) applications as well as in wireless communication systems. In the following, the probe design procedure is described in detail and its characteristics are presented.

3.1 Optical modulation: perturbation-free MST implementation

In any type of MST probe, an external low frequency signal (modulating signal) is transferred to the probe. The modulation causes tagging of the electromagnetic field at the position of the probe. In electrical modulation, a pair of metallic or resistive wires is used to carry modulation signals to the MST probe, while a fiber is used in optical modulation. The presence of wires in the NF region of interest may perturb the measured fields strongly.

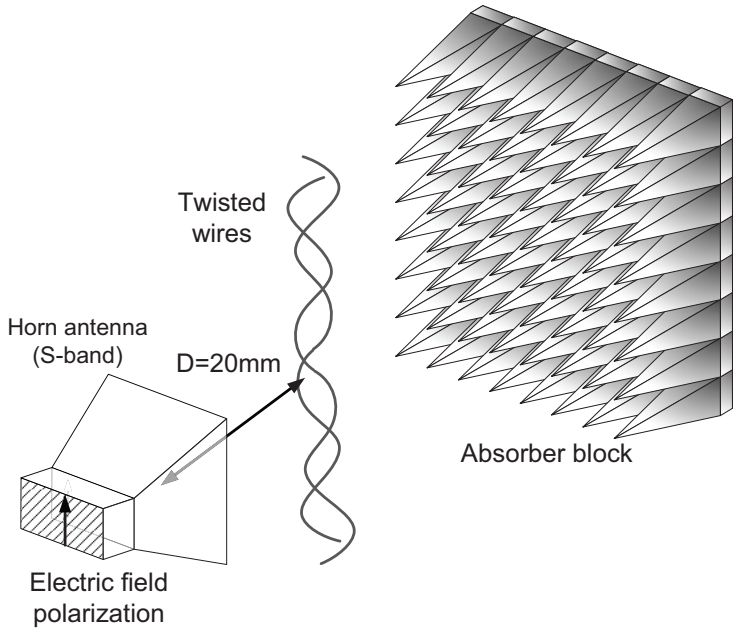

Figure 3.1 Schematic of the setup used to study the effect of transmission media on the field to be measured.

In order to illustrate this effect, a simple experiment was done by holding different types of straight transmission media of equal length in front of an AUT (Figure 3.1), while measuring the AUT's return loss with a vector network analyzer (VNA). In the experiment, transmission media consisting of twisted pairs of copper and resistive (394 Ω-cm^{-1}) wires, and pieces of optical fiber were used. These scatterers were held 20 mm away from the horn antenna's aperture (AUT). The horn was fed with a WR-284 rectangular waveguide with a cut-off frequency of 2.08 GHz. The change in the antenna return-loss above this frequency is interpreted as an influence of the transmission line and fibers on the NF distribution of the AUT. As seen in Figure 3.2, the metallic twisted pair clearly causes reflections of the AUT fields. Such disturbances may cause significant errors in the case of near-field RCS measurements in which the fields scattered by the target are usually very weak. In the case of resistive wires, the disturbances are much smaller but nevertheless reach up to 5 dB compared to the horn's intrinsic return loss. Finally, the invisibility of the fiber to the electromagnetic exposure is clearly demonstrated, as almost no perturbation is visible in this case.

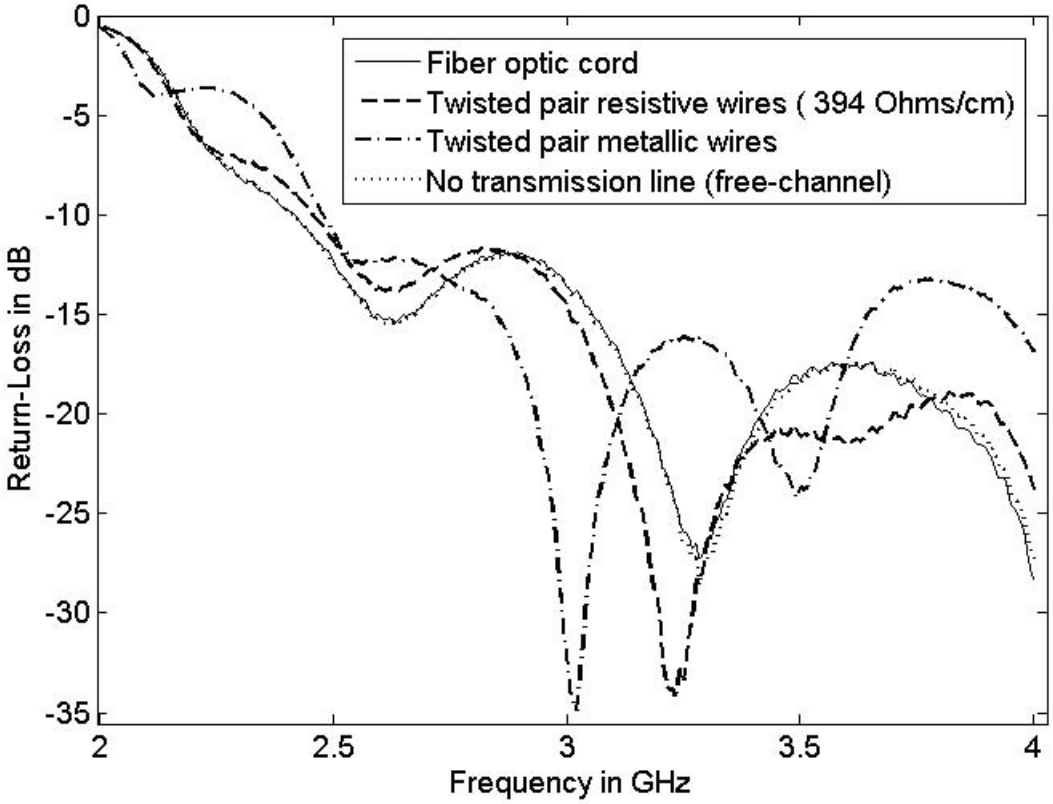

Figure 3.2 Measured return-loss of a horn antenna for different types of transmission lines causing scattering.

3.2 Optical probe design and implementation

The probe is modulated by an optical signal that is provided by a coupled optical fiber to the photoactivated component. It is switched ON and OFF at an audio frequency causing field modulation.

In the following, the design and implementation of an optically modulated scatterer (OMS) is explained and discussed. Criteria for antenna type and modulator selection, matching network design and implementation, and an OMS probe assembly will be also covered. Finally, the probe is characterized to ensure the desired requirements such as sensitivity, accuracy, and dynamic range are achieved.

3.2.1 Antenna type

Not only the modulating wires but the measuring probe itself plays a key role in improving the accuracy and resolution of the measured field profile. Usually, the scatterer should have minimum interaction with a source of radiated fields to be measured (as small as possible). The dynamic range of the measurement system depends on the minimum and maximum field levels the probe is able to scatter, and the detection threshold and saturation level of the receiver. Achieving a high dynamic range necessitates using a larger scatterer at the expense of oscillations in field measurements and deviation from the true field. In general for electrically small probes, the smaller the dimension of the scatterer the smaller the expected disturbance, but at the cost of lower sensitivity. Thus, a trade-off between the dynamic range and sensitivity of the probe has to be made.

In practice, a limited number of antenna types that can perform as an MST probe consisting of dipoles, loops, horns and microstrip antennas have been reported. The leading criterion to select the type of antenna is to keep the influence of the probe on the field to be measured low. The concept of a "minimum scattering antenna" (MSA) provides us with an appropriate guideline for selecting the scattering antenna. Conceptually, an MSA is invisible to electromagnetic fields when it is left open-circuited [68, 69] or connected to an appropriate reactive load [70]. The horn and microstrip antennas do not fulfill MSA requirements due to their bulky physical structures and large ground plane, respectively. They cause significant structural-mode [69] scattering regardless of antenna termination. The short-dipole ($\lambda < 10$) and small-loop approach the desired MSA behaviour. A dipole probe might be a better choice because of its simpler structure than the loop. Moreover, a loop probe may measure a combination of electric and magnetic fields if it is not properly designed [29]. Figure 3.3 shows a drawing of a short-dipole and a small-loop antenna loaded with Z_L. The scattered fields by the short-dipoles (i.e., E_S) and small-loop antennas (i.e., H_S) due to the incident waves (i.e., E_{inc} and H_{inc}) are also demonstrated in the same figure. $E_S = 0$ or $H_S = 0$ for the short-dipole or small-loop antenna, respectively, if they are left open circuit (i.e., $Z_L = \infty$) or loaded with proper reactive load.

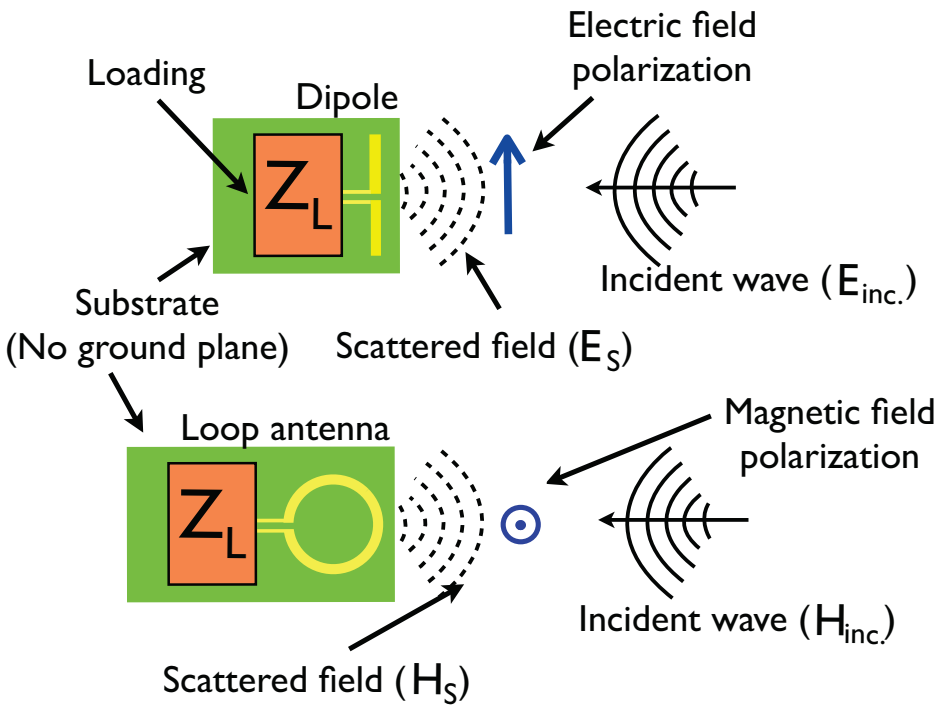

Figure 3.3 Minimum scattering antenna: dipole and loop antennas.

3.2.2 Modulator selection criteria

From the concept of AM-modulation, we can introduce modulation index (m) as ratio of the crests (1+μ) and troughs (1-μ) of the modulated signal envelop (see Figure 3.4), where μ is level of AM-modulation [29]. Therefore, "m" can be defined by Equation 3.1.

$$m = \frac{crest - trough}{crest + trough} \tag{3.1}$$

Assuming two states of the modulator with load impedance Z_{ON} and Z_{OFF}, and a probe impedance Z_p=Z_{dipole}+Z_{mn}, where Z_{mn} stands for the matching network impedance (It is assumed that this network consists of a series reactance in this

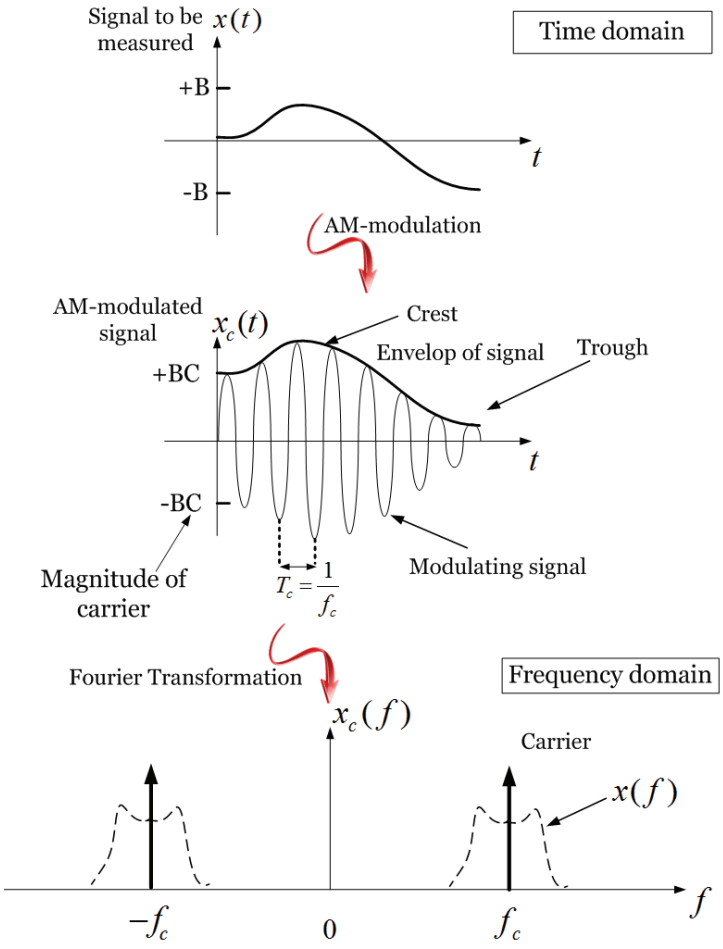

Figure 3.4 AM-modulation principle.

example but other topologies are of course possible.), the modulation index of the signal scattered by the probe is given by [29]:

$$m = \frac{|Z_p + Z_{ON}| - |Z_p + Z_{OFF}|}{|Z_p + Z_{ON}| + |Z_p + Z_{OFF}|} \tag{3.2}$$

whereas the ratio of the currents flowing in the probe terminals in both states is given by:

$$CR \equiv \frac{|I_{ON}|}{|I_{OFF}|} = \frac{|Z_p + Z_{OFF}|}{|Z_p + Z_{ON}|} \tag{3.3}$$

We can thus write:

$$m = \frac{1 - CR}{1 + CR} \tag{3.4}$$

If a small resonant probe is used, the real and imaginary parts of Z_p+Z_{mn}, can be made very small, and possibly negligible compared to Z_{ON} and Z_{OFF}, such that:

$$m \approx \frac{|Z_{ON}| - |Z_{OFF}|}{|Z_{ON}| + |Z_{OFF}|} \qquad CR \approx \frac{|Z_{OFF}|}{|Z_{ON}|} \tag{3.5}$$

The maximum possible magnitude of the modulation index occurs when $CR = 0$ ($m = 1$) or $CR \to \infty$ ($m = -1$).

Ideally, it is desired to maximize $|m|$ in order to have the strongest possible sideband response for a given level of a measured field. The selected modulated load should have either $|Z_{ON}| \gg |Z_{OFF}|$ or $|Z_{OFF}| \gg |Z_{ON}|$. In other words, input impedance of the device in the ON and OFF states should differ significantly.

The probe proposed here is based on a photodiode manufactured by Albis® (PDCS30T). This device was selected due to its high impedance variation as a function of input light level at a target test frequency of 2.45 GHz. The input impedance of the photodiode was measured on a wafer probing station using an Agilent 8510 vector network analyzer (VNA) for different optical power levels (no light, and with a sweep from -10dBm to 13 dBm) in the 2-3 GHz frequency range. The optical power in this measurement, was applied to the photodiode via an optical fiber, which was held above its active area by an accurate x-y positioning device. Before making the measurement, the VNA was calibrated using SOLT (i.e., Short-Open-Load-Thru) standard to remove all the errors (i.e., VNA and probes' errors) up to the tip of the probes.

Figure 3.5 shows the impedance magnitude, revealing saturation for light power greater than +6dBm. This level was taken as the optimal point for the design of the matching network in Section 3.2.4. The impedance of the diode in the "no-light" or OFF state and +6dBm or ON state is shown in Figure 3.6. The diode can be modelled approximately by a series RC circuit, with $R_{OFF} = 38.8\Omega$ and $C_{OFF} = 0.31pF$. In the ON state, a similar model with $R_{ON} = 15.8\Omega$ and $C_{ON} = 13.66pF$ can be assumed. These models are approximately valid on a narrow frequency band centered on 2.45GHz. According to Equation 3.3, at 2.45 GHz these measured data lead to $CR = 13.38$ (22.dB) and $m = -0.86$.

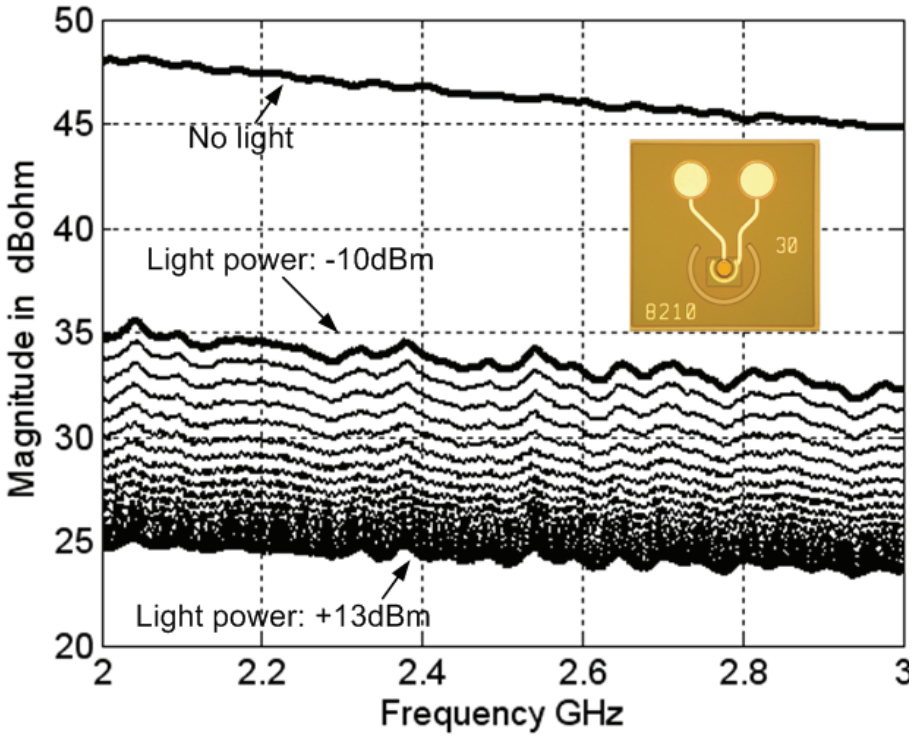

Figure 3.5 Input impedance magnitude of the photodiode.

3.2.3 Selection of OMS probe length

The length of the dipole results from a tradeoff between resolution and sensitivity. The first MST probe reported by Richmond [33] had a length of 0.31λ (λ is the wavelength in free space). Liang et al. used a length ranging between 0.05λ-0.3λ in order to make fine and disturbance-free field maps [59]. Measured electromagnetic fields were also reported in [57] for operation in the 2-18 GHz band using MST probes that are150 μm, 250 μm, and 350 μm long. A length of 8.3 mm was used by Hygate [32] for signals below 10 GHz. Nye also used 3 mm and 8 mm MST probes at f=10 GHz to obtain NF maps of antennas or any passive scatterers [14]. The probe presented here has a length of $\lambda/12$ at a design frequency of 2.45 GHz. The impedance of the printed

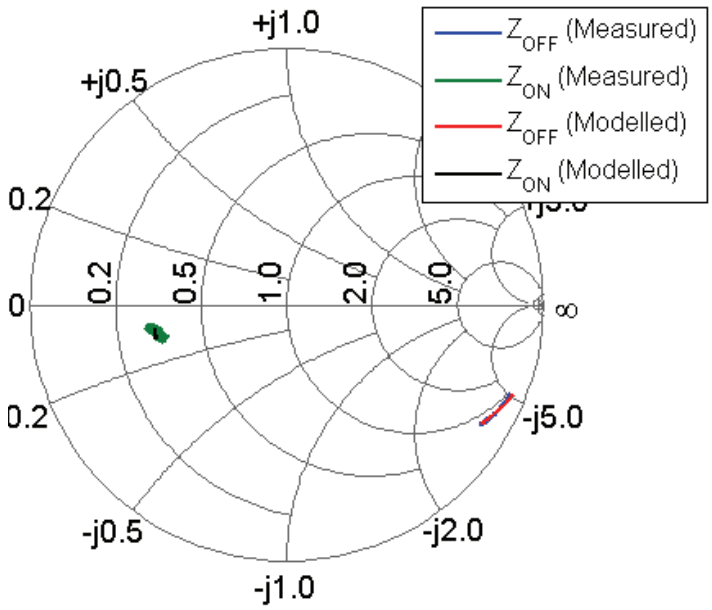

Figure 3.6 Input impedance (normalized to 50 Ω) of the photodiode chip in the 2-3 GHz range with and without illumination. The measurement results and that obtained from modelling of the photodiode are compared.

short dipole at this frequency, as obtained by simulations with an ADS-Momentum® planar solver from Agilent, is $Z_P = 1.22 - j412\Omega$.

In order to ensure that the probe with length of $\lambda/12$ not only meets the requirements of MSA but also has a negligible influence on the field to be measured, we look at the measurement mechanism by MST probe using network approach (i.e., [V]=[Z][I]) as demonstrated in Figure 3.7. The AUT in this figure acts as a radiating source and also a collecting antenna (i.e., port #1), and the scatter represents a measuring probe (i.e., port #2) which is loaded with Z_L (e.g., input impedance of the modulator) [29].

$$V_1 = Z_{11}I_1 + Z_{12}I_2 \tag{3.6}$$

$$V_2 = Z_{21}I_1 + Z_{22}I_2 \tag{3.7}$$

The induced current on the probe (i.e., I_2) yields voltage $V_2 = -I_2Z_L$ across the

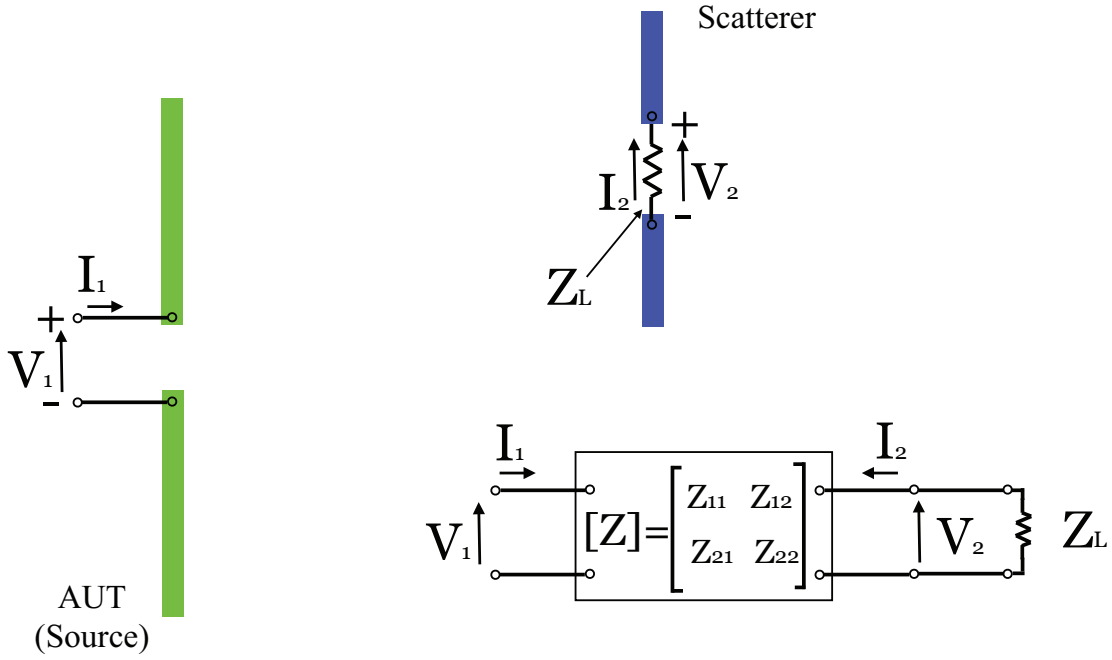

Figure 3.7 Modelling of measurement mechanism using network approach, monostatic implementation.

terminal. One can obtain 3.8 by solving Equation 3.7 for V_1:

$$V_1 = \left(Z_{11} - \frac{Z_{12}Z_{21}}{Z_{22} + Z_L} \right) I_1 \tag{3.8}$$

It is also assumed that the voltage across terminal #1 in the absence of the scatterer is given by $V_1^0 = Z_{11}^0 I_1$, where Z_{11}^0 is the input impedance of the AUT. Then, by subtracting it from Equation 3.8, it yields,

$$V_1 - V_1^0 = \Delta V_1 = \left[(Z_{11} - Z_{11}^0) - \frac{Z_{12}Z_{21}}{Z_{22} + Z_L} \right] I_1 \tag{3.9}$$

The Equation 3.9 shows that the measuring probe has two separate effects at the receiver's terminal, namely, the effect due to its physical structure (i.e., structural mode) and its loading (i.e., antenna mode). On the right hand side, the first term is present even when the probe is left open-circuited (i.e., when $Z_L \to \infty$) and it

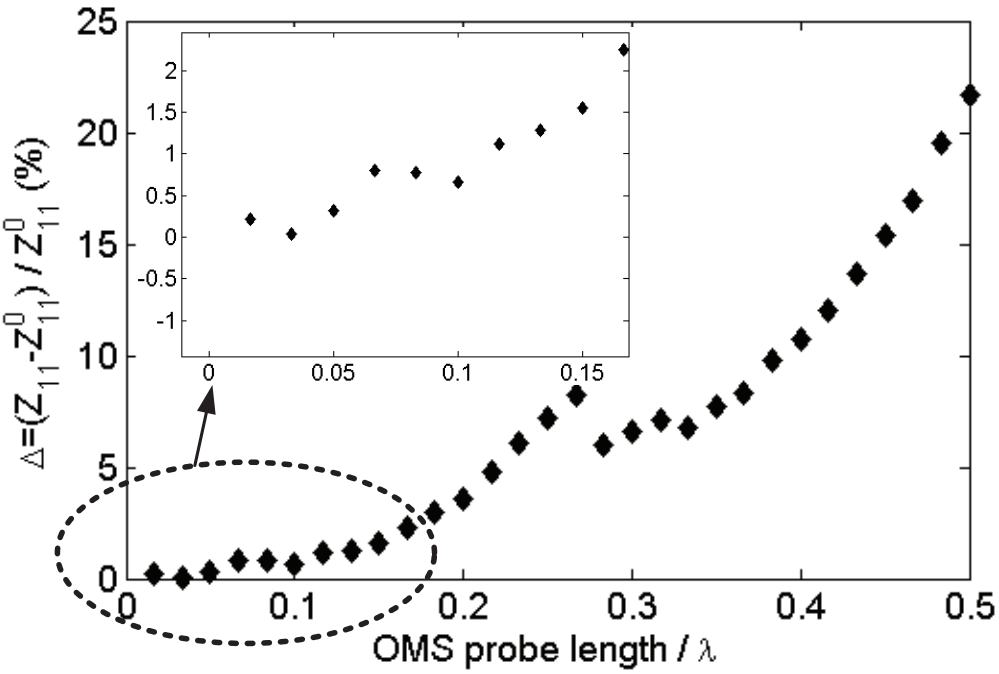

Figure 3.8 AUT impedance variation due to the probe's structural modes, as a function of the probe's lenght.

therefore stands for the probe structural mode (i.e, $(Z_{11}-Z_{11}^0)I_1$). The second appears when the probe loading (i.e., Z_L) is finite or zero. In MST-based probes only the latter term is modulated. The first term is present and varies when the probe is moved from one measurement point to another but those variations are slow compared to the rate of modulation. It can thus be assumed that they will not affect the measurement at the modulation frequency. By considering an open-circuited scatterer (i.e., $Z_L \rightarrow \infty$), ΔV_1 gives $Z_{11} - Z_{11}^0$; this represents the variation of the induced voltage across the AUT's terminal compared to the case in absence of the scatterer. Ideally, it is supposed $\Delta V_1 \rightarrow 0$ for MSA antennas, namely no structural mode radiation should occur.

Now, in order to investigate whether the chosen length (i.e., $\lambda/12$) for the OMS probe fulfills the requirements of MSA antenna (i.e., reduced structural mode), we performed a simulation in HFSS, a 3D full wave finite element solver, wherein, a

planar dipole with the length of L, width of $w = 1mm$ and a gap $g = 100\mu m$ between the arms of the dipole were considered. The dipole was positioned in front of the aperture of the horn antenna used in Section 3.1. Then, the value of $\Delta = \frac{Z_{11}-Z_{11}^0}{Z_{11}^0}$ versus the length for probe was calculated and plotted in Figure 3.8. The results show that Δ variation is less than 1% for probes shorter than 0.15λ. Therefore, an OMS probe consisting of a short dipole with length of $\lambda/12$ can be considered as a good MSA when it is used to characterize this horn antenna. The derivation shown here highlights the fact that MSA operation depends on Z_{11} of the AUT and not only the characteristics of the NF probe.

3.2.4 Matching network design

As shown in [29], scattering by the probe can be increased by adding an inductive reactance in series with a capacitive short-dipole (i.e., $Z_p = Z_{dipole} + j\omega L$) so that a resonance occurs in one of the two states. The inductance value should be chosen such that the numerator or the denominator in Equation 3.3 is minimized, leading to an increased modulation index. This effect, however, is frequency selective. The implementation of the inductive load between the photodiode and the short-dipole is illustrated in Figure 3.9. A simple planar spiral inductor is used and a wire bond is made between the photodiode and the central landing pad. It is also connected to the OMS probe antenna terminal from its rear. The symmetry of the OMS probe before adding the spiral inductor is maintained by splitting the spiral inductance into two and putting one at each terminal of the balanced dipole.

The value of the inductance should make the loaded short dipole resonant when the light is ON (denominator of Equation 3.3 minimized) and increase its impedance when the light is OFF. To find the optimum inductance value, we tried to maximize CR. The measured input impedance values of the photodiode in both states were used (see Figure 3.5). Figure 3.10 represents CR versus inductance. The inductance of 25 nH associated with the peak in the curve is referred to as the optimal point of the matching network and it can be seen that the maximum CR is close to the estimated value 22.5 dB. The minimum of CR near $L = 42nH$ also leads to a local maximum of $|m|$ but it is not as high.

The OMS probe scattering properties (i.e., modulation depth) can be improved

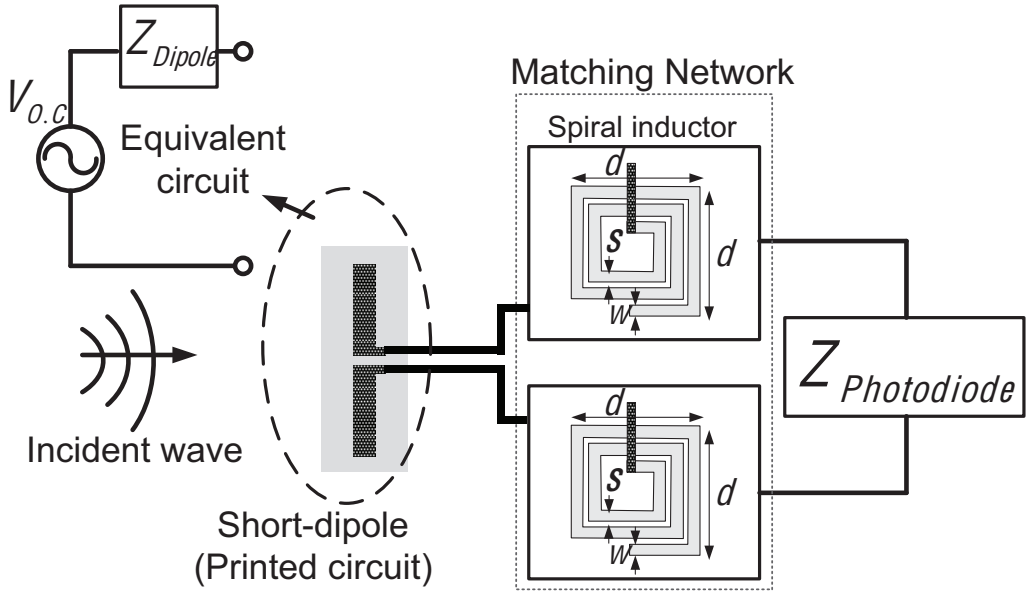

Figure 3.9 Matching network for the proposed OMS probe (d=0.99 mm, s=63.5 μm and w=50.8 μm. Dipole length: 1 cm. Drawing is not to scale.

by adding an inductive reactance in series with the capacitive short-dipole, however it creates a resonance in one of the two states. This will be discussed in Section 3.2.4. The schematic of the OMS probe implementation incorporating the inductive load between the photodiode and the short-dipole is illustrated in Figure 3.9.

Matching network impact on the OMS probe performance

The impact of the matching network on the probe performance is presented here. The difference between the scattered field when the dipole is in ON and OFF states (i.e. $Z_{OFF} = 38.8 - j206.2$ and $Z_{ON} = 15.9 - j4.8$) was calculated versus frequency for two cases: with and without considering a matching network in an OMS probe structure. To do this, a method of moment code was developed to calculate the differences within the 1-4 GHz frequency range.

In this model, the scattered field was calculated 1 cm away from the dipole when a uniform plane wave illumination is considered. The results shown in Figure 3.11 exhibits a significant improvement of about 23 dB in scattered field by an OMS

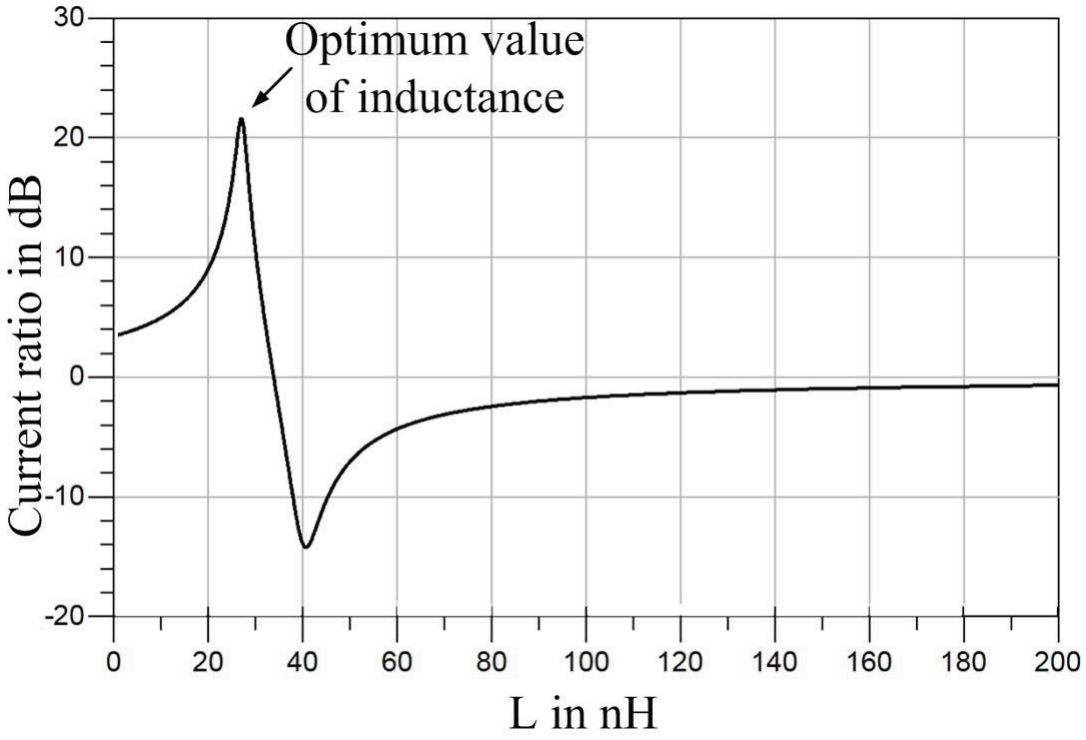

Figure 3.10 Current ratio versus the inductance value used for matching.

probe when a matching network is added. As a consequence, the sensitivity of the OMS probe will significantly improve. The high and low peaks on the solid curve correspond to resonances that occur in the ON and OFF states of the OMS probe. In order to show that, the equivalent circuit of the OMS probe shown in Figure 3.12 was considered. Then, we tried to predict the resonance frequencies of the probe in the ON and OFF states.

ON and OFF state resonance frequencies

Let us assume that the input impedance of the photodiode in ON and OFF states are given by $Z_{ON} = R_p(ON)+1/j\omega C_p(ON)$ and $Z_{OFF} = R_p(OFF)+1/j\omega C_p(OFF)$, that the dipole and matching network is given by $Z_{dipole} = R_d+1/j\omega C_d$ and $Z_{mn} = 2j\omega L_1$. Since, the imaginary part of the dipole input impedance is much greater than the real part (i.e., $R_d \ll 1/j\omega C_d$), it can be assumed that $Z_{dipole} \approx 1/j\omega C_d$. In addition, by considering only the imaginary part of the photodiode's input impedance, the

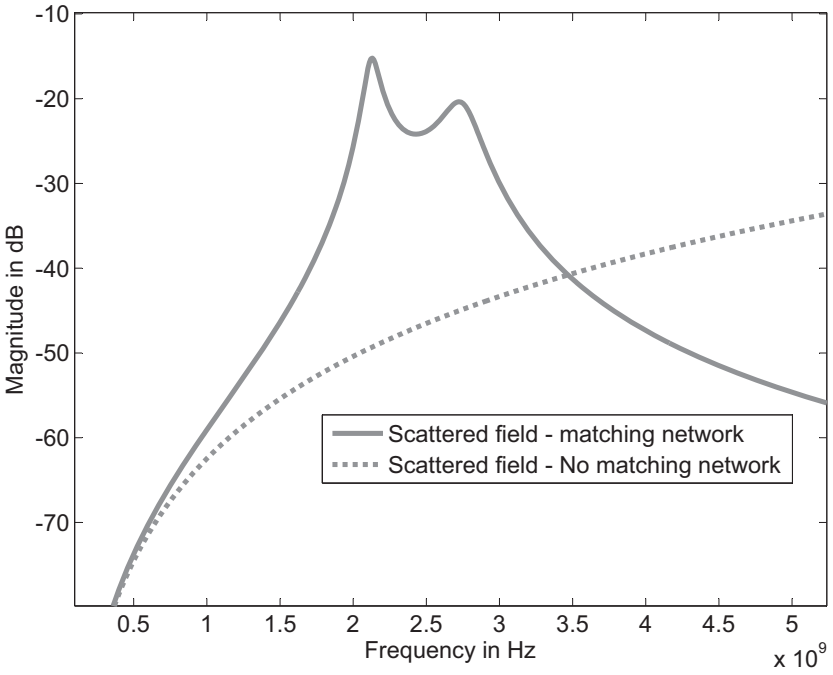

Figure 3.11 Frequency response of an OMS probe: Solid line probe with matching network and dashed line probe without matching network.

equivalent circuit forms a series LC circuit whose resonance frequency is calculated approximately using $f_0 = 1/\sqrt{LC}$. The calculation of f_0 showed that the resonance frequencies of the OMS probe in ON and OFF states are 2.59 GHz and 3.14 GHz respectively, which correspond to the peak of the curves in Figure 3.11, however, a frequency shift ($\sim 200MHz$) for both frequencies is seen. We also simulated the circuit shown in Figure 3.12 (i.e., equivalent circuit for the OMS probe) using Advance Design System (ADS) simulator to ensure the accuracy of the calculated f_0s based on our simplifications. In this simulation, the current induced on the dipole was estimated versus frequency for both ON and OFF states. Figure 3.13 shows two resonance frequencies corresponding to ON and OFF states, confirming the calculation results. As it can be seen, the curves' resonances occur close to the frequencies which were calculated above.

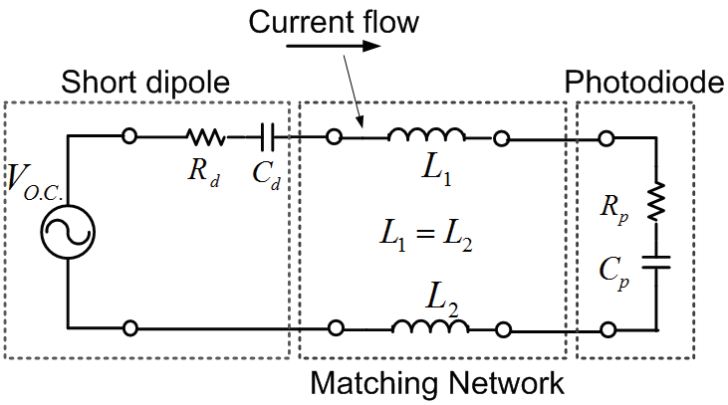

Figure 3.12 Schematic depicting the equivalent circuit of the OMS probe, wherein $R_d = 1.22\ \Omega$, $C_d = 0.15\ pF$, $R_p(ON) = 15.85\ \Omega$, $C_p(ON) = 13.65\ pF$, $R_p(OFF) = 38.78\ \Omega$, $C_p(OFF) = 0.31\ pF$ and $L1 = L2 = 12.7\ nH$.

3.3 OMS probe fabrication

The OMS probe is fabricated on a thin ceramic substrate (alumina) with a thickness of 10 mil, a relative permittivity of 10.2 and $tan\delta = 0.004$. An optical fiber is coupled to the active surface of the photodiode using a precision positioning system and by monitoring the output DC current while light is applied in the fiber. Finally, the fiber is permanently fixed by pouring epoxy glue when in the position corresponding to the current peak. In addition, in order to prevent any damage to the coupling by mishandling the probe, a strain relief structure made of a low permittivity material ($\epsilon_r \approx 2.7$) is added. Figure 3.14 shows the photograph of the completed probe assembly. The dipole length and width are 10 mm and 1 mm respectively, whereas the dimensions of the ceramic substrate are 7 mm and 15 mm. Each of the spiral inductors occupies an area of 0.99 mm by 0.99 mm. The photodiode area is 500 μm^2. Wire-bonding provides the electrical contacts between the photodiode and the inductor terminals on the substrate (no ground plane).

3.4 Validating the fabrication process

Once the OMS probe was fabricated including fiber coupling, it is necessary to verify whether the probe operates at the optimum frequency at which it was designed (see

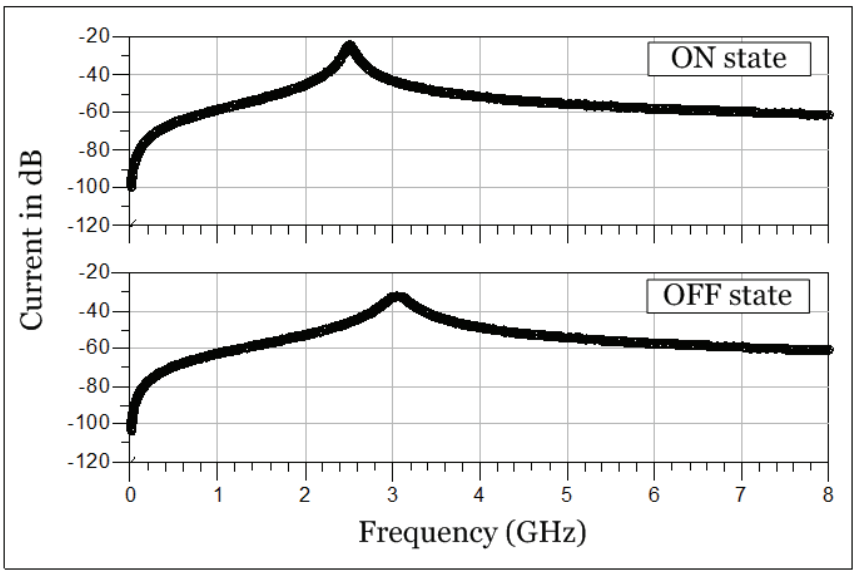

Figure 3.13 Magnitude of the induced current on the OMS probe antenna (i.e., dipole) as a function of frequency in ON and OFF states.

Section 3.2.2). Assuming that the photodiode is saturated when the optical power reaches +6 dBm (see Figure 3.5), it is implied that beyond this limit the photodiode will not be able to modulate more fields if the applied optical power is increased.

To do this, the OMS probe was exposed to a constant power electric field (e.g., near a horn antenna or microstrip transmission line) at 2.45 GHz. Then, the modulated optical power applied to the probe was swept from -10 dBm to 13 dBm while recording the generated sidebands power level, reflected at the port of the horn with a spectrum analyzer. Figure 3.15 represents the results obtained by this experiment. The results shows that the sidebands level (normalized to its maximum) increases linearly with the optical power when it is smaller than +6 dBm. Beyond this limit as presumed, the probe is not able to scatter more fields. This test not only confirms that the probe is operating at a desired working point, it also shows the quality of fiber/photodiode coupling.

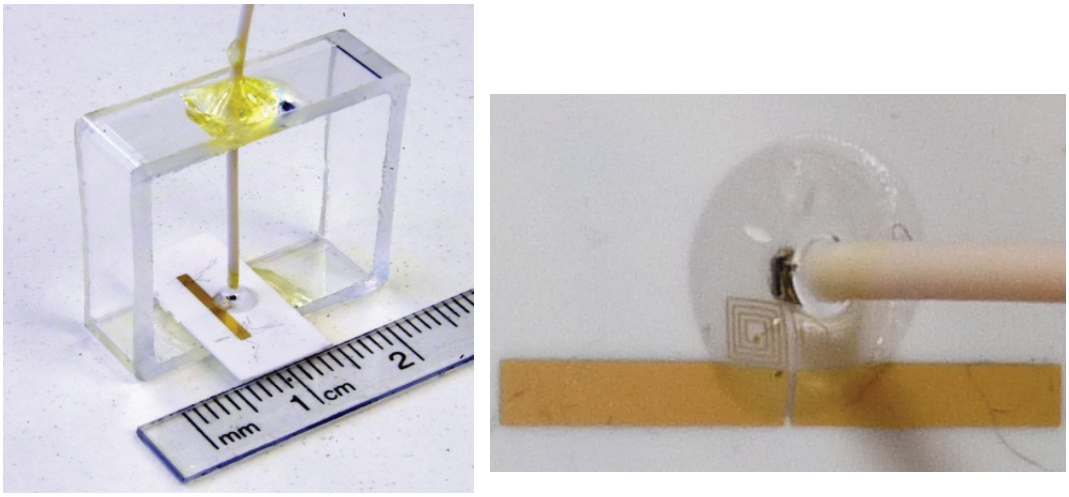

Figure 3.14 Photograph of the implemented OMS probe.

Loop antenna: not a precision MST probe

The major drawback associated with using a small-loop in an MST probe is the potential of the loop to pick up both magnetic and electric fields simultaneously [29, 71]. This means that the results are the combination of the two fields (i.e., magnetic and electric) with an unknown contribution from each. Thus extracting the desired magnetic field [29] is not possible or else is very complicated. As a consequence, the field measurement with this type of probe will not be accurate compared to that of short-dipole MST probe.

In [29], it is explained how to approximately calculate the percentage of magnetic and electric modulations by means of a loop MST probe. The variables m_E and m_H are denoted for the electric and magnetic fields modulation level and calculated using Equations 8.41 and 8.42 in [29]. The derivation of the formulas for calculating m_E and m_B is discussed extensively in [29].

The results of an m_E and m_B variation for an MST loop probe are shown in Figure 3.16. In this calculation, the width of the small-loop MST probe is kept constant (i.e., W$\propto 0.041\lambda$) while the length of the probe (L) changes from $0.05 - 0.5\lambda$. This MST probe consists of two modulating loads (i.e., PDCS30T photodiodes used in the preceding sections). It is worth mentioning that using two photodiodes can improve the ratio of $\frac{m_B}{m_E}$ by making the loop symmetric. The results shown in Figure 3.17

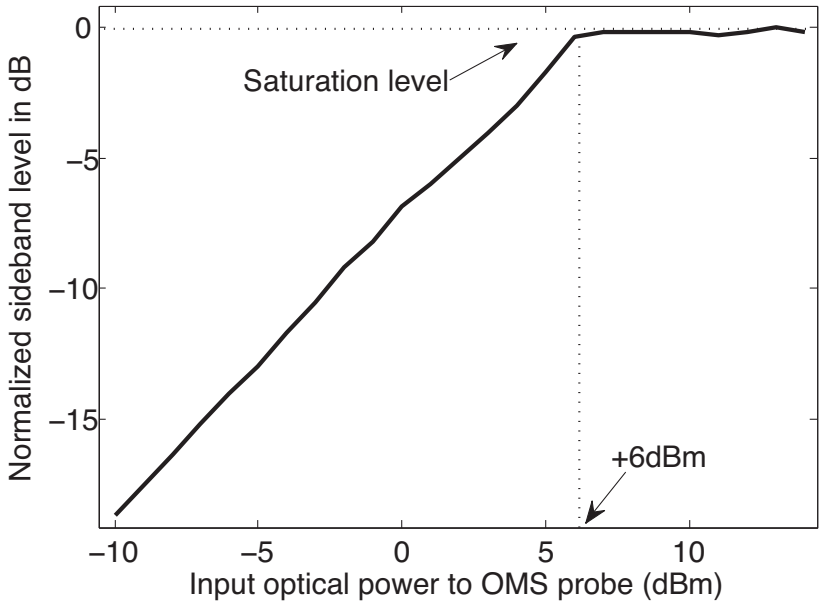

Figure 3.15 Variation of sideband power level (dB) versus input optical power (dBm) to the OMS probe.

clearly exhibit the susceptibility of the loop MST probe to picking up both fields, except where the length of the probe is $\sim 0.17\lambda$ where almost not magnetic field is picked up. The results also reveal that by choosing a value for the length of the probe less than about 0.1λ may guarantee acceptable performance from a small-loop as a magnetic MST probe.

It can be concluded that a small-loop MST probe is strongly susceptible to measuring both magnetic and electric fields simultaneously, which is not desirable. Thus, it is not recommended to use a small-loop in building an MST probe. Moreover, we need two photodiodes and two fibers in construction of a small-loop MST probe, which may not be cost-effective

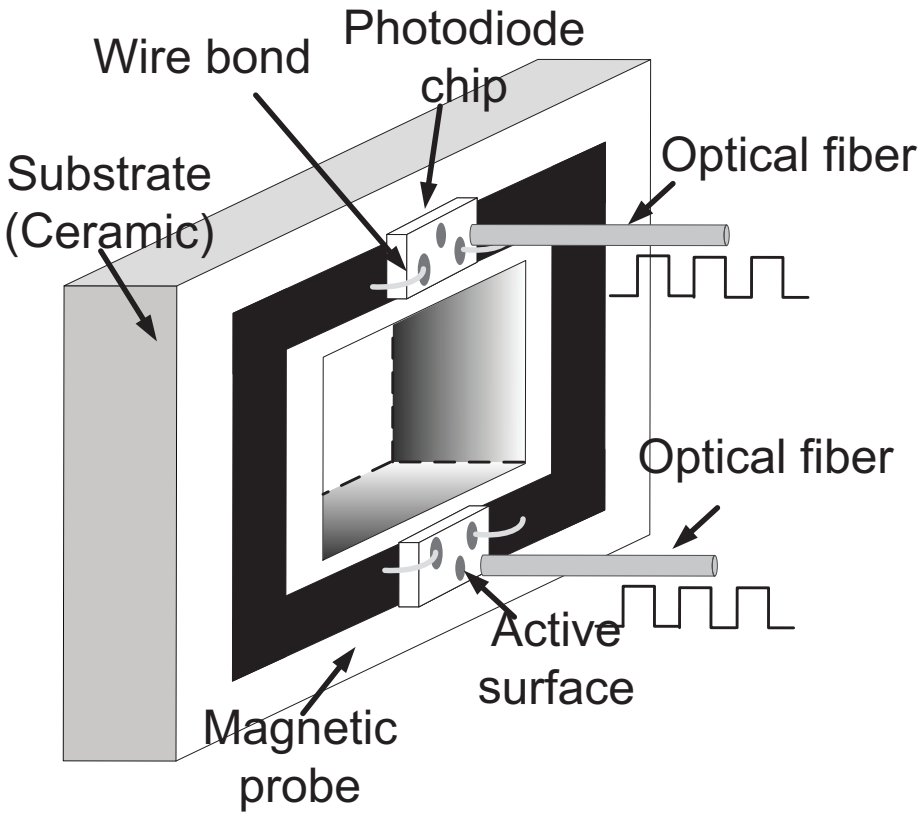

Figure 3.16 Schematic of a symmetric MST loop probe.

3.5 Omni directional and cross-polarization characterization

3.5.1 Omni directional

Simulation

A desirable feature for a near-field probe is to be able to measure a field component, in this case the component of the E-field parallel to the dipole, independently from the direction of arrival of the incoming wave(s). For a thin-wire dipole, rotational symmetry of the response about the dipole axis is expected. However, the presence of a substrate, the flat strip geometry of the dipole and the presence of the dielectric support structure break the symmetry. A detailed model of the probe including these elements was simulated with Ansoft-HFSS® as shown in Figure 3.18. In these

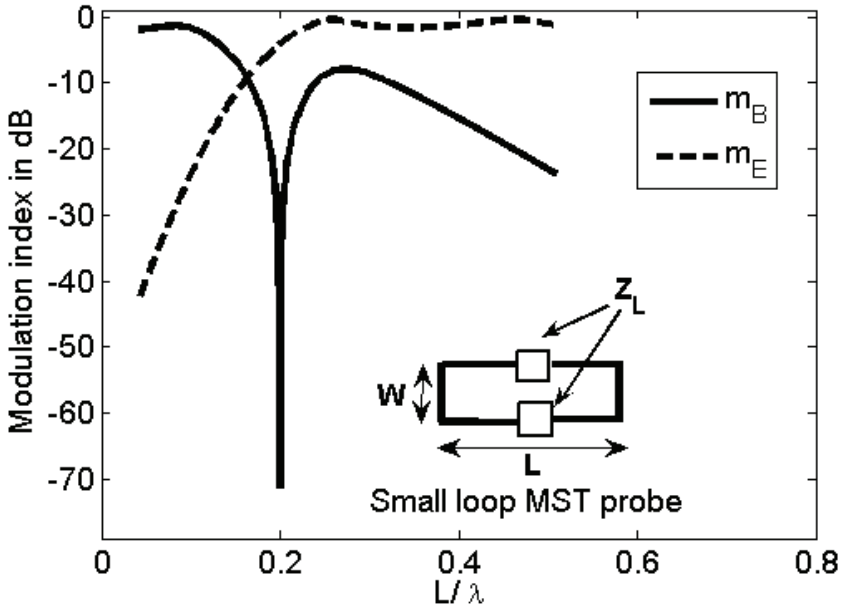

Figure 3.17 The estimation of the magnetic and electric fields' modulation depth by a loop MST probe.

simulations, the probe is on the z-axis and centered at the origin. A near-field plot of E_z and E_ϕ on a 36 mm circle and in plane $z = 0$ are shown in Figure 3.19. The probe operates as a transmit antenna but the response in the receive mode are the same due to reciprocity. The results show a fluctuation of less than 0.45 dB of the desired E_z component, and very low level of cross-polarization.

Measurement

Rotational symmetry of the response was also studied experimentally with the setup shown in Figure 3.20. In this case, the probe operates in the receiving mode and it is located near the aperture of a horn antenna. The experiment was done by rotating the OMS probe about its axis while recording the sidebands' power levels on a spectrum analyzer.

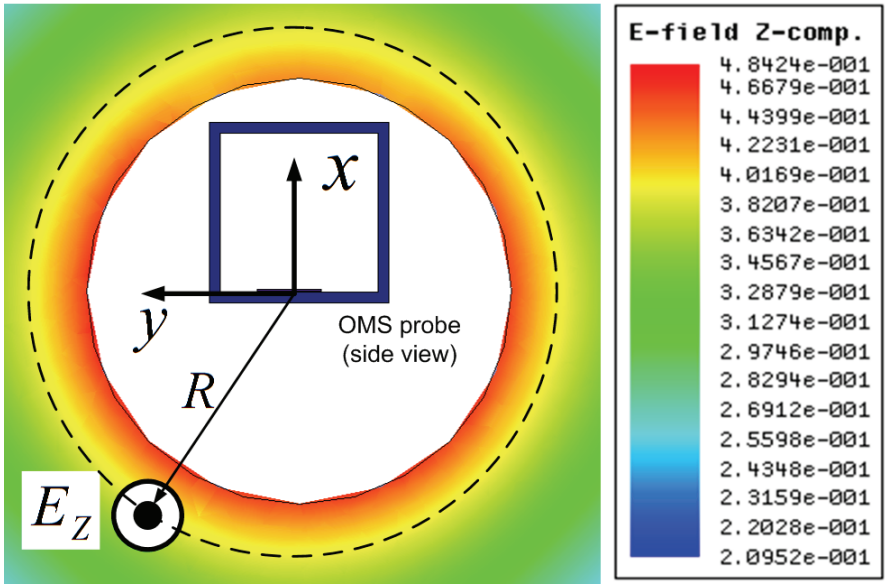

Figure 3.18 Schematic of the OMS probe when investigated for omnidirectivity charateristic.

The measured pattern at distance of 12.2 cm (one free-space wavelength) shown in Figure 3.21 exhibits a fluctuation of about 0.6 dB. The figure also shows simulation results obtained with HFSS. In this case, the magnitude of the difference between the horn's S_{11} parameter, in absence and presence of the rotated probe, is plotted. The experimental and simulated curves were normalized to make the comparison easier. In the simulation results, the effect of the dielectric substrate and support structure is barely perceptible. On the contrary, the experimental curve does not exhibit such a good rotational symmetry, as a difference of 0.6 dB can be observed between the maximum and minimum values. It is believed that this fluctuation might be due to mutual interactions between the probe rotation fixture and the horn antenna, that were not taken into account in the simulations.

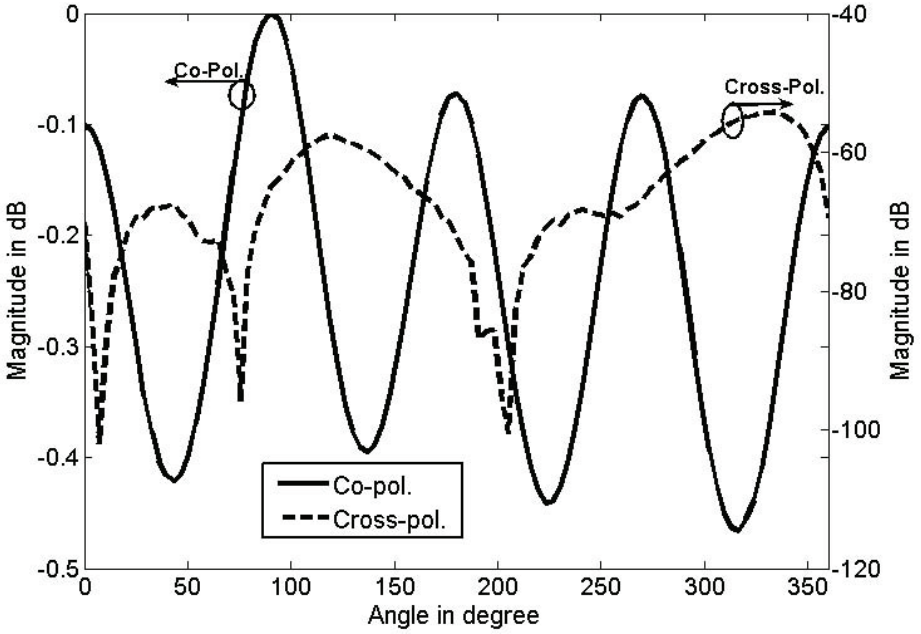

Figure 3.19 Co- (E_z) (solid line) and Cross-polarization (E_ϕ) (dashed line) radiation of the OMS probe in the H-plane at a distance of 36 mm from the probe axis, as predicted by HFSS (the data is normalized with respect to the maximum value of E_z).

3.5.2 Cross polarization

The cross-polarization rejection ratio of the probe was studied theoretically and experimentally.

Simulation

As can be seen in Figure 3.22, E_ϕ is considered the cross-polarization of the OMS probe. Using the simulation data obtained for E_x and E_y in Section 3.5.1, the cross-polarization of the OMS probe was calculated using Equation 3.10.

$$E_\phi = -E_x \sin(\phi) + E_y \cos(\phi) \tag{3.10}$$

HFSS simulations predicts a cross-polarization rejection of more than 55 dB (E_ϕ) for the OMS probe.

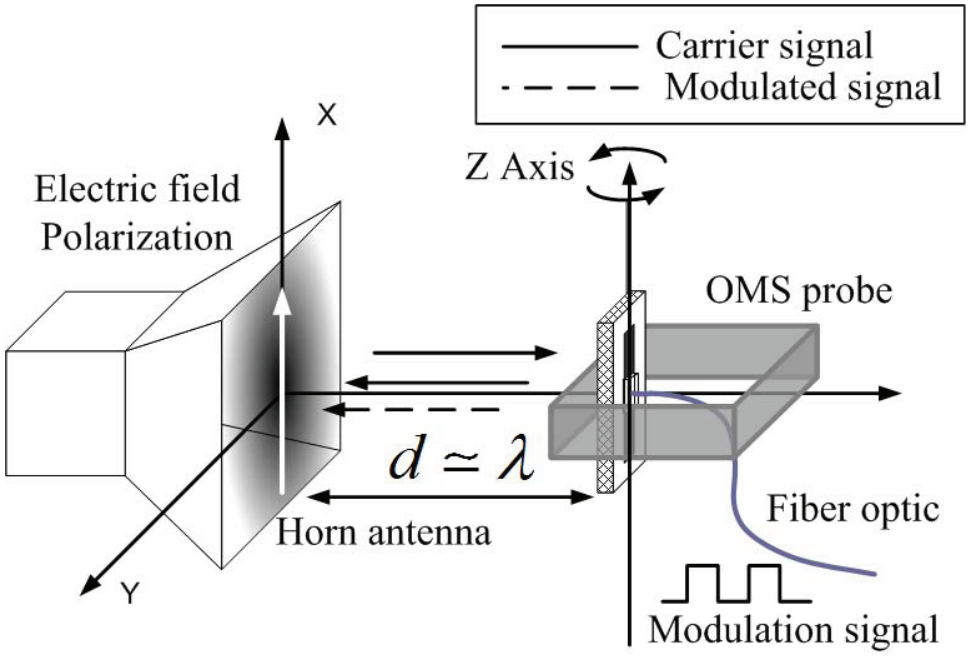

Figure 3.20 The setup for checking the omnidirectivity performance of an OMS probe.

Measurement

To verify this result experimentally, the coupling between two identical open-ended WR-284 rectangular waveguides that face each other (Figure 3.23) was measured. Although rectangular waveguides already have very good on-axis cross-polarization rejection, it was further improved by inserting a grid of parallel metal-strips (3 strips per cm) printed on a thin polyimide substrate (thickness of 5 mil and a relative permittivity of 3.2). These polarizers were mounted on the apertures of the transmit and receive waveguides. The strips, illustrated on the Tx antenna in Figure 3.23, are oriented perpendicular to the radiated field. The Tx waveguide did not show significant change of the return-loss after adding the sheets. In the experiment, the apertures were aligned and set one wavelength apart from each other. Then, the OMS probe was mounted on a fixture made of foam transparent to microwaves ($\epsilon_r \approx 1$) and was inserted between the waveguides' aperture as illustrated in Figure 3.23. The setup operated in a bistatic mode, i.e. the sidebands generated by the OMS probe were measured at the output port of the receive waveguide. Measurements were made with the receive waveguide rotated about its axis by 0 and 90 degrees; the level of the

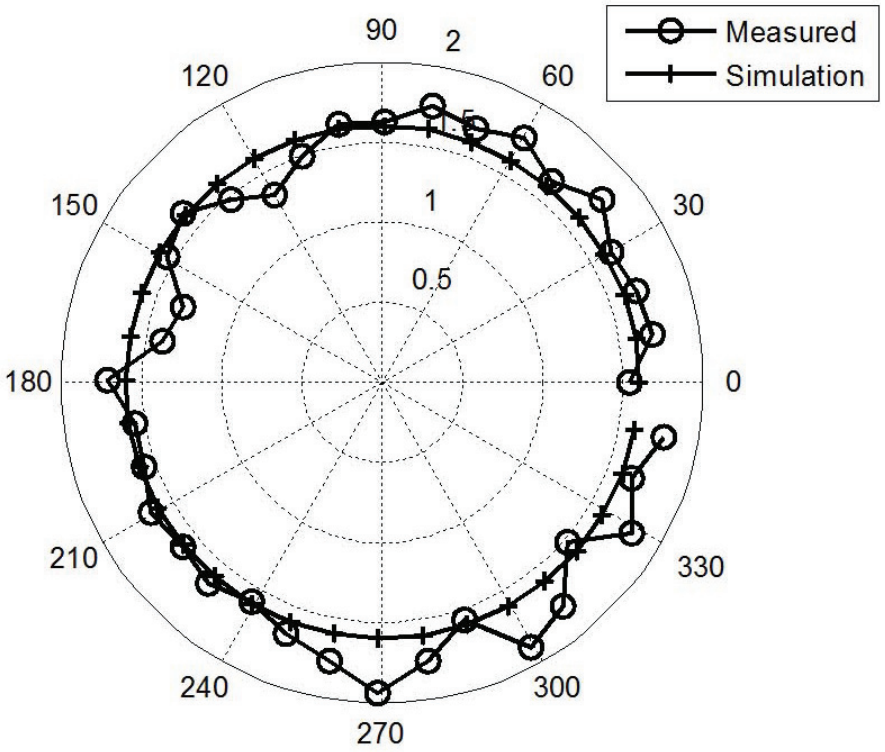

Figure 3.21 Measured radiation pattern in the probe H-plane at a distance of one wavelength from the illuminating waveguide (magnitude in dB).

sidebands introduced by the probe changed by 60.55 dB. This should be considered as a lower bound on the probe-induced cross-polarization, as the rejection of the polarizers is not infinite in practice.

3.6 OMS probe frequency response

The frequency response of the probe was investigated experimentally and compared with simulation results obtained in Section 3.2.4.

In these tests, a monostatic scheme is used with the probe inserted in a rectangular WR-284 rectangular waveguide and aligned with the main component of the E-field. With the probe in the OFF state, the waveguide was connected to a calibrated vector

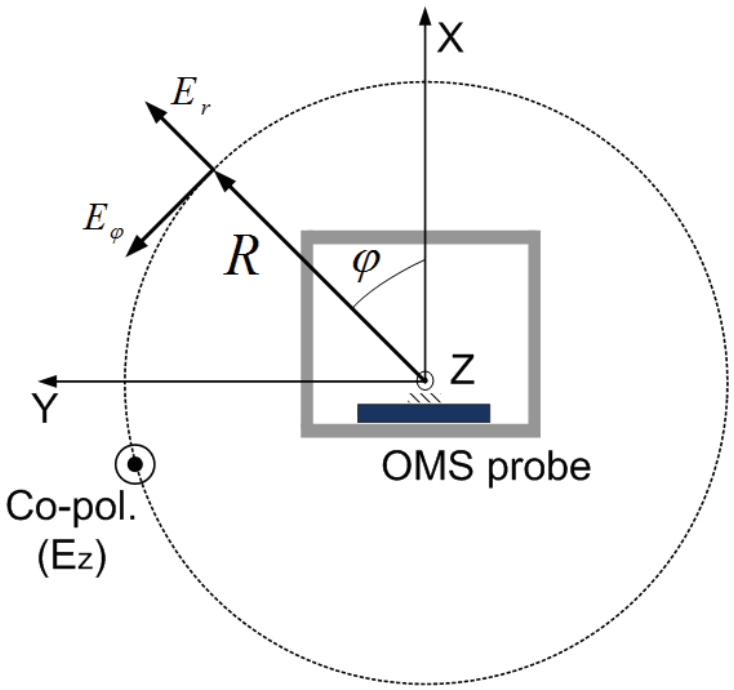

Figure 3.22 Schematic for calculating cross-pol. radiation of the OMS probe.

network analyzer through a 3-stub tuner that was adjusted to give the minimum possible reflection coefficient (less than -65 dB) over the tested frequency band. Then, an optical power level of +6 dBm was applied to put the probe in the ON state. The difference between the complex reflection coefficient in both states was then normalized to have the maximum at 0 dB. The results displayed in Figure 3.24 show to peaks. It is believed that they are due to the different resonance frequencies of $Z_p + Z_{ON}$ and $Z_p + Z_{OFF}$. In fact, if a simple capacitor model is assumed for the short dipole in free-space, resonance frequencies of 2.53 GHz and 3.09 GHz can be calculated for the ON and OFF states respectively. Results from a simulation done with the thin-wire method of moment are also shown in the figure. In the simulation, the probe is illuminated with a uniform plane wave in free space. This shows the normalized difference between the squared scattered field taken 1 cm away form the dipole in the two states. The results also exhibit a double peak response. In the measurement, the resonance observed in the waveguide are shifted to lower frequencies. This shift is thought to be due to imperfections in the construction and uncertainty in the

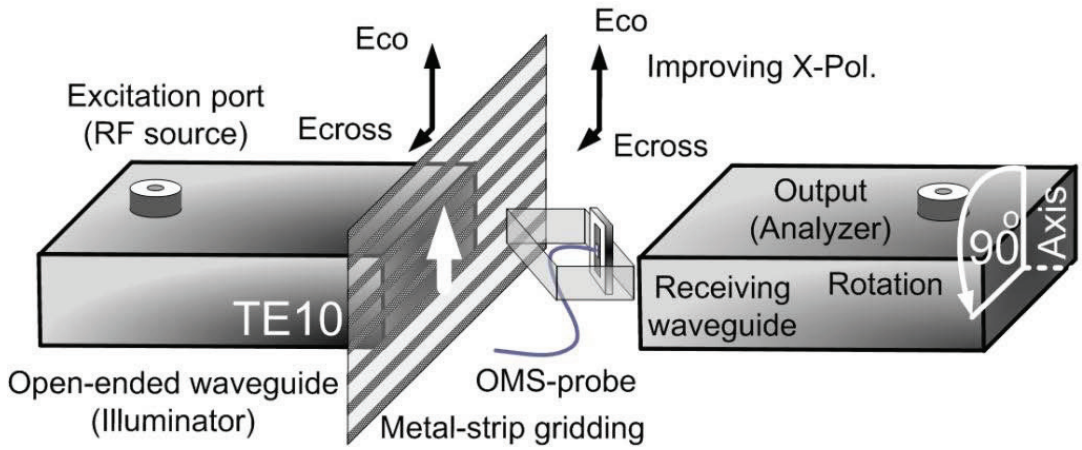

Figure 3.23 Setup to measure co-to-cross polarization rejection of the OMS probe (only one of the polarizer sheets is shown for clarity).

substrate's constitutive material parameters. Furthermore, the value of Z_p in free-space is not the same as in the waveguide where the dipole is interacting with the metallic walls. Finally, as these reflection differences are obtained by subtracting very similar measured values, the results are susceptible to measurement and simulation inaccuracies. Both curves exhibits a maximum sensitivity near the design frequency of 2.45 GHz. Finally, the waveguide measurement process described above was simulated in HFSS. The reflection coefficient difference shown in Figure 3.24 exhibits peaks near 2.7 GHz and 3 GHz. It should be noted that this curve is derived from differences between S_{11} values with a variation smaller than 5×10^{-5} in magnitude. Therefore, the frequency shift compared to the other two curves may be partly due to simulation inaccuracies.

3.7 The NF imager microwave and optical circuitries

This section describes the implementation of the microwave electronic, and optical circuitries necessary to transmit/receive and process the scattered fields by an OMS probe in the NF imager. The schematic depicted in Figure 3.25 demonstrates the imager circuitries, including the other existing parts in the imager that will not be

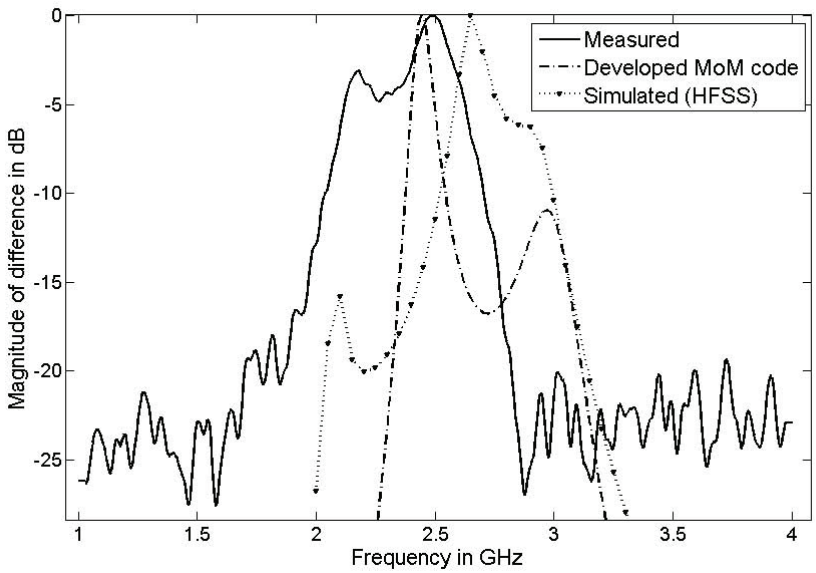

Figure 3.24 Difference of frequency response for the OMS probe in ON and OFF states: solid line is the measured reflection coefficient; dashed line is the simulated scattered field; dotted line is simulated reflection coefficient.

discussed in detail. The microwave part consists of an RF source, an active circuit equivalent to a conventional I-Q demodulator and a carrier canceller circuit. Baseband analog and digital parts include a lock-in amplifier (LIA), SR830, manufactured by Stanford Research Systems, which provides signal vector measurement (magnitude and phase), a current driver exciting and controlling a laser diode, and a digital controller that generates the lock-in signal required by an LIA and also that addresses the RF SPDT switch. This controller also sends commands to a laser diode illuminating the OMS probe and modulating it. The whole setup is controlled by a computer software developed using LabView.

3.7.1 NF imager microwave circuitry

Proposed I-Q demodulator

In homodyne detector, the received (i.e., modulated) signals generated by the OMS probe, are down-converted to IF signals (i.e., $f_{IF} = \omega_{IF}/2\pi$) using an I-Q demodulator, demonstrated in Figure 2.7. The I-Q demodulator applies two in-phase and

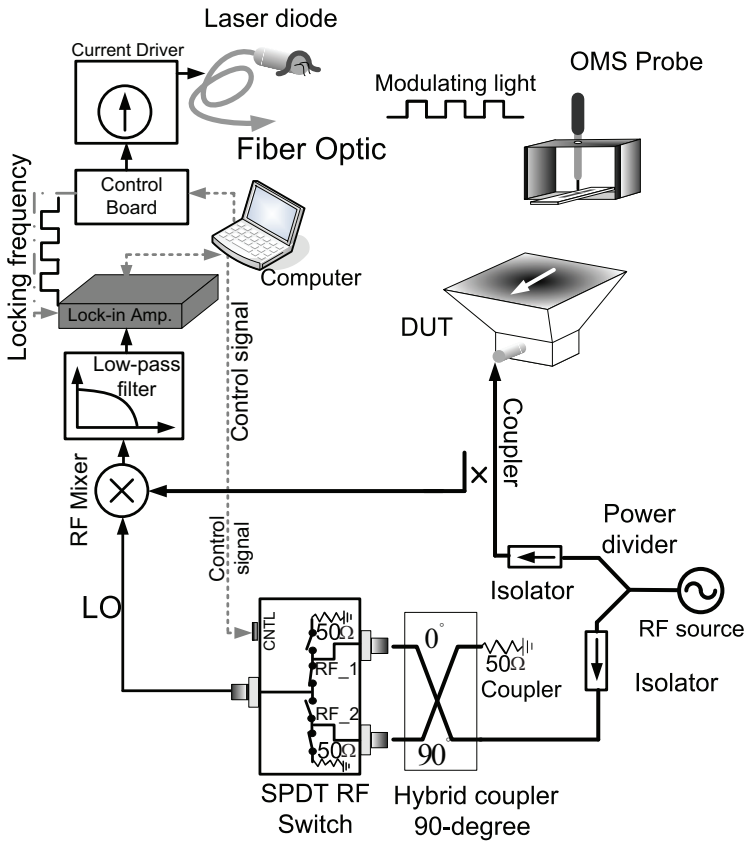

Figure 3.25 Schematic of the developed microwave circuitry.

quadrature (i.e., $\pi/2$ out-phase) reference signals to the mixers at carrier frequency (i.e., $f = \omega/2\pi$) for generating I and Q signals. These signals are then used by lock-in amplifier (LIA) to make magnitude and phase measurement of the modulated signals. In the following, we develop a set of formulas to show how I and Q signals are related to magnitude and phase of the received signal and consequently, that of the scattered fields. For a generalized equations to obtain I an Q signals in homodyne detectors, one can see Annex B [24].

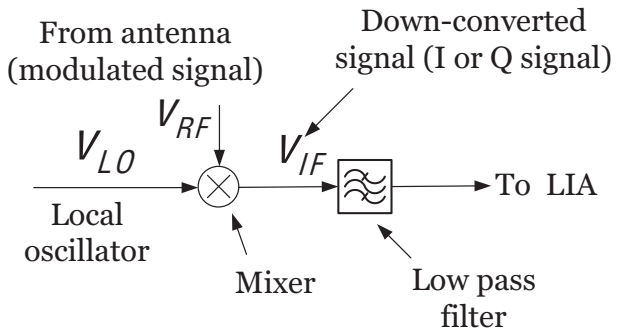

Figure 3.26 Schematic of the circuit used for down-converting the scattered signal.

In-phase down-converting

Let us assume that $v_{LO} = C\cos(\omega t)$ and that the signals to be measured are given by Equation 3.11.

$$v_{RF} = A\cos(\omega t + \phi_0) + B\cos(\omega_1 t + \phi_0) + B\cos(\omega_2 t + \phi_0) \tag{3.11}$$

where, $\omega_1 = \omega + \omega_{IF}$, $\omega_2 = \omega - \omega_{IF}$ and a fixed position in space is assumed for the probe. Also, ϕ_0 is an arbitrary phase offset in Equation 3.11. As the first step to obtain magnitude and phase of the RF signal, it is required to perform a down-convertion of the received signal by multiplying it with v_{LO} in a mixer (see Figure 3.26, which yields v_{IF}),

$$\begin{aligned} v_{LO} \times v_{RF} &= AC\cos(\omega t)\cos(\omega t + \phi_0) \\ &+ BC\cos(\omega t)\cos(\omega_1 t + \phi_0) \\ &+ BC\cos(\omega t)\cos(\omega_2 t + \phi_0) \end{aligned} \tag{3.12}$$

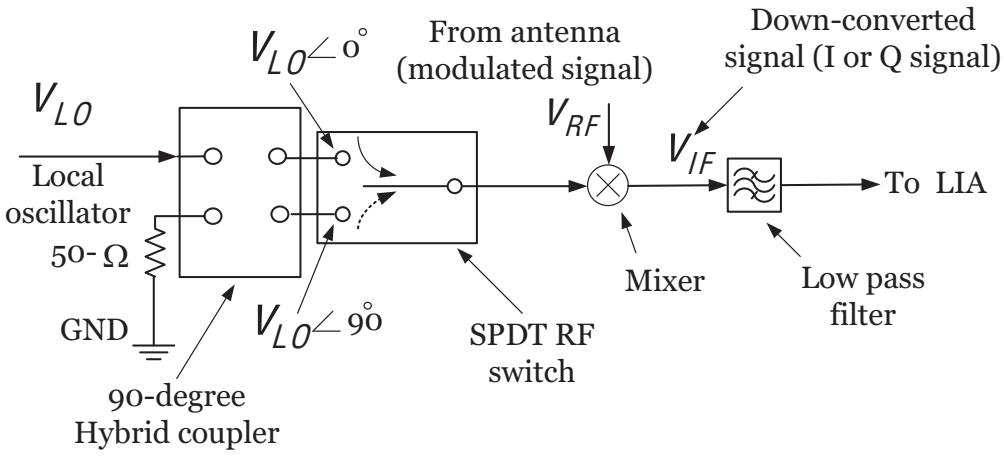

Figure 3.27 Schematic of the proposed circuit for I-Q demodulator using a mixer.

using $cos(x).cos(y) = \frac{1}{2}[\cos(x+y)+\cos(x-y)]$, v_{IF} can be simplified to Equation 3.13.

$$\begin{aligned} v_{IF} &= \frac{AC}{2}[\cos(2\omega t + \phi_0) + \cos(\phi_0)] \\ &+ \frac{BC}{2}[\cos((\omega + \omega_1)t + \phi_0) + \cos((\omega - \omega_1)t - \phi_0)] \\ &+ \frac{BC}{2}[\cos((\omega + \omega_2)t + \phi_0) + \cos((\omega - \omega_2)t - \phi_0)] \end{aligned} \tag{3.13}$$

In Equation 3.13, $\omega + \omega_1 = 2\omega + \omega_{IF}$, $\omega + \omega_1 = 2\omega + \omega_{IF}$, $\omega - \omega_1 = \omega_{IF}$ and $\omega - \omega_2 = +\omega_{IF}$. As can be seen, Equation 3.13 shows that v_{IF} not only has low-frequency components (IF signals) but also DC and higher harmonics of the carrier signal. Finally, v_{IF} can be rewritten in terms of ω_{IF} (Equation 3.14).

$$\begin{aligned} v_{IF} &= \frac{AC}{2}[\cos(2\omega t + \phi_0) + \cos(\phi_0)] \\ &+ \frac{BC}{2}[\cos((2\omega + \omega_{IF})t + \phi_0) + \cos((\omega_{IF})t + \phi_0)] \\ &+ \frac{BC}{2}[\cos((2\omega - \omega_{IF})t + \phi_0) + \cos((\omega_{IF})t - \phi_0)] \end{aligned} \tag{3.14}$$

After filtering to keep only the IF component, v_{IF} becomes:

$$v_{IF} = \frac{BC}{2}[\cos(\omega_{IF}t + \phi_0) + \cos(\omega_{IF}t - \phi_0)] \tag{3.15}$$

After simplifying Equation 3.15, v_{IF} (i.e., $v_{IF}(I)$ or I signal) is given by Equation 3.16. This equation contains information on magnitude (i.e., B) and phase (i.e., ϕ_0) of the RF signal (i.e., sideband), however, they can not be extracted using only this equation.

$$v_{IF}(I) = BC\cos(\omega_{IF}t)\ \cos(\phi_0) \tag{3.16}$$

Quadrature down-converting

Similar to $v_{IF}(I)$, we can obtain $v_{IF}(Q)$ (or Q signal) by following the same procedure as $v_{IF}(I)$. The only difference in the calculation of $v_{IF}(Q)$ is that $v_{LO} = Ccos(\omega t - \pi/2)$ used.

$$v_{IF(Q)} = BC\cos(\omega_{IF}t)\ \sin(\phi_0) \tag{3.17}$$

Once, I (i.e, $v_{IF}(I)$) and Q (i.e, $v_{IF}(Q)$) were obtained, we can use them to calculate magnitude and phase of the received signal using Equation 3.18. For simplifying the equation, the magnitude of v_{LO} is assumed unity (i.e., $C = 1$).

$$\begin{aligned} B &= \sqrt{v_{IF}(I)^2 + v_{IF}(Q)^2} \\ \phi_0 &= tan^{-1}\frac{v_{IF}(Q)}{v_{IF}(I)} \end{aligned} \tag{3.18}$$

In practice, in order to generate I and Q signals, an active circuit equivalent to conventional I-Q demodulator with low conversion loss was proposed and implemented. This circuit consists of only a diode mixer, an RF SPDT switch and a 90-degree hybrid coupler. The switch selects between the I or Q component of the scattered field. In Figure 3.27 the microwave circuitry of the proposed I-Q demodulator is demonstrated.

Carrier Cancellation Circuit

Due to the inherent nonlinear operation of the mixer, this component is subject to saturation in case of high-level signals, which limits the dynamic range of the

proposed system. The strongest signal incident on the receiver is the carrier. This signal conveys no information on the measured E-field.

Chapter 5 will address an automated technique to suppress the carrier signal continuously at the receiver front-end while leaving the sidebands carrying the information of interest intact. Such cancellation maintains the imager in a linear operating zone, and prevents it from saturation. Keeping the carrier level lower than an allowed upper limit enables us to amplify I and Q and to avoid working close to the noise floor of the LIA. Consequently, the imager can achieve a larger dynamic range.

3.7.2 Modulated laser diode

In practice, in order to send a modulation signal to the OMS probe it is necessary to use a controlled laser diode. We designed a digital controller to provide proper signalling to the probe. The controller also produces a reference signal used by the LIA. The stability of this reference signal was assured by using an 8 MHz crystal that prevented phase jitter in the measured data. This controller is driven by a software developed in LabView.

Laser diode driver- current controller

The optical output of the laser diode is directly set by the current flowing through its junction. Having a constant optical output necessitates enforcing a constant current to compensate for room temperature, voltage instability, laser diode self-warm up and other factors. In order to mitigate these factors, a current driver was designed and implemented, by using a chip (i.e., IC-WJZ) manufactured by iC-Haus®. It uses the feedback current from the built-in monitoring diode in the laser to adjust input current. The current driver, which is actually a closed loop controller, maintains the input current of the laser diode at a set point, resulting in constant optical output. Figure 3.28 shows the schematic of a current driver used for driving the laser diode. The laser diode is set to generate +6 dBm of optical power, illuminating the OMS probe [72]. To do this, the value of the feedback resistor R_f is set to approximately 12 Ω.

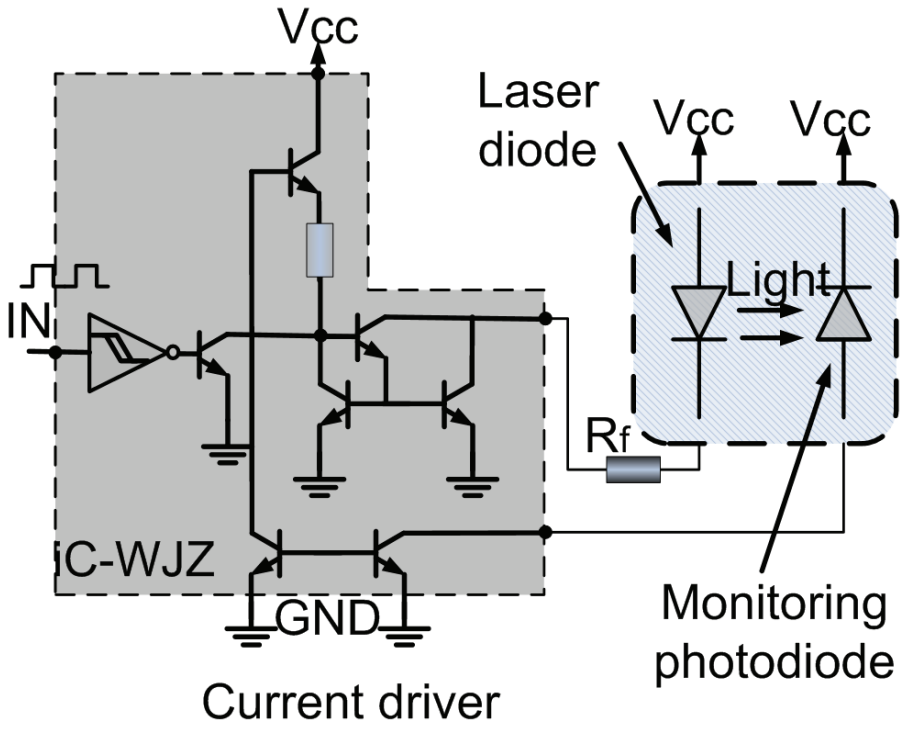

Figure 3.28 Schematic showing a laser diode and its driver.

3.8 Linearity and dynamic range tests

Before validating the accuracy of the measurements, the linearity of the receiver system consisting of the demodulator and the LIA must be ensured. Dynamic range and maximum sensitivity are other important aspects to be investigated when qualifying the developed NF setup.

To test the linearity of the system, measurements were taken at different power levels. To simulate practical power conditions, a controlled attenuator (11-bit) with an attenuation range of ∼80 dB and an accuracy of 0.04 dB was used. First, the attenuator was characterized using a well-calibrated vector network analyzer (VNA). The attenuator was then inserted in the measurement system, before the receiver, and a swept-attenuation measurement was taken by applying the same attenuation

sequence.

The measured attenuation, shown in Figure 3.29, is almost linear over a range of 60 dB. The LIA measurement shows a noise-interference floor at -60dB. This is attributed to cross-talk within the measurement chain due to the finite *RF-LO* isolation. For a given test configuration, this parasitic coupling has a fixed magnitude and phase and thus it can be compensated through proper calibration.

The complex interfering signal is simply obtained by measuring with the maximum attenuation and then averaging the I and Q signals over a long period. These average values are then subtracted from the measurements. The result is illustrated in Figure 3.29 where a gain of about 10 dB in the linearity range can be seen in the compensated case. However, measurements are still affected by noise at very low power, which limits the dynamic range of the system to about 70 dB. Figure 3.29 does not exhibit nonlinear saturation effects for high power levels; it is simply due to power limitations of the generator. It can thus be expected that the actual dynamic range of the system exceeds 70 dB.

3.9 OMS probe results validation

3.9.1 Monostatic configuration

In order to verify the performance of the developed OMS- probe, it was set to measure the electric field distribution of a 50 Ω microstrip transmission line in monostatic mode, where the measured signal is proportional to square of electric field ($v \propto E^2$). The transmission line was fabricated on a Rogers® substrate (RO3035) with a relative permittivity of 3.8 and a thickness of 60 mil (Figure 3.30). The rapidly varying fields near the line are highly suitable to assess the resolution and the dynamic range. In this measurement, the probe is scanned across the microstrip line at a height of 3 mm above it, and measures the transverse electric field distribution along x (i.e., E_x) (Figure 3.30). The transmission line was terminated with a matched load.

To validate the measurement results, we also included the field distribution of the transmission line predicted by HFSS® (Figure 3.31).The results obtained from simulation needs to be post-processed to take into account the effect the finite length of the measuring probe (see Figure 3.32). This topic will be discussed later in Section 3.9.1.

Taking the square root: sign ambiguity removal

When the NF imager operates in monostatic mode, the measured signals are subject to taking the square root to obtain the electric field ($E \propto \sqrt{v}$). As discussed in Section 2.4.1, the square root of a complex signal $v = X_I + jX_Q$ has two answers and it is necessary to pick the proper one. The procedure might be straightforward when the electric fields take nonzero values. So, one needs to ensure continuity of the phase distribution in the whole data. In contrast, sign retrieval will not be an easy task if at some locations nulls occur (i.e., $E = 0$). In these cases, no clear method has been addressed to choose the sign of the points correctly. However, a technique in [44] was reported for some particular cases.

For example, in the case of a microstrip line when the transverse electric fields are measured (E_x in Figure 3.30), there is a null on the top of the strip. Thus, choosing the sign of the electric field on the other side is impossible without *a prior* knowledge. Here, it is assumed that when a contour with zero E field is crossed, the phase changes by π.

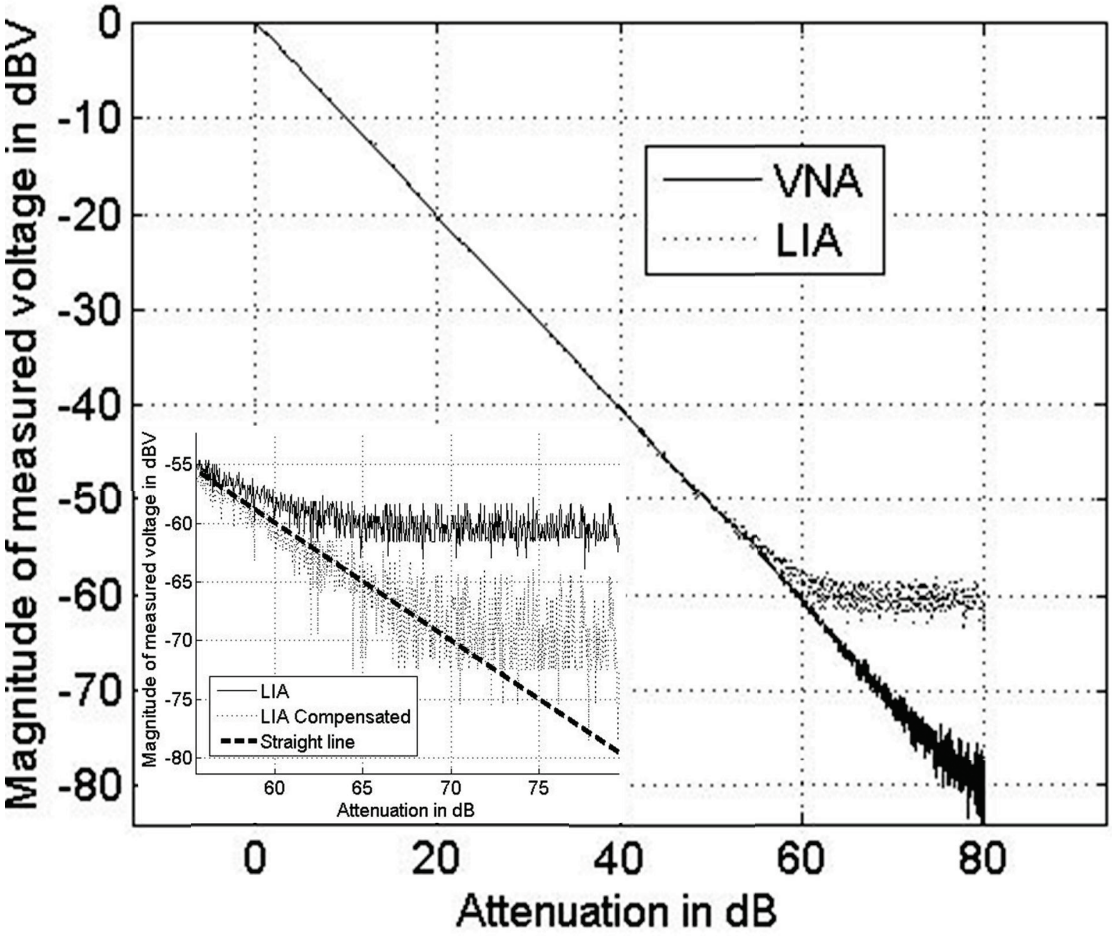

Figure 3.29 Linearity of the developed NF imager

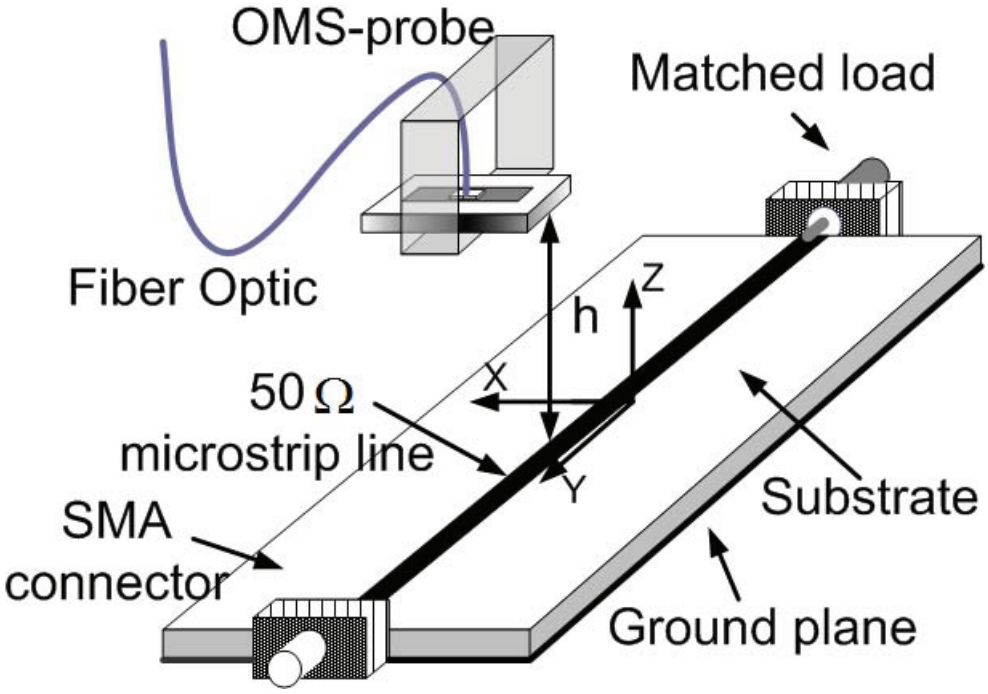

Figure 3.30 Schematic of the probe and microstrip transmission line under test.

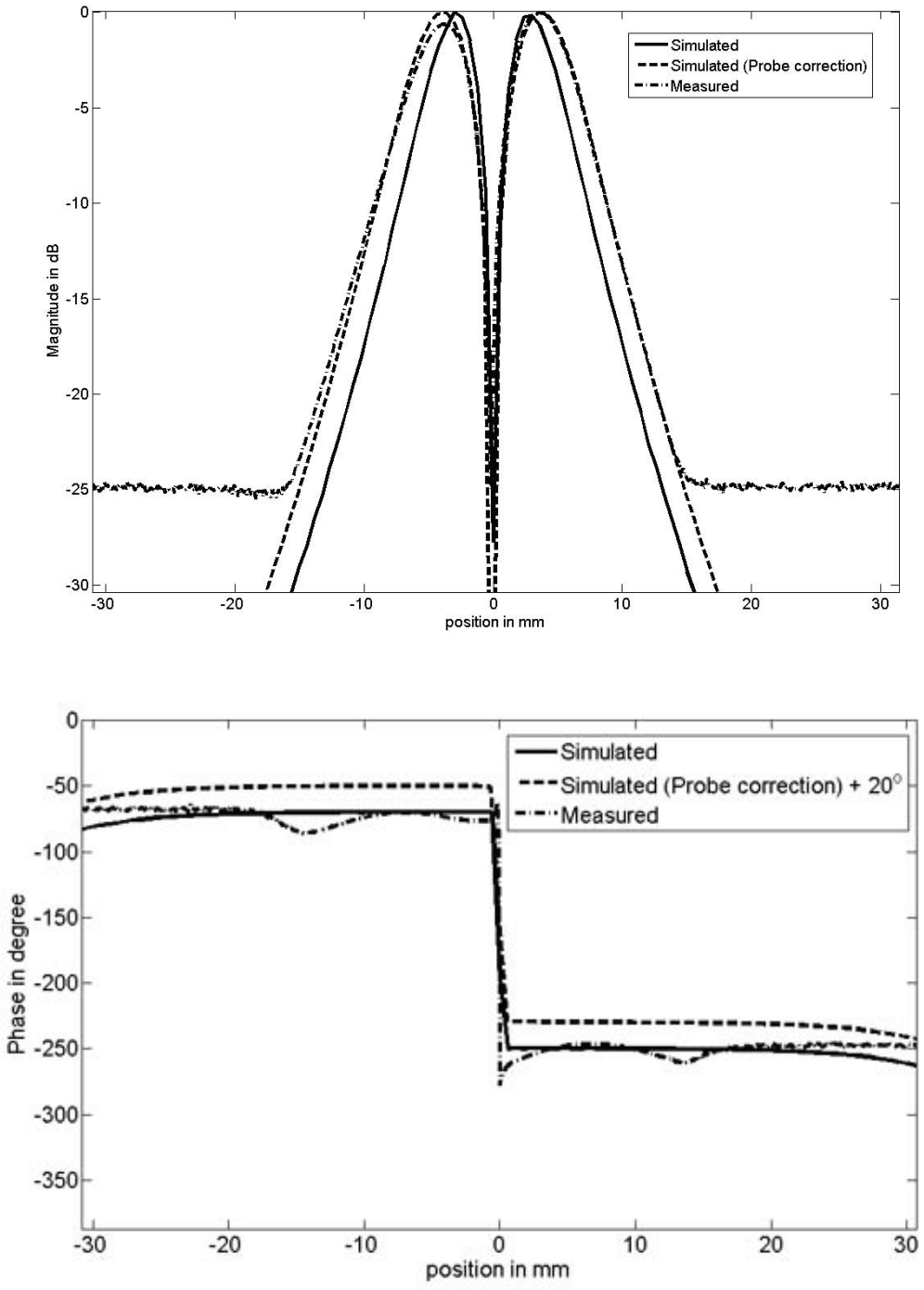

Figure 3.31 Measurement result (magnitude and phase) of electric field (E_x) at h =3mm.

Probe correction

To take into account the effect of the length of the OMS probe, we used the induced *e.m.f* method for calculating the induced voltage across the probe's terminal generated by an incident E-field (see Figure 3.33). In this method, we need to show the current distribution (J) on the probe when it is radiating, i.e., acting as a transmitting antenna. Since the length of the probe is shorter than 0.1λ, one can approximately assume that J has triangular current distribution (see $I_2(z)$ in Equation 3.19), as shown in Figure 3.33 by the dashed line.

$$J_{probe} = J_{probe}(0)\left[1 - \frac{2|z|}{L}\right]u_z \tag{3.19}$$

Then the field-current convolution was calculated for every point using Equation 3.20 (see Figure 3.34) based on the E field obtained with the HFSS simulation (the Ez component is shown in Figure 3.31).

$$V_{probe} = -\frac{1}{J_{probe}(0)}\int_L \bar{E}_i.u_z J(z)dl \tag{3.20}$$

The simulations, after applying convolution, probe correction, and measurements are in very good agreement with each other in magnitude and in phase plots, which proves the excellent performance of the probe. Within the ± 15 mm interval, the average difference between the simulated (with probe correction) and measured fields was 6.4% in magnitude and 3.2 degrees in phase. It is noteworthy to mention that the probe correction does not alter phase information and in order to distinguish simulated curves, we plotted one of them with a 20-degree offset.

When a matched load is used to terminate the microstrip line, the reflection of the carrier signal at the end of the line is minimized, which leads to a reduced carrier-to-sideband ratio in the receiver. In our measurements, when the probe was on one of the peaks visible in Figure 3.31, this ratio was 46 dB. We repeated this test with a short circuit termination. The x coordinate of the the probe stayed the same and then the probe was moved in the z direction to find the minimums and maximums of the standing wave pattern. The carrier-to-sideband ratio increased to 60 dB on a maximum and to 93 dB on a minimum. This made it clear that without modulation, characterization of the transmission line fields with a monostatic setup would be highly susceptible to isolation problems.

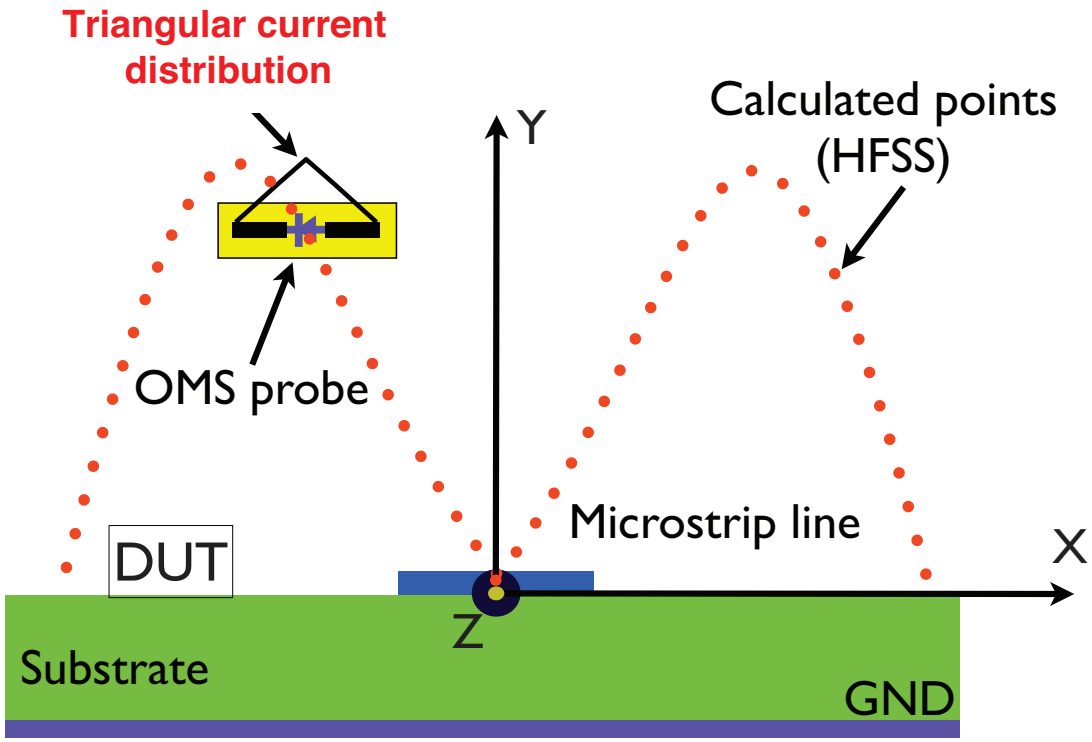

Figure 3.32 Schematic showing the effect of a probe lenght on the field to be measured.

3.9.2 Bistatic configuration

The electric field distribution of the same microstrip transmission line used in Section 3.9.1 was also measured when the NF imager operated in bistatic mode. In this mode, the imager requires an auxiliary antenna to receive the scattered fields and transfer voltages to the measuring instruments (Figure 3.35), while, there is no need for any couplers or circulators in the imager.

It is demonstrated in Figure 3.35 that S_{21}, coupling between the DUT and measuring probe, measurement will be the field distribution of the transmission line under test. However, the measuring probe scatters the fields toward the collecting antenna, that coupling between them is shown by S_{32}. Therefore, the measurement results will include not only the field distribution of the transmission line but also the coupling between the measuring probe and the receiving antenna ($v \propto S_{21}.S_{32}$). By com-

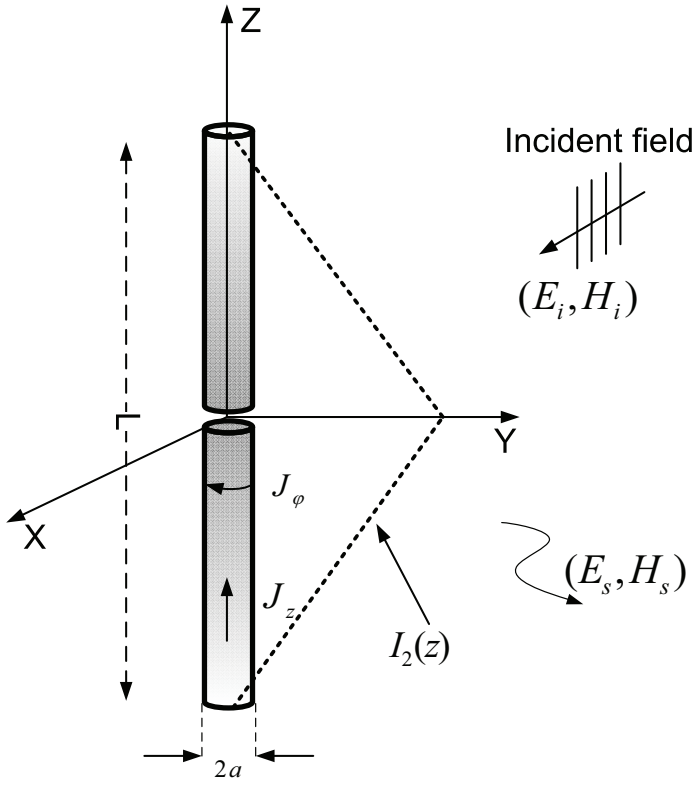

Figure 3.33 Geometry for calculating the induced current on the OMS probe.

pensating the outcome results for the radiation pattern of the receiving antenna i.e., accounting for the change of S_{32} due to the displacement of the probe, the electric field distribution of the transmission line will be obtained.

To overcome the issue mentioned above, the OMS probe and the receiver-antenna, demonstrated in Figure 3.35, were moved to together. By doing this, S_{32} which is the coupling between the probe and antenna, should be independent of the probe position and there is no need to compensate the measured field for radiation pattern of the receiving antenna. Such assumption (i.e., unchanged S_{32}) is only true if the presence of the DUT has a negligible effect on the coupling between the probe and receiving antenna.

In order to investigate the accuracy of the bistatic setup, it was set to measure the field distribution of a DUT (i.e., 50-Ω microstrip line) and the results were compared

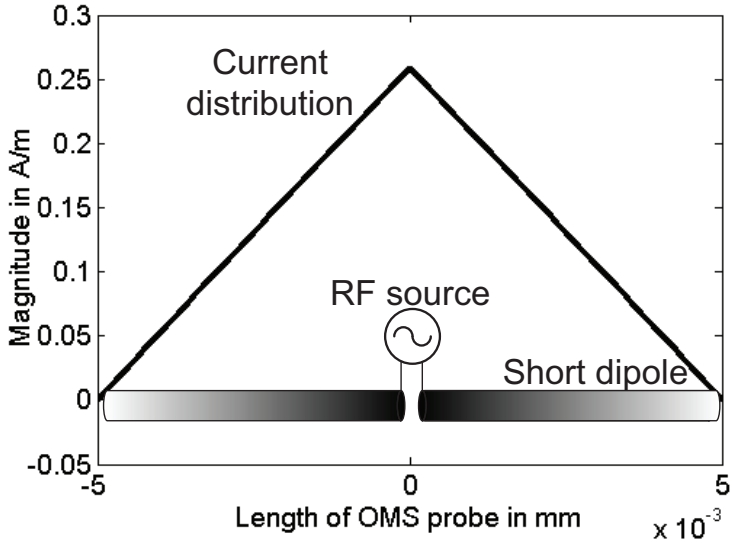

Figure 3.34 The calculated current distribution on the OMS probe's dipole antenna.

with that of the monostatic setup. Figure 3.36 shows the magnitude and phase of the transmission line measured in bistatic mode. The fields have a better dynamic range than its monostatic counterpart by about >20 dB. Phase measurement in the bistatic mode shows a deviation from the monostatic ones, that may be due to interaction between the receiving antenna and the DUT. The compensation for these interactions will be discussed in Chapter 4. By increasing the coupling between the probe and auxiliary antenna by locating it closer, the dynamic range can be improved at the expense of multiple reflections between the DUT and antenna. Thus, a trade-off between the dynamic range and accuracy of the results has to be made.

3.10 Sensitivity

The sensitivity of the measurement system is dependent on the modulation index of the loaded probe, but also on the sensitivity and noise floor of the receiving equipment measuring the sideband signal. The magnitude of this signal is proportional to $\Delta\rho$ the difference in the AUT reflection coefficient in the ON and OFF states. It can be proved that for a monostatic test configuration this difference is proportional to S_{21}^2

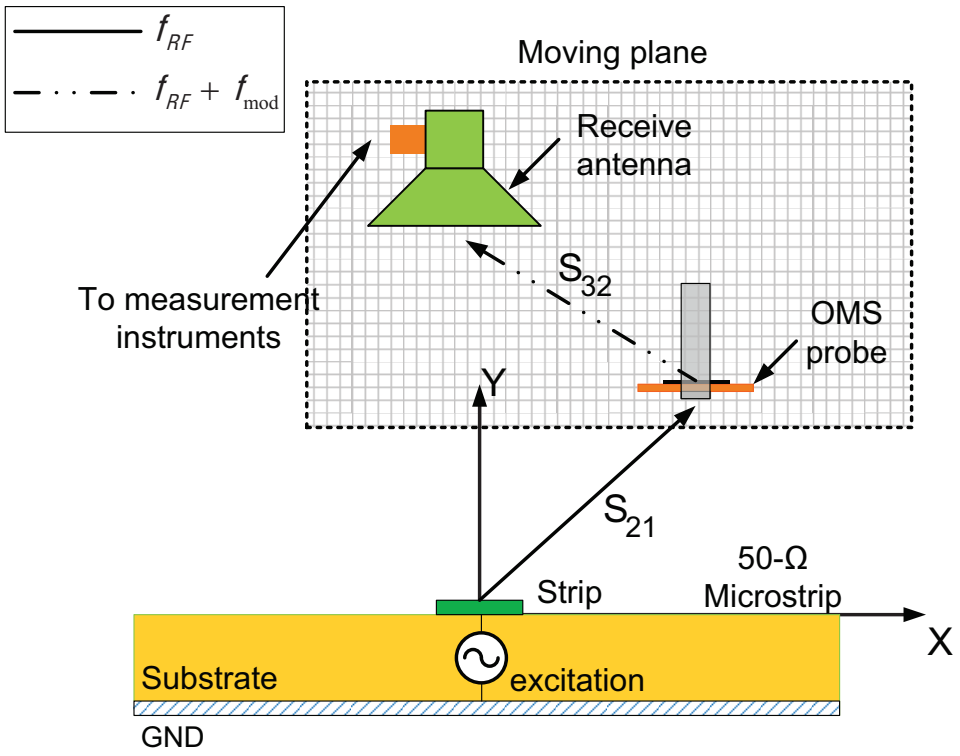

Figure 3.35 Schematic of a microstrip transmission line under test in bistatic mode.

(Equation 3.21), where S_{21} represents coupling between the DUT and probe ports (Figure 3.37).

$$\Delta_\rho \propto S_{21}^2 \rightarrow \Delta_\rho = K_1 S_{21}^2 \tag{3.21}$$

Furthermore, we also have that the field incident on the probe is proportional to S_{21} as shown by Equation 3.22.

$$E \propto S_{21} \rightarrow E = K_2 S_{21} \tag{3.22}$$

Using Equations 3.21 and 3.22, we can obtain:

$$E = K\frac{\Delta\rho}{S_{21}} \tag{3.23}$$

The sensitivity of the system can be given in terms of minimum possible reflection coefficient that can be accurately measured, namely $\Delta\rho_{min}$. Consequently, the sensi-

tivity of the system is simply given by

$$E_{min} = |K\frac{\Delta\rho_{min}}{S_{21}}| \tag{3.24}$$

where $K = K_2/K_1$ is a constant. The field sensitivity will therefore depend on the DUT. For a radiation structure, we expect a higher value of S_{21} and therefore a better sensitivity, than for a guiding structure such as a microstrip line. To illustrate this, we have estimated the sensitivity for two DUTs: the horn used in Section 3.1 and the microstrip line terminated with a matched loaded presented here. By simulation, we obtained the field incident on the probe for an incident input power of 1 watt at the DUT's input port. The same configuration was then repeated experimentally, that is to say with the probe located at the same point as in the simulations. With the probe in this fixed position to keep S_{21} constant, the incident power was reduced with an attenuator until the receiver's noise floor was reached. The field sensitivity was then obtained by scaling the E-field value obtained in simulations by the square root of the threshold power level (in watts) obtained experimentally. In the case where the probe was in the aperture of the horn (large S_{21}), the sensitivity was 0.037 V/m. When it was at a height of 3 mm above the microstrip line (small S_{21}), the sensitivity degraded to reach 54.3 V/m. This large difference illustrates a weakness of the monostatic configuration for characterizing non-radiating structures. We nevertheless used the microstrip line in our validation tests because it has steep field variations. This allows better observation of the probe's spatial resolution.

3.11 Applications of NF imager

As an example and in order to show the performance of the developed imager, the E-field distribution above a bandpass filter was scanned and presented in this section. The design and implementation of this filter were addressed in [73] for wireless applications. Figure 3.38 demonstrates the filter under test, which is passband at 2.45 GHz. The field distribution of the filter was measured and both the magnitude and phase of E-fields are presented in Figure 3.39. A dynamic range of ∼70 dB can be obtained for the NF imager operating in bistatic mode. The phase information shown in Figure 3.39, illustrates a 180-degree phase change of the electric field on both sides of the slots. It also shows a zero-crossing line of the CPW line, which is a

little inclined due to misalignment of the positioning system and the filter under test.

3.12 Conclusions

An accurate, high-sensitivity, frequency selective near-field probe using a modulated scatterer technique has been designed and practically realized. The use of an optical modulation guarantees almost perturbation-free measurement due to the invisibility of the optical fiber to the radio frequency electromagnetic radiation. The omnidirectivity and cross-polarization rejection performances of the OMS probe were studied as well. In the omnidirectivity test, the probe showed an absolute deviation of about ± 0.3 dB with respect to an unidirectional response. The co-to-cross polarization ratio was measured and found to be better than 60 dB. The frequency response of the probe was studied theoretically and experimentally in order to qualify the performance of the matching network and to assess its impact on the frequency response of the OMS probe. The performance of the probe was validated by measuring the near field distribution of a 50-Ω microstrip transmission line. The measurements were compared with results of simulations using HFSS®. Measurement and simulation results are in very good agreement over a 26 dB and 40dB for monostatic and bistatic modes.

The probe presented in this chapter was originally designed for use in a breast tumour imaging system. This is why it was optimized for operation in an ISM band (i.e., at 2.45 GHz). This is also a frequency at which there is a high contrast between healthy and malignant breast tissue. However, the proposed design is not limited to this frequency. Other measurements (not shown here) have shown that the ratio $\frac{Z_{ON}}{Z_{OFF}}$ of the unbiased photodiode is high, over 1-4 GHz frequency band, which indicates that the frequency bandwidth of the probe would be determined by the capacity to achieve broadband impedance tuning over this band.

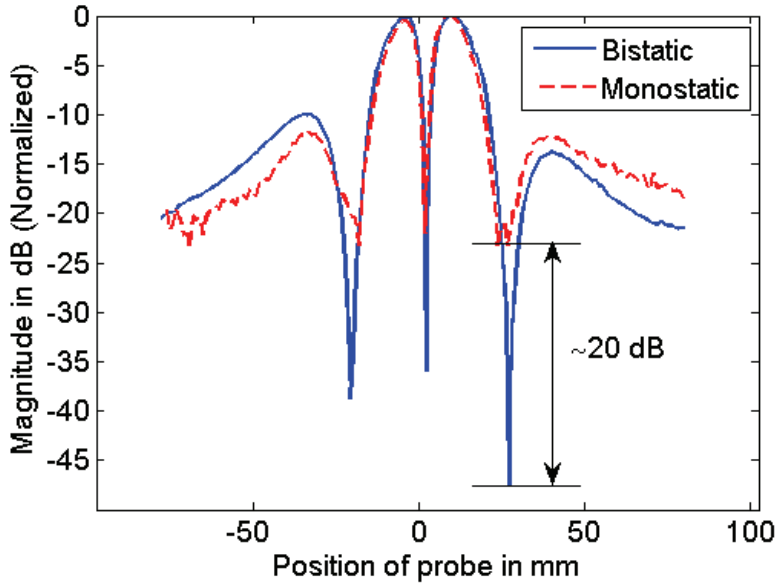

(a)

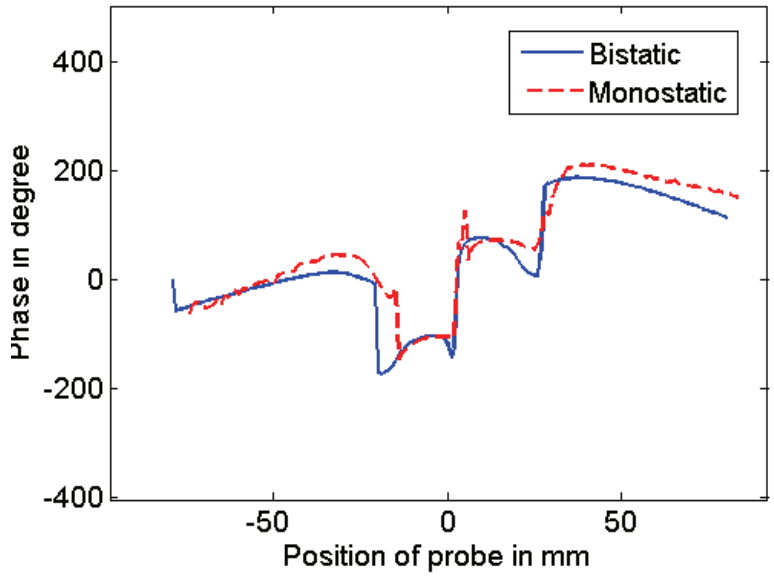

(b)

Figure 3.36 Comparison between the measurement results (magnitude and phase) obtained using the OMS probe when the NF imager is operating in monostatic and bistatic modes. (a) magnitude and (b) phase.

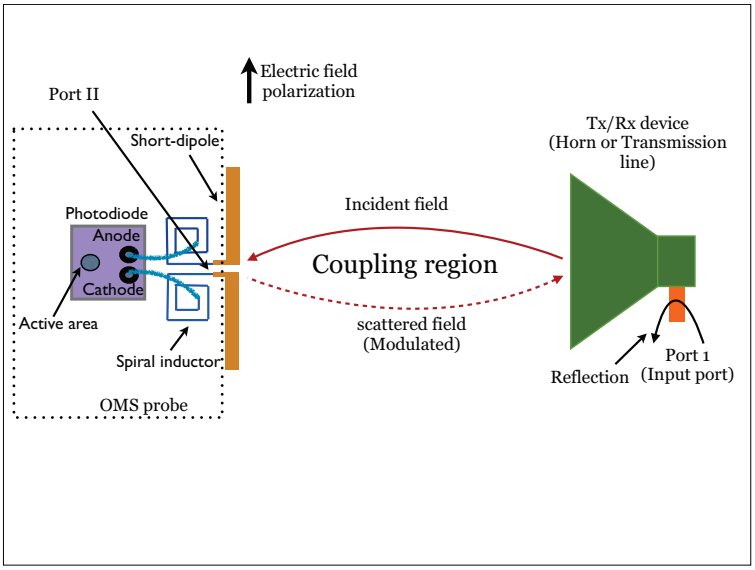

Figure 3.37 Drawing of the setup used to measure sensitivity of the OMS probe.

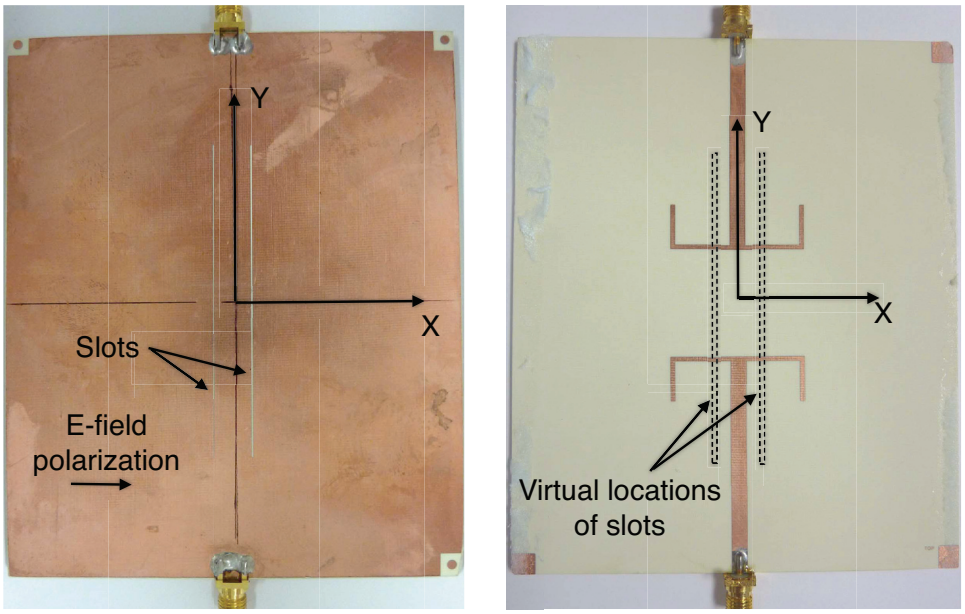

Figure 3.38 The photograph of the filter under test; top and bottom layers [73].

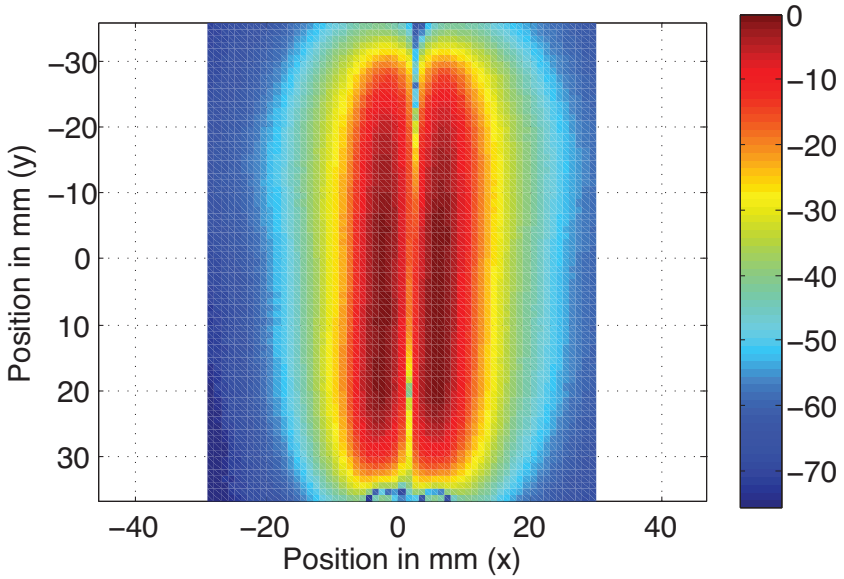

(a)

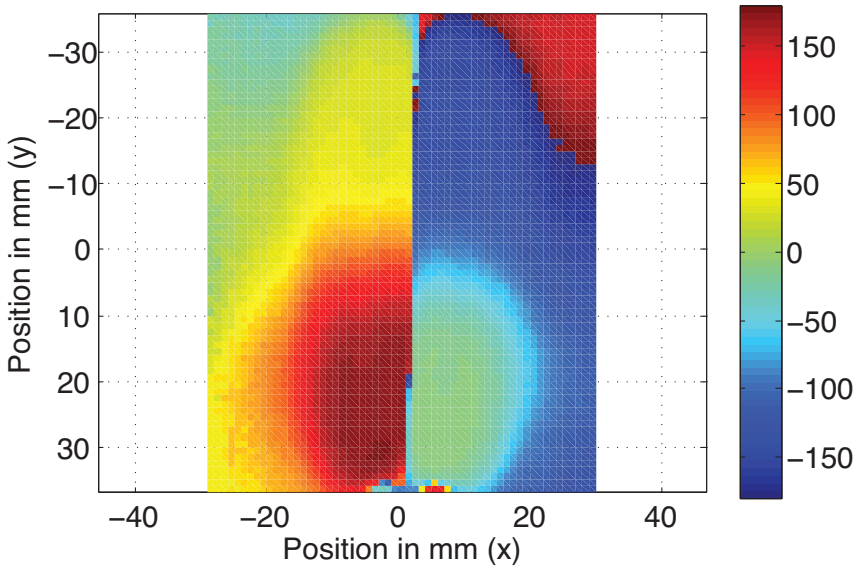

(b)

Figure 3.39 Measured E-field (i.e., E_x) distribution of the filter under test at the height of 3 mm above it; (a) Magnitude and (b) phase.

Chapter 4

Optically Modulated Scatterer (OMS) Probes Array: Improving Measurement Speed in an NF Imager

The planar NF imager equipped with an isolated OMS probe, which was discussed in Chapter 3, mainly suffers from long measurement time due to the mechanical translation of the OMS probe within the region where the NF measurement in required. Also, the supports, holders and actuators of the positioning system can perturb the field.

To overcome time-consuming measurement, the use of an array of OMS probes was suggested. The probes can be arranged into 1D (i.e. linear), 2D (i.e. planar) and even circular and radial arrangements (see Section 2.6.1). From a practical point of view, some arrangements are complicated and also costly to implement.

In this chapter, a linear array of precision and sensitive OMS probes to increase the measurement speed of the NF imager is proposed. Characterization of the array due to phenomena such as mutual coupling and shadowing will be discussed. Finally, the results of an OMS probe array will be investigated by comparing them with a known field distribution (e.g., simulations).

4.1 OMS probe array

A linear array of the OMS probes discussed in Chapter 3 is presented. The probes are laid in parallel along a line perpendicular to the probes' axes (see Figure 4.1). The array is moved mechanically along one direction, while being moved electronically (as well as mechanically if finer measurement resolution is required) in the orthogonal

direction so as to scan a $2D$ grid. Thus, this arrangement reduces mechanical movement in only one direction. The number of movements by the array is reduced by a factor equal to the number of probes.

4.1.1 Calculation of measurement duration by an NF imager: linear array configuration

It is shown in [47] that not only the probe translations by the positioning system but also the switching time between the probes remarkably slow down the total measurement speed of the NF imager. Thus, to achieve a very fast measurement, it is necessary to pay attention to both aspects simultaneously.

To theoretically estimate the measurement duration using a linear array (see Figure 4.1), parameters such as mechanical delays, switching time, system were considered in developing an explicit formula (i.e., Equation 4.1) that estimates accurately the measurement duration (i.e., T_{total}). Detailed discussion in developing the formula is available in Annex A.

In Equation 4.1, T_{total} represents the measurement duration taken by the array to scan a 2D grid.

$$T_{total} = N_y t_{aux} + (N_y - 1)(t_{movy} + t_s) \tag{4.1}$$

where, N_x and N_y are the number of points in x and y directions. The time taken by the positioning system to move the array along x (or y) direction is denoted as t_{movx} (or t_{movy}) . The time t_{aux} is given by Equation 4.2.

$$t_{aux} = N_p t_{single\ point} + (\frac{N_x}{N_p} - 1)(t_{movx} + t_s) + N_p t_{sw} \tag{4.2}$$

$$t_{single\ point} = t_s + 2t_p + t_{switch} - t_{p1}$$

We define t_s as the settling time of a 2D positing setup in both directions x and y. The switching time between I and Q signals, which is done by an SPDT switch, is represented by t_{switch}. Moreover, the time it takes to switch the probe ON and OFF, the microwave components detection time and the time taken by the LIA for completing a measurement are denoted by t_{p1}, t_{p2}, t_{p3}, respectively, and t_p represents their summation. Also, the time taken for switching between two probes is defined as t_{sw}. In Equation 4.2, N_p stands for numbers of the OMS probes used in the array.

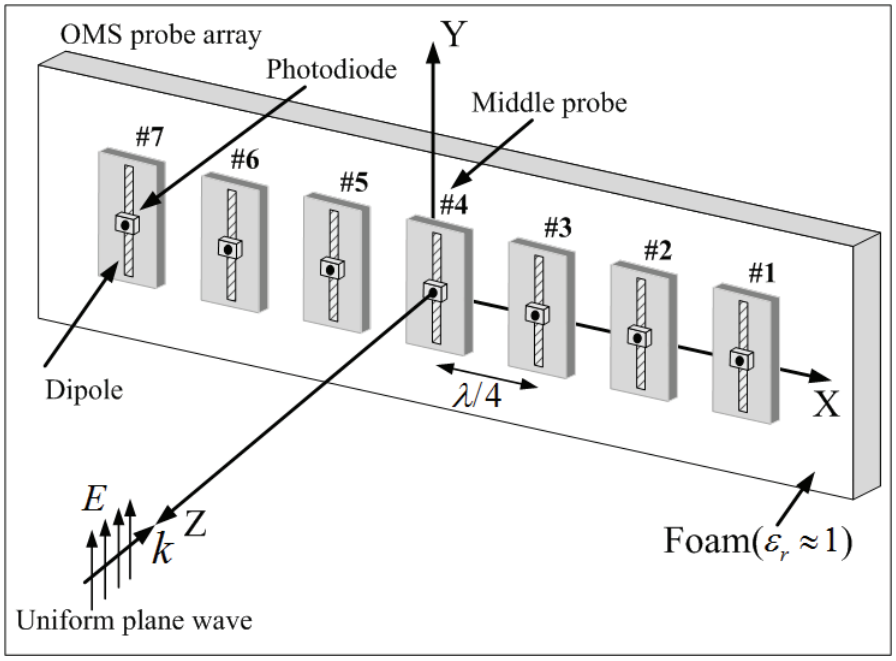

Figure 4.1 Schematic depicting an array of seven OMS probes with H-plane distribution. The spacing between the probes is $\lambda/4$.

In order to see the impact of the switching time and the number of probes on the total measurement time, we assumed a typical case where a 2D surface is scanned by the OMS probe array shown in Figure 4.1 over a 210 mm (x direction) by 240 mm (y direction) area with a 1 mm step size in both directions. The positioning system is set to move the array every t_{movx}= t_{movy}=200 msec to the next successive measurement position. The total measurement time (T_{total}) for the different numbers of probe (N_p) and switching times (t_{sw}) is illustrated in Figure 4.2. Obviously, fast switching quickly reduces the measurement duration. However, the number of probes beyond a certain value does not lead to significant improvement. On the other hand, the measurement speed is not improved if the switching time is not set at an adequately fast speed as shown in Figure 4.2. The results also demonstrate that switching times shorter than 0.1 sec will improve measurement speed and make the use of an OMS probe array faster than a one-probe system. Otherwise, fields in the region of interest can be measured faster using a single OMS probe.

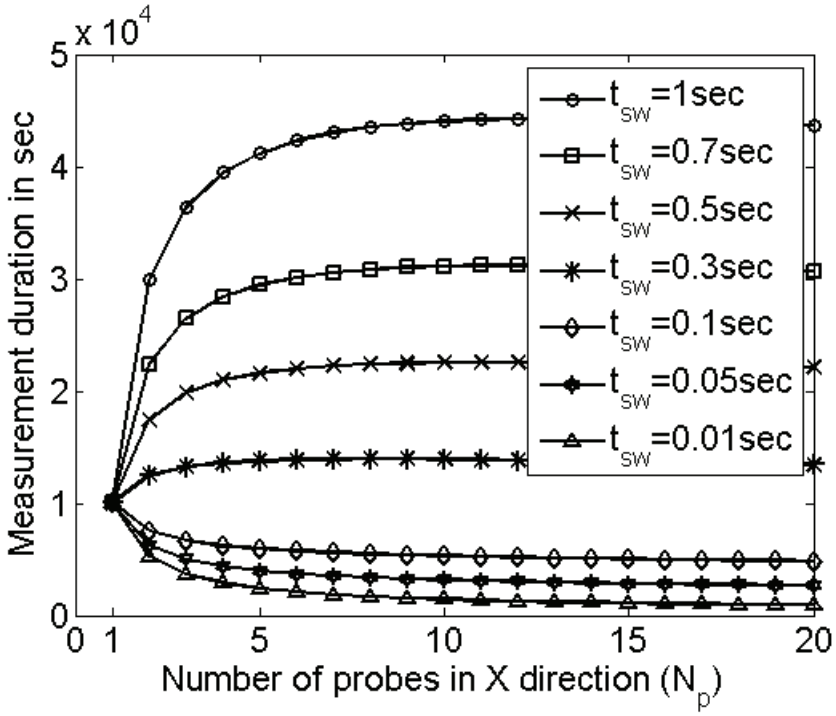

Figure 4.2 Measurement durations by an OMS array.

4.2 Characterizing the OMS Probe Array

4.2.1 Mutual coupling

Probe arrays may lead to inaccurate results due to the interaction between the array elements, dispersion in sensitivity, frequency of the probes and the interaction between the AUT and the measuring array [74].

Interaction between the array elements, also known as mutual coupling, happens when the measuring probe (i.e., the probe being modulated) receives fields from the AUT and also from the neighbouring probe. This phenomenon causes deviation of the measured results from the AUT's true fields' distribution.

In order to investigate how mutual coupling affects the measurement results, an array of seven OMS probes was considered, as illustrated in Figure 4.1. A quarter of wavelength spacing between the probes was assumed. For convenience, it was assumed that the array is illuminated with a uniform plane wave propagating in the z direction with its E-field polarized along y (see Figure 4.3). Due to the symmetry

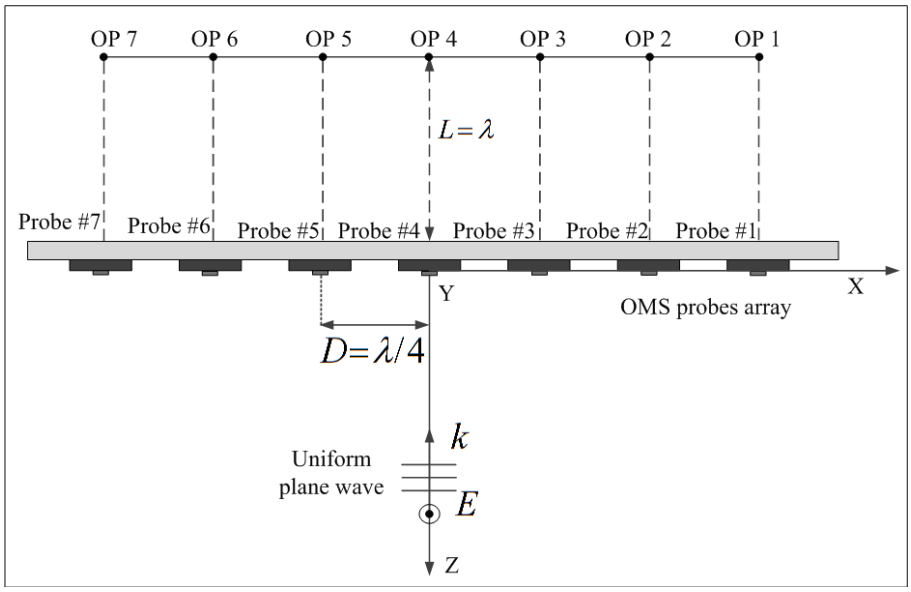

Figure 4.3 Schematic depicting the setup for the mutual coupling test. OP: observation point.

of the structure with respect to yz plane, we only provide the results for one side of the central probe (i.e., probe #4). Observation points (i.e. OP_i; i=1, 7) are chosen on the back of the array, opposed to the illuminated side of the array as Figure 4.4 demonstrates. These points are one wavelength away from the array, along the direction of the propagation of the plane wave.

The scattered E field at each observation point (i.e., OP_i; i=1, 7) is calculated by subtracting the fields corresponding to OFF and ON states of each probe (probe #i), while the other probes are switched OFF. Simulation results obtained from HFSS are shown in Figure 4.4. To quantify the mutual coupling effect on the array's measurements, the same measurement was repeated using an isolated OMS probe. The results obtained by an array normalized to that of the isolated probe are plotted in Figure 4.4. The results reveal that the measurements deviate from that of the isolated probe increases for the probes located closer to the end of array.

By adding two dummy elements (passive probes) loaded with the input impedance

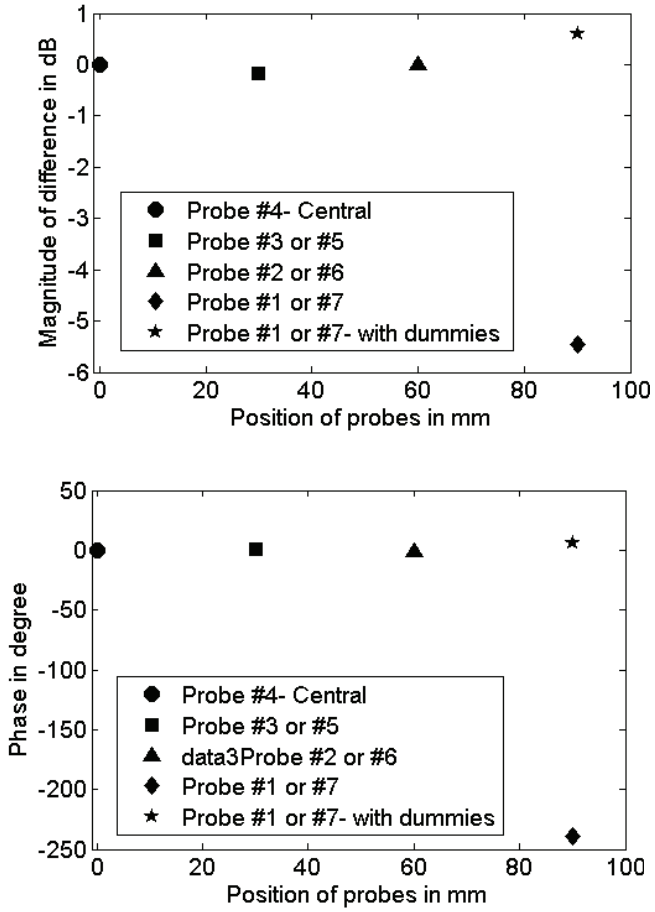

Figure 4.4 Simulation results demonstrating the effect of mutual coupling on the field to be measured.

of the photodiode in the OFF state, one on each end of the array a quarter wavelength away from probe #1 and #7, the agreement between the results improved as illustrated in Figure 4.4. It can be seen that adding the dummy elements adjusted the magnitude and phase of the probe #1 (or probe #7) by $\sim$ 5dB and $\sim$180 degrees. It can be concluded that one simple way to reduce the influence of mutual coupling is to add an adequate number of passive probes (unmodulated) to the array. However, the difference in magnitude and phase resulting from mutual coupling will be fully compensated for only when the probes are calibrated.

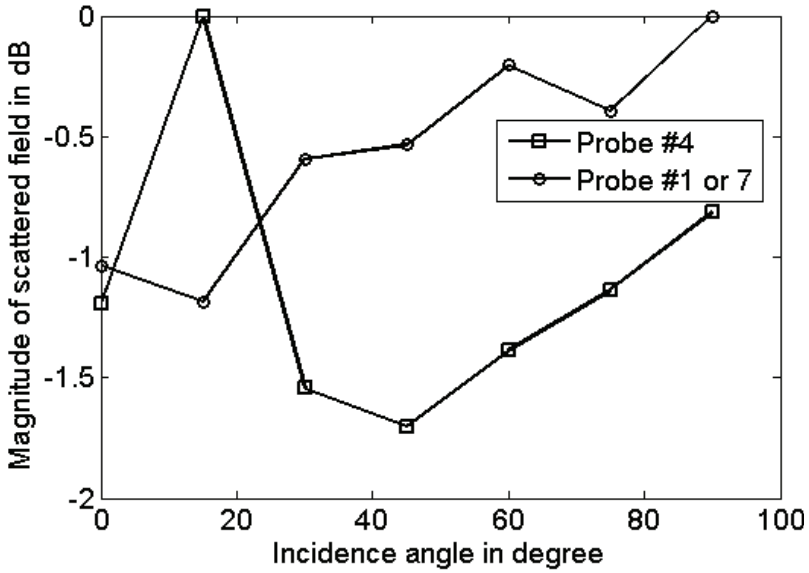

Figure 4.5 Magnitude of the scattered field by the OMS probe array versus different incidence angle. The solid-squared line: probe #4; the solid-circled line: probe #7.

4.2.2 Probe shadowing by neighbours

In some applications, when the array is illuminated from the side or measures a field distribution very close to the AUT (e.g. close to aperture of a waveguide) some of the probes measuring the fields may be shadowed by neighbouring probes.

To investigate this effect, the incidence angle of the illuminating plane wave was swept from 0 to 90 degrees and the scattered fields by the probes were calculated when the probes were ON and OFF. The two fields then were subtracted to get scattered fields at the observation point (i.e., OP_i; i=1, 7 in Figure 4.3) corresponding to each probe. To do this, we considered probe #4 (central), which is illuminated by a plane wave at 2.45 GHz. In Figure 4.5, the solid-squared line shows the normalized scattered fields measured by probe #4 as a function of the incidence angle. A variation of $\sim$ 1.2 dB is observed, which is believed to be due to the interaction between the probes. We also calculated the scattered field measured by probe #7 (the same as probe #1) located at the very end of the array. In the same figure the solid-circled line reveals the results with a variation of $\sim$1.7 dB for probe #7, which makes it clear that this probe is more sensitive to oblique incidence than probe #4. However, such

a difference is reduced for angles greater than 45 degree.

As mentioned above, when the array is set to measure the E-field distribution of an AUT, the probes located close to the middle of the array may receive fields from the AUT close to normal, whereas those located on both sides of the probes at the centre and on the very end of the array in particularly may receive a signal beyond the limit of 45 degrees. As a consequence, the NF measurement will show some fluctuations caused by the phenomenon discussed here.

4.2.3 OMS probe array frequency dispersion

Grouping a number of OMS probes as an array, such as the one shown in Figure 4.1, may cause the probes to show a different frequency response (frequency dispersion) than that of an isolated probe due to the interactions between them. This phenomenon can lead to inaccurate measurement results particularly when the array is set to measure at different frequencies. In order to control this effect, one can adjust the spacing between the probes in order that the interaction is minimized.

To estimate how the resonance frequency of the probes is altered in the array shown in Figure 4.1, where the spacing between the probes is chosen $\lambda/4$, we followed the same procedure discussed in Section 4.2.1 for calculating the field scattered by each probe at different frequencies. Figure 4.6 shows the frequency response of an isolated probe, which is the reference here for comparison. It also demonstrates the frequency response of probe #4 (i.e., central) and that of probe #7. The results reveals that resonance frequencies of the probes regardless of their locations in the array, occur at $\sim$ 2.4 GHz, which is exactly the resonance frequency of the isolated probe (i.e., reference). As can be seen in this figure, the frequency response of the probes are different at other frequencies. By calibrating the array at desired frequencies, one can overcome such differences between the frequency responses.

4.3 OMS probes array implementation

The principle of the MST technique and the design and implementation of an OMS probe prototype with the desired characteristics operating at 2.45 GHz were addressed in Chapter 3. Seven OMS probes were mounted onto a thick planar foam ($\varepsilon_r \approx 1$) with a spacing of 3 cm between the probes. The foam has a thickness of 1.2 cm and

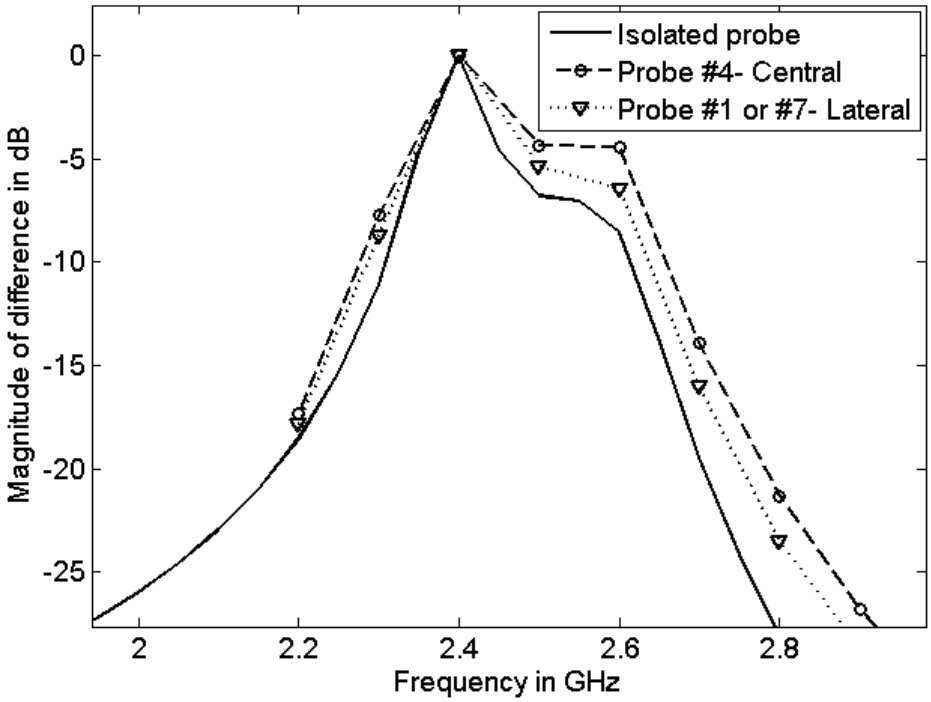

Figure 4.6 Frequency response of the OMS probe array shown in Figure 4.1.

is very rigid. It also prevents the array from vibrating when a very fast measurement is made. Figure 4.7 shows a photograph of the array. The photograph also shows the optical fibers coupled to the probes.

The microwave electronic and optical circuitries necessary to transmit/receive and process the scattered fields of the OMS probe array are similar to what is proposed in Section 3.7.1. Figure 4.8 shows the microwave circuitry of the NF imager including the essential parts. The only difference is an optical switch, which will be discussed in section 4.3.1. The carrier cancellation part shown in Figure 4.8 will be discussion in Chapter 5.

4.3.1 Laser diodes array: custom-designed optical switch

In practice, in order to send a modulation signal to the designated probe in the array and switch the modulating light between the probes, it is necessary to use an optical switch.

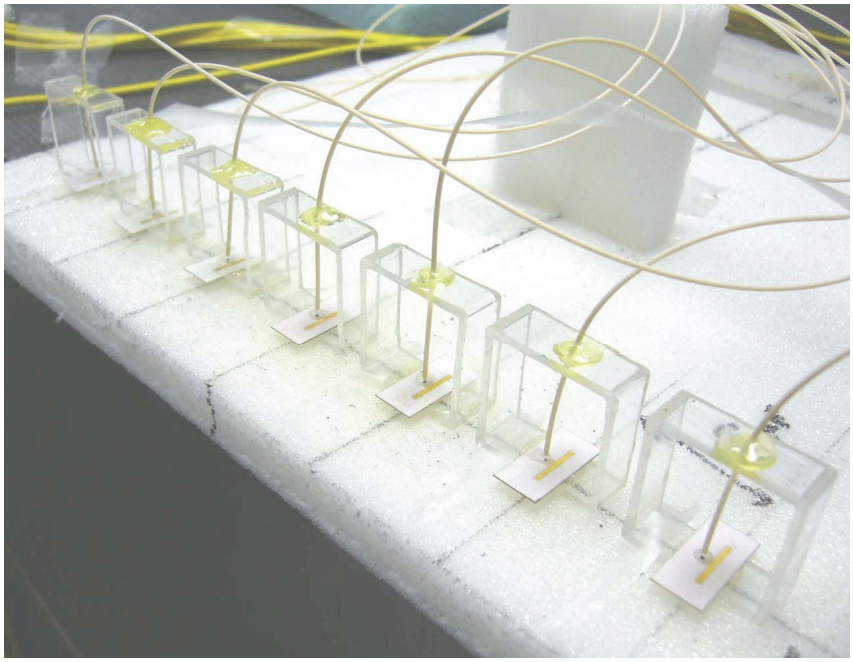

Figure 4.7 Photography of the developed array of seven OMS probes.

To this end, an array of controlled laser diodes (see Figure 4.9) was designed and developed. The array consists of laser diodes, each individually connected to a probe (see Figure 4.8)). By modulating a laser diode, the corresponding OMS probe is modulated (switched ON/OFF). A digital controller was also implemented to provide proper signaling to the probe. The controller produces a reference signal used by the LIA. The stability of this reference signal was assured by using an 8 MHz crystal, preventing phase jitter in the measured data. The controller is driven by a software developed in Labview®.

The electronically switched feature of the array not only increases the measurement speed but also eliminates cross-talk between the outputs, which was seen with the mechanical optical switch used in [75, 76]. As a result, we obtained a 14-times improvement in the measurement time compared to the setup reported in [75] in which a commercial opto-mechanical switch was used.

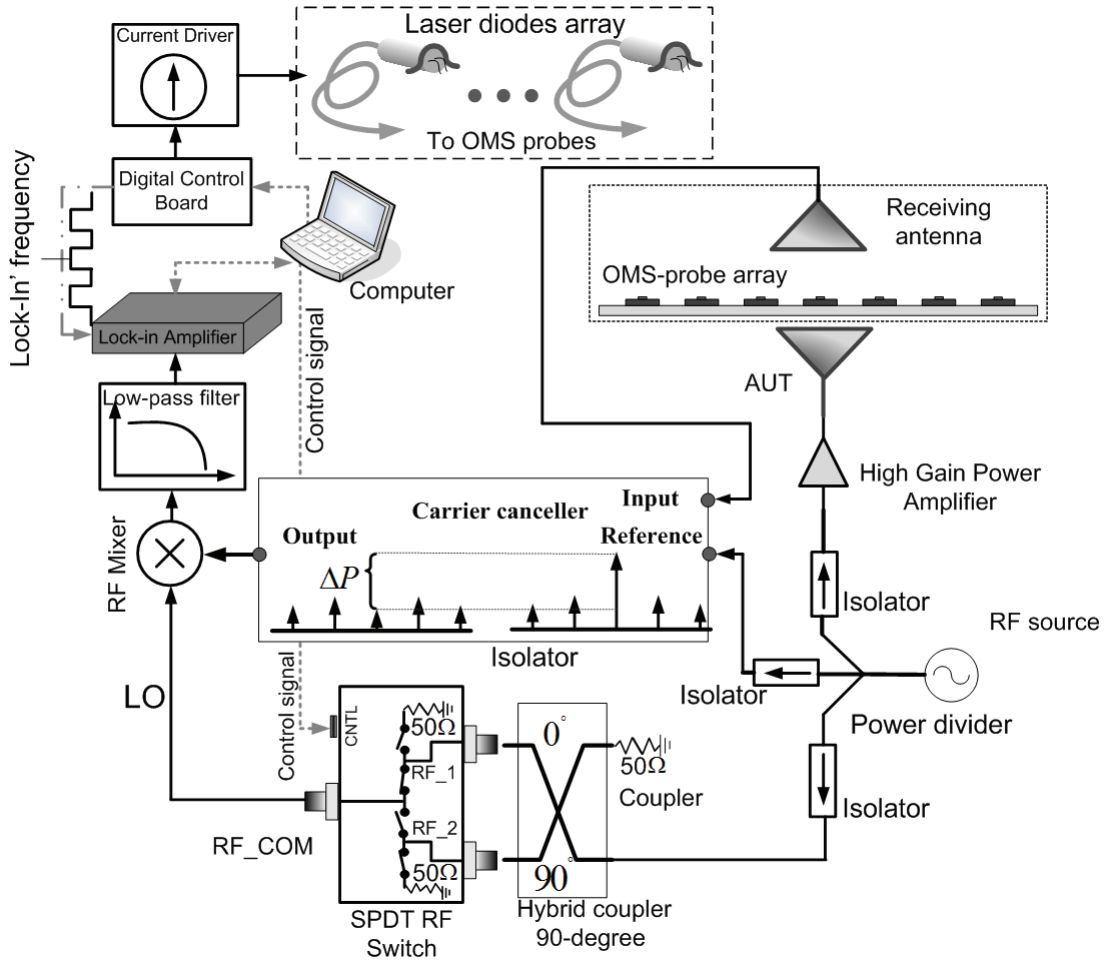

Figure 4.8 Near-field imager microwave circuitry for the bistatic OMS probe setup.

4.4 Validating the developed NF imager equipped with array of OMS probes

4.4.1 Array calibration

It is practically impossible to make several OMS probes with identical characteristics. Differences in the probes' responses can be caused by differences in the photodiode and materials used, optical fiber/photodiode coupling quality and many other factors [77]. In order to quantify these differences in the probes, we performed a simple monostatic field probing experiment in which seven probes are set to measure the E

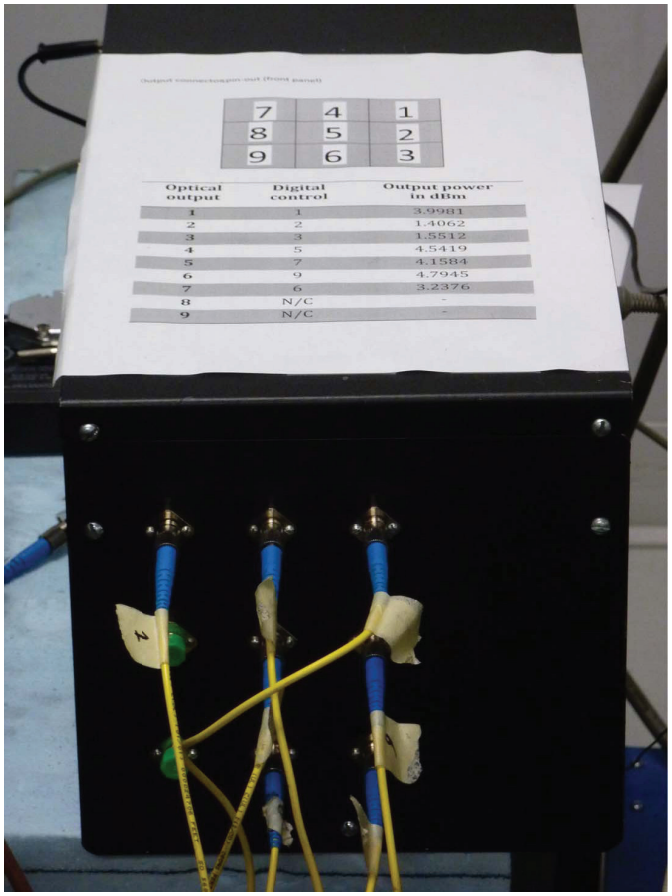

Figure 4.9 Photograph of the custom-designed switched laser diodes array.

field at one fixed point near a DUT . It is also worth mentioning that we could not follow the well-proved procedure addressed in [77] for calibrating the probes because of the unavailability of a uniform plane-wave illumination. The obtained results are then used to compute a complex correction factor (CF) corresponding to each probe using Equation 4.3 [78].

$$CF = \frac{E_{ref}}{E_{Probe\#i}}; i = 1, 7 \tag{4.3}$$

In this experiment, a dielectric antenna with a highly concentrated near-field distribution was used as a DUT. The antenna incorporates a cylindrical waveguide loaded with a material (e.g., ceramic) with a dielectric constant about 15. It is able to strongly illuminate a small area where the probe under test is located while weakly

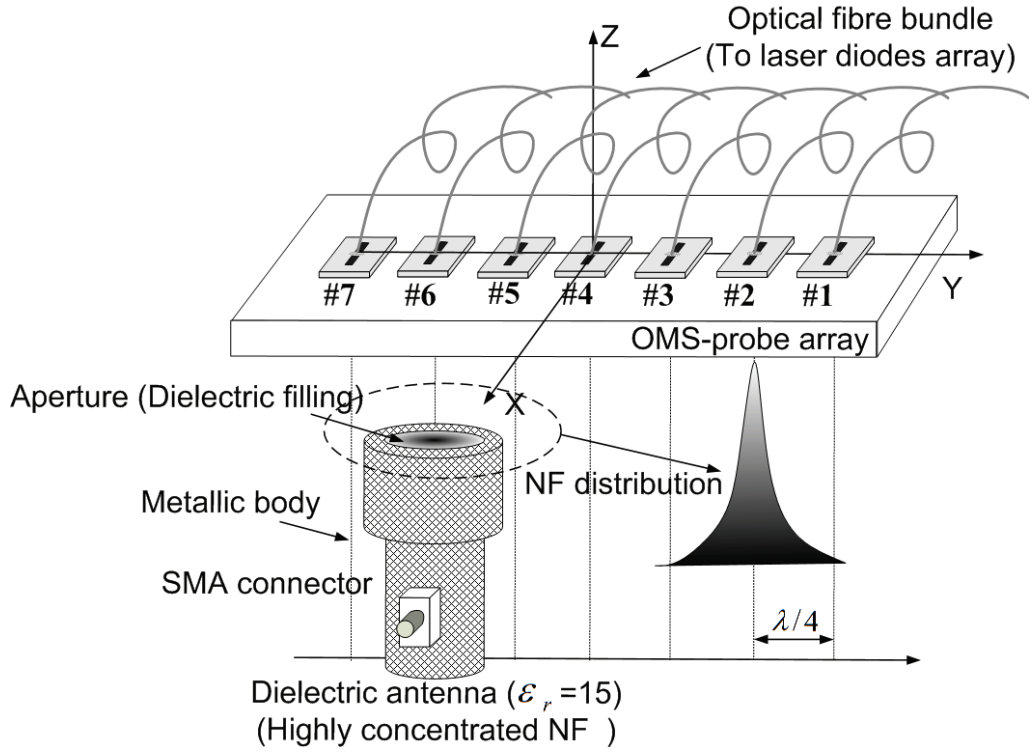

Figure 4.10 The setup used in monostatic mode for the calibration of the probes.

illuminating the other probes, which are switched OFF. The probes are positioned within the illuminated region near the antenna and the fields in the E-plane of the illuminating antenna are scanned (Figure 4.10). Ideally, it is expected the probes will measure the same field distribution. Due to the reason discussed earlier, they do not. Therefore as an effective compensation technique, a probe in the array is used as a reference (e.g., probe#4) to which the rest of the probes are weighted by a complex number (e.g., correction factor). The correction factors can be obtained for several points and averaged to get a better agreement between the probes' responses. The computed correction factors based on the method explained here, are illustrated in Table 4.4.1. The effect of applying correction factors on the measurement results will be discussed in Section 4.5.

Table 4.1 The measurement results of a known field using individual probes (all measurements has been normalized to the result of probe #4).

Probe #	CF	$\|CF\|$	$\angle CF(deg)$
1	0.8704+j0.0218	0.8706	1.4347
2	0.9645-j0.0806	0.9678	4.7724
3	0.959-j0.0511	0.9603	-3.050
4	1+j0	1	0
5	1.0007-j0.0091	1.0007	-0.5210
6	1.0252+j0.0258	1.0255	1.4415
7	1.0432+j0.0406	1.0439	2.2287

4.4.2 Receiving antenna compensation

In the bistatic test setup, the receiving part of the NF imager incorporate an open-ended waveguide aperture to pick up the scattered fields by probes and send them to the coherent system as illustrated in Figure 4.11. During the scan, the waveguide is moved together with the array and the phase centre of the waveguide has a minimum distance from the central probe (i.e., probe#4). In this configuration, the rest of the probes are placed evenly on both sides of probe #4. When the probes are addressed successively, they scatter the fields at their locations in order. As can be observed in Figure 4.11, the scattered fields propagate along different paths to reach the receiving antenna (i.e., r_i; i=1, 7). It should be mentioned here that this compensation technique takes also into account the difference between the probes. Then, the picked-up signals will not be identical even if they measure the same fields. So, we need to compensate the measured data (raw data) for the NF radiation pattern of the waveguide aperture.

The compensation for this phenomenon is implemented as follows. We first set the waveguide to operate as an illuminator in a monostatic mode (TX/RX device) illustrated in Figure 4.11. In this experiment, the probes are addressed successively and then moved to a new position until they array scans the region of interest. This test not only gives a means to compensate for the NF pattern of the receiving antenna but also for the interaction between the AUT/waveguide and the AUT/array if the test is performed in the presence of the AUT. Ideally, it is expected to get a flat response over the region in which each probe scans, but given the interaction of the

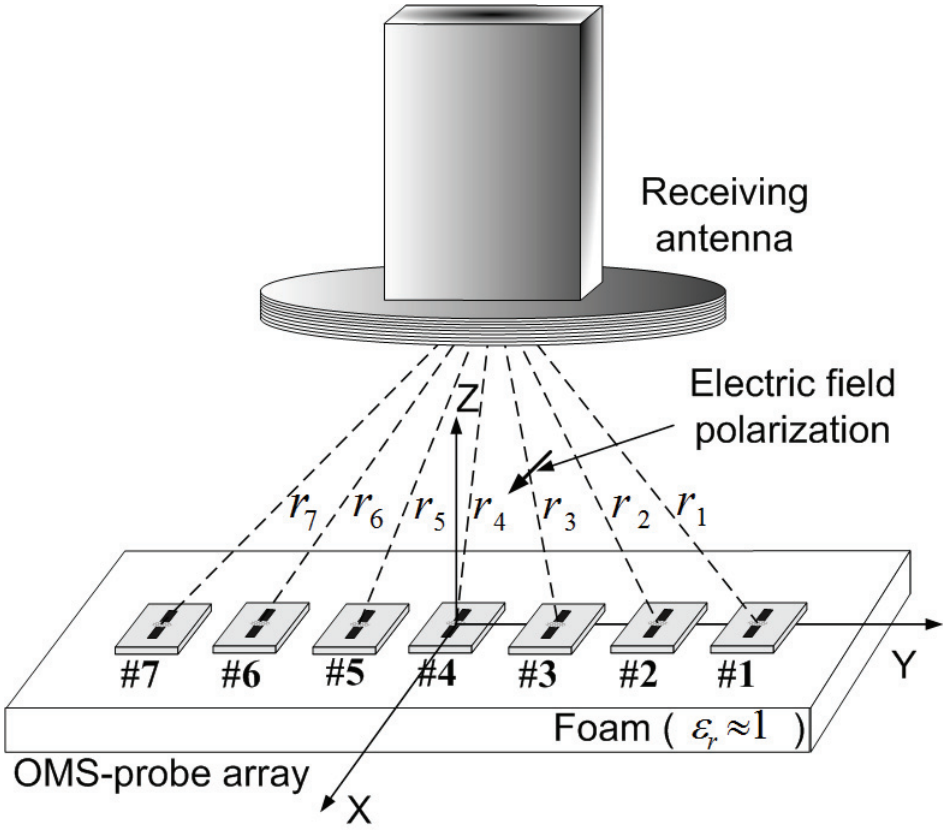

Figure 4.11 Depiction of the method used for compensating the data due to the radiation pattern of the receiving antenna.

array with the surrounding area and the interaction between probes, the measured results show some deviations from the ideal one as illustrated in Figure 4.12. The ideal results are the ones shown by broken line in Figure 4.12, which mean no interactions conceived between the probes with the AUT and the receiving antenna, in addition to the interaction between the probes and surrounding area. The asymmetry of the curves occurs because of discrepancies in the probes of the array, probes' displacement and misalignment. Even though each of the probes is at a constant distance from the receiving antenna the results reveal that measurements of a constant fields by them are not identical. The results also demonstrate the importance of the compensation before any comparison is made to validate the imager's results [74].

4.5 OMS probes array: validation results

The electric field distribution of a planar inverted-F antenna (PIFA) (Figure 4.13) radiating at 2.45 GHz was measured in bistatic mode on a plane located at $\lambda/4$ above the antenna's ground plane [79]. Such an antenna is commonly used in portable devices (e.g., cellphone) and communication systems. Therefore, the PIFA antenna is one of the best alternatives, that can be considered as an AUT for validating the results of the array.

The near-field distribution of the PIFA was measured using a monostatic setup (its performance and the validity of its results have been already investigated in Chapter 3). Then, the imager was set to operate in the bistatic mode and the same fields were measured. These results were corrected by compensating for the NF pattern of the receiving antenna.

Figure 4.14 shows 2D simulation results of the AUT E-field distribution obtained with HFSS at a distance of $\lambda/4$ above the PIFA ground plane. The magnitude plot shows a dynamic range of $\sim$ 25 dB over a scan area of 240 mm by 210 mm. The uncompensated E-field distribution (i.e., 2D scan) obtained by the NF imager operating in bistatic mode $\lambda/4$ above the ground plane are illustrated in Figure 4.15. As it can be seen in this figure, both magnitude and phase plots show discontinuities between two adjacent strips (the area scan by a probe), that are due to differences between the probes. Such differences between the strips are more obvious in the phase plot than that of the magnitude. After correcting the data due to the probes' discrepancies in response and compensating for the receiving antenna NF pattern, we obtain 2D results for both magnitude and phase as shown in Figure 4.16. The results show the effectiveness of the calibration and compensation techniques as the discontinuities between the adjacent strips have been reduced.

For clarity, we show two slice cuts of measurement in Figure 4.17 and Figure Figure 4.18 for E- and H-planes. Figure 4.17 shows the variation of both magnitude and phase of the measured E-field, which are compared with simulations and also the field distribution obtained by the NF imager operating in the monostatic mode. The three curves (i.e., magnitude of E-field) are in good agreement. However, that of the monostatic deviates from the true field starting from -20 mm toward negative x values. The measured phase information in the E-plane of the PIFA in three cases are in good agreement over the whole measurement. In order to quantify the difference

between the measurement results and the true field distribution of the PIFA, the mean square error of the data was calculated. The error associated with E-plane and H-plane cuts are 0.12% and 0.06%, respectively.

In Figure 4.18, the results obtained in bistatic mode are compared with simulations. We also included the variation of both magnitude and phase of the E-field from monostatic measurements. Figure 4.18 also demonstrates the effectiveness of the applied calibration on the raw data. Good agreement is seen in both planes, even if the measured distributions appear slightly wider than the simulated ones.

Ripples are seen in Figure 4.18 at both end of the results, particularly in the curves for the magnitudes. These are due to the fact that the probes located at both ends of the array (i.e., probe #1 and #7) show different scattering characteristics than the ones that are closer to the center as discussed in Section 4.2.2.

In the measurement, these probes receive signals at $\theta_3 = 68° - 74°$ degree in their H-plane as shown in Figure 4.19, considering that the measurement high is $\lambda/4$ from the AUT's ground plane. As the results in Figure 4.5 show, there is nearly a difference of -1.2 dB compared to normal incidence. Therefore, the scattered fields measured by the probes located at both ends of the array change and consequently lead to the ripples appearing in the results.

4.6 Conclusions

An array of OMS probes with low-cost elements has been conceived and implemented to increase the measurement speed significantly compared to an opto-mechanically switched system. Parameters such as mutual coupling, shadowing and frequency dispersion that influence the measurements were also studied to confirm that a $\lambda/4$ is an appropriate probe spacing for minimum inter-element interactions. In order to improve the accuracy of the measurements, the raw measurement data was corrected to remove discrepancies in the probes' responses, leading to a better calibration technique. This imager has shown that it is able to make accurate and rapid E-field measurements in the NF region of DUTs, in good agreement with the simulations.

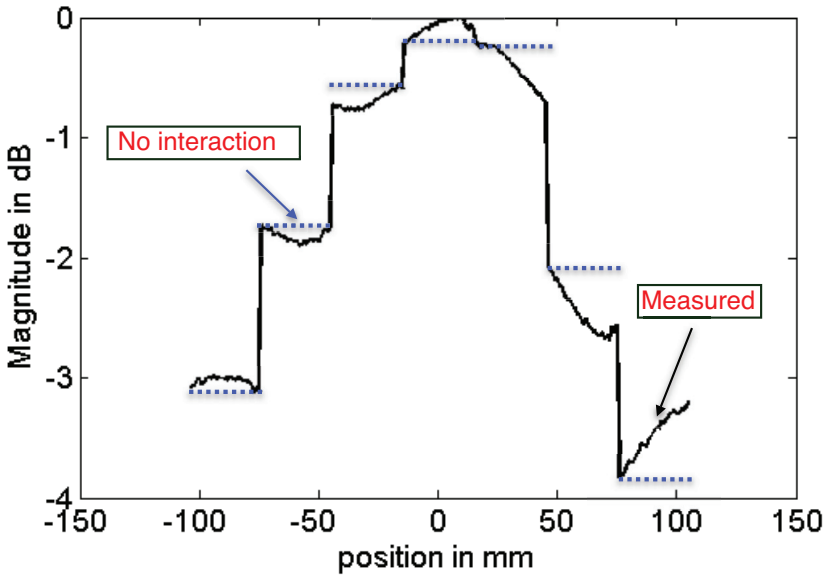

(a)

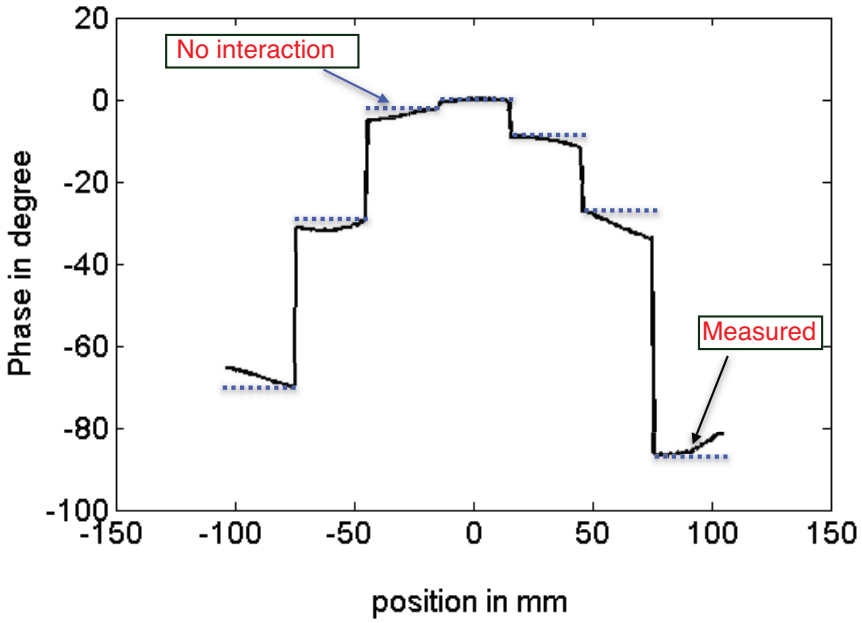

(b)

Figure 4.12 The measurement result obtained in the test to compensate for the radiation pattern of the receiving antenna; (a) magnitude and (b) phase of the measured E fields.

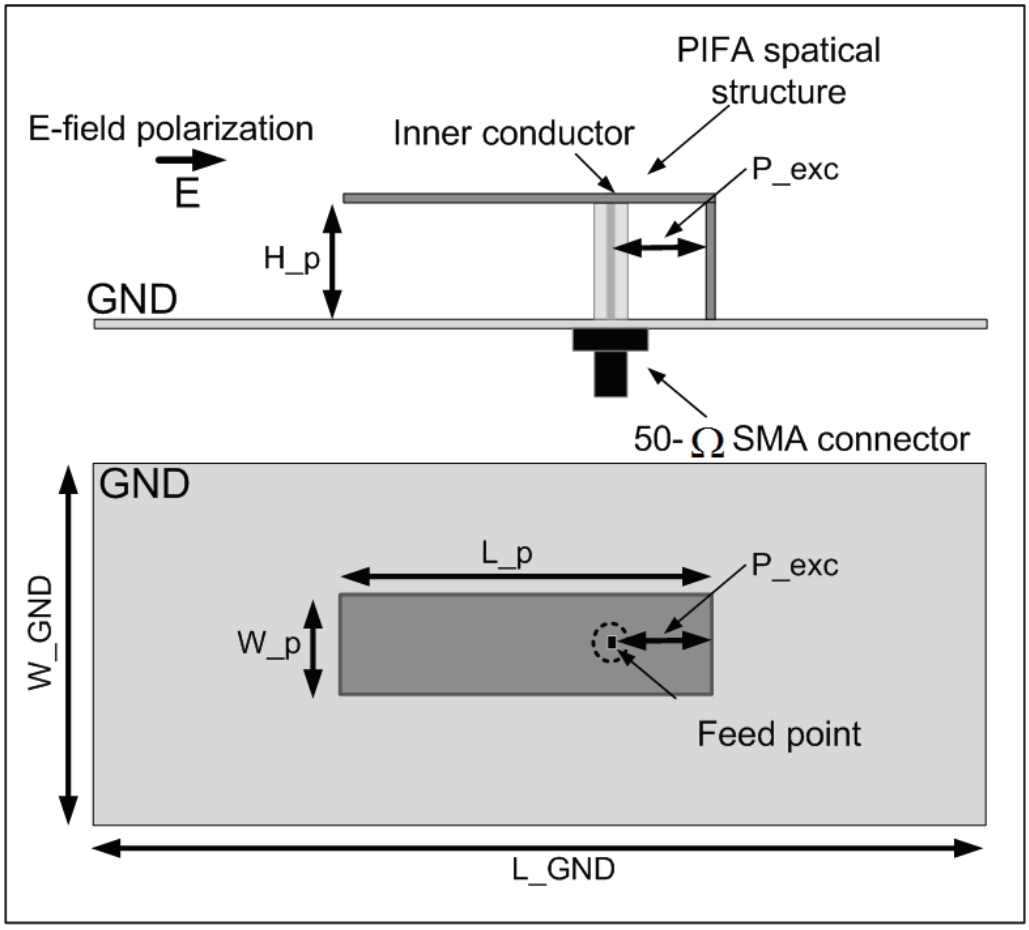

Figure 4.13 Antenna under test (AUT). PIFA antenna operating at 2.45 GHz with measured return-loss of about 12 dB; the physical dimensions of the PIFA are as follows: L_p=27 mm, W_p=13 mm, H_p=7 mm, P_{exc}=7 mm, W_{GND}=70 mm and L_{GND}=137 mm.

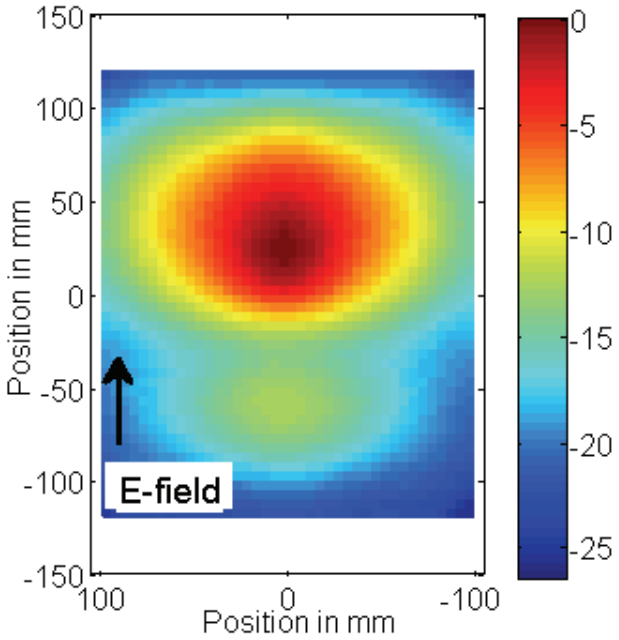

(a)

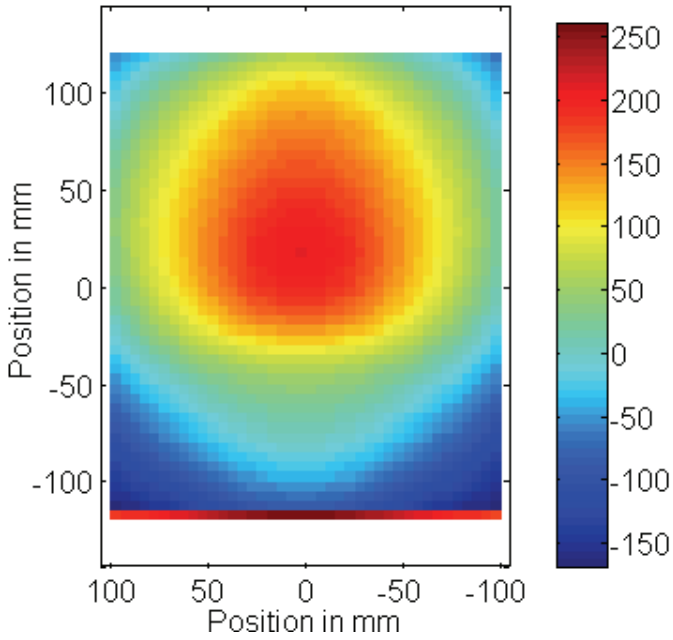

(b)

Figure 4.14 2-D map of electric field distribution of the AUT obtained by HFSS® at a height of 30 mm; (a) magnitude and (b) phase.

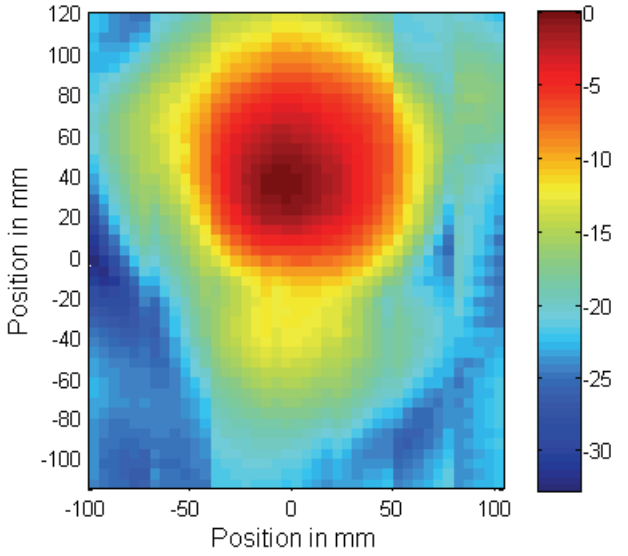

(a)

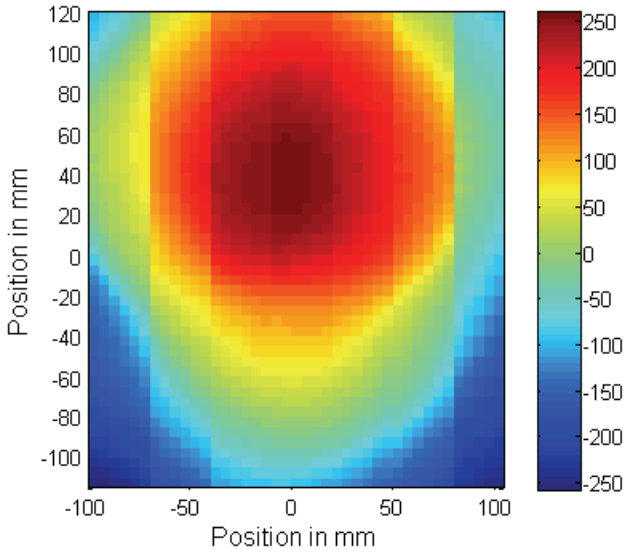

(b)

Figure 4.15 2-D map of electric field distribution measured at a distance of $\lambda/4$ above AUT; uncompensated data: (a) magnitude (dB) and (b) phase (deg.)

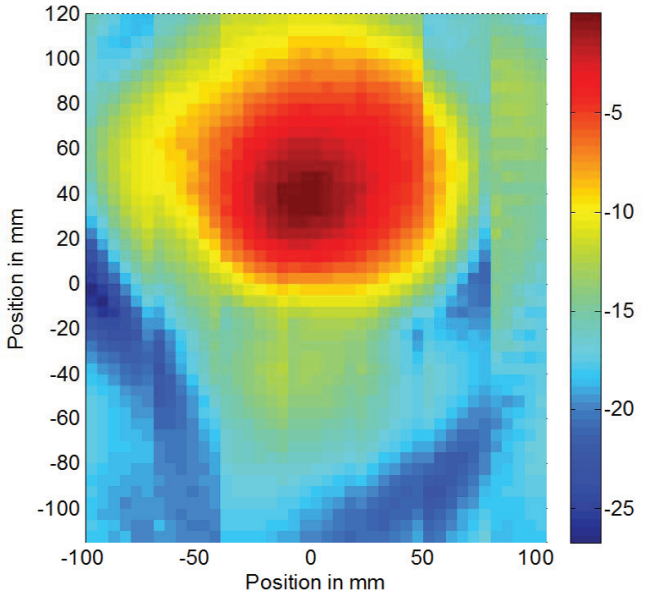

(a)

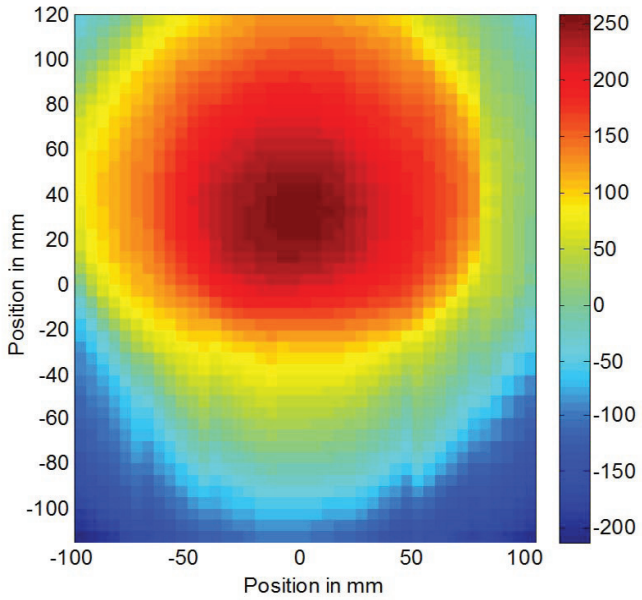

(b)

Figure 4.16 2-D map of electric field distribution measured at a distance of $\lambda/4$ above AUT; (a) magnitude (dB) and (b) phase (deg.)

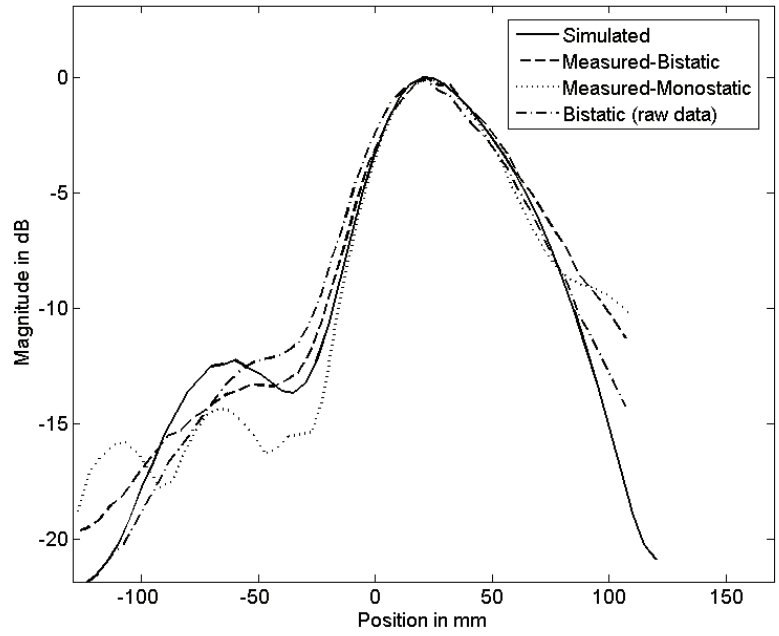

(a)

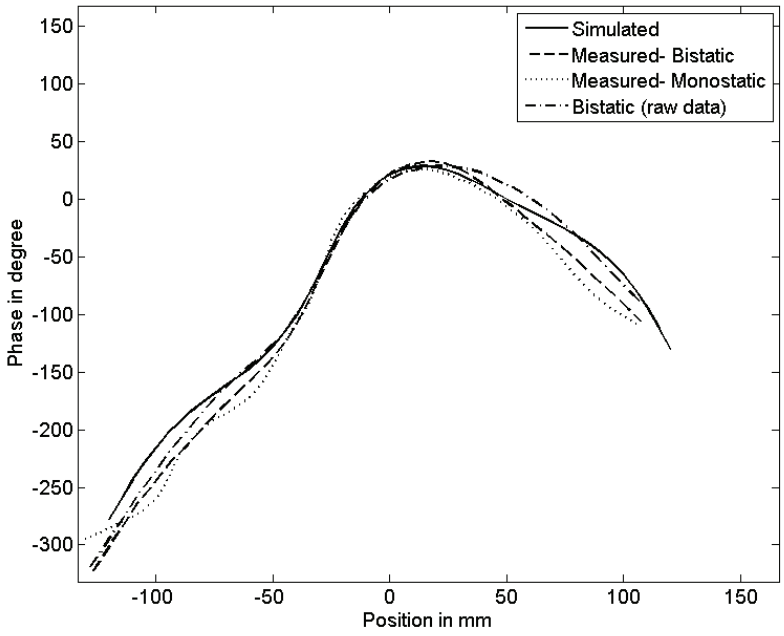

(b)

Figure 4.17 E-plane cut of the measured E-field at a distance of $\lambda/4$ from the PIFA antenna's ground plane; (a) magnitude (dB) and (b) phase (deg.)

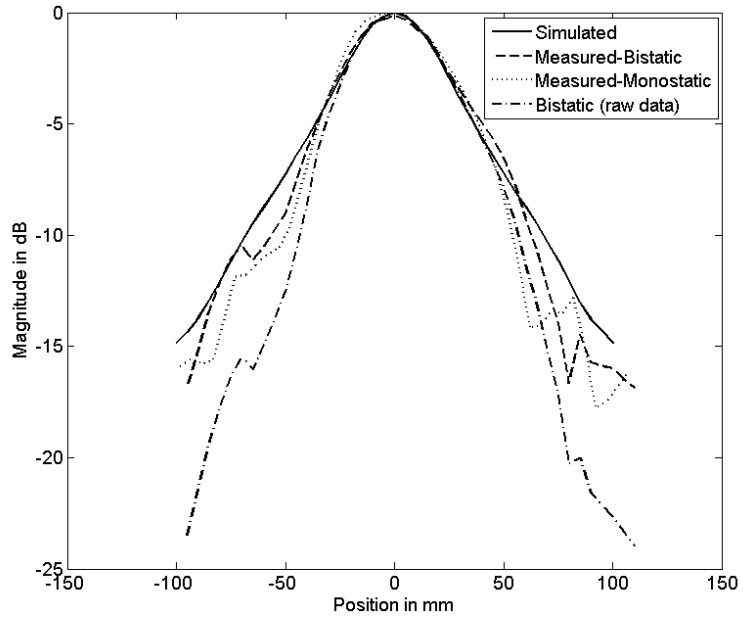

(a)

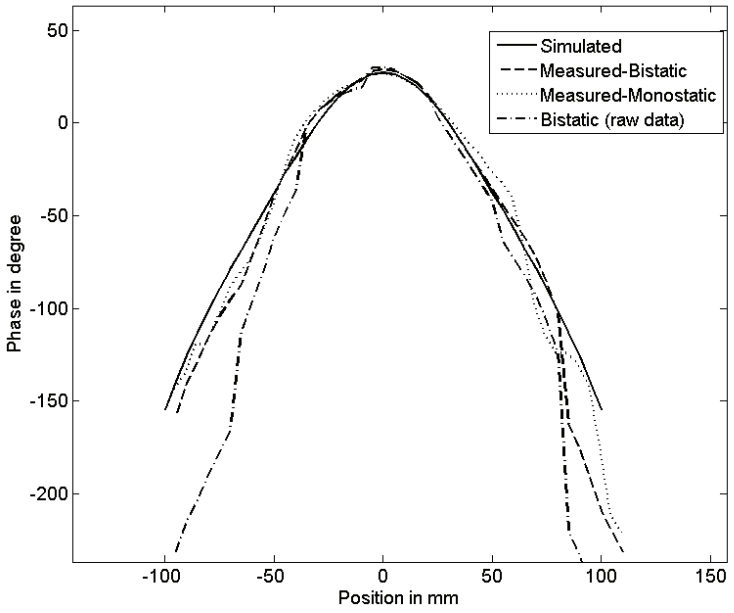

(b)

Figure 4.18 H-plane cut of the measured E-field at distance of $\lambda/4$ from the PIFA antenna's ground plane; (a) magnitude (dB) and (b) phase (deg.)

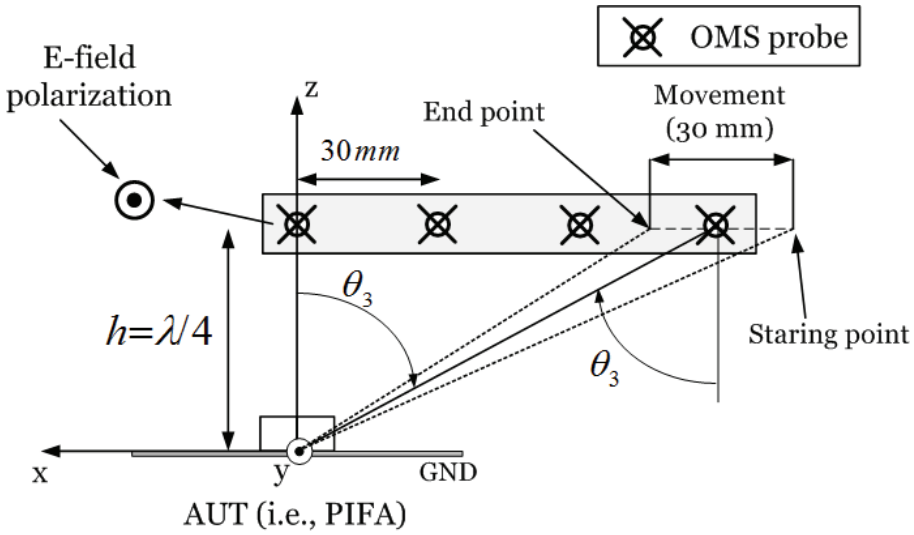

Figure 4.19 Schematic of the AUT (i.e. PIFA) measured by NF imager equipped with an OMS probe array. The schematic shows only one half of the array for simplicity.

Chapter 5

Carrier Cancellation: NF Imager Dynamic Range and Linearity Improvement

5.1 Principle of carrier cancellation in the MST-based NF imager

In an MST-based NF imager the received signals (modulated) consist of a carrier and sidebands signal, independent of the setup mode (i.e., monostatic or bistatic). However, the probe itself is able to reflect the fields at the carrier frequency, that is almost negligible compared to the other reflections in the measurement system. In the modulated signal, the carrier is generally stronger (e.g., $\sim 50dB$) than the sidebands. Receiving fairly high-power carrier, can cause nonlinear behaviour such as saturation and compression in the receiver [80, 81] particularly beyond a certain level. High power carrier signals can also increase gain (i.e., $\max|I|) \neq \max|Q|)$ and phase imbalances of I and Q signals in I-Q modulators, resulting in a distorted field measurement [82].

Suppressing the carrier at the receiving stage would not only eliminate the measurement errors associated with the results but also provide the potential to increase the excitation power, leading to a higher dynamic range for which the receiver operates in linear regime. Keeping the carrier level lower than an allowed upper limit enables us to amplify I and Q with out causing compression and saturation and while avoiding working close to the noise-floor of the LIA.

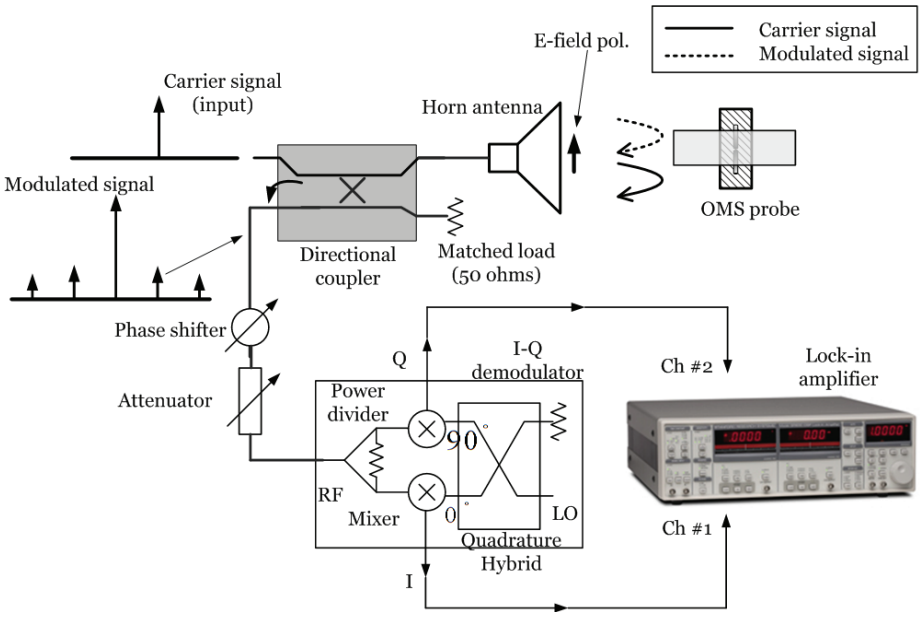

Figure 5.1 Schematic of the circuit used to investigate the effect of high power carrier. The solid and dashed line indictors are to show reflections at carrier and modulated frequencies.

5.2 High power carrier at the receiver: destructive effect

In the homodyne systems that are used in the imager, in-phase (I) and quadrature (Q) signals are produced by down-converting from RF to IF frequencies. The conversions by the mixer are not perfect and linear due to its inherent nonlinear operation. This component is subject to saturation and high conversion-loss in case of high-level signals, which limits the dynamic range of the measured results [82].

In order to study the NF imager for possible imbalances corresponding to the different carrier power, a variable phase shifter and an attenuator with a dynamic range of 60 dB were added in the receiving channel front-end, as demonstrates in Figure 5.1. The measurement was performed first by adjusting the phase shift to equalize the I and Q signals. The attenuation was then applied. The measurement

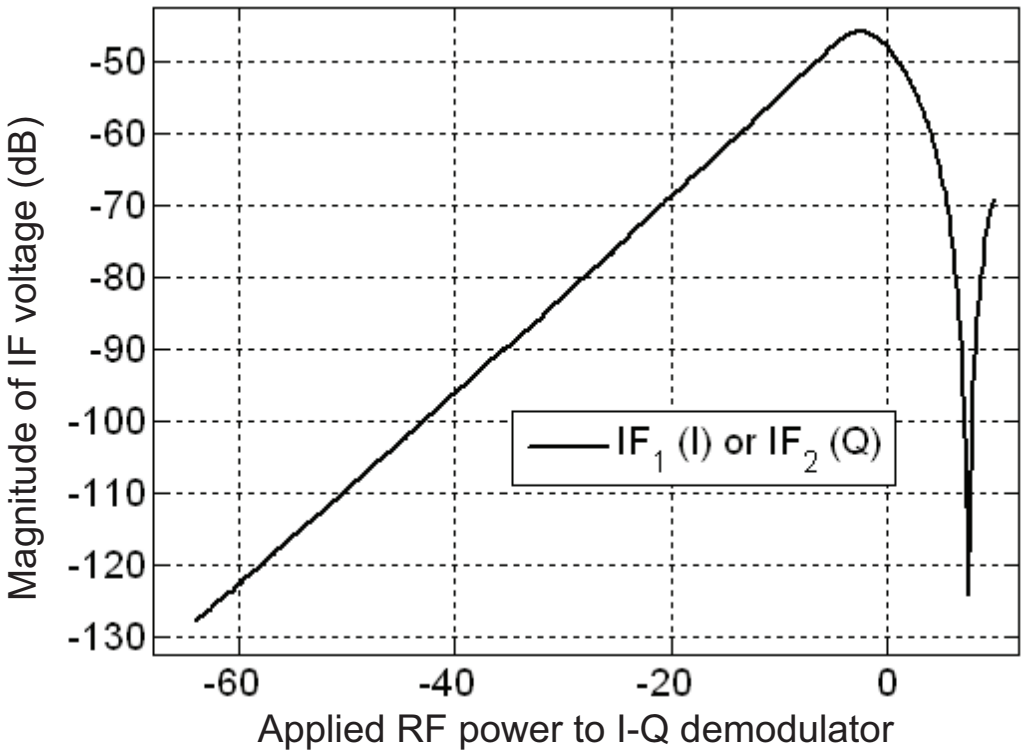

Figure 5.2 Effect of high power on the performance of the I-Q demodulator.

results (see Figure 5.2) show saturation and compression in the mixers when the received power is higher than -3 dBm. Above this level, the measurement results will be distorted and will not be reliable.

In practice, the carrier is always much stronger than the sidebands in the modulated signal. Therefore, it can be predicted that the nonlinearity is directly related to the carrier power, not the sidebands [83]. Because the field information to be measured is not transmitted at the carrier frequency, carrier elimination will not perturb the result but it will prevent the receiver from operating in a nonlinear regime.

The presence of the carrier at the receiving stage, is mainly due to the poor impedance matching at the DUT's input port, low directivity of the coupler or circulator used (monostatic mode), and of course to scattering (structural and antenna

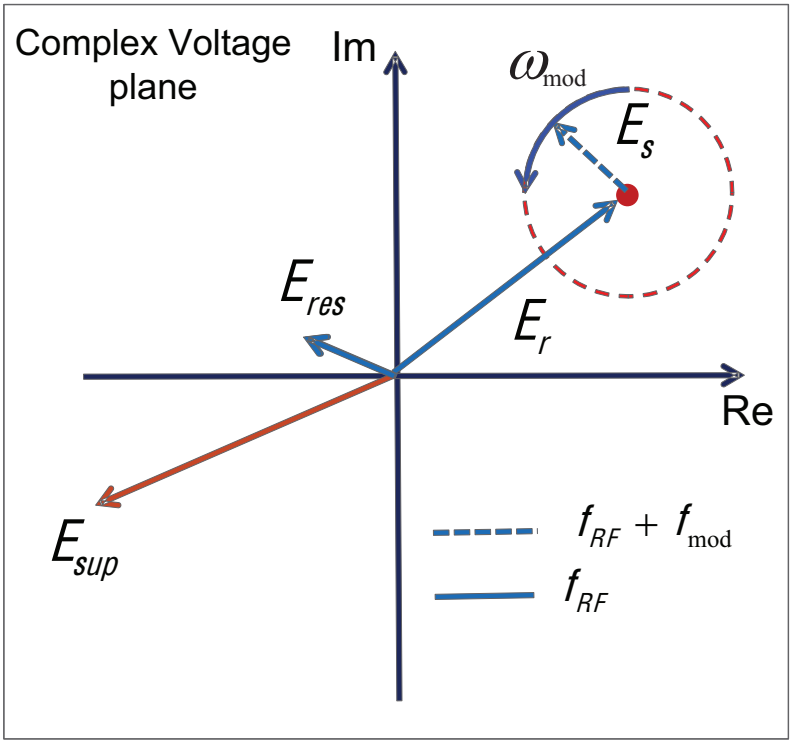

Figure 5.3 Illustration of vectorial carrier cancellation.

modes) of the near-field probe. In the bistatic mode, direct coupling between the transmitting and receiving antennas is seen as the major reason.

5.3 Phasor representation of the cancellation principle

Conceptually, the carrier signal (i.e., E_r) at the receiver can be suppressed completely if the magnitude and phase of a canceller signal (i.e., E_{sup}) are automatically set to have the same magnitude but be 180-degree out of phase [80]. Figure 5.3 illustrates a vectorial of the cancellation technique at the receiver. In this plot, the phasor representation of E_{sup} is fixed whereas the total voltage is the superposition of a fixed phasor E_r plus a time varying part E_s resulting from modulation. Superposition of the total voltage with E_{sup} leaves only the time-varying phasor E_s. In practice, it is

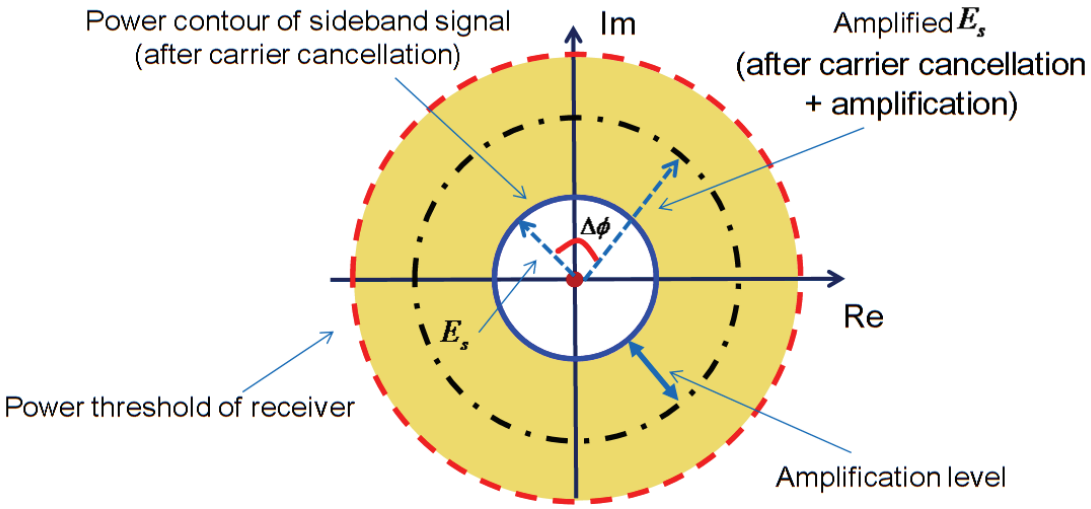

Figure 5.4 Advantages of carrier cancellation.

not possible to completely suppress the carrier signal at the receiver and a residual phasor E_{res} remains at the carrier frequency.

$$E_{res} = E_r + E_{sup} \tag{5.1}$$

5.4 Advantages of carrier cancellation

Once the carrier is suppressed at the receiving stage (i.e., $E_{res} = E_r + E_{sup} \approx 0$), the sideband signal (i.e., E_s in Figure 5.4) can be amplified in order to achieve a larger dynamic range. Figure 5.4 shows the amplification potential provided by a carrier canceller (see black line). This amplification limit is up to the tolerable power level the receiver is able to handle (Section 5.2), as shown in Figure 5.4 by the broken line. In Figure 5.4, $\Delta\phi$ represents the amount of phase shift applied due to transfer function of the amplifier (see section 5.6.4) used to boost I and Q signals after carrier cancellation.

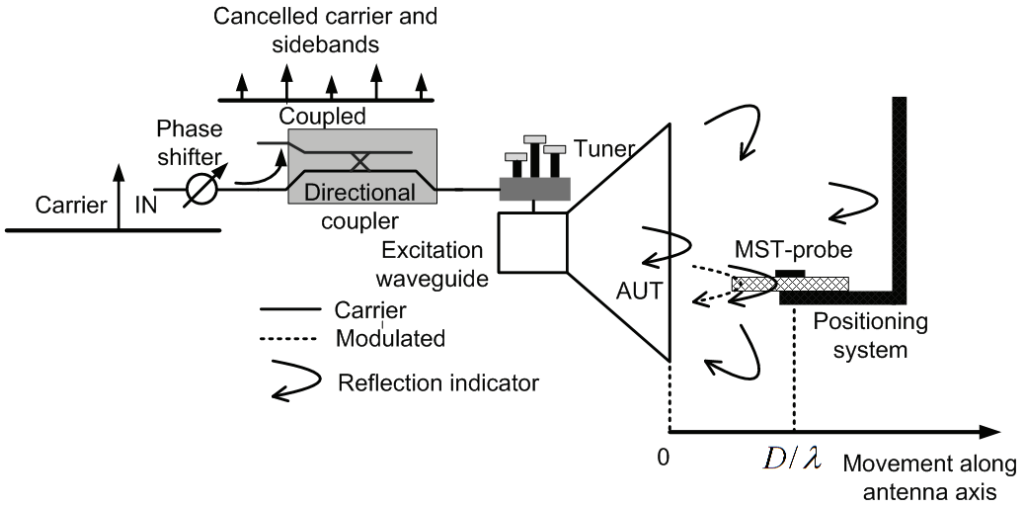

Figure 5.5 Schematic of the manual carrier cancellation.

5.5 Cancellation methods

5.5.1 Manual approach

As a first trial to suppress the carrier from the modulated signal, a microwave tuner was added before the antenna under test (AUT) terminal as illustrated in Figure 5.5. The tuner was set up by holding the OMS probe as close as possible to the AUT (this corresponds to position 0 in Figure 5.6) with the *coupled* output connected to a spectrum analyzer.

The manual tuner was adjusted until the carrier power was as low as possible. The tuner adjusts the AUT reflections so that they become 180 degrees out-of-phase with the canceller signals at the input of demodulator terminal. The parts of the setup contributing to field reflections are shown in Figure 5.5.

It is clear that the sidebands are only slightly attenuated by the tuner. As shown in Figure 5.6 for the probe in position 0, manual tuning can reduce the carrier power from -6 dBm to -64 dBm, whereas the level of the sidebands remains close to - 45 dBm. The settings are sensitive to probe displacement. Even for slight translations,

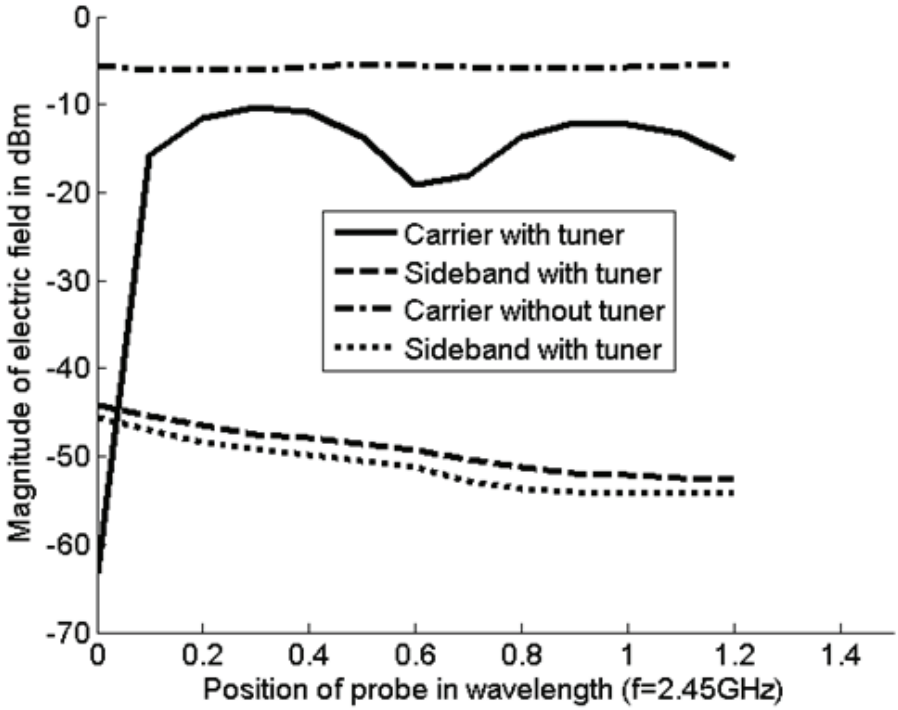

Figure 5.6 The results of manual carrier cancellation.

the carrier cancellation never returns to the level observed at the initial position. This increase comes from changes in reflections from the positioning system, probe, etc. By moving the probe further away from the initial position, the carrier power oscillates with a period of approximately $\lambda/2$. The abrupt change, especially after the first movement, may move the receiver to a nonlinear operating zone and distortion on the measurement is expected as a consequence.

The constellation curve of the demodulator was also measured by adding a variable phase shift at the receiving port. The measurement is performed for three different conditions, namely where the probe is at its initial position (closest distance from AUT), moved 5 cm (i.e., $\sim 0.4\lambda$) and moved 10 cm (i.e., $\sim 0.81\lambda$) away to reduce the signal strength. The results are compared to a reference circle (bullets) shown in Figure 5.7. The first measurement at D=0 cm (D: Displacement) is in good agreement with the reference but other curves at $D = 0.4\lambda$ and $D = 0.81\lambda$ become increasingly distorted because of severe gain and phase imbalances. This phenomenon is highlighting from another perspective the benefit of carrier cancellation. Of course,

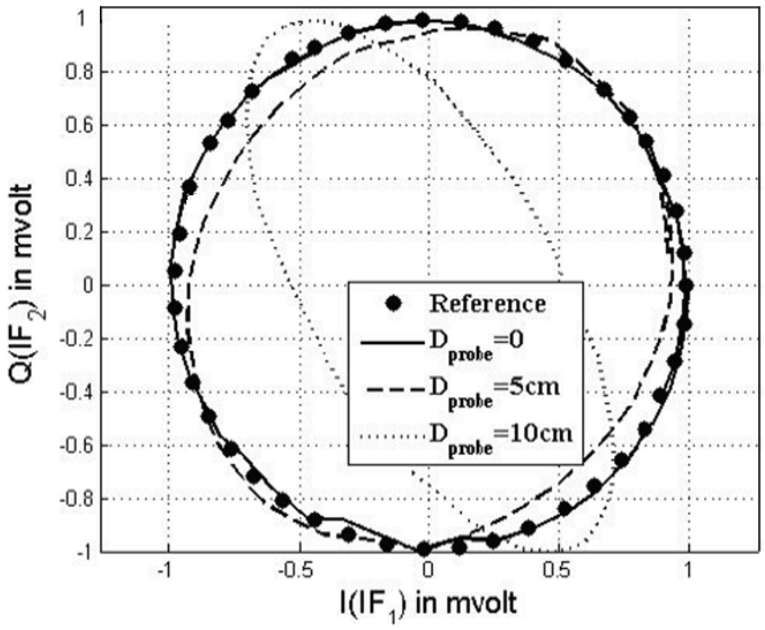

Figure 5.7 Constellation curve of the demodulator for different locations of the OMS probe.

using a fixed tuner can only cancel carrier reflections from static components and as Figure 5.7 illustrates, there is a need to adaptively cancel the carrier as the NF probe is moved in the vicinity of the DUT.

5.5.2 Automated carrier suppression

The system has to be able to adjust the magnitude and phase of the canceller signal to suppress or at least minimize the carrier under the permitted level in which the imager operates in a linear zone [84, 85].

5.6 Carrier cancellation implementation

In the canceller system, the canceller signal should be in anti-phase with and have the same magnitude as the carrier signal from the AUT. Figure 5.8 shows the proposed

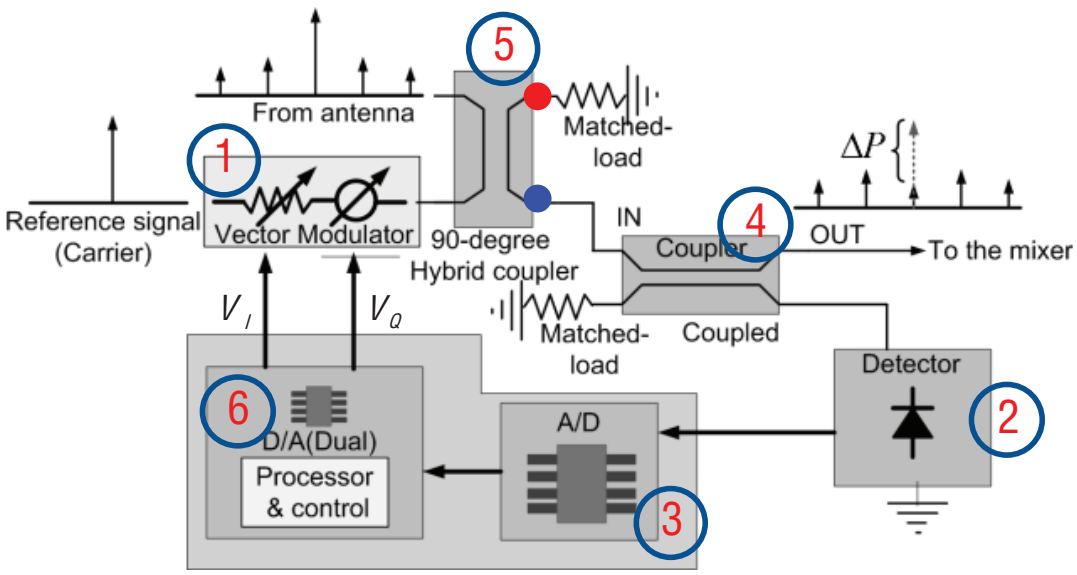

Figure 5.8 Schematic of automated carrier cancellation system.

cancellation circuit consists of six essential parts: an RF vector modulator (part #1), a power detector (part #2), A/D and D/A converters (part #3), a coupler (part#4), a 90- or 180-degree hybrid coupler (part #5), and microprocessor (part #6). In this section the role of each part will be discussed individually and then important practical considerations in the implementation of the canceller will be addressed.

The canceller operates as follows. The composite signal from the AUT comprising the reflected carrier and the induced sideband is fed to the hybrid coupler (top left port on the figure). Another pure signal, i.e. CW at the carrier frequency, whose phase and magnitude can be controlled by the vector modulator is fed to the hybrid coupler (lower port of the left side). The output signal at the two other ports of the coupler are respectively proportional to the sum and difference of these two inputs. The signal at the different port (indentified with a blue circle) is fed to coupler (#4). If the carrier is effectively cancelled, the total power measured at the power detector connected to the coupled port should be minimum, and in this case the carrier frequency's signal should be absent, or at least highly attenuated at the direct output port of this coupler. The output of this coupler is therefore highly suitable

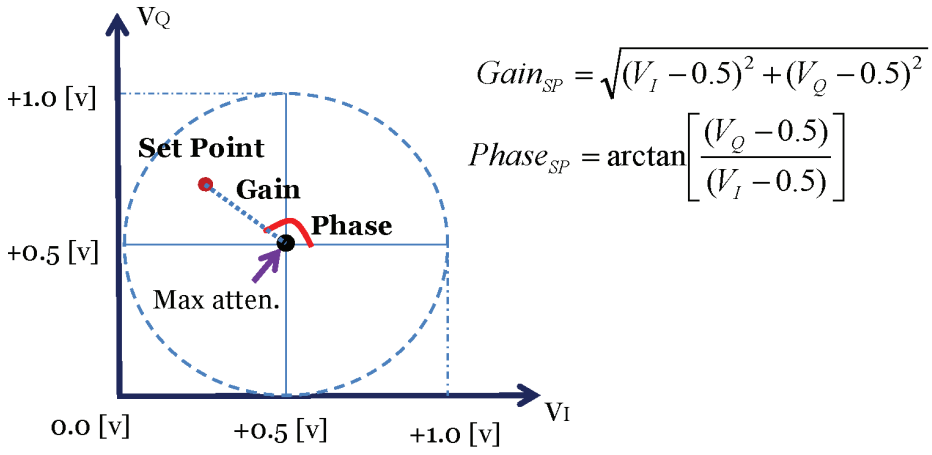

Figure 5.9 Principle of an RF vector modulator (part #1).

for detection and it is then fed to the receiver's input port. The role of the controller is therefore to constantly monitor the power level on the detector diode and then adaptivley modify the magnitude and phase settings of the RF vector modulator so that the power measured by the diode is minimized.

5.6.1 RF vector modulator

The vector modulator controls the magnitude and phase of the CW carrier signal. This is accomplished by varying two control signals V_I and V_Q. The equations governing the attenuation rate and phase change (i.e. Set Point (SP)) of the output signal are given in Figure 5.9.

The modulator used in the canceller is based on AD8341 chip manufactured by Analog Devices®. The control ranges are of 30 dB in magnitude and 360-degree in phase shift to the RF signal. This modulator can handle the RF signal when the power is lower than 8 dBm. A photograph of the modulator is shown in Figure 5.10. The output stage incorporates a differential output and in order to convert it to a singled-ended output, a balun (i.e., 3W525) manufactured by Anaren was used (see Figure 5.10) with a insertion-loss less than 0.38 dB. The modulator is constructed on the RT/Duroid6006 substrate with a permittivity of 6.15 and $tan\delta$ of 0.0014.

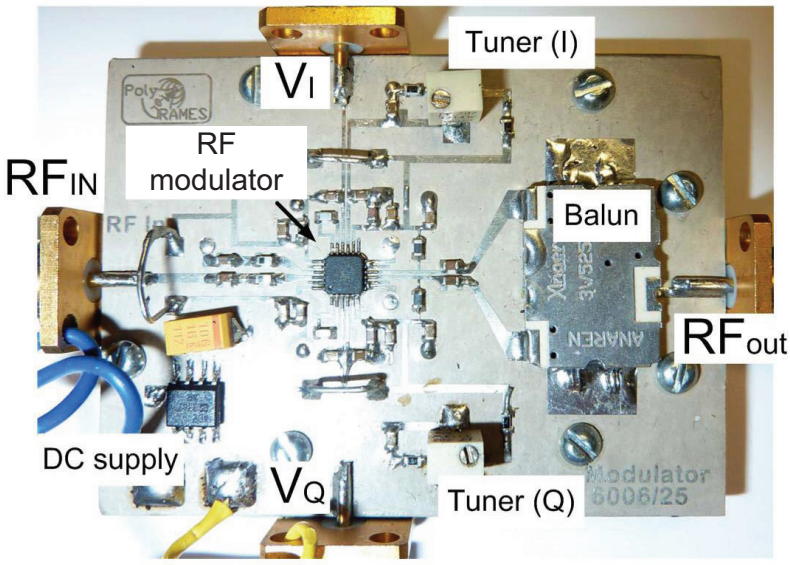

Figure 5.10 Photograph of an RF modulator.

Precaution for cancellation of low power carrier

Suppressing the carrier signal coming from antenna when its power level is 30 dB lower than the power of the LO (i.e., reference signal) signal fed to the RF modulator needs considering some precautions. In such circumstance, the RF modulator tries to reduce the magnitude of the LO signal (E_{sup}) to make it as small as the carrier signal E_r, but due to its limited dynamic range (30 dB) it is not capable of suppressing the carrier completely.

Investigation on the RF modulator showed that achieving a larger dynamic range, up to 65 dB, is possible if it is tuned properly and very fine voltage steps are used for the control signals (V_I and V_Q). In practice, the control signals are applied to the modulator using two 8-bit D/A converters. So, the signal steps may not be fine enough to force the RF detector to apply higher attenuation. Figure 5.11 shows the control signals grid and the position of maximum attenuation (i.e., red dot). In order to tune the RF modulator to achieve the highest possible range of attenuation, we need to shift the control signal grid so that one point of the grid falls on the red dot. In practice, two potentiometers (see Tuner (I) and Tuner (Q) shown in Figure 5.10)

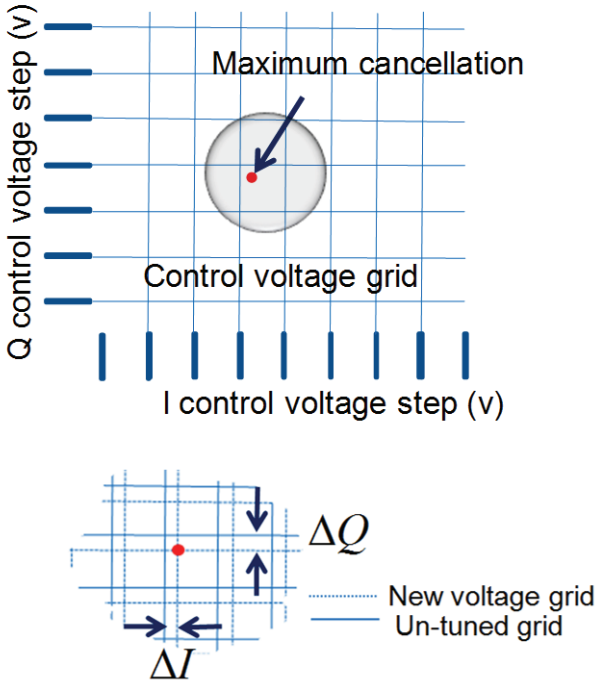

Figure 5.11 Tuning the control signals V_I and V_Q, voltage grid of the RF modulator to achieve higher range of attenuation.

were added to the RF modulator to vary the reference voltage slightly about 0.5 volt indicated in Figure 5.11. As a consequence, the modulator can operate within a larger dynamic range. It also allows the carrier cancellation circuit to operate with lower power level.

5.6.2 Power detector

A power detector (part#2) manufactured by Hittite Co. was used in the canceller to detect the output power level of the second coupler, as illustrated in Figure 5.8. It has a wide dynamic range for RF detection, from +2 dBm to -70 dBm, with nearly linear characteristics. The detector is non-reflective with a return-loss better than -10 dB. Figure 5.12 shows a photograph of the implemented detector fabricated on the same substrate used for the modulator (RT/Duroid6006 with ε_r= 6.15 and $tan\delta$ of 0.0014).

Characterizing the detector over a range of 90 dB shows that it nearly has an output slope of $\sim 25mv/dB$ over ~70 dB dynamic range when the input signal varies

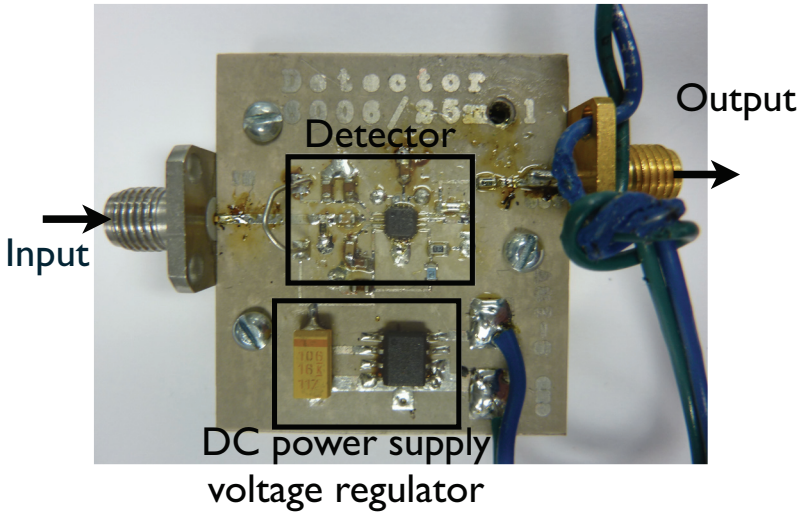

Figure 5.12 Photograph of the RF detector used in the carrier cancellation circuit.

between -70 dBm to 2 dBm (Figure 5.13). The detector's input/output characteristics reveals also two saturations, a first one when the input power reaches the lower detection limit (i.e., -75 dBm) and another one at 5 dBm. Beyond these limits the detector does not return a correct voltage value corresponding to the input power. In addition, the input impedance of the detector remains nearly constant over a large range of input power. Figure 5.14 shows the input impedance of the detector over a range of 80 dB. These results also demonstrate that the input impedance changes are considerable only when the input power reaches the upper limit.

5.6.3 Digital controlled board

A control board fabricated in-house and equipped with an 8-bit dual D/A an A/D converters and a microcontroller (ATMEGA8535L-8PU) is used to to apply V_I and V_Q values computed by a minimization algorithm (see Section 5.7) to the vector modulator. A photograph of the implemented control board is shown in Figure 5.15.

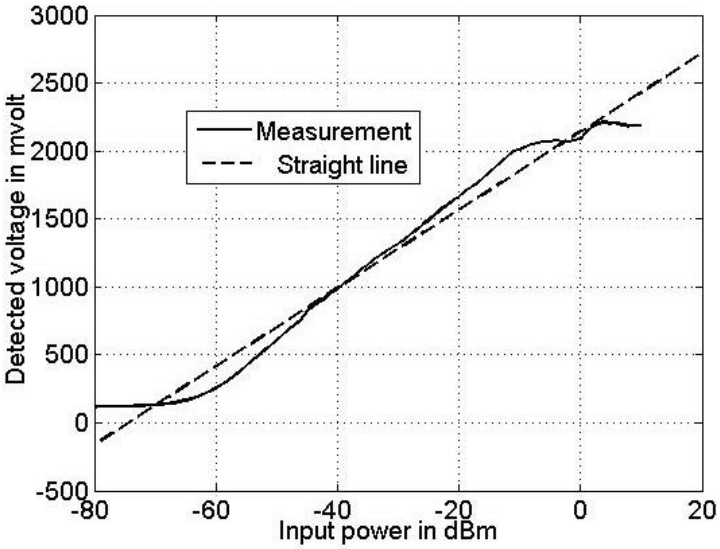

Figure 5.13 Power detector characteristic curve: detected voltage [mVolt] versus input power (dBm).

5.6.4 Power amplifier

In order to boost the I and Q signals after the carrier cancellation circuit, a power amplifier (i.e., SZM-2166Z) manufactured by Sirenza Microwaves, was used. The photograph of this power amplifier mounted on a bonded heat sink is shown in Figure 5.16. It is able to generate $>$ 2W (33.01 dBm) of RF power within the frequency range of 2.4–2.5 GHz. It also shows 37 dB gain at the same frequency band which is quite high. The position of this part in the NF imager will be shown later.

5.7 Minimization algorithm

There are many minimization algorithms that can be used to calculate a pair of V_I and V_Q control signals such as conjugate gradient and simulated annealing, which are very efficient and need limited iteration to converge. However, sophisticated programs are required for their implementation. Here, the minimization is done by sweeping the control signals individually when the other one is kept unchanged. At

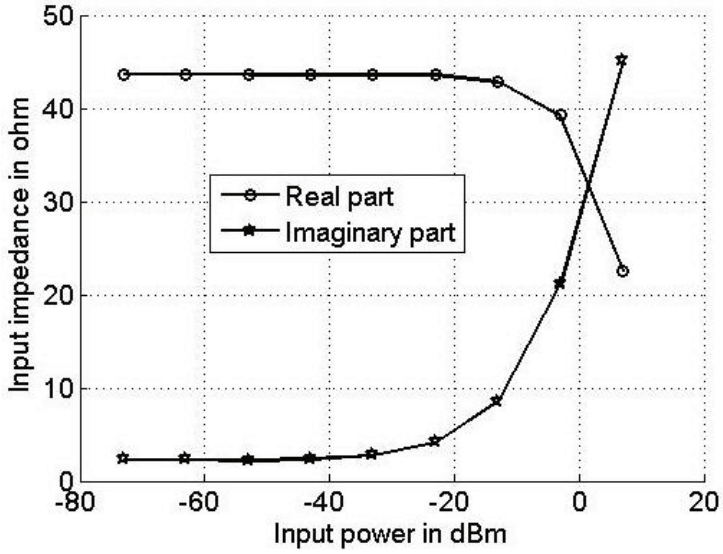

Figure 5.14 Input impedance of the detector versus input power level.

each iteration, the voltage step size of the control signals is reduced. This process is repeated until the power level (corresponding to the carrier) is below a desired threshold (cancellation level).

The minimization algorithm was implemented using a microprocessor manufactured by ATMEL®. A built-in A/D in the microprocessor structure digitizes the DC voltage on the RF detector. After the calculation of control signals levels is done, the microprocessor sends them to a dual external D/A to be converted to analog signals and applied to the modulator. Figure 5.17 shows the procedure used for minimization. In this flowchart, V_D and $V_{Threshold}$ are respectively the output of the power detector and its minimum acceptable value, under which it is assumed that the carrier has been effectivley cancelled.

5.8 Cancellation performance test

Before using the canceller in the NF imager, we tried to cancel the carrier manually by finding proper settings for the V_I and V_Q pair. For this test, V_I and V_Q inputs of the vector modulator were driven by external DC power supplies instead of the

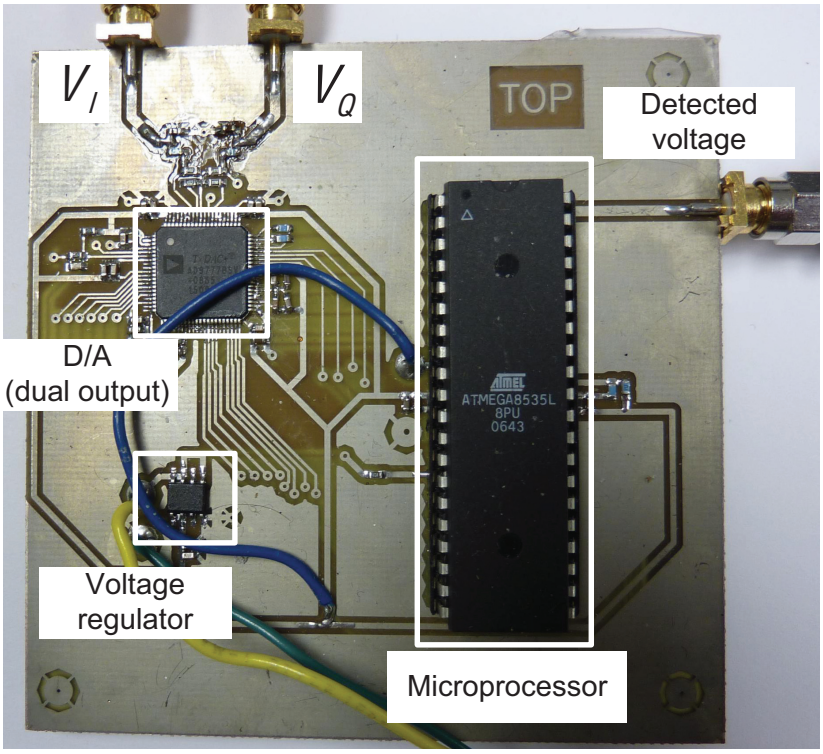

Figure 5.15 Photograph of the digital control board used in the carrier cancellation circuit.

microprocessor. The procedure simply consisted in minimizing the output carrier power on a spectrum analyzer by iteratively adjusting the power supply knobs manually. The result is shown in Figure 5.18. The manual setting could achieve only 12 dB of cancellation because of low-precision control voltages, which indicates that the cancellation level strongly depends on the resolution of the controlled V_I and V_Q signals.

5.9 Carrier canceller stability

It is crucial in the imager to ensure that the cancellation process itself, including delays, sampling and digitization, has no destructive effect on the fields to be measured. In order to investigate these effects, an OMS probe was set at fixed points,

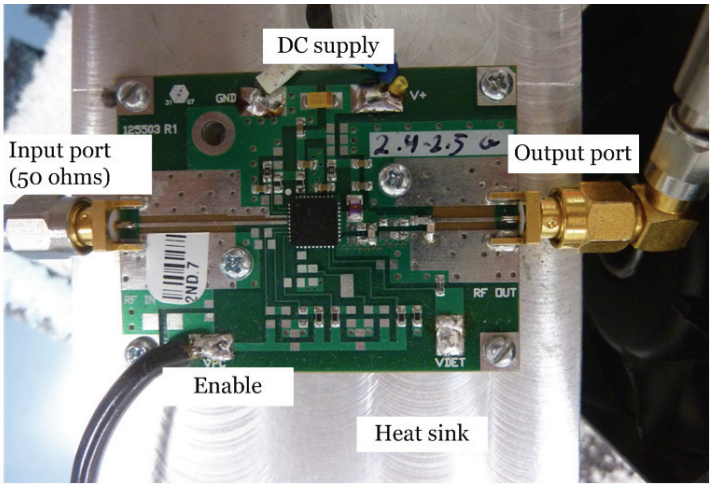

Figure 5.16 Photograph of the power amplifier used in the NF imager.

very close to a DUT where a strong field concentration is present. Then, the setup started measuring fields for several points over a period of time. Ideally, it is expected to get a constant magnitude and phase as the probe is in a stationary position. In practice, however, it is not possible due to many parameters such as components' response time, delays, frequency instability and possibly other factors. Figure 5.19 shows a variation of less than 0.1 dB and 1.5 degree for the magnitude and phase of the sidebands after cancellation, respectively.

We also show in Figure 5.20a a modulated signal with its carrier and sideband power levels of about -14 dBm and -56 dBm, respectively. Figure 5.20b the same spectrum after the signal has passed the proposed carrier cancellation system. It can be seen that the carrier level has been reduced by 64 dB, whereas the sidebands have decreased to 4 dB, which is essentially due to insertion loss in the two coupler and transmission lines. This measurements were performed using an spectrum analyzer to which the signal is fed via a 10-dB coupler. Therefore, the actual levels of the signals demonstrated in the figure is 10 dB higher.

5.10 Measurement performance assessment

Before investigating the measurement accuracy of the NF imager when it is equipped with the carrier canceller circuit, it should be assured that adding the canceller ef-

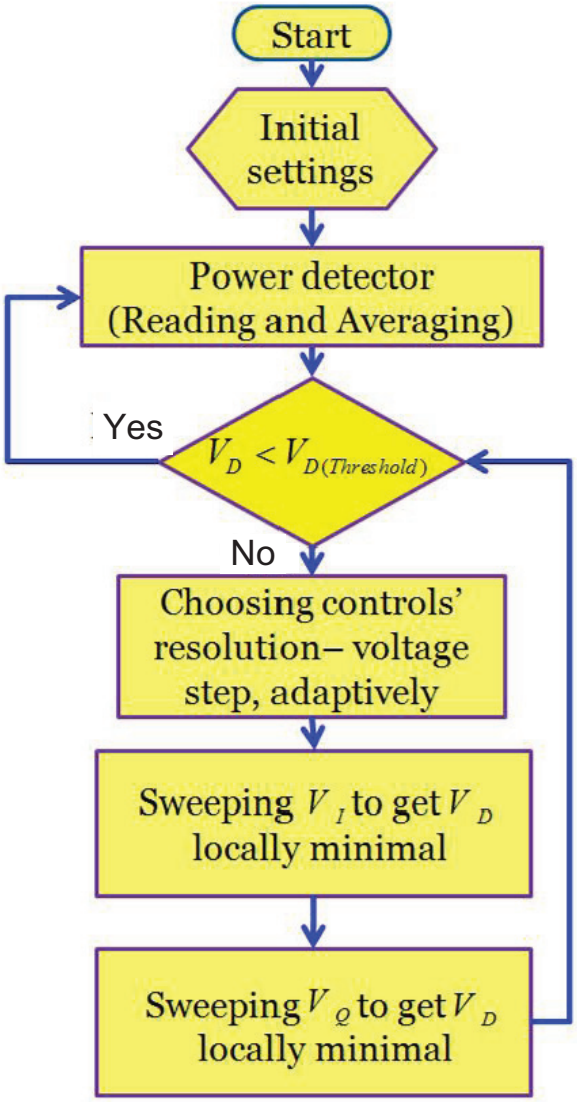

Figure 5.17 Minimization flowchart

fectively improves linearity and dynamic range in the receiver. To do this, the setup shown in Figure 5.21 was used in which the carrier canceller circuit was added before the I-Q demodulator equivalent circuit. By varying the phase shifter setting shown in the same figure between 0– 360° and reading the I and Q signals on the LIA amplifier, the constellation curve of the proposed I-Q demodulator incorporating the carrier canceller circuit was obtained (see Figure 5.22), when the input power level

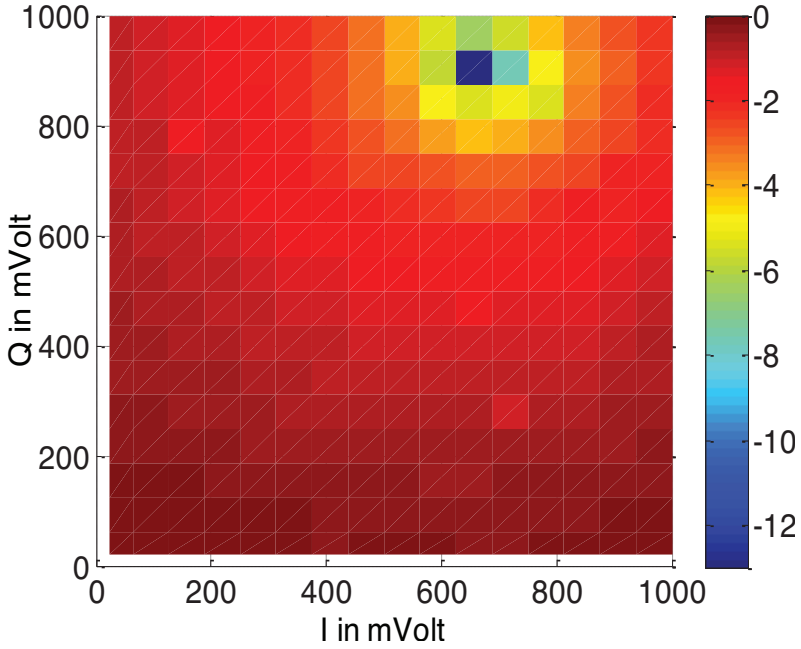

Figure 5.18 Power of the carrier signal at the output of the canceller measured using a spectrum analyzer at 2.45 GHz when V_I and V_Q are adjusted manually. The results are normalized and shown in dB.

in the AUT was about 36 dBm and the OMS probe was located very close the AUT in order that the sidebands level became as strong as carrier after cancellation. The results including both measured and reference curves are in very good agreement.

The performance of carrier cancellation was investigated by comparing the NF field distribution of a 50 Ω CPW transmission line with and without the canceller. Figure 5.23 shows the schematic of the NF imager equipped with the carrier cancellation circuit. Here, a the CPW was considered as a DUT and the OMS probe was set to measure the transverse E-field (E_x).

In this experiment, RF power is fed to the CPW (DUT) line terminated with a short circuit. The reason for using short circuit termination is to generate strong reflection of the carrier. The wave propagating in the transmission line is received by the OMS probe, which is scanned over the CPW. The imager was set to operate in the monostatic scheme. A first measurement was performed with the received signal, comprising the carrier and the sidebands, fed directly to mixer stage. In this case, the carrier power was about 5.56 dBm which is beyond the power limit of the

mixer as shown Figure 5.2. The measured E-field distribution in this case is show in Figure 5.24. The high power carrier causes the receiver to operate within its nonlinear region. Consequently, the measured fields distribution are distorted. After performing the carrier cancellation, the same measurement was repeated and the results are demonstrated in Figure 5.24, where no distortion is seen (i.e., without cancellation). We also repeated the same measurement after adding the power amplifier discussed in Section 5.6.4. The measurement results show a 5 dB improvement of the dynamic range when no amplification is used in conjunction with the canceller. When the amplifier is added the dynamic range enhancement reaches 18 dB.

The measurement results of the transmission line were also compared to simulations. Figure 5.25 demonstrates both the magnitude and phase of the fields 3 mm above the line on a linear scan in a direction perpendicular to the line. As discussed in Chapter 3, the simulation results were corrected to take into account the effect of the probe's current distribution. The agreement between simulations and measurements is excellent.

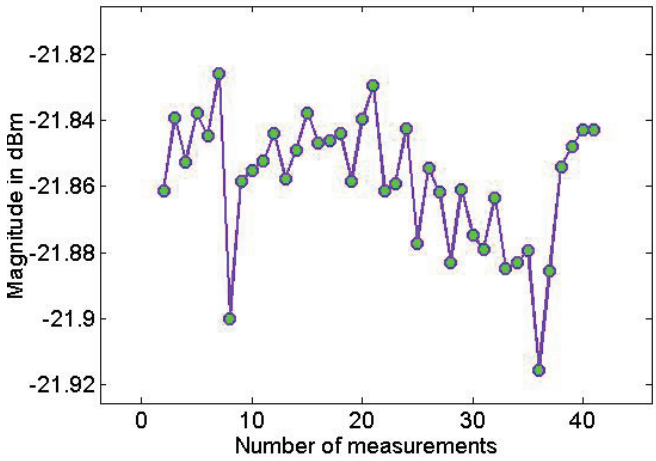

(a)

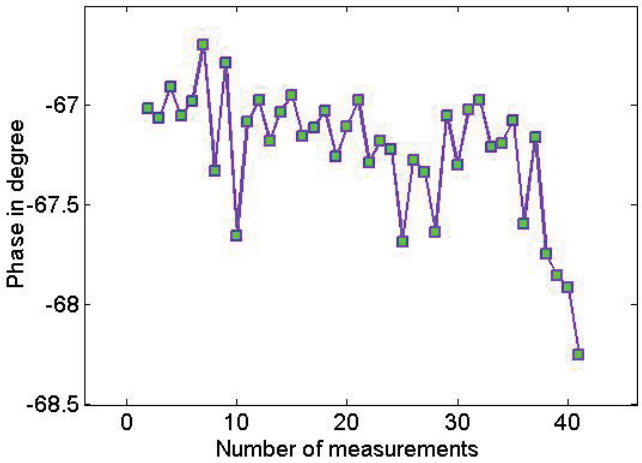

(b)

Figure 5.19 Stability of the carrier canceller; (a) magnitude and (b) phase.

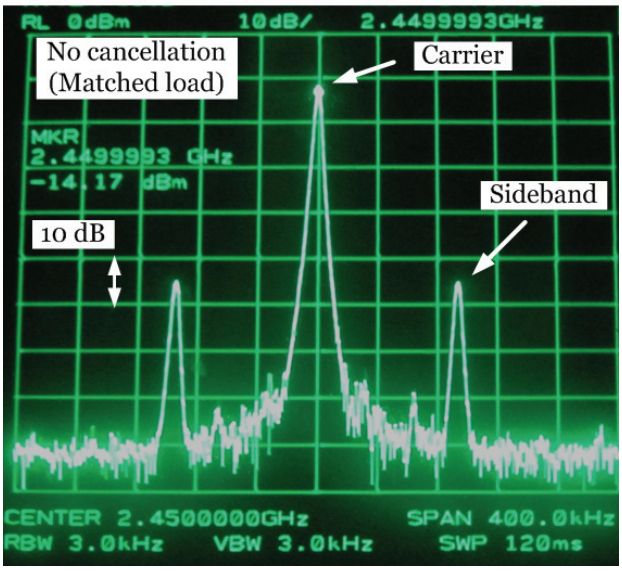

(a)

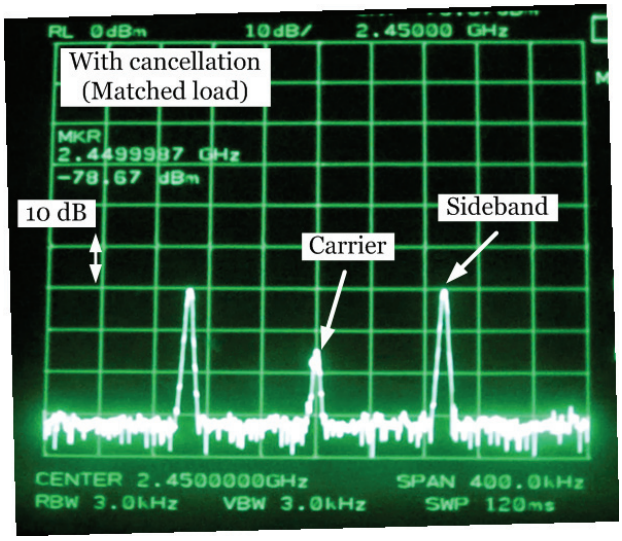

(b)

Figure 5.20 Two screen snapshots from the display of a spectrum analyzer before and after passing through the carrier cancellation circuit.

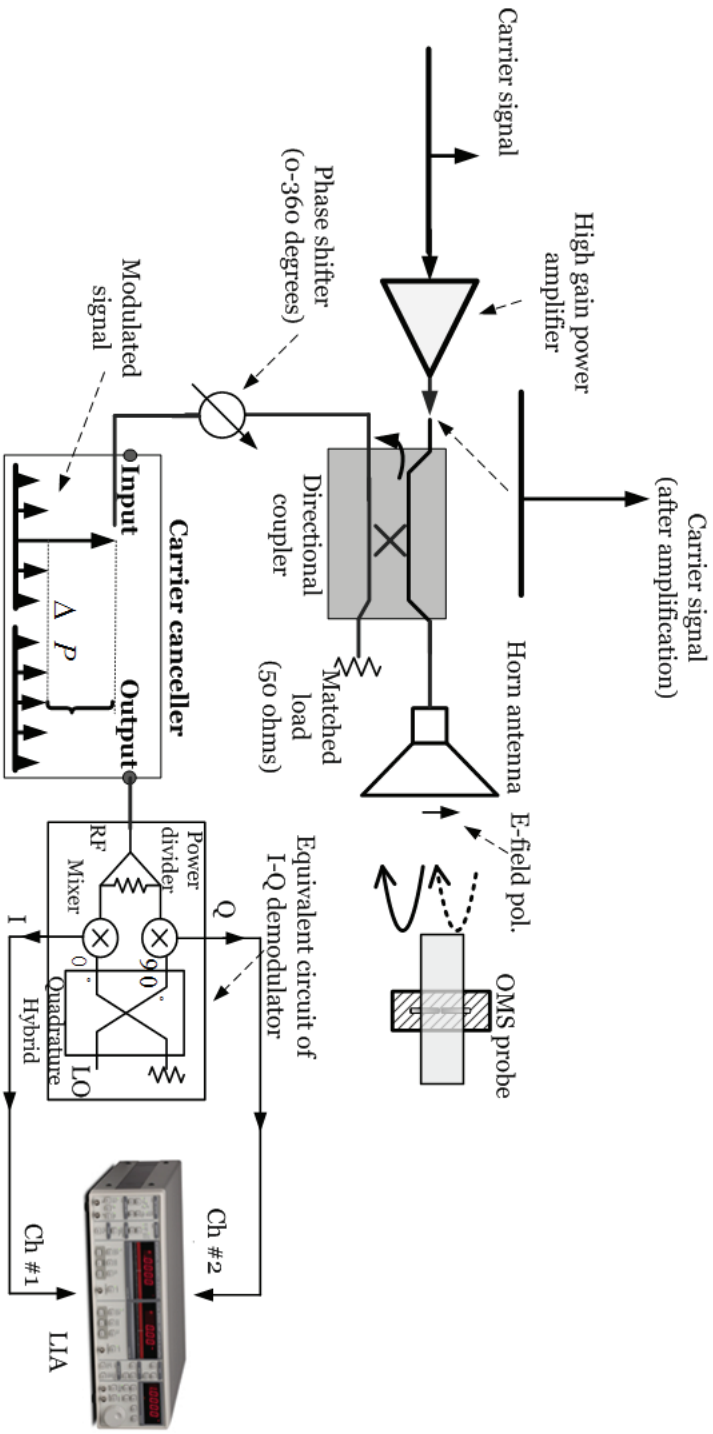

Figure 5.21 The schematic of the setup used to derive the constellation curve of the proposed I-Q demoduator.

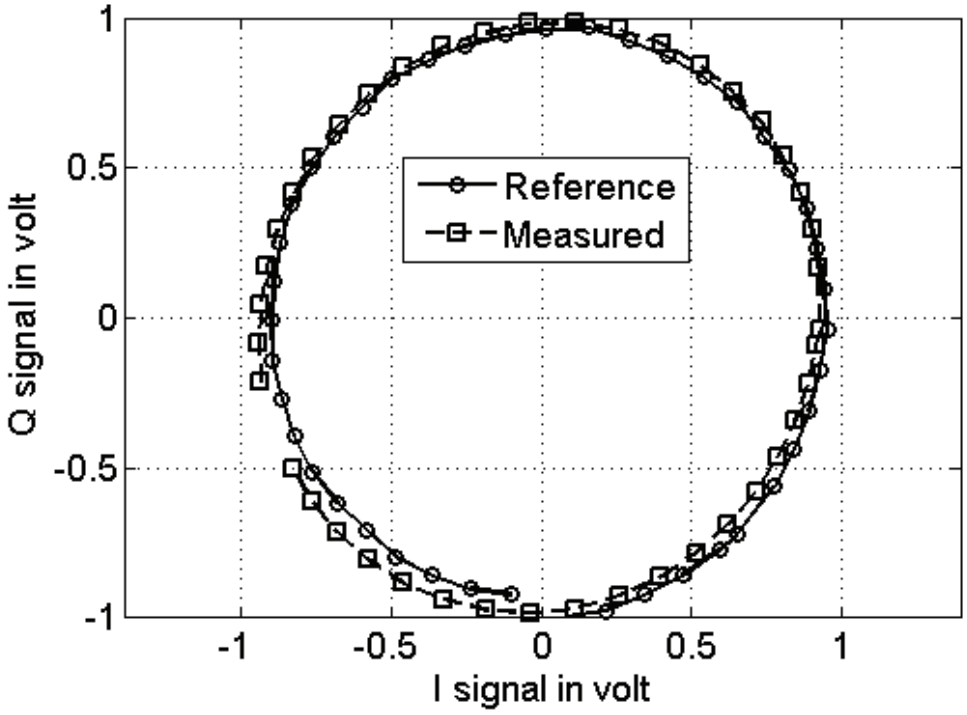

Figure 5.22 Constellation curve of the proposed I-Q demodulator obtained after carrier cancellation.

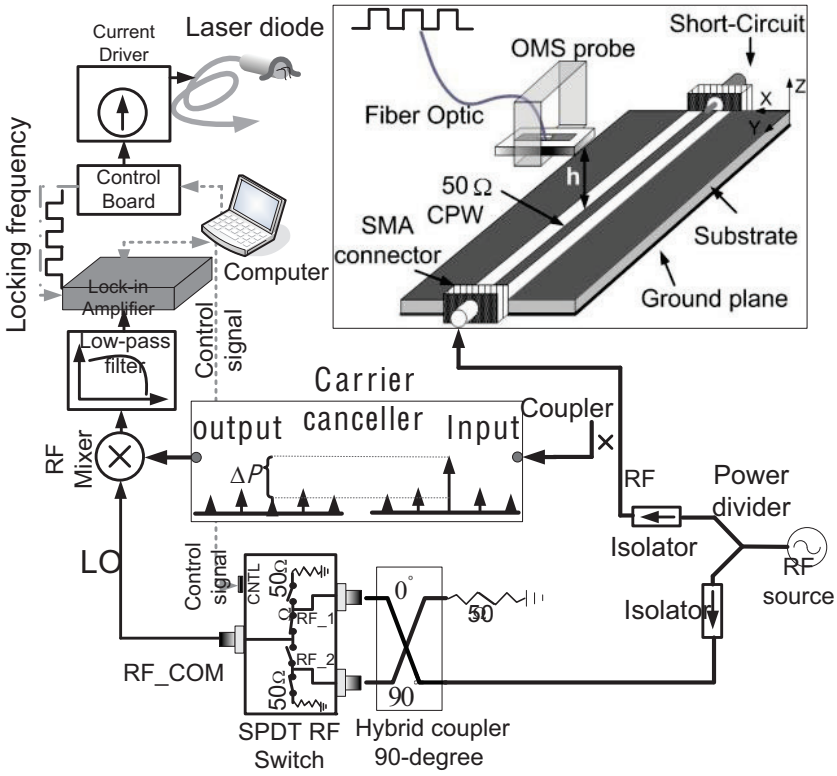

Figure 5.23 Schematic of the setup equipped with a carrier cancellation circuit.

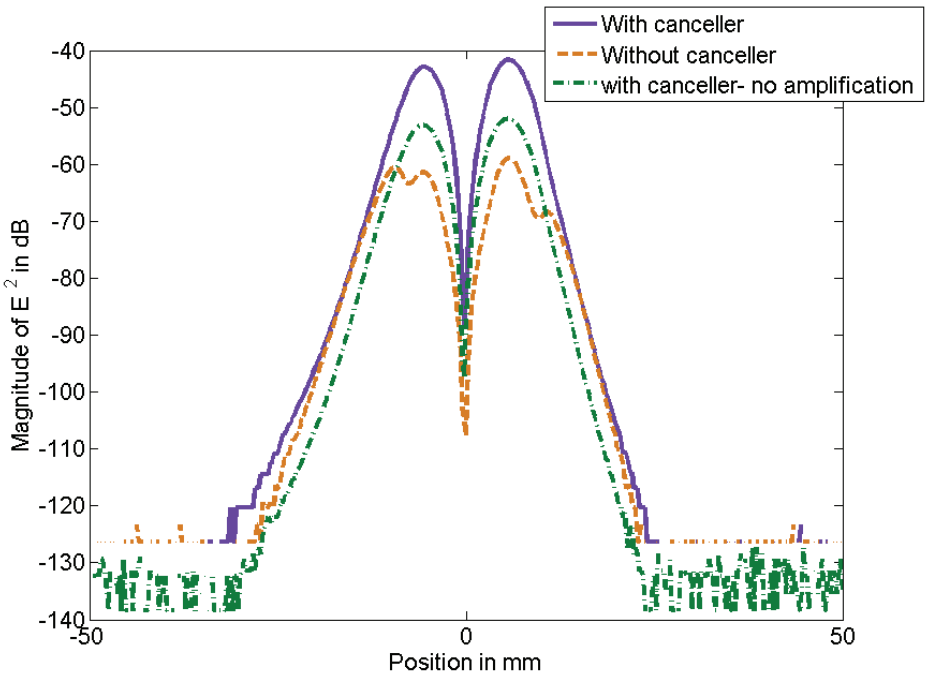

Figure 5.24 The result showing the effect of a high power carrier level at the receiver.

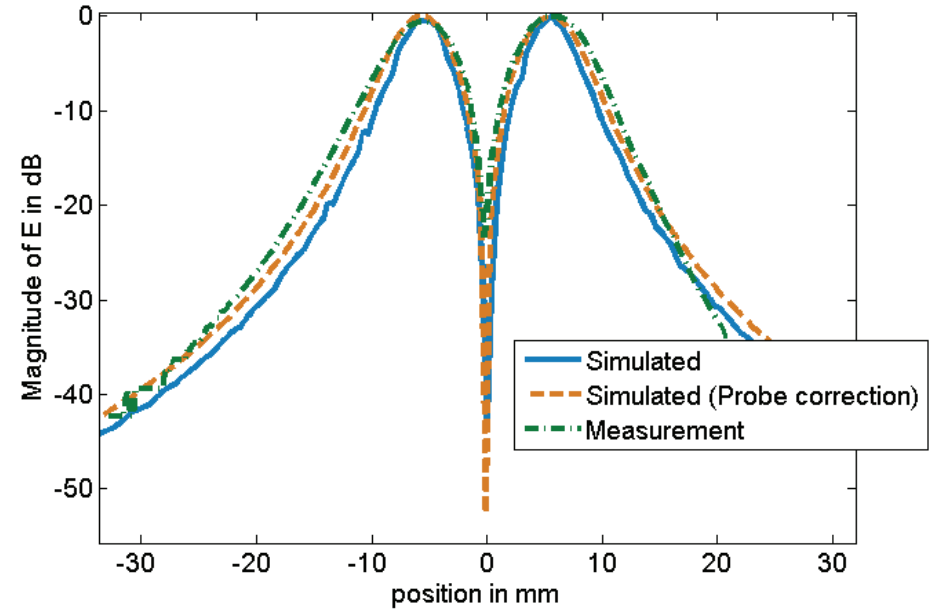

(a)

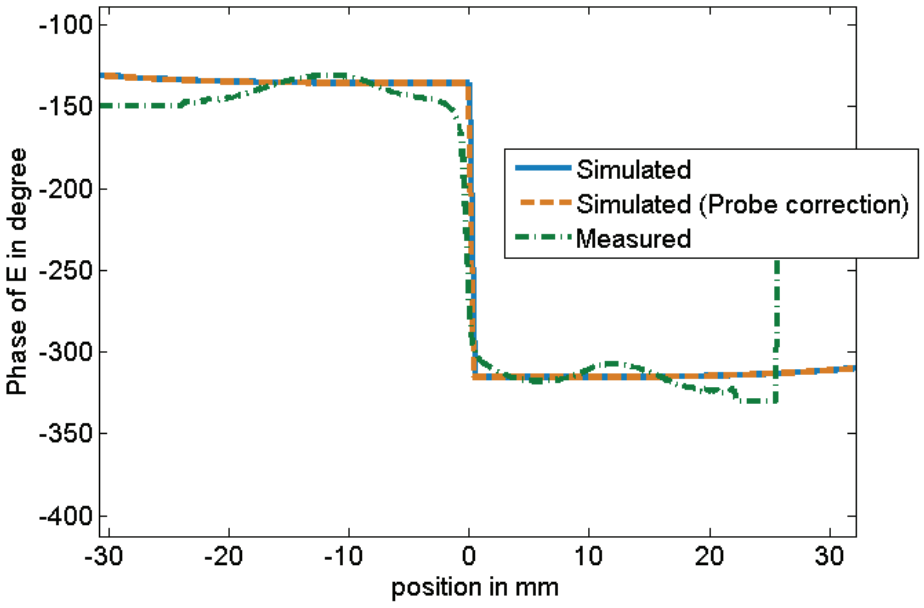

(b)

Figure 5.25 Comparison of the measurement and simulation results.

5.11 High-dynamic range NF imager: Example of Application

Once the carrier canceller is ready and activated in the NF imager, the imager can be used to characterize microwave circuits, radiating devices, etc., in which accurate and wide dynamic range is required.

As an example, E-field distribution above a bandpass filter operating at 2.45 GHz was considered. The NF image was obtained in bistatic mode at a distance of 3 mm above the traces over a planar surface with dimensions of L_{scan}=5 cm by W_{scan}=6 cm. Figure 5.26 shows photograph of the filter under test. The filter was match-loaded during measurement.

In order to characterize the bandpass filter, a measurement was performed at 1.8 GHz, which is in the stop band of the filter. It should be noted that although the probe was designed to have optimal performance at 2.45 GHz, it is neverthreless possible to use it in a certain frequency band centered on this frequency. The results shown in Figure 5.27 includes both magnitude and phase of E_x. They confirm the cutoff operation of the filter at 1.8 GHz. The filter also was characterized at 2.45 GHz. In this case, the power is expected to propagate through the filter and reach the match-load. Figure 5.28 shows the field distribution above the filter at 2.45 GHz, confirming that the signal is in fact propagating to the output port. Phase measurement results are also shown in Figure 5.28. The achieved dynamic range in both results is ∼80 dB.

5.12 Conclusions

In this chapter, the benefit of implementing a technique to suppress the carrier is demonstrated. Cancellation in the adaptive circuit is performed by applying the proper phase and gain to a canceller signal so that has approximately the same magnitude but is 180 out-of-phase with the modulated signal. The performance of the canceller was investigated experimentally and discussed. The results indicate an improvement in the linear behavior of the NF imager and that an increase of 18 dB or more in the dynamic range is possible.

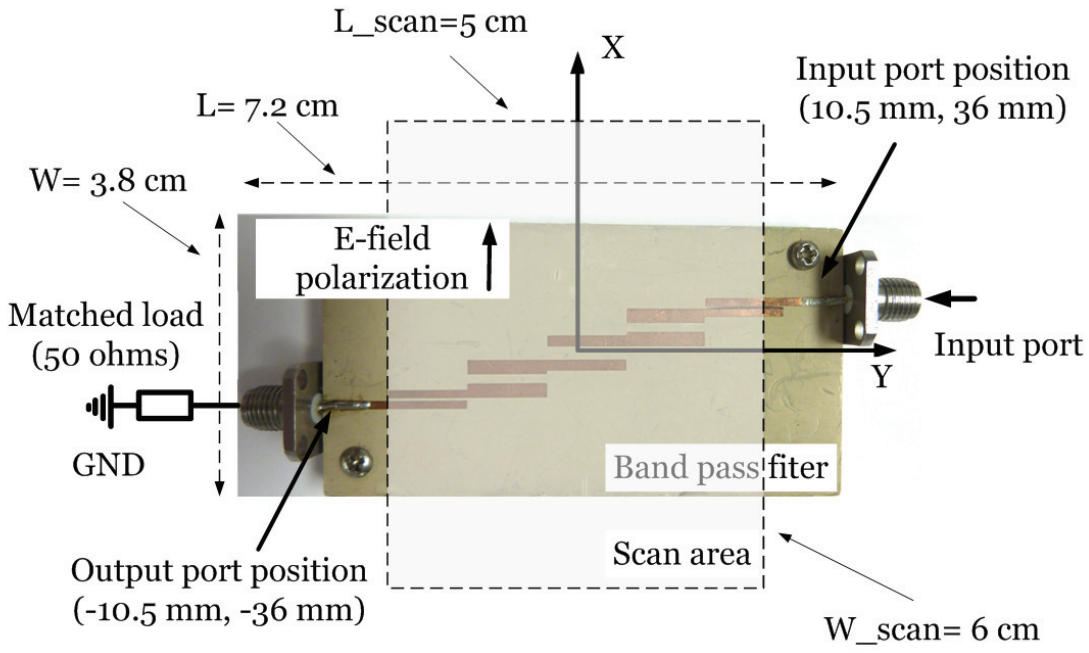

Figure 5.26 Photograph of the bandpass filter to be measured for transverse electric field distribution (E_x)

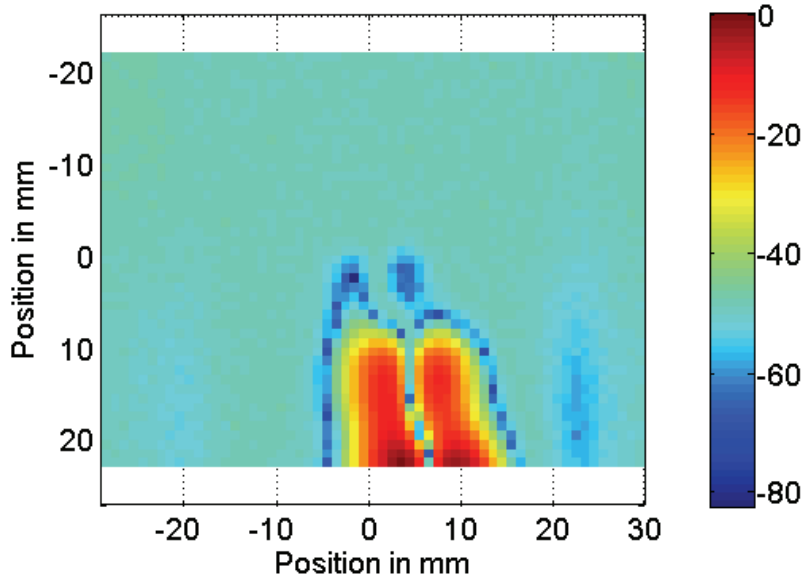

(a)

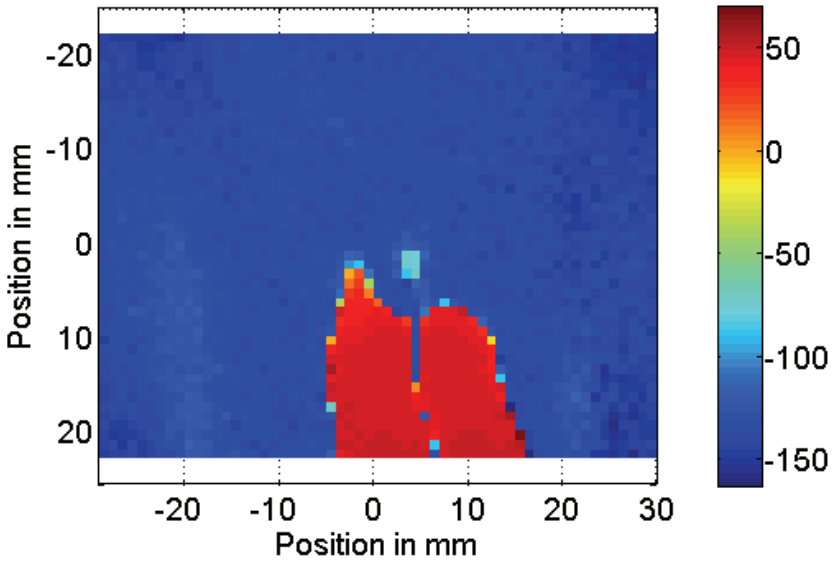

(b)

Figure 5.27 The measurement results of the transverse E-field above a bandpass filter at 1.8 GHz; (a) magnitude and (b) phase.

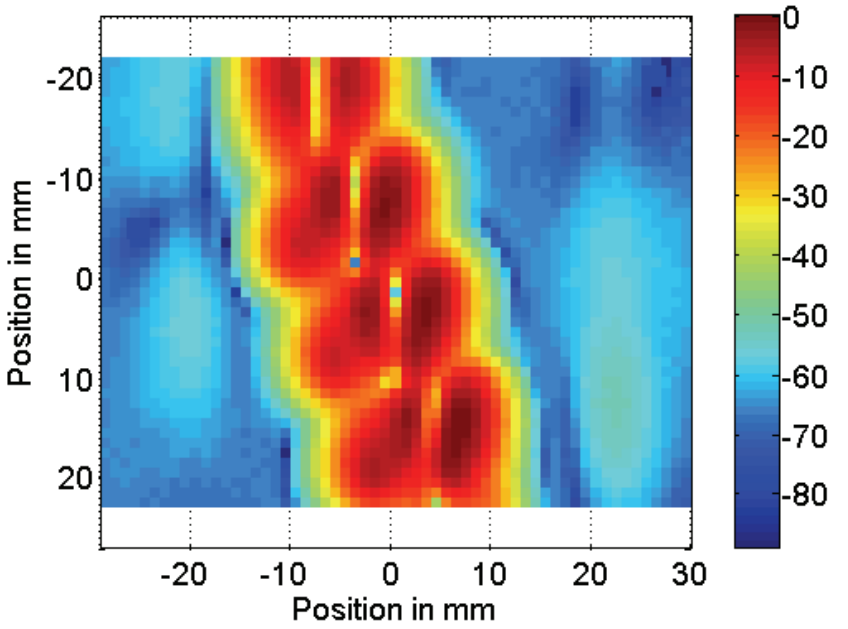

(a)

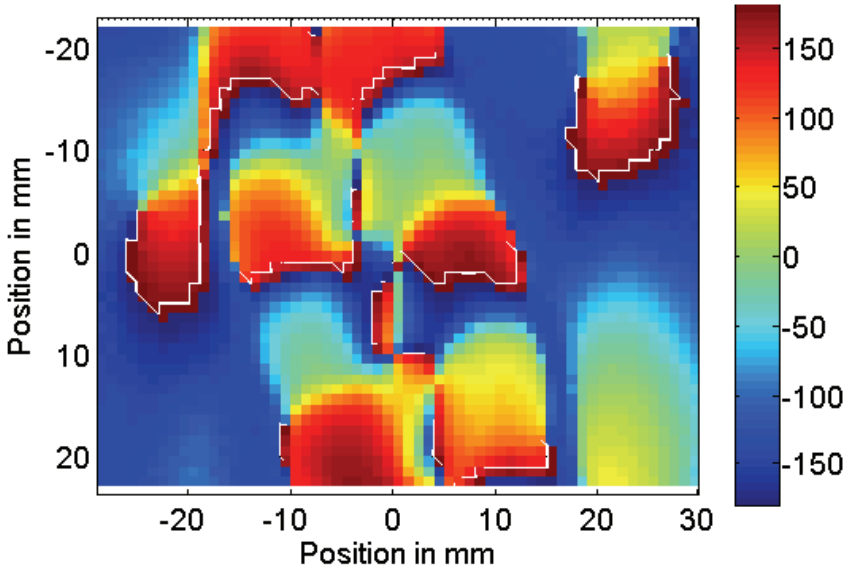

(b)

Figure 5.28 The measurement results of the transverse E-field above a bandpass filter at 2.45 GHz; (a) magnitude and (b) phase.

Chapter 6

Realization of a Microwave Imager Setup Suitable For Early Breast Cancer Detection

6.1 Setups for breast cancer detection

Examples of setups available for breast cancer detection are shown in Figure 6.1. These setups should meet all clinical conditions such as patient comfort and compatibility of the body under test (BUT) to some extent. Generally, they are categorized into two types as demonstrated in Figure 6.1. In the first type, the patient should lie down on her/his stomach and place her/his breast in hole [86]. The detector rotates on the periphery of the pendant breast [87], while in the other setups (Figure 6.1b), the breast is held between flat plates to eliminate any possible movement while X-ray image is taken. If we apply this compression setup in microwave imaging, it is conjectured that the reduced thickness of the breast will enhance the likelihood of tumour detection [88]. As well, knowing one of the dimensions (i.e., the separation between the plates) is useful *a priori* information in finding the solution to the inverse problem. Breast flattening also causes the BUT to take a uniform thickness. The setup of Figure 6.1b consists of three important parts: an illuminator, the breast holder (or matching plates) and a receiver. The illuminators differ depending on the method of detection (i.e., X-ray or microwave tomography). The type of receiver can vary and includes a sensitive film and RF sensors (antennas).

6.1.1 Microwave tomography

In microwave tomography (MT),"dielectric properties of the biological tissues are strong indictors of their functionalities and pathological characteristics" [89]. Prac-

(a)

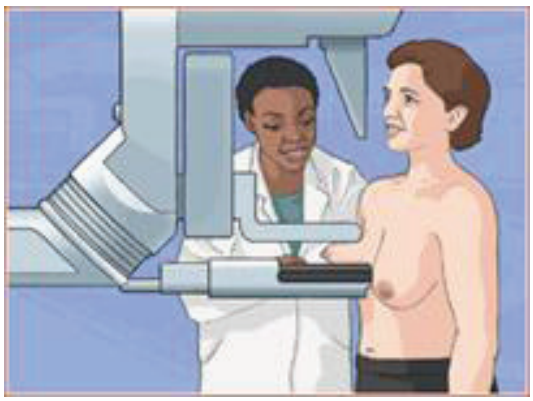

(b)

Figure 6.1 Breast cancer detection setups. (a) microwave tomographic setup (University of Bristol) and (b) X-ray imaging.

tically, in MT the BUT is illuminated with RF waves using a transmitting antenna (i.e., Tx) and the scattered fields by breast/tumour(s) are picked-up by the receiving (Rx) antennas [20]. Figure 6.2 illustrates a basic MT setup. The RF source is located beneath the planar breast holder (see Figure 6.2) or in some setups the illumination

is performed from the side.

A horn antenna could be used for illumination purposes in MT because of its unique characteristics such as medium radiation gain. Although, the horn antenna benefits from such characteristics, it generates a wide angle field distribution even very close to its aperture (near-field zone $\sim \lambda/4$). Due to this unlocalized radiation characteristic and the long wavelength compared to the typical size of an early tumour, it could be difficult to discriminate between two adjacent tumours that are localized close to one another. Consequently, the horn illumination may lead to a lower resolution of the reconstructed permittivity distribution.

Thus, it can be concluded that the Basic MT setups suffer from two problems: the low spatial resolution as well as reflections of the incident and scattered fields at the air/breast interface. In addition, scattering and reflection from the surrounding objects such as supports, actuators for mechanical movement and metallic transmission lines may have an effect on the signal to be measured and can easily degrade MT diagnostic performance.

To overcome the aforementioned disadvantages associated with the conventional setup, a new setup shown in Figure 6.3 is proposed. In this setup, the breast under test is compressed between two plates and illuminated from different angles by an array of Tx antennas located on the periphery of the breast [90]. Using an array of this kind will allow a great variability of illumination, which leads to better conditioning of the nonlinear inverse problem to be solved (i.e., permittivity and conductivity reconstruction [91]). In the proposed setup, the measuring part is the NF imager equipped with a linear array of OMS probes (its design and implementation were addressed in Chapter 4). Then, the NF imager is set to operate in bistatic mode; where the array scans the breast over the region of interest and scatterers the picked-up fields toward a receiving antenna.

6.2 Realization of a microwave tomography (MT) setup

In general, the setups used in microwave tomography, and breast cancer detection in particular, consist of a measurement setup and computerized algorithm to solve the associated inverse scattering problem using measured data. In the following sections,

the parts of the setup that are relevant to the scope of this thesis will be discussed.

6.2.1 Measurement approach

The measurement setup considering the ISM frequencies used (e.g., 915 MHz, 2.45 GHz and/or 5.8 GHz) can be set to measure the BUT at difference distances. Scanning the BUT can be done in the near-field or far-field of the BUT. The potential for more accurate measurements within the NF region than the FF zone is because of the following reasons: 1) NF zone is richer because of the presence of evanescent waves, 2) better signal to noise ratio (SNR). Therefore, MT within the NF region can be a leading approach to achieve"early breast cancer detection" [92]. Additionally, the setup in the NF will be more compact compared to the optimum wavelength than that of FF [93].

6.2.2 Phantom

In MT setups and before performing any imaging, it is necessary to investigate the accuracy of the results obtained from their measurement systems and the inverse scattering algorithms used. To do this, it is tried to model and implement an accurate and realistic artificial model of a healthy breast. The model needs to be robust enough to include versatile range of breasts in term of size and constitutive materials. In [94], extensive research has been done to determine the dielectric properties of a breast's internal organs which are mostly fat, muscle, and water. By using the information provided in this report and choosing equivalent materials to breast tissue in terms of permittivity and conductivity [95], colleague, Mr. Alvaro Diaz Bolado designed and implemented a physical model (i.e., phantom). The phantom is believed to present approximately the same RF characteristics of a healthy breast. Figure 6.3 demonstrates the phantom used in our research group.

The proposed phantom forms a dielectric waveguide incorporating dielectric material compressed between two Plexiglass plates, that supports even and odd modes within the filled-in dielectric. The illuminating part of the the phantom consists of two antennas that are excited in phase (even mode) and 180-degree out of phase (odd mode) (see Figure 6.3). In the even mode (i.e., TM_0 mode), the E field has a cosine distribution between the plates with the fields concentration happening more in the middle of the phantom than the top and bottom. Thus, this mode will be more effec-

tive in detecting tumours located in the middle of the phantom. As demonstrated in Figure 6.3, in odd mode (i.e., TM_1 mode) the illuminating antennas are out of phase and concentrate the incident fields close to the top and bottom of the phantom. In this case, the imaging system will be able to detect tumours in the vicinity of the plates (i.e., near breast skin).

6.2.3 Solution for inverse scattering problem

This part is beyond the scope of this thesis and will not discussed here. However, inverse scattering problems [86, 21] and the solutions were studied and programmed by Dr. Paul-André Barrière, my colleague in Poly-Grames Research Centre, during his Ph.D. program [96].

6.3 Results

In order to verify the measurement capability of the proposed setup consisting of an NF imager and a developed phantom, the imager was set to measure E fields scattered by the phantom over a region of interest, which is demonstrated in Figure 6.4. The phantom was filled by glycerin with a complex permittivity of $7.17 + j23.41$ at 2.45 GHz. In this experiment, the E-field distribution was measured twice over the phantom, first when a scatterer (air-filled cylinder with a diameter of 1 in) was inserted into the phantom at D_s=-50mm, where D_s is the distance of the cylinder from measurement origin, and then in the absence of the scatterer. In the first measurement the cylinder's axis was 0.7 in above the center of the phantom. The obtained results in both measurements, were then subtracted to obtain the scattered fields.

Figure 6.5 and Figure 6.6 show the magnitude and phase of the scattered fields in even and odd modes, respectively. In both modes, the scattered fields peak exactly at the position of the scatterer. The measurement results are in good agreement with a simulation using CST. The measurement results show the ability of the imager to measure the scattered field with dynamic range $\sim$ 30 dB.

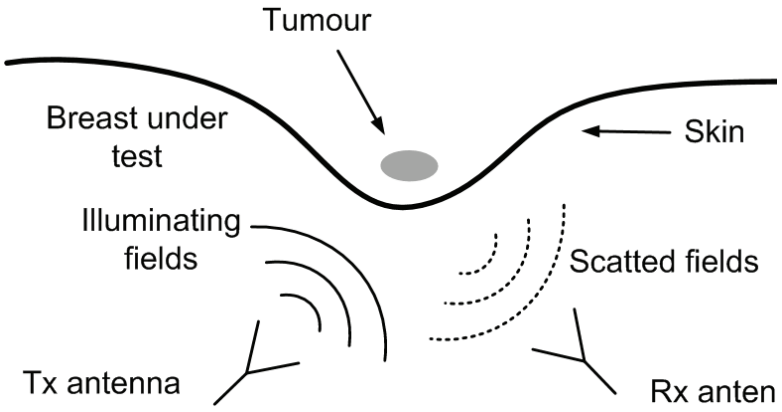

(a)

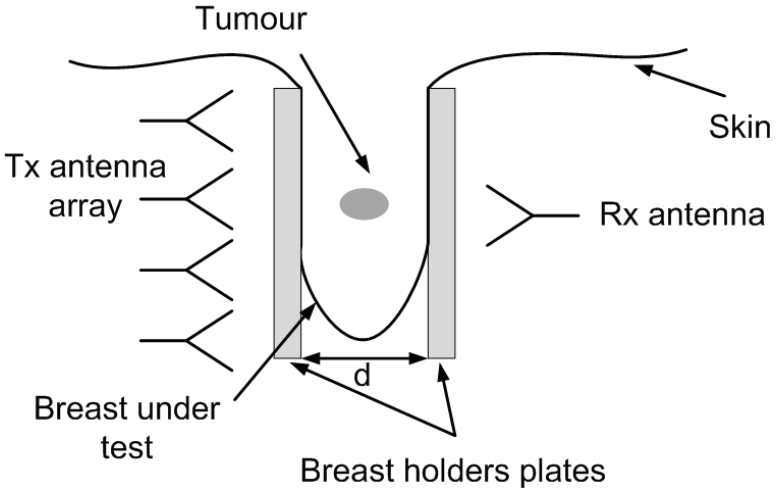

(b)

Figure 6.2 Basic breast microwave imaging setups. (a) pendant and (b) compressed breast under test.

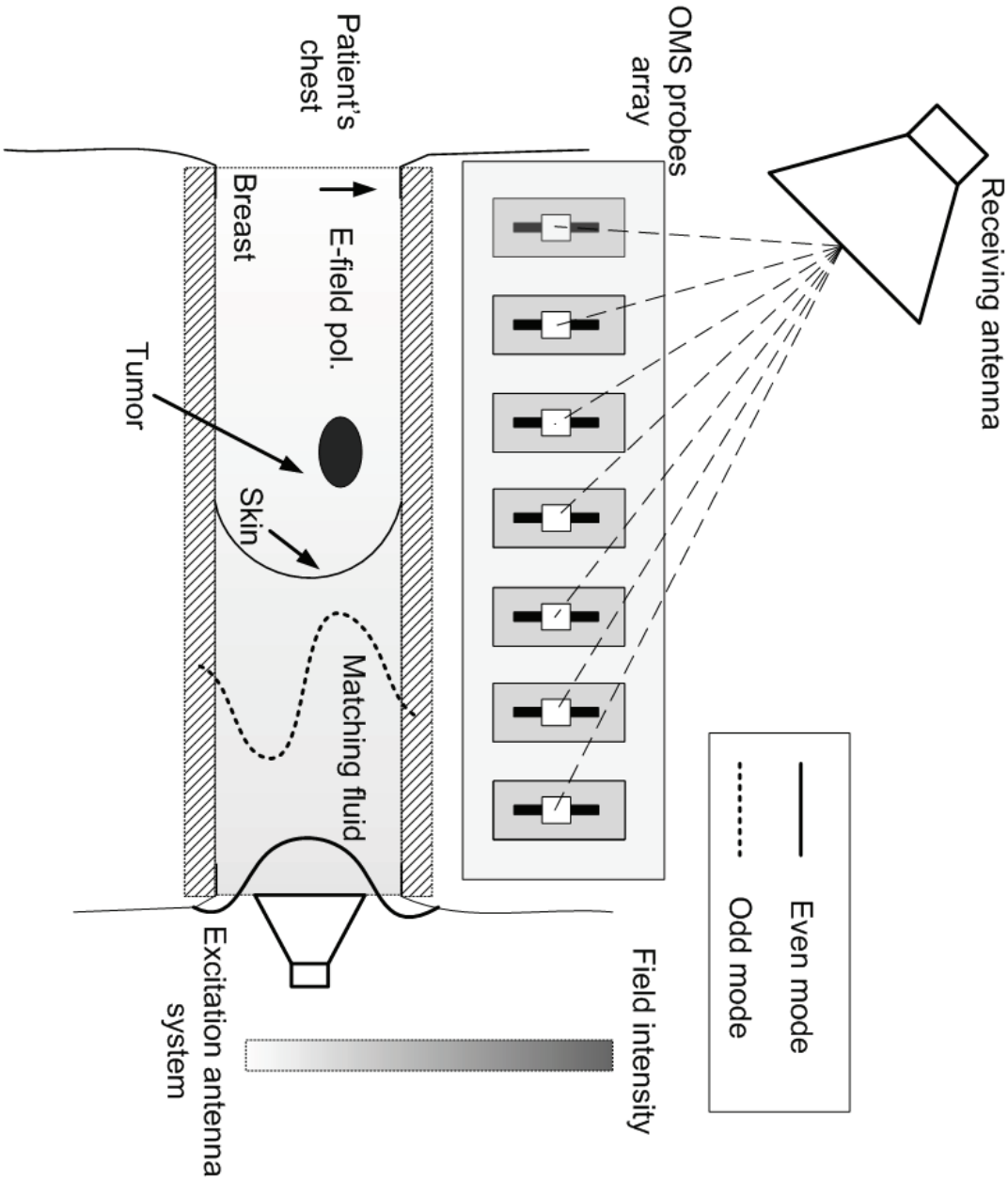

Figure 6.3 The schematic of the microwave tomography setup proposed for early breast cancer detection.

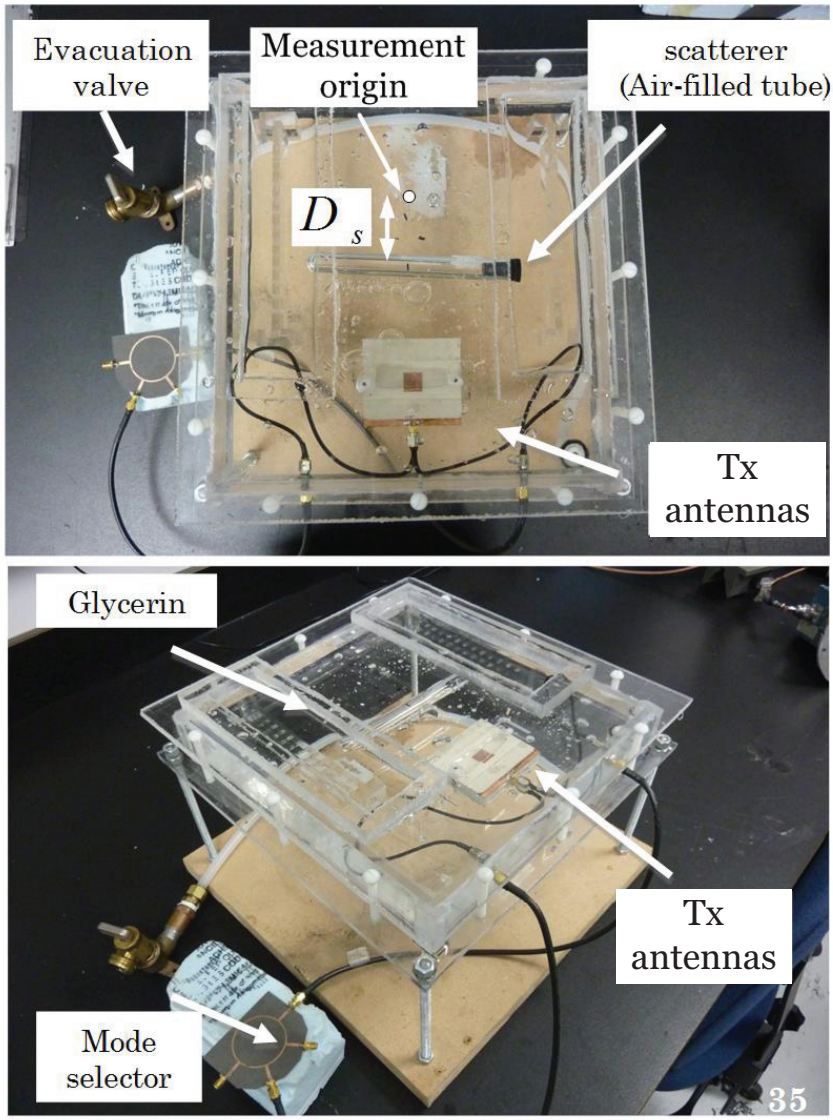

Figure 6.4 The photograph of the phantom used in this project, with courtesy from Mr. Alvaro Diaz Bolado.

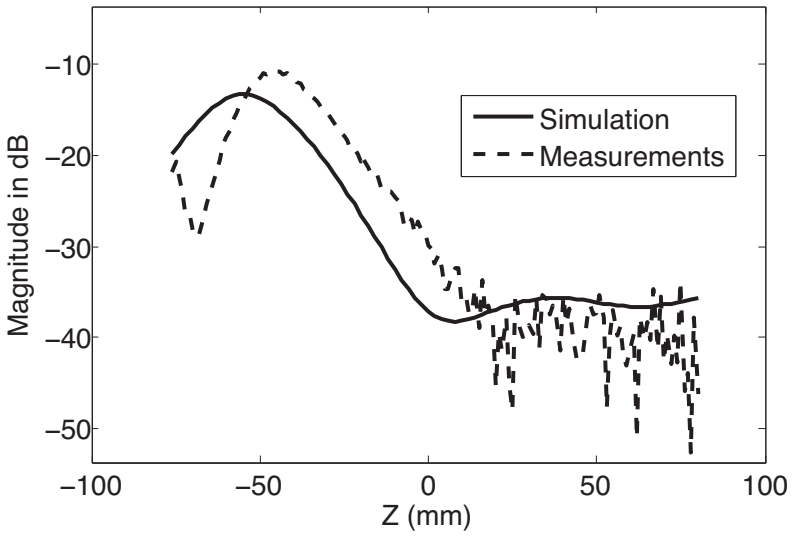

(a)

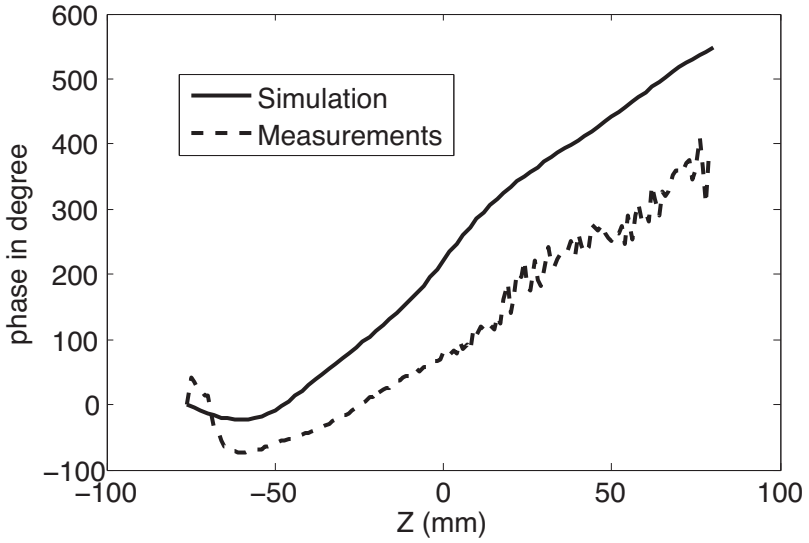

(b)

Figure 6.5 The scattered fields of an air-filled cylinder measured in even mode; (a) magnitude and (b) phase.

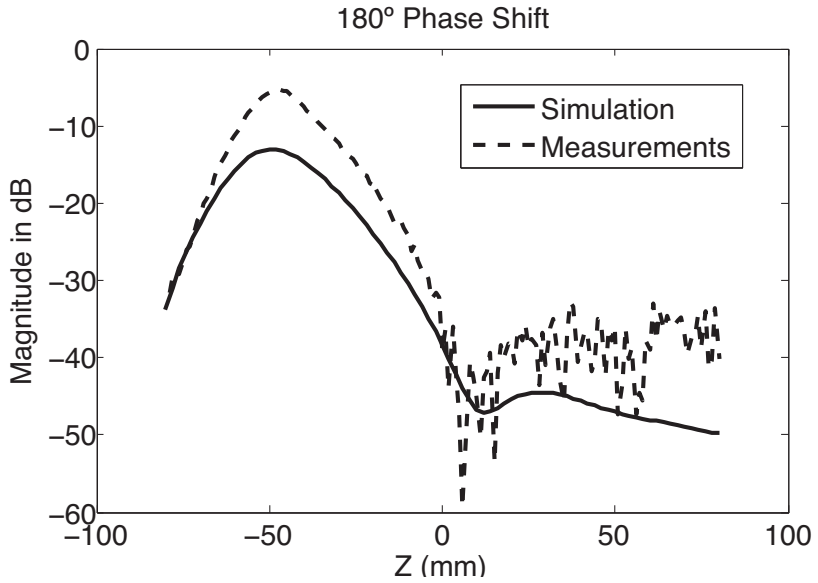

(a)

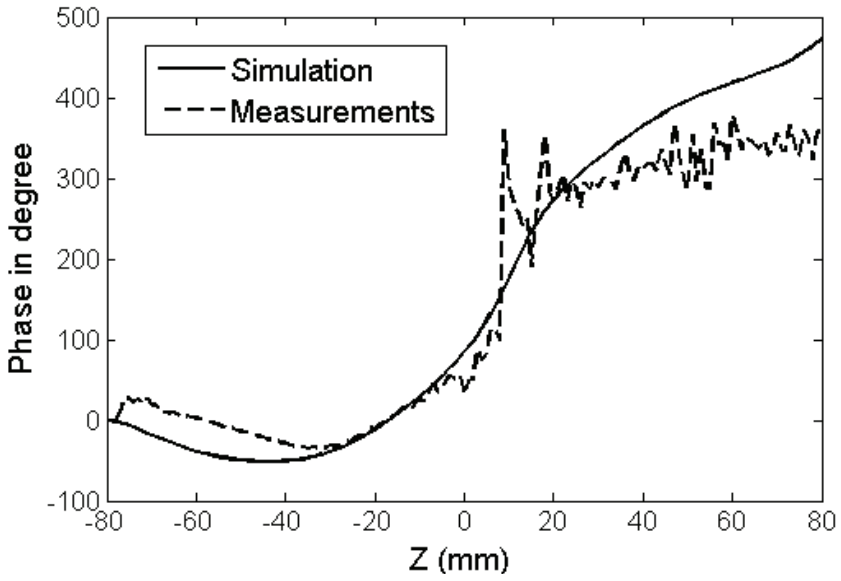

(b)

Figure 6.6 The scattered fields of an air-filled cylinder measured in odd mode; (a) magnitude and (b) phase.

Chapter 7

Conclusions and Future Work

Near-field (NF) measurement has gained the interest of many researchers because of its high resolution, accuracy, high signal-to-noise ratio (SNR) and wide range of applications. These applications include broad categories such as antenna [5], microwave [6] circuits and devices emission tests [7] as well as logic [8] circuits. The measurements can also be used to measure the wave penetration into materials [9, 10] and their RF characterization [43]. Microwave imaging for health monitoring [11, 97] is another impressive application of NF measurement [9, 89]. The many applications have therefore allowed researchers to focus on near-field measurements.

7.1 Contributions of this thesis

This thesis addressed and discussed the design and implementation of a NF imager based on the modulated scatterer technique (MST) extensively. The imager consists of several optically modulated scatterer (OMS) probes that are very accurate, highly sensitive and also frequency selective. Each OMS probe was optimized to operate at 2.45 GHz, which is one of target frequencies in biomedical applications. The invisibility to microwave signals of optical fibers used in developing the OMS probes was investigated and verified. This probe, guarantees almost perturbation-free measurements. The OMS probes were also studied and verified for omnidirectivity and cross-polarization rejection performance. In the omnidirectivity test, the probes showed an absolute deviation of about ± 0.3 dB with respect to an unidirectional response. The co-to-cross polarization ratio was measured and found to be better than 60 dB. The frequency response of the probe was studied theoretically and experimentally in order to qualify the performance of the matching network and to assess its impact on the frequency response of the OMS probes. The performance of the probes was validated by measuring the NF distribution of a 50-Ω microstrip transmission line. The measurements were compared with results of simulations using HFSS®. The

results also showed that the sensitivity of the OMS probe can be better that 0.037 V/m. The associated error with both magnitude and phase measurement results are 6.4% and 3.2 degrees, respectively, compared to simulations.

By developing a linear array of OMS probes, the measurement speed for an E-field measurement was increased more than 100 times (see Figure 4.2) compared to commercially available opto-mechanically switched systems [98]. Parameters such as mutual coupling and the effect of shadowing, which influence measurements were also studied to get minimum inter-element interactions, leading to the choice of an appropriate probe spacing ($\lambda/4$). To improve the accuracy of measurements using the array, the raw measurement data were corrected using the proposed calibration technique, to compensate for uncertainties in the probes' responses. The E-field measurements made with the developed imager were in good agreement with the simulations and were very rapid.

Benefiting from carrier cancellation, the isolation between the input and output ports of the imager was improved by about 60 dB. This enabled us to increase the signal fed to the NF imager and increase the overall dynamic range by 18 dB in the monostatic mode. The actual improvement is probably higher than this but the system was not tested with sufficient power to cause saturation.

The results from the imager were validated by comparing them with known fields when it was set to measure the E-field distribution of several microwave components such as a microstrip transmission line, a co-planar waveguide as well as radiating antenna (e.g. PIFA, antenna). The results were all in good agreement with simulations.

Finally, the imager together with a phantom representing biological tissue (i.e., the breast) was verified in order to asses its performance in the context of breast cancer imaging. The measured scattered fields were compared with simulation, which showed very good agreement.

7.2 Future work

To extend the project beyond the scope of this thesis based on the developed technology, it is first necessary to look at the restrictions that currently exist in the setup and try to overcome them. Possible directions for future work include:

- Development of broadband OMS probes;

- Implementation of a wide-band homodyne detector;
- Development of more compact OMS probes;
- Real-time imaging using a 2D OMS probe array;
- Development of an optically-excited probe.

7.2.1 Broadband OMS probe

A limitation of the current imager is the narrow bandwidth of its probes, which is partly due to the addition of a matching network to the probes optimized for operation at 2.45 GHz. We could improve the probes' bandwidth by implementing a state-of-the-art matching network with larger bandwidth so that the probes measure in a wider frequency range. As discussed in Chapter 3, scattering properties of the OMS probe can be improved by making it resonant at desired frequencies. This can be done, by adding an inductive reactance in series with the short-dipole which has a capacitive input impedance, so that a resonance occurs in one of the two states of its photodiode (i.e. ON and/or OFF states). Such a matching network (simple inductive circuit; first order) limited the frequency bandwidth of the OMS probe to approximately 400MHz. In order to increase this bandwidth, higher order matching network (i.e., multiple inductor and capacitor circuit) can be used. For a preliminary test, a matching network consisting of three inductors where two of them are on each arm of the dipole, and the third one is across the dipole arms, was investigated. The equivalent circuit of the OMS probe incorporating the proposed matching network and photodiode as well as a short-dipole is illustrated in Figure 7.1. An OMS probe consisting of such a matching network has been fabricated and is shown in Figure 7.2. The operation of the proposed matching network was also investigated. Figure 7.3 demonstrates the frequency response of the probe measured by reading the power of the sideband ($f_{RF} \pm f_{IF}$) generated by probe using a spectrum analyzer. The results show the relative sideband of the probe over the 1-4 GHz bandwidth. To see the improved bandwidth of the probe, one can compare the bandwidth of this probe with the probe discussed in Chapter 3 (See Figure 3.24).

At the end, the E-field measurements obtained using the proposed probe were verified by setting the probe to measure an E-field distribution of a 50-Ω transmission

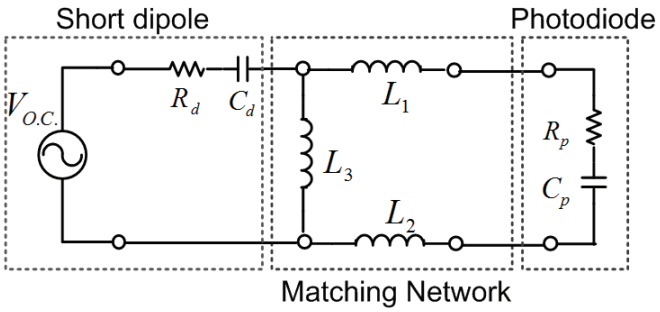

Figure 7.1 Equivalent circuit of the proposed OMS probe with its matching network.

line at different frequencies and making a comparison with simulation. Figure 7.4 demonstrate the E-field measurement of the transmission line at a distance at a distance of 3 mm from the line at frequencies of 2, 2.6, 3 and 4 GHz. Due to the lack of a wide-band homodyne detector, it was not possible to show actual dynamic range of the probe at frequencies other than 2.45 GHz. Therefore, the dynamic range shown in Figure 7.4, is not due to the probe's performance, whereas it is because of limited dynamic range of the spectrum analyzer used.

7.2.2 Wide-band homodyne detector

In order to make magnitude and phase measurements at other frequencies than 2.45 GHz using the current setup, not only a broadband probe but also a wide-band homodyne detector capable of handling signals at the desired frequencies, is required. Mixers, which are the essential parts in homodyne detector, should be operating in wide band of frequency range. Thus, choosing a mixer having the above mentioned characteristics is a key part in development of a wide-band homodyne detector. Figure 7.5 shows a wide-band mixer (SGM-03-13) operating up to 7 GHz, manufactured by Linear Technology Co., which can be one the suitable alternatives. The mixer has a conversion-loss and LO/RF isolation about 7 dB and more than 20 dB respectively up to 7 GHz. The mixer was mounted of a Duroid RT/6006 substrate but was not tested in the developed imager.

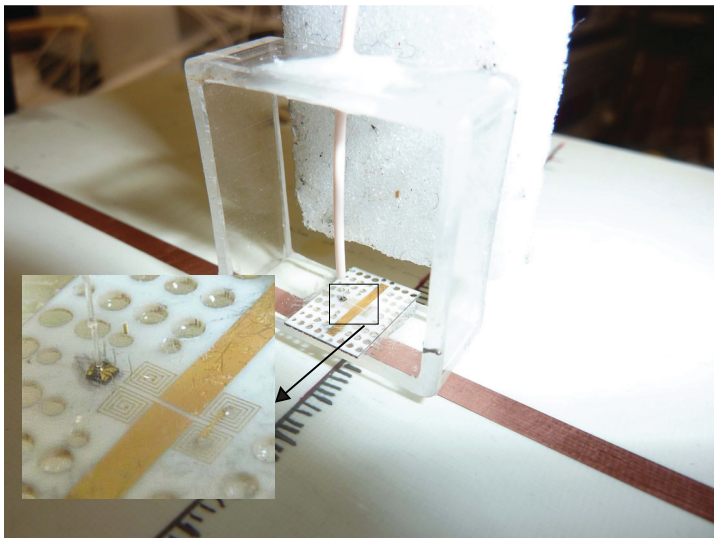

Figure 7.2 Photograph of the developed OMS probe. The zoom in the left corner shows the layout of the photodiode, matching network and wire bonds.

7.2.3 Compact OMS probe

To prevent using a strain relief structure (optical fiber fixture) in the OMS probe construction (see Figure 7.2 for the optical fiber fixture) and consequently to make the probe more compact; it is suggested to use one of the two following methods in coupling optical fiber to the OMS probe photodiode: 1) planar (i.e., horizontal) coupling, 2) side-illuminated photodiode.

Planar optical fiber coupling

To make a planar coupling between an optical fiber and a photodiode, one can polish the tip of a single mode fiber at 45 degrees. A 45-degree cut causes the end of the fiber to act as a mirror, and totally reflects optical power at 90 degree with respect to the fiber axis. Then, the polished fiber can be fixed above the photodiode where maximum optical power couples to its active area, as schematically shown in Figure 7.6.

In order to prove the above mentioned coupling technique, a single mode optical fiber was polished at a 45-degree angle. A photograph of the angled-cut fiber and a measurement of the light reflected by its built-in mirror perpendicular to the axis of

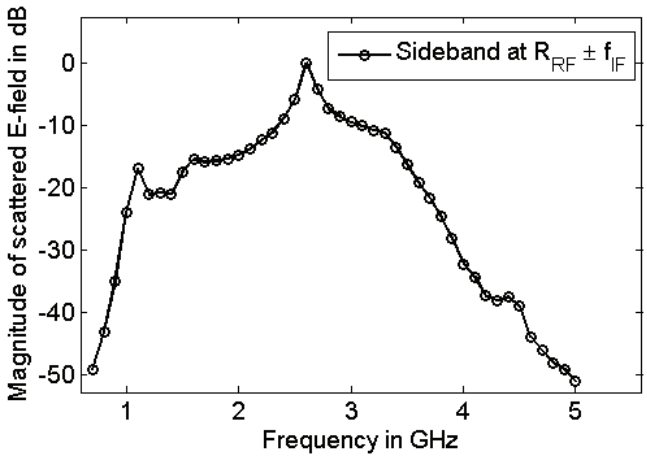

Figure 7.3 Frequency response of the broadband OMS probe

the optical fiber are shown in Figure 7.7.

In the developed OMS probe discussed in Chapter 3, the illuminating laser diode operates at a wavelength of 1550 nm within the wavelength is in the interval (i.e., 1490-1636 nm) at which the performance of the angled-cut optical fiber is maintained.

Side-illuminated photodiode

Another approach to improve the compactness of the imager by avoiding perpendicular coupling between of the optical fiber and photodiode consists in using side-illuminated photodiodes. Figure 7.8 shows a side-illuminated photodiode manufactured by Enablence Co. In this case, the optical fiber can easily be coupled to the photodiode from its photo-sensitive facet (i.e., carved facet) located on its side.

7.2.4 Array of 2D OMS probes

Measurement speed in the current imaging system is limited because of the requirement to translate the probes. So, in order to achieve faster field scanning of a device under test, it is suggested to develop a 2D array of OMS probes so as to completely remove all mechanical translations. Instead electronic switching between the probes is used. A schematic depicting a 2D OMS array is shown in Figure 7.9, in which the

angle-cut optical fiber as proposed earlier has been used to achieve a low-profile array [55].

7.2.5 Optically-excited probe: Generating RF emission using an optical signal

The antenna consists of a small radiating metallic structure such as a short-dipole or small loop, together with two photodiodes to which optical fibers are coupled. In order to excite the probe and make it radiate, it is illuminated through a fiber by light modulated (see Figure 7.10) at a desired RF frequency. Then, the photodiode converts the optical signals to microwave signals which are radiated by the antenna. In practice, the photodiode needs to be biased at a certain voltage. This can be done by a second photodiode which is in parallel with the modulated photodiode. This photodiode receives a continuous optical signal and converts it into a biasing voltage applied to the RF modulated photodiode. Figure 7.11 shows schematic of such an optically-excited radiator. It is also worth mentioning that a zero-bias photodiode, which is desirable in the case of the optically modulated probe described in this thesis, leads to limited conversion gain and bandwidth. Therefore, a trade-off between the modulation index and the bandwidth/gain of the probe is needed.

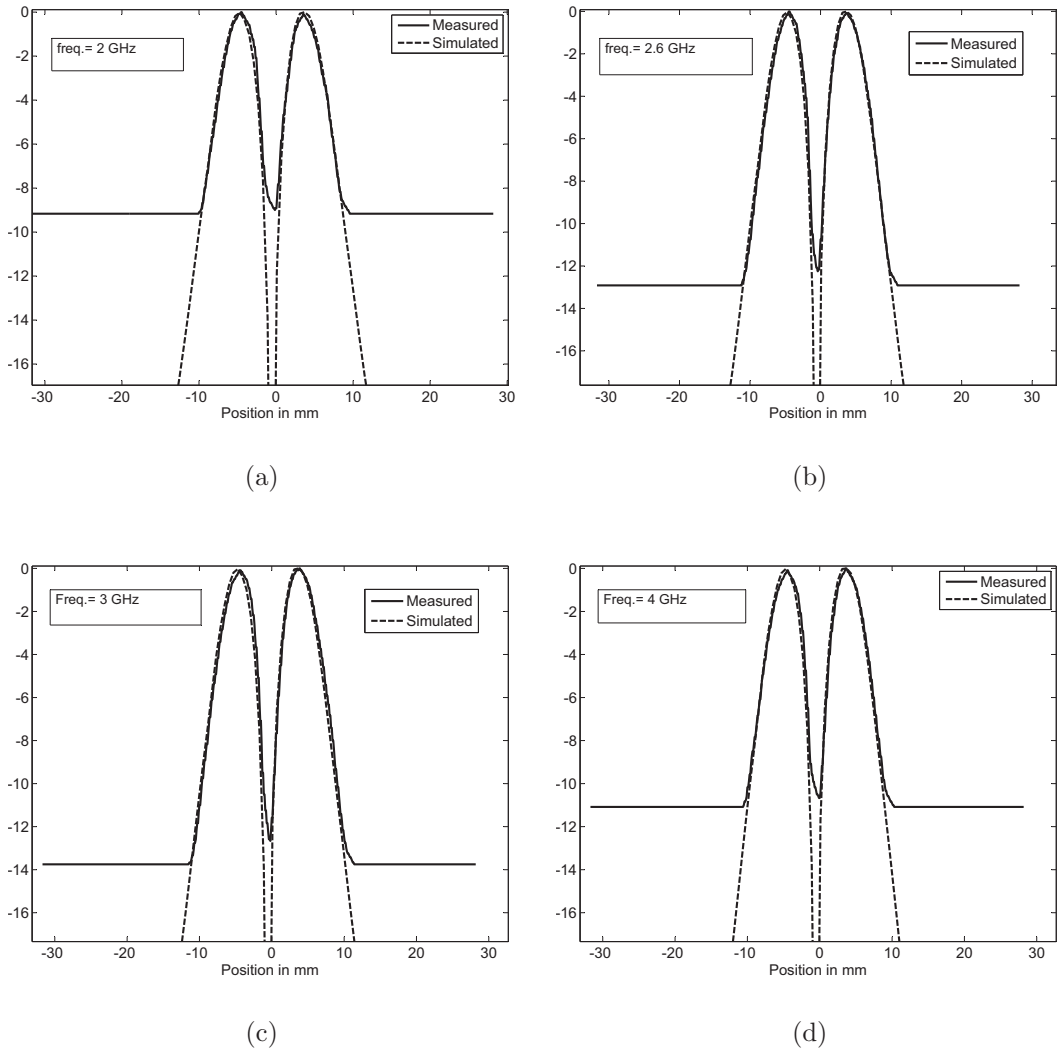

Figure 7.4 Magnitude (in dB)of the transverse E-field of the microstrip transmission line under at a distance of 3 mm at different frequencies; (a) 2 GHz; (b) 2.6 GHz; (c) 3 GHz; (d) 4 GHz.

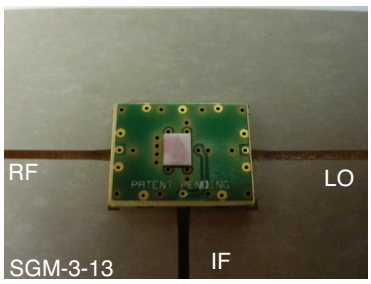

Figure 7.5 Photograph of the a wide-band mixer operating up to 7 GHz, manufactured by Linear Technology Co.

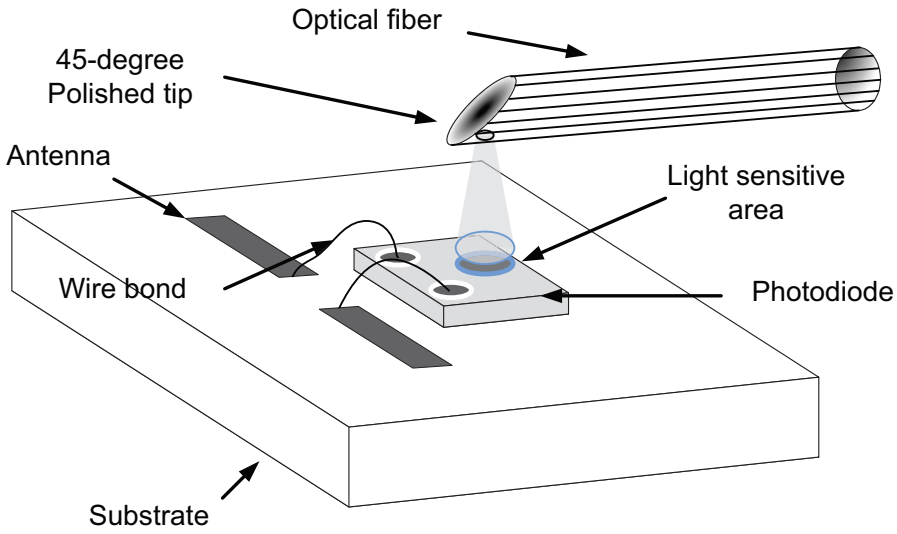

Figure 7.6 Schematic depicting an OMS probe with planar optical fiber coupling.

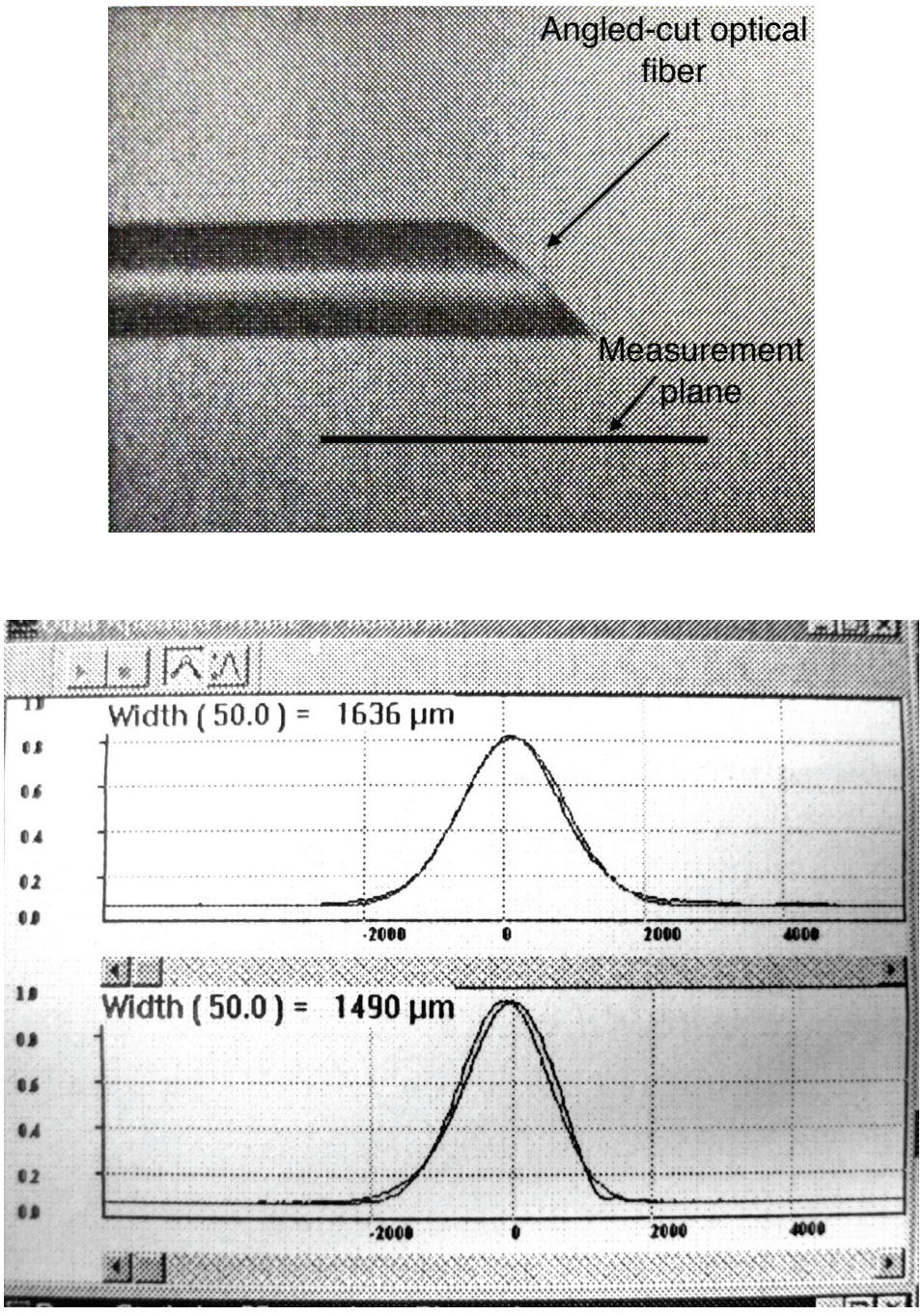

Figure 7.7 The photograph of a 45-degree angled-cut an optical fiber and the measurement results at 1490 and 1636 nm.

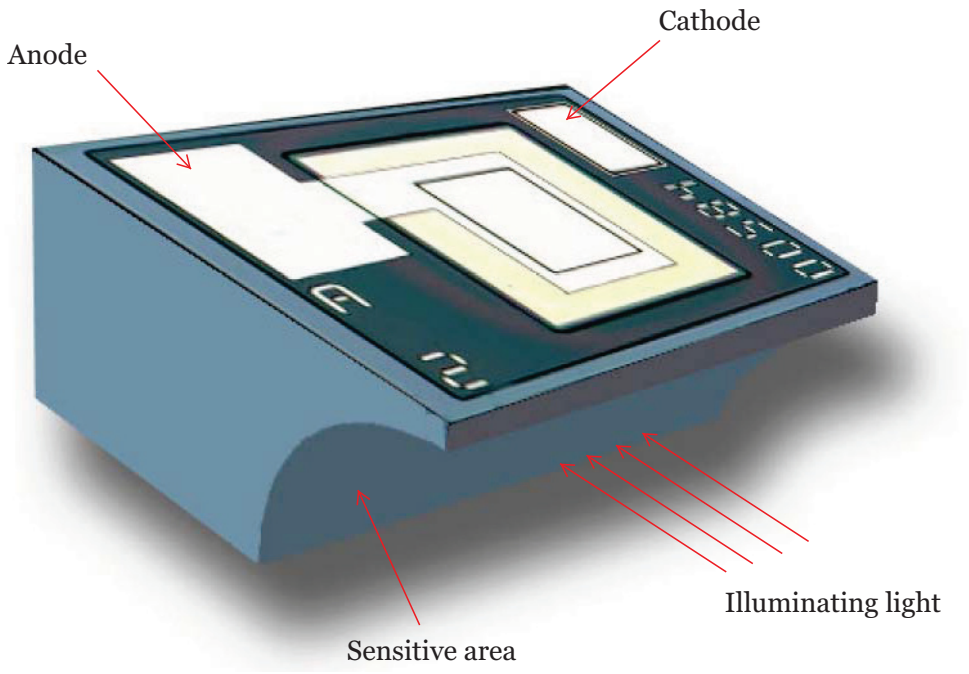

Figure 7.8 Photograph of a side-illuminated photodiode (PDCS200E) manufactured by Enablence Co.

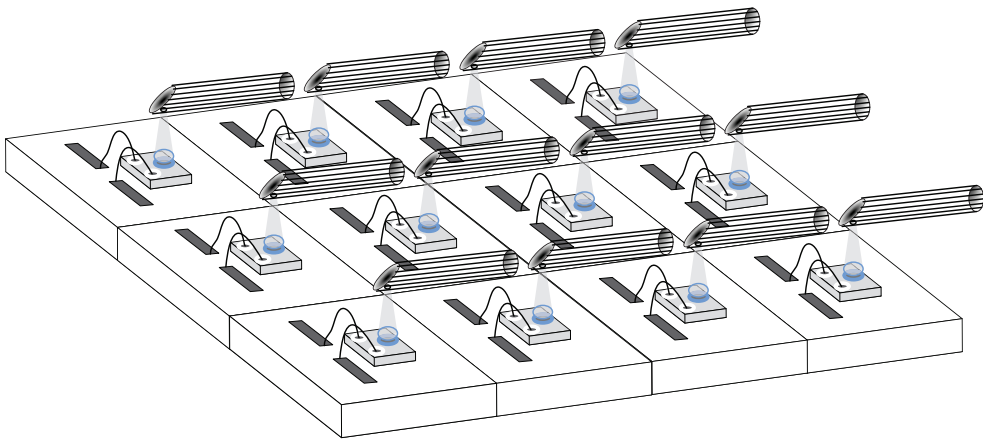

Figure 7.9 Schematic of the proposed OMS probe array.

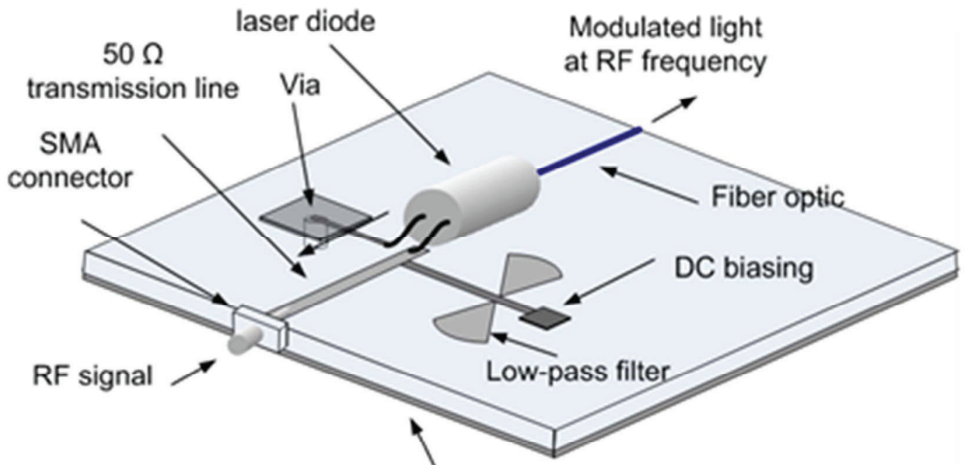

Figure 7.10 Example of microwave circuit for modulating optical signal.

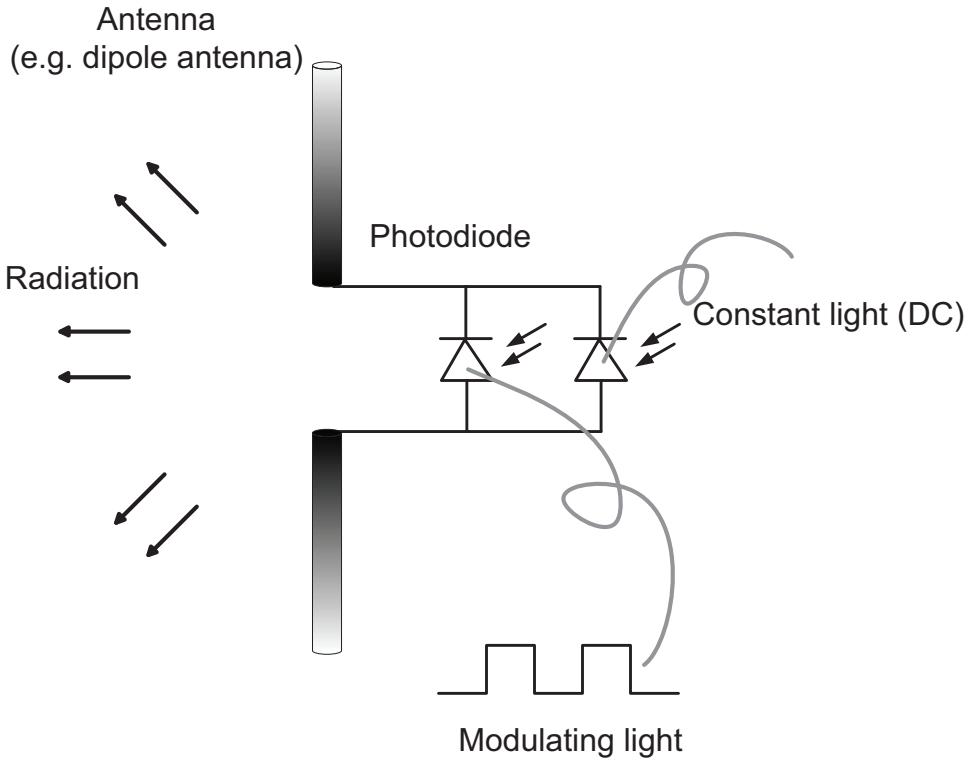

Figure 7.11 Schematic of an optically-excited probe-antenna.

References

[1] W. Stutzman and G. Thiele, Antenna Theory and Design. John Wiley, 1998.

[2] Q. Han, K. Inagaki, and T. Ohira, "Array antenna characterization technique based on evanescent reactive-near-field probing in an ultra-small anechoic box," in Microwave Symposium Digest, 2003 IEEE MTT-S International, vol. 3, June 2003, pp. 1841–1844 vol.3.

[3] C. Balanis, Antenna Theory: Analysis and Design. John Wiley, 1989.

[4] S. Laybros, P. Combes, and H. Mametsa, "The "very-near-field" region of equiphase radiating apertures," Antennas and Propagation Magazine, IEEE, vol. 47, no. 4, pp. 50–66, Aug. 2005.

[5] J.-J. Laurin, J.-F. Zurcher, and F. Gardiol, "Near-field diagnostics of small printed antennas using the equivalent magnetic current approach," Antennas and Propagation, IEEE Transactions on, vol. 49, no. 5, pp. 814–828, May 2001.

[6] S. Bokhari, J.-F. Zurcher, J. Mosig, and F. Gardiol, "Near fields of microstrip antennas," Antennas and Propagation, IEEE Transactions on, vol. 43, no. 2, pp. 188–197, Feb 1995.

[7] B. Fourestie, J.-C. Bolomey, T. Sarrebourse, Z. Altman, and J. Wiart, "Spherical near field facility for characterizing random emissions," Antennas and Propagation, IEEE Transactions on, vol. 53, no. 8, pp. 2582–2589, Aug. 2005.

[8] T. Dubois, S. Jarrix, A. Penarier, P. Nouvel, D. Gasquet, L. Chusseau, and B. Azais, "Near-field electromagnetic characterization and perturbation of logic circuits," Instrumentation and Measurement, IEEE Transactions on, vol. 57, no. 11, pp. 2398–2404, Nov. 2008.

[9] K. Munoz, A. Perrey, and R. Zoughi, "Potential application of the modulated scatterer technique to multilayered material evaluation and health monitoring," in Instrumentation and Measurement Technology Conference Proceedings, 2008. IMTC 2008. IEEE, May 2008, pp. 1643–1647.

[10] ——, "Embedded modulating dipole scattering for near-field microwave inspection of concrete: Preliminary investigation," in Subsurface sensors and applications, Denver, Colorado, July 1999, pp. 208–214.

[11] B. Omrane, J.-J. Laurin, and Y. Goussard, "Subwavelength-resolution microwave tomography using wire grid models and enhanced regularization techniques," Microwave Theory and Techniques, IEEE Transactions on, vol. 54, no. 4, pp. 1438–1450, June 2006.

[12] D. Baudry, C. Arcambal, A. Louis, B. Mazari, and P. Eudeline, "Applications of the near-field techniques in emc investigations," Electromagnetic Compatibility, IEEE Transactions on, vol. 49, no. 3, pp. 485–493, Aug. 2007.

[13] B. Yan, S. Saoudy, and B. Sinha, "A low cost planar near-field/far-field antenna measurement system," in Antennas and Propagation Society International Symposium, 1997. IEEE., 1997 Digest, vol. 1, Jul 1997, pp. 152–155 vol.1.

[14] J. Nye, "A simple method of spherical near-field scanning to measure the far fields of antennas or passive scatterers," Antennas and Propagation, IEEE Transactions on, vol. 51, no. 8, pp. 2091–2098, Aug. 2003.

[15] R. Azaro and S. Caorsi, "Mst probes for electromagnetic fields measurements for emc applications," in Electromagnetic Compatibility, 2001. EMC. 2001 IEEE International Symposium on, vol. 1, 2001, pp. 357–362 vol.1.

[16] ——, "Mst measurement technique for emc calibrations and exposure hazard evaluation," in Electromagnetic Compatibility, 2003. EMC '03. 2003 IEEE International Symposium on, vol. 1, May 2003, pp. 58–61 Vol.1.

[17] M. Quilez, M. Aragon, A. Atienza, M. Fernandez-Chimeno, P. Riu, and F. Silva, "A near-field probe for in situ emi measurements of industrial installations," Electromagnetic Compatibility, IEEE Transactions on, vol. 50, no. 4, pp. 1007–1010, Nov. 2008.

[18] ——, "A near-field probe for in situ emi measurements of industrial installations," Electromagnetic Compatibility, IEEE Transactions on, vol. 50, no. 4, pp. 1007–1010, Nov. 2008.

[19] J. Mallorqui, N. Joachimowicz, A. Broquetas, and J. Bolomey, "Quantitative images of large biological bodies in microwave tomography by using numerical and real data," Electronics Letters, vol. 32, no. 23, pp. 2138–2140, Nov 1996.

[20] A. Joisel, J. Mallorqui, A. Broquetas, J. Geffrin, N. Joachimowicz, M. Lossera, L. Joire, and J. Bolomey, "Microwave imaging techniques for biomedical applications," in Instrumentation and Measurement Technology Conference, 1999. IMTC/99. Proceedings of the 16th IEEE, vol. 3, 1999, pp. 1591–1596 vol.3.

[21] J. Candy and C. Pichot, "Active microwave imaging: a model-based approach," Antennas and Propagation, IEEE Transactions on, vol. 39, no. 3, pp. 285–290, Mar 1991.

[22] J. Bolomey, A. Izadnegahdar, L. Jofre, C. Pichot, G. Peronnet, and M. Solaimani, "Microwave diffraction tomography for biomedical applications," Microwave Theory and Techniques, IEEE Transactions on, vol. 30, no. 11, pp. 1998–2000, Nov. 1982.

[23] J. Bolomey and C. Pichot, "Microwave tomography: From theory to practical imaging systems," Imaging System and Technology, International Journal of, vol. 2, no. 1, pp. 144–156, Oct. 1990.

[24] J. Bolomey and F. Gardiol, Engineering applications of the modulated scatterer technique. Artech House, 2001.

[25] D. N. Lu, "Breast cancer," 2010. [Online]. Available: http://www.breastcancer.com/

[26] "Breast cancer," 2010. [Online]. Available: http://www.cancer.gov/

[27] G. Smith, "Limitations on the size of miniature electric-field probes," Microwave Theory and Techniques, IEEE Transactions on, vol. 32, no. 6, pp. 594–600, Jun 1984.

[28] ——, "Analysis of miniature electric field probes with resistive transmission lines," Microwave Theory and Techniques, IEEE Transactions on, vol. 29, no. 11, pp. 1213–1224, Nov 1981.

[29] R. J. King, Microwave Homodyne System. Wiley New York, 1978.

[30] H. Bassen and G. Smith, "Electric field probes–a review," Antennas and Propagation, IEEE Transactions on, vol. 31, no. 5, pp. 710–718, Sep 1983.

[31] J. Polivka, "An overview of microwave sensor technology," in High Frequency Electronics, Summit Technical Media, LLC, vol. 6, no. 4, April 2007, pp. 32–42.

[32] G. Hygate, "Measuring microwave fields with a minimum of perturbation," in Precision Electromagnetic Measurements, 1990. CPEM '90 Digest., Conference on, Jun 1990, pp. 198–199.

[33] J. Richmond, "A modulated scattering technique for measurement of field distributions," Microwave Theory and Techniques, IRE Transactions on, vol. 3, no. 4, pp. 13–15, July 1955.

[34] R. Justice and V. Rumsey, "Measurement of electric field distributions," Antennas and Propagation, IRE Transactions on, vol. 3, no. 4, pp. 177–180, October 1955.

[35] M. Abou-Khousa, S. Kharkovsky, and R. Zoughi, "Novel near-field millimeter-wave differential probe using a loaded modulated aperture," Instrumentation and Measurement, IEEE Transactions on, vol. 58, no. 5, pp. 1273–1282, May 2009.

[36] M. Hu, "On measurements of microwave e and h field distributions by using modulated scattering methods," Microwave Theory and Techniques, IRE Transactions on, vol. 8, no. 3, pp. 295–300, May 1960.

[37] R. King and Y. Yen, "Probing amplitude, phase, and polarization of microwave field distributions in real time," Microwave Theory and Techniques, IEEE Transactions on, vol. 29, no. 11, pp. 1225–1231, Nov 1981.

[38] Q. Chen, S. Kato, and K. Sawaya, "Estimation of current distribution on multilayer printed circuit board by near-field measurement," Electromagnetic Compatibility, IEEE Transactions on, vol. 50, no. 2, pp. 399–405, May 2008.

[39] J.-H. Choi, J.-I. Moon, and S.-O. Park, "Measurement of the modulated scattering microwave fields using dual-phase lock-in amplifier," Antennas and Wireless Propagation Letters, IEEE, vol. 3, pp. 340–343, 2004.

[40] R.-R. Lao, W.-T. Shay, J. Hsu, and J.-H. Tarng, "Optically modulated scatterer technique for radiation pattern measurement of small antennas and rfid tags," Antennas and Wireless Propagation Letters, IEEE, vol. 8, pp. 76–79, 2009.

[41] R.-R. Lao, W.-L. Liang, W.-T. Shay, R. Thompson, R. Dudley, O. Merckel, N. Ribiere-Tharaud, J.-C. Bolomey, and J.-H. Tarng, "High-sensitivity optically modulated scatterer for electromagnetic-field measurement," Instrumentation and Measurement, IEEE Transactions on, vol. 56, no. 2, pp. 486–490, April 2007.

[42] D. Lawrence and K. Sarabandi, "Electromagnetic scattering from vibrating penetrable objects using a general class of time-varying sheet boundary conditions," Antennas and Propagation, IEEE Transactions on, vol. 54, no. 7, pp. 2054–2061, July 2006.

[43] R. Wang and M. Tabib-Azar, "Super resolution imaging of material properties using mems near-field microwave spatial modulator arrays," in Nano/Micro Engineered and Molecular Systems, 2006. NEMS '06. 1st IEEE International Conference on, Jan. 2006, pp. 1540–1545.

[44] G. Hygate and J. F. Nye, "Measuring microwave fields directly with an optically modulated scatterer," Measurement Science and Technology, vol. 1, no. 8, pp. 703–709, 1990. [Online]. Available: http://stacks.iop.org/0957-0233/1/703

[45] P. Garreau, K. Van't Klooster, J. Bolomey, and D. Picard, "Optimization of the arrangement compact range-modulated scattering probe array for rapid far-field antenna measurement," in Antennas and Propagation, 1993., Eighth International Conference on, 1993, pp. 376–379 vol.1.

[46] J.-C. Bolomey, B. Cown, G. Fine, L. Jofre, M. Mostafavi, D. Picard, J. Estrada, P. Friederich, and F. Cain, "Rapid near-field antenna testing via arrays of modulated scattering probes," Antennas and Propagation, IEEE Transactions on, vol. 36, no. 6, pp. 804–814, Jun 1988.

[47] B. Cown and J. Ryan, C.E., "Near-field scattering measurements for determining complex target rcs," Antennas and Propagation, IEEE Transactions on, vol. 37, no. 5, pp. 576–585, May 1989.

[48] C. Paul, Introduction to Electromagnetic Compatibility. John Wiley, 1992.

[49] M. Kanda, "Standard probes for electromagnetic field measurements," Antennas and Propagation, IEEE Transactions on, vol. 41, no. 10, pp. 1349–1364, Oct 1993.

[50] E. Suzuki, S. Arakawa, M. Takahashi, H. Ota, K. Arai, and R. Sato, "Visualization of poynting vectors by using electro-optic probes for electromagnetic fields," Instrumentation and Measurement, IEEE Transactions on, vol. 57, no. 5, pp. 1014–1022, May 2008.

[51] K. Yang, G. David, J.-G. Yook, I. Papapolymerou, L. Katehi, and J. Whitaker, "Electrooptic mapping and finite-element modeling of the near-field pattern of a microstrip patch antenna," Microwave Theory and Techniques, IEEE Transactions on, vol. 48, no. 2, pp. 288 –294, feb 2000.

[52] E. Suzuki, T. Miyakawa, H. Ota, K. Arai, and R. Sato, "Optical magnetic field sensing with a loop antenna element doubly-loaded with electro-optic crystals," in Electromagnetic Compatibility, 2003 IEEE International Symposium on, vol. 1, Aug. 2003, pp. 442–447 vol.1.

[53] T. Calazans, H. Griffiths, A. Cullen, D. Davies, and R. Benjamin, "Antenna radiation pattern measurement using a near-field wire scattering technique," Microwaves, Antennas and Propagation, IEE Proceedings -, vol. 145, no. 3, pp. 263–267, Jun 1998.

[54] D. Land, "Application of the nonresonant perturbation technique to the measurement of high-frequency fields in biological phantom materials," Electronics Letters, vol. 24, no. 1, pp. 70–72, Jan 1988.

[55] A. Franchois, A. Joisel, C. Pichot, and J.-C. Bolomey, "Quantitative microwave imaging with a 2.45-ghz planar microwave camera," Medical Imaging, IEEE Transactions on, vol. 17, no. 4, pp. 550–561, Aug. 1998.

[56] J.-F. Zurcher, "High performance near field measurements for antennas and microstrip circuits," in Precision Electromagnetic Measurements, 1994. Digest., 1994 Conference on, Jun-1 Jul 1994, pp. 376–377.

[57] T. Budka, S. Waclawik, and G. Rebeiz, "A coaxial 0.5-18 ghz near electric field measurement system for planar microwave circuits using integrated probes,"

Microwave Theory and Techniques, IEEE Transactions on, vol. 44, no. 12, pp. 2174–2184, Dec 1996.

[58] A. Vural, D. Cheng, and B. Strait, "Measurement of diffraction fields of finite cones by a scattering technique using light modulation," Antennas and Propagation, IEEE Transactions on, vol. 11, no. 2, pp. 200–201, Mar 1963.

[59] W. Liang, G. Hygate, J. Nye, D. Gentle, and R. Cook, "A probe for making near-field measurements with minimal disturbance: the optically modulated scatterer," Antennas and Propagation, IEEE Transactions on, vol. 45, no. 5, pp. 772–780, May 1997.

[60] J. F. Nye and G. Hygate, "Measuring a microwave field close to a conductor," Measurement Science and Technology, vol. 2, no. 9, pp. 838–845, 1991. [Online]. Available: http://stacks.iop.org/0957-0233/2/838

[61] A. Sowa and J. Witkowski, "Field calibration system implementing 3-d optically modulated scatterers for immunity test site purposes," Electromagnetic Compatibility, IEEE Transactions on, vol. 46, no. 4, pp. 648–654, Nov. 2004.

[62] S. Capdevila, M. Jofre, J. Rodriguez, M. Guardiola, A. Papio, F. De Flaviis, and L. Jofre, "Uwb mst mems-based near-field imaging system," in Antennas and Propagation Society International Symposium, 2008. AP-S 2008. IEEE, July 2008, pp. 1–4.

[63] M. Ghasr, M. Abou-Khousa, S. Kharkovsky, R. Zoughi, and D. Pommerenke, "A novel 24 ghz one-shot, rapid and portable microwave imaging system," in Instrumentation and Measurement Technology Conference Proceedings, 2008. IMTC 2008. IEEE, May 2008, pp. 1798–1802.

[64] R. Azaro, S. Caorsi, and P. M., "A 3-GHz microwave imaging system based on a modulated scattering technique and on a modified born approximation," Imaging Systems and Technology, International Journal of, vol. 9, no. 5, pp. 395 – 403, 1998.

[65] A. Broquetas, J. Romeu, J. Rius, A. Elias-Fuste, A. Cardama, and L. Jofre, "Cylindrical geometry: a further step in active microwave tomography,"

Microwave Theory and Techniques, IEEE Transactions on, vol. 39, no. 5, pp. 836–844, May 1991.

[66] M. Lazebnik, M. Okoniewski, J. Booske, and S. Hagness, "Highly accurate debye models for normal and malignant breast tissue dielectric properties at microwave frequencies," Microwave and Wireless Components Letters, IEEE, vol. 17, no. 12, pp. 822 –824, dec. 2007.

[67] G. Freiburger and R. Zoughi, "Dielectric material characterization by complex ratio of embedded modulated scatterer tecnoqie states," in Instrumentation and Measurement Technology Conference, 2005. IMTC 2005. Proceedings of the IEEE, vol. 1, May 2005, pp. 67–71.

[68] P. Rogers, "Application of the minimum scattering antenna theory to mismatched antennas," Antennas and Propagation, IEEE Transactions on, vol. 34, no. 10, pp. 1223–1228, Oct 1986.

[69] R. Hansen, "Relationships between antennas as scatterers and as radiators," Proceedings of the IEEE, vol. 77, no. 5, pp. 659–662, May 1989.

[70] K. Iigusa, T. Sawaya, M. Taromaru, T. Ohira, and B. Komiyama, "Experimental proof of electrically invisible state of inductively loaded dipole and proposal of electrically invisible meander-lines," Antennas and Propagation, IEEE Transactions on, vol. 54, no. 11, pp. 3374–3382, Nov. 2006.

[71] S. Jarrix, T. Dubois, R. Adam, P. Nouvel, B. Azais, and D. Gasquet, "Probe characterization for electromagnetic near-field studies," Instrumentation and Measurement, IEEE Transactions on, vol. 59, no. 2, pp. 292–300, Feb. 2010.

[72] H. Memarzadeh-Tehran, J.-J. Laurin, and R. Kashyap, "Optically modulated probe for precision near-field measurements," Instruments and Measurement, IEEE Transactions on, To appear 2010.

[73] J.-W. Baik, T.-H. Lee, and Y.-S. Kim, "Uwb bandpass filter using microstrip-to-cpw transition with broadband balun," Microwave and Wireless Components Letters, IEEE, vol. 17, no. 12, pp. 846 –848, dec. 2007.

[74] F. Boulahchiche, "Adaptation de la methode de diffusion modulee a la mesure du sar induit par un radiotelephone commercial," Ph.D. dissertation, University Paris XI, Orsay France, 2000.

[75] H. Tehran, J.-J. Laurin, and R. Kashyap, "A low-perturbation near-field imager equipped with optical mst probes," in Antennas and Propagation, 2009. EuCAP 2009. 3rd European Conference on, March 2009, pp. 3649–3653.

[76] H. Tehran, N. Laflamme-Mayer, J.-J. Laurin, and R. Kashyap, "A near-field measurement setup using an array of optically modulated scatterers," in Signals, Systems and Electronics, 2007. ISSSE '07. International Symposium on, 30 2007-Aug. 2 2007, pp. 481–484.

[77] M. Mostafavi, J.-C. Bolomey, and D. Picard, "Experimental study on compensation of array element pattern of collinear dipole array sensor," EICE Trans Commun, Inst Electron Inf Commun Eng., vol. E88-B, no. 8, pp. 3314–3316, Aug 2005.

[78] K. Awai, D. Aizawa, K. Taira, K. Sawaya, and R. Sato, "Compensation of element pattern in 3-element array sensor for estimation of electromagnetic source location," in Electromagnetic Compatibility, 2003. EMC '03. 2003 IEEE International Symposium on, vol. 1, May 2003, pp. 131–134 Vol.1.

[79] B. Fankem and K. Melde, "Nested pifas for dual mode of operation: Gps and global communications," Antennas and Wireless Propagation Letters, IEEE, vol. 7, pp. 701–705, 2008.

[80] T. Brauner and X. Zhao, "A novel carrier suppression method for rfid," Microwave and Wireless Components Letters, IEEE, vol. 19, no. 3, pp. 128–130, March 2009.

[81] G. Lasser, R. Langwieser, and A. Scholtz, "Broadband suppression properties of active leaking carrier cancellers," in RFID, 2009 IEEE International Conference on, April 2009, pp. 208–212.

[82] S. Roome, "Analysis of quadrature detectors using complex envelope notation," Radar and Signal Processing, IEE Proceedings, vol. 136, no. 2, pp. 95–100, Apr 1989.

[83] A. Sadeghfam and H. Heuermann, "Electrically tunable bandpass filter with integrated carrier suppression for uhf rfid systems," in Microwave Conference, 2008. EuMC 2008. 38th European, Oct. 2008, pp. 1727–1730.

[84] W.-K. Kim, M.-Q. Lee, J.-H. Kim, H. sun Lim, J.-W. Yu, B.-J. Jang, and J.-S. Park, "A passive circulator with high isolation using a directional coupler for rfid," in Microwave Symposium Digest, 2006. IEEE MTT-S International, June 2006, pp. 1177–1180.

[85] J. Kim, H. Yoon, J. Park, and J. Burm, "A method to improve isolation for rfid applications," in Wireless Technology, 2005. The European Conference on, Oct. 2005, pp. 427–430.

[86] Z. Q. Zhang, Q. H. Liu, C. Xiao, E. Ward, G. Ybarra, and W. Joines, "Microwave breast imaging: 3-d forward scattering simulation," Biomedical Engineering, IEEE Transactions on, vol. 50, no. 10, pp. 1180–1189, Oct. 2003.

[87] K. Paulsen and P. Meaney, "Nonactive antenna compensation for fixed-array microwave imaging. i. model development," Medical Imaging, IEEE Transactions on, vol. 18, no. 6, pp. 496–507, June 1999.

[88] A. Diaz-Bolado and J. Laurin, "A new configuration for enhancing contrast in microwave tomography applied to breast cancer detection," in URSI, 2008. IEEE, June 2008.

[89] S. Semenv, V. Posukh, A. Bulyshev, T. Williams, Y. Sizov, A. Souvorov, P. Clark, A. Pavlovsky, and B. Voinov, "Microwave tomography for biomedical applications," in 2003-2004 MIPS/GE Medial System/Amersham Health, Molecular Imaging Seminar Series, May 2004.

[90] J. Rius, C. Pichot, L. Jofre, J. Bolomey, N. Joachimowicz, A. Broquetas, and M. Ferrando, "Planar and cylindrical active microwave temperature imaging: numerical simulations," Medical Imaging, IEEE Transactions on, vol. 11, no. 4, pp. 457–469, Dec 1992.

[91] S. Pan and A. Kak, "A computational study of reconstruction algorithms for diffraction tomography: Interpolation versus filtered-backpropagation,"

Acoustics, Speech and Signal Processing, IEEE Transactions on, vol. 31, no. 5, pp. 1262–1275, Oct 1983.

[92] L. Markley and G. Eleftheriades, "A near-field probe for subwavelength-focused imaging," in Microwave Symposium Digest, 2009. MTT '09. IEEE MTT-S International, June 2009, pp. 281–284.

[93] ——, "Two-dimensional subwavelength-focused imaging using a near-field end-fire antenna-array probe," Antennas and Wireless Propagation Letters, IEEE, vol. 8, pp. 1025–1028, 2009.

[94] D. Winters, E. Bond, B. Van Veen, and S. Hagness, "Estimation of the frequency-dependent average dielectric properties of breast tissue using a time-domain inverse scattering technique," Antennas and Propagation, IEEE Transactions on, vol. 54, no. 11, pp. 3517–3528, Nov. 2006.

[95] A. Peyman and C. Gabriel, "Development and characterisation of tissue equivalent materials for frequency range 30-300mhz," Electronics Letters, vol. 43, no. 5, pp. 19–20, 1 2007.

[96] P. Barrier, "Développement d'algorithmes d'inversion rapides et propositons relatives à la configuration du montage de mesures dans un contexte de tomographie micro-ondes appliquée a détection du cancer du sein," Ph.D. dissertation, Ecole Polytechnique de Montreal, Montreal (QC), Canada, 2008.

[97] S. Semenov, R. Svenson, A. Boulyshev, A. Souvorov, V. Borisov, Y. Sizov, A. Starostin, K. Dezern, G. Tatsis, and V. Baranov, "Microwave tomography: two-dimensional system for biological imaging," Biomedical Engineering, IEEE Transactions on, vol. 43, no. 9, pp. 869–877, Sept. 1996.

[98] H. Tehran, N. Laflamme-Mayer, J.-J. Laurin, and R. Kashyap, "A near-field measurement setup using an array of optically modulated scatterers," in Signals, Systems and Electronics, 2007. ISSSE '07. International Symposium on, 30 2007-Aug. 2 2007, pp. 481–484.

Appendix A

Estimation of Measurement Duration in NF Imager Equipped with OMS Probes

Total measurement duration can be estimated by dividing it into the times taken at each part of the NF imager, comprising mechanical movements (translation and settling time of probes), switching time of the probes, start-up, buffering and data acquisition/recording.

In this estimation, it is assumed the probe is about to be placed in a new point where E-field measurement is required. We define as t_s the settling time of a 2D positing setup in both directions x and y. Moreover, the time it takes to switch the probe ON and OFF, the microwave components detection time and the time taken by the LIA for completing a measurement are denoted by t_{p1}, t_{p2}, t_{p3}, respectively, and t_p represents their summation. In the NF imager as explained in Chapter 4, it is necessary to measure I and Q signals at each physical point. Thus, switching time (t_{switch}) between two states, which is done by an SPDT switch, is an effective parameter when estimating total measurement. Equation A.1 is used to calculate the measurement time taken for a single point.

$$t_{singlepoint} = t_s + 2t_p + t_{switch} - t_{p1} \tag{A.1}$$

For an imager equipped with a single probe, the total measurement time also includes the time the positioning system needs to scan the probe over the region of interest. The movement duration between two adjacent points along x and y directions are assigned by t_{movx} and t_{movy}, respectively. Depending on the number of points, the total time can be calculated by Equation A.2.

$$t_{fullscan} = N_x N_Y t_{singlepoint} + (N_y - 1)(N_x - 1)t_{movx} + (N_y - 1)t_{movy} \quad \text{(A.2)}$$

In the case of an array (e.g. linear array), the measurement duration includes the switching time between the array elements (t_{sw}), which is a key parameter in the estimation. A slow switching time between the array's elements not only prevents a reduced measurement time but also may lead to longer measurements compared to an isolated probe. After some mathematical developments, the estimated time by a linear array can be obtained with Equation A.4:

$$t_{arrayscan} = N_y t_{aux} + (N_y - 1)(t_{movy} + t_s) \quad \text{(A.3)}$$

where, N_x and N_y are the number of points in x and y directions, and t_{aux} is given by Equation A.5

$$t_{aux} = N_p t_{singlepoint} + (\frac{N_x}{N_p} - 1)(t_{movx} + t_s) + N_p t_{sw}$$

$$t_{arrayscan} = N_y t_{aux} + (N_y - 1)(t_{movy} + t_s) \quad \text{(A.4)}$$

where, N_x and N_y are the number of points in x and y directions, and t_{aux} is given by Equation A.5

$$t_{aux} = N_p t_{singlepoint} + (\frac{N_x}{N_p} - 1)(t_{movx} + t_s) + N_p t_{sw} \quad \text{(A.5)}$$

Table A summarizes the parameters used in the estimation of a measurement duration and their values in the NF imager equipped with a linear OMS probes array.

Table A.1 Timing of the individuals in the imager.

Timing	t_s	t_{movx}	t_{movx}	t_{movy}	t_{sw}
Typical value	10 msec	30 msec	40 msec	20 msec	20 msec

Appendix B

Mathematical Background of Homodyne Detection using Modulated Scatterer Technique

In [24], the authors developed the mathematical equations of a homodyne detection system using the modulated scatterer technique (MST). The development is shown below.

The received signal from the body under test (BUT) at the antenna port (monostatic, and bistatic) can be decomposed into a modulated (i.e., $\gamma(t)$) and an unmodulated part (i.e., $\chi_0(t)$):

$$\chi(t) = \chi_0(t) + \gamma(t) \tag{B.1}$$

The modulated part contains the information on the field to be measured, while the unmodulated part is produced by carrier residual and parasitic reflections. For an amplitude modulation scheme, the above equation becomes:

$$\chi(t) = a_0 cos(\omega_0 t + \phi_0) + km(t)E_p^n cos(\omega_0 t + \phi) \tag{B.2}$$

where $E_p^n cos(\omega_0 t + \phi)$ is the field component to be measured at the probe location, while $a_0 cos(\omega_0 t + \phi_0)$ represents the unmodulated contribution at the angular frequency ω_0. The bistatic case corresponds to n=1, the monostatic case to n=2, k is a proportionality constant, and $m(t)$ is the low-frequency modulating signal. The signal (i.e., $\chi(t)$) can be treated by homodyne or heterodyne detection.

When homodyne detection is used, the signal is mixed with the following high frequency reference signal $r(t)$:

$$r(t) = a_r cos(\omega_0 t + \phi_r) \tag{B.3}$$

The $\chi(t)$ and $r(t)$ are multiplied within the mixer, producing the in-phase component $i(t)$:

$$i(t) = \langle \chi(t) r(t) \rangle = a_0 a_r cos(\phi_0 - \phi_r) + k a_r m(t) E_p^n cos(n\phi_p - \phi_r) \tag{B.4}$$

In a similar way, the quadrature component $q(t)$ is obtained by means of the same operation, but with the reference signal shifted by $\pi/2$ with respect to the in-phase component:

$$q(t) = \langle \chi(t) r(t + T_0/4) \rangle = a_0 a_r sin(\phi_0 - \phi_r) + k a_r m(t) E_p^n sin(n\phi_p - \phi_r) \tag{B.5}$$

The modulation signal is periodic with frequency f_{mod} and , consequently, can be expanded as an infinite Fourier series, as follows:

$$m(t) = \sum_{k=0}^{\infty} cos(2\pi f_{mod} k t) \tag{B.6}$$

By simplifying the Equations B.4 and B.5 using $sin(x).cos(y) = \frac{1}{2}(sin(x+y) + sin(x+y))$ and making use of a reference signal at the same modulation frequency, a coherent detection then provides two DC signals respectively proportional to the real and imaginary parts of the modulated component:

$$I = K m_1 a_r E_p^n cos(n\phi_p - \phi_r) \propto \Re\{E_p^n e^{j(n\phi_p - \phi_r)}\} \tag{B.7}$$

$$Q = K m_1 a_r E_p^n sin(n\phi_p - \phi_r) \propto \Im\mathfrak{m}\{E_p^n e^{j(n\phi_p - \phi_r)}\} \tag{B.8}$$

Equations B.7 and B.8 reveal that the phase information of the field to be measured will be maintained at mixing procedure of homodyne detection. So, the I and Q can be used by the lock-in amplifier to measure magnitude and phase of the field component.

In heterodyne detection, both the RF signal and reference are translated to an intermediate frequency IF by mixing them with a different signal produced by a local oscillator. The phase shifts and amplitudes ratios are maintained through the mixing procedure. In the next step, the I and Q components at IF are coherently detected by comparison with a reference signal at the same frequency. The resulting signals

are then coherently detected, just as they are in homodyne detection.